Search for Weakly-interacting Long-lived Particles in Proton-Proton Collisions at $\sqrt{s} = 8$ TeV with the ATLAS Detector

Orin Michael Harris

A dissertation submitted in partial fulfillment of
the requirements for the degree of

Doctor of Philosophy

University of Washington

2013

Reading Committee:

Gordon T. Watts, Chair

Henry J. Lubatti

Laurence G. Yaffe

Program Authorized to Offer Degree:
Physics

University of Washington

Abstract

Search for Weakly-interacting Long-lived Particles in Proton-Proton Collisions at $\sqrt{s}$ = 8 TeV with the ATLAS Detector

Orin Michael Harris

Chair of the Supervisory Committee:
Professor Gordon T. Watts
Physics

A search for the decay of a light Higgs boson to a pair of weakly-interacting, long-lived particles in 20.8 fb^{-1} of proton-proton collisions at $\sqrt{s}$ = 8 TeV recorded in 2012 by the ATLAS detector is presented. The strategy requires that both of the long-lived particles decay just before or inside the hadronic calorimeter. No statistically significant excess of events is observed above the expected background and limits on the Higgs boson production and branching ratio to weakly-interacting, long-lived particles are derived as a function of the particle's proper decay length.

TABLE OF CONTENTS

Page

LIST OF FIGURES

LIST OF TABLES

INTRODUCTION

Our current best understanding of nature at small distance scales is based on a reductionistic philosophy. That is, the enormous variety and complexity of matter we see in the universe is ultimately made out of combinations of just a few types of fundamental particles. And that, furthermore, all of the enormous complexity and variety of the *behavior* of matter is ultimately the result of just a few types of fundamental interactions, or *forces*, between those few types of fundamental particles. The so-called Standard Model of particle physics represents a catalog of the few fundamental types of matter particles, but further than that it *predicts* some of the few kinds of fundamental ways in which matter particles can interact. In other words, the Standard Model predicts fundamental forces of nature.

What are particles, and what are forces? In the Standard Model everything is ultimately described by quantum fields. A field is a mathematical description that specifies a magnitude and/or a direction at every point in space and time. The wind is an example of a physical phenomenon that can be described by a field. A quantum field is a field that behaves according to the rules of quantum mechanics. Both matter and forces are described by quantum fields: there are matter fields and there are force fields. Like classical fields, quantum fields can vibrate. However quantum fields differ from classical fields in that their vibrations are quantized: they come in particle-like units of minimum energy. Particles are modeled as quantized vibrations in quantum fields: matter particles are vibrations in matter fields, and force particles are vibrations in force fields. Forces result from the interaction between fields (specifically interactions involving force fields), causing vibrations to attract or repel.

Historically there are four known forces. The first known force is gravity, which is by far the weakest of the four forces. All matter attracts all other matter gravitationally and so, despite the gravitational force between any two individual particles being exceedingly small, the forces between large numbers of particles add up on large distance scales, keeping us planted on the surface of the earth, causing the planets in our solar system to orbit the sun, and our sun to orbit around our galaxy.

On smaller distance scales, however, the gravitional force is so weak as to be negligible compared to the remaining three forces. The Standard Model is concerned with matter at small distances scales and makes no attempt to describe the gravitational interaction.

There are three forces described by the Standard Model. The electromagnetic force describes electric and magnetic fields, electromagnetic waves, and the interaction between electrically charged particles. The electromagnetic force is responsible for the attraction between electrons and nuclei (which together form atoms) and is the force largely active in chemical and biological processes. The particle associated with waves in the the quantum field associated with the electromagnetic force is called the photon (γ). The weak force is responsible for radioactive decay, and is important in nuclear fusion processes. The particles associated with waves in the quantum fields associated with the weak force are the W bosons and the Z boson. The strong force is responsible for binding quarks into hadrons such as the proton and neutron, as well as for binding protons and neutrons into atomic nuclei. The particles associated with waves in the quantum fields associated with the strong force are called gluons (g).

There are two main types of matter fields observed in nature, and the particles corresponding to waves in those fields are called *quarks*, and *leptons*. Quarks interact through all three of the forces described by the Standard Model, while leptons do not interact strongly. Both quarks and leptons can be further subdivided into two types which differ in how they interact electromagnetically. The full particle content of the Standard Model will be described in the next section.

The Standard Model is a very successful model of nature, however it does not describe everything we see in nature. For example there is evidence that particles exist that may be largely invisible to us and so very difficult to detect. Furthermore, while there are only a handful of fundamental particles in the Standard Model, there is no strong reason to suspect that there might not be more particles we have not yet discovered. There are two main reasons why we may not have discovered such new particles: 1) they may be difficult to see, or 2) they may be so massive that it requires a tremendous amount of energy in order to produce them.

For over half a century particle accelerators have been used to compress a large amount of energy into a small amount of space, and therefore, because of Einstein's famous relation $E = mc^2$, they have been able to convert energy into matter. Over the years particle accelerators have gotten more and more powerful, and they have correspondingly become capable of creating particles of greater and greater mass. As particle accelerators have increased in energy, every decade or so a new, more massive fundamental particle has been discovered. The idea of the Large Hadron Collider is to do just that: to compress so much energy into so small a space that new and more massive fundamental particles may be discovered.

This thesis is about a search for new particles that may be both difficult to see, and which may require the production of massive new fundamental particles at the Large Hadron Collider in order to be discovered.

The logical structure of this thesis is as follows. In Chapter 1 (“Theoretical Background”) the Standard Model and the physics of proton-proton collisions are described, followed by an introduction to beyond-the-Standard-Model physics and the particular type of new physics being searched-for in this analysis. In Chapter 2 (“Experimental Apparatus”) the Large Hadron Collider and the ATLAS detector are described. In Chapter 3 (“Reconstruction”) the reconstruction of physics signatures with the ATLAS detector is described. In Chapter 4 (“Monte Carlo”) the computer simulation of physics processes is described. Finally in Chapter 5 (“Analysis”) the analysis that is the subject of this thesis is presented: a search for long-lived neutral particles with the ATLAS detector at the Large Hadron Collider.

Chapter 1

THEORETICAL BACKGROUND

1.1 The Standard Model

1.1.1 Introduction

Currently the most predictive description of the fundamental particles and interactions in nature is the so-called Standard Model. The Standard Model consists of a Lagrangian with 19 arbitrary parameters that must be determined by experiment. Understood within the framework of relativistic quantum field theory, this Lagrangian describes and predicts the elementary particles and three of the four known interactions in nature (the gravitational force is not described by the Standard Model). The particles are: 6 quarks (up, down, charm, strange, top, bottom) and corresponding anti-quarks, 6 leptons (electron, electron neutrino, muon, muon neutrino, tau, tau neutrino) and corresponding anti-leptons, 12 gauge bosons (photon, W^+ , W^- , Z, and 8 gluons), and the Higgs boson. The quarks differ from the leptons mainly in that they carry *color* charge – they interact through the strong-interaction, which causes them to form bound states called *hadrons*. The quarks and leptons are both *fermions* – particles that come in half-integer units of intrinsic angular momentum, or *spin* – while the *bosons* have integer spin. Fermions and bosons are distinguished phenomenologically[1] by the fact that spin is conserved, and as a result neither bosons nor fermions can emit or absorb a fermion, while both bosons and fermions can interact by emitting or absorbing a boson. Multiple fermions cannot simultaneously occupy the same state, and are called "matter particles," while the bosons, which can be emmitted and absorbed, are called "mediators." The matter particles come in three "generations", each generation an exact copy of the last but with a higher mass, and in an "up" variety and "down" variety that differ in charge.

Within the approximation framework known as perturbation theory, the gauge bosons and their couplings describe the interactions between particles – photons are responsible for the electromag-

---

[1] Note to experts: the Spin-Statistics Theorem motivates this description. The fact that fermions and bosons obey different statistics can be deduced from a consideration of their spins, and vice-versa.

netic force, W and Z bosons for the weak force, and gluons for the strong force. Higgs bosons are the quanta of the Higgs field, a field whose coupling to fermions and to the W and Z gauge bosons is responsible for giving them mass.

For over 40 years the Standard Model's predictions have (with very few exceptions) withstood experimental tests. The Standard Model successfully predicted the charm and top quarks, the gluon, and the W and Z and Higgs bosons before their discovery, and it's numerical predictions agree with experiment to good (and in some cases remarkable) precision. As will be seen, the forces (and therefore the types of particles) within the Standard Model are not arbitrary; they are in fact *predicted* by symmetry principles. The particle content of the Standard Model is shown in Figure 1.1 [1].

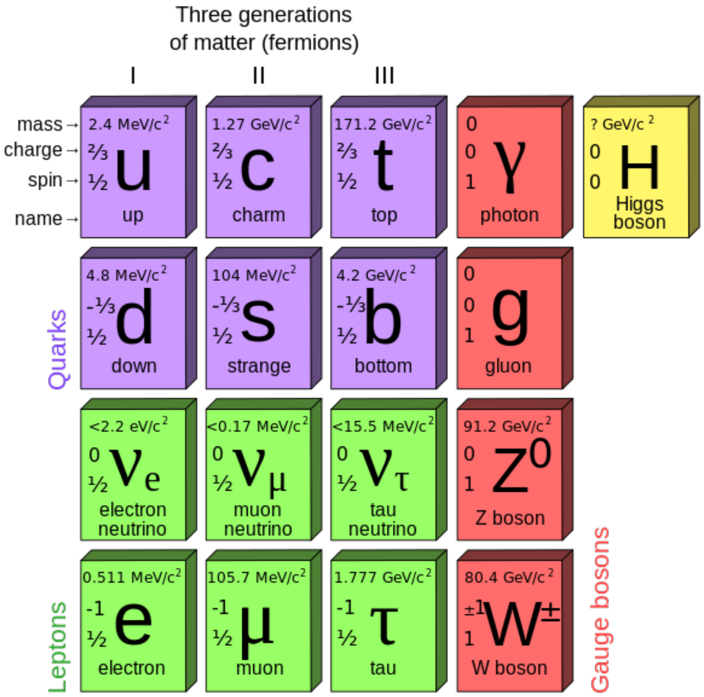

Figure 1.1: The particle content of the Standard Model.

The organization of this theory section is as follows. First there will be an introduction to some of the underlying mathematical principles that have lead to the Standard Model, in particular the role of symmetry as a guiding principle. Then the Standard Model itself will be introduced and examined, starting with the introduction of the fundamental forces and ending with a discussion of the Higgs mechanism.

1.1.2 The Principle of Stationary Action

In the 17th century Pierre de Fermat suggested that the behavior of light can be understood as the consequence of it choosing to follow a path between two given points so as to minimize its travel time. This is now known as the *principle of least time* or *Fermat's principle*. It turns out that this principle can be generalized to describe not only the behavior of light, but of all quantum mechanical systems. The more general principle is that the system follows every possible sequence of configurations, and that each such "history" is weighted by a quantum mechanical phase that depends on the so-called *action* of that history. When all of the histories are added together the phases constructively interfere such that the most highly weighted history of the system's evolution is the one in which the action is *stationary*[2]. This principle is therefore called the *principle of stationary action*. The action is defined as the integral of the *Lagrangian* between two points in time; the Lagrangian encodes a full description of the system's dynamics.

Incidentally, this more general formulation of Fermat's principle solves a deep conceptual mystery: how does light know *beforehand* which path will end up taking the least time (after all, the light must "start-off" going in the right direction, even before reaching whatever obstacles are placed in its path)? The solution is that the light does not choose a single path; the light *takes every path*, and constructively interferes only along the path of least time. This amazing fact is experimentally manifest in *diffractive phenomena* which are exhibited even by individual particles of light, and, more generally, by all of matter.

The above example illustrates the general principle that a system follows every possible sequence of configurations, a tendency which is a reflection of nature's apparent desire to exhibit symmetry. Though not often phrased in this way, the principal of stationary action is a principle of symmetry: nature chooses not to follow some arbitrary sequence of configurations, but rather chooses to exploit all of them in such a way that no sequence of configurations is a priori special.

The principal of stationary action is so general and fundamental a principle that it can be applied

---

[2] The action is stationary if it is approximately invariant under small perturbations of the system's evolution, such as when the action is minimized or maximized.

to derive the phenomenology of all theories of modern physics. In other words the specification of all of the dynamics of a theory amounts only to a specification of its Lagrangian.

The principle that a system follows "all possible paths" could be more generally called a "principle of fecundity", or more to the point, a "principle of symmetry," in that the dynamics of the system are the result of symmetric, non-arbitrary behavior. Light doesn't follow an *arbitrary path*; it follows *every path*. A quantum system doesn't exist in an *arbitrary state*; it exists in *every state*. Leaving aside the quantum-interpretational question of whether the wave function "collapses," it is the *Lagrangian* of a system that seems to add an element of the arbitrary; weighting some paths, or histories, more than others. The Lagrangian alone determines the dynamics that emerge from the interference between alternate possibilities. Can it be similarly motivated by principles of symmetry?

1.1.3 The Standard Model as a Gauge Theory

In the course of exploiting the principle of stationary action to yield the equations of motions for various physical systems, it was noticed that symmetries play a crucial role in constraining a system's behavior. In 1915 mathematician Emmy Noether proved that any differentiable symmetry of the action of a physical system has a corresponding conservation law. Examples include the conservation of energy and linear momentum (the Lagrangian is invariant with respect to global translation in time and space), the conservation of angular momentum (the Lagrangian is rotationally invariant), and even the conservation of charge (the Lagrangian is invariant with respect to global changes in quantum mechanical phase).

Noether's theorem tells us that the symmetries of a given Lagrangian are deeply connected with the dynamics that result from the application of the principle of stationary action. Being just a theorem, it does not, however, constrain the form of the Lagrangian itself, and therefore does not constrain the form of the many possible interactions that might or might not exist between the fundamental constituents of matter. It does, on the other hand, hint that one way of restricting the set of possible interactions is by imposing further types of symmetry on the Lagrangian.

A *gauge theory* is an example of a field theory that possesses a further type of symmetry: it is a theory in which the Lagrangian is invariant under a continuous group of local transformations. To see the power of such a theory, consider the Lagrangian for a non-interacting complex scalar field with mass m:

$$\mathscr{L} = \frac{1}{2}(\partial_\mu \phi)^2 - \frac{1}{2}m^2\phi^*\phi \tag{1.1}$$

It can be checked that for such a field the Lagrangian is invariant with respect to globally rotating the complex phase of the field by any angle. Thus the Lagrangian exhibits *global U(1) phase invariance*, which, by Noether's theorem, corresponds to a conserved quantity we call a *charge*[3]. To make this a *gauge theory* we must insist that the Lagrangian be invariant with respect to *local* changes in complex phase, in other words, invariant with respect to changes of the phase of the field at every space-time point. This requires that a compensating field $\hat{A}^\mu$ (the *gauge field*) that is coupled to the matter field be added to the Lagrangian. We can say that the charge that results from the global symmetry acts as a *source* of the force-carrying gauge field. The form of the Lagrangian is uniquely determined by the requirement of local U(1) invariance, and turns out to describe the interaction of an electric charge with the electromagnetic field. Thus, starting with a non-interacting theory and requiring that the Lagrangian be invariant under local U(1) transformations, we can derive the necessary existence of the electromagnetic field and the electromagnetic interaction between charges.

When a gauge theory is quantized (moved from a classical to a quantum description), the quanta (the minimal vibration) of the gauge fields are called *gauge bosons*. Such bosons are naturally associated with the gauge field that is required by gauge invariance to be coupled to the matter field, and, since the matter field is initially non-interacting, the gauge bosons are therefore associated with the mediation of any interaction between the matter field and itself. The gauge bosons are therefore sometimes referred to as "force carriers" or "force mediators," the force itself having been derived as a consequence of requiring gauge invariance of the theory.

If a Lagrangian is invariant under a global SU(N) transformation[4], Noether's theorem tells us

---

[3] Incidentally, it is a theorem that any Lorentz-invariant quantum field theory must possess a discrete global symmetry under spatial reflection, momenta-reversal, and inversion of charge. Thus for each charged particle in nature an oppositely-charged particle of equal mass and spin, called an *anti-particle*, is necessary in order for this symmetry to be realized.

[4] SU(N) stands for "special unitary group" and represents the symmetry group of n×n unitary matrices with determinant 1. The U(1) symmetry described above corresponds to the case n=1.

that there are $N^2 - 1$ conserved charges, the generators of the Lie group. When promoted to a gauge theory, the same number of gauge fields are necessary to mediate the interaction between the charges in order for the Lagrangian to be locally invariant under SU(N). Therefore the charges act as sources of the force-carrying gauge field.

1.1.4 The Standard Model Lagrangian

The Standard Model (SM) is a relativistic quantum field gauge theory that is invariant under local SU(3)×SU(2)×U(1) gauge symmetry transformations (the "relativistic" means that it is globally invariant under Poincaré symmetry[5]). The requirement that the Lagrangian be locally invariant under this gauge symmetry group uniquely determines the dynamical structure of the theory, though with 19 arbitrary parameters that must be determined by experiment. The three factors of gauge symmetry are associated with the three fundamental interactions. The global SU(3) symmetry gives rise (via Noether's theorem) to the conserved color charge, and the local SU(3) gauge symmetry gives rise to the *strong force* between colored objects. The part of the Standard Model Lagrangian that governs the strong force between matter fields is called the *QCD sector*. The global SU(2)×U(1) symmetry gives rise to the conserved weak isospin charge (corresponding to the generators of SU(2)) and weak hypercharge (corresponding to the generator of U(1)). The more familiar *electric charge* turns out to be a conserved combination of weak hyper charge and the third component of weak isospin. The local SU(2)×U(1) gauge symmetry gives rise to three W's (from SU(2) gauge symmetry) and one B (from U(1) gauge symmetry) gauge fields which mix to form the *weak* and *electromagnetic* forces. The part of the Standard Model Lagrangian that governs the electroweak force between matter fields will be called the *electroweak sector*. The Standard Model Lagrangian can be broken into three pieces:

$$\mathscr{L}_{SM} = \mathscr{L}_{gauge} + \mathscr{L}_{int} + \mathscr{L}_{mass} \tag{1.2}$$

$\mathscr{L}_{gauge}$ describes the massless gauge fields, $\mathscr{L}_{int}$ describes the massless matter fields and the interaction between the matter fields and the gauge fields, and $\mathscr{L}_{mass}$ contains the mass terms of the gauge and matter fields. The reason for separating out the mass terms will be made clear shortly. The

---

[5] The spacetime symmetries in Special Relativity corresponding to translations, rotations, and Lorentz boosts.

$\mathscr{L}_{gauge}$ term is given by:

$$\mathscr{L}_{gauge} \;=\; \int -\frac{1}{4}B_{\mu\nu}B^{\mu\nu} - \frac{1}{4}W_{\mu\nu}W^{\mu\nu} - \frac{1}{4}G_{\mu\nu}G^{\mu\nu} \tag{1.3}$$

Where traces are assumed over an index "a" (hidden for clarity) of the generators of the gauge groups, and where each field strength tensor is defined by:

$$\mathscr{F}^a_{\mu\nu} = \partial_\mu A^a_\nu - \partial_\nu A^a_\mu + g f^{abc} A^b_\mu A^c_\nu \tag{1.4}$$

where f^{abc} are the structure coefficients of the gauge group, which define the group's properties, A^a_ν is the gauge field indexed by the generators of the gauge group, and "g" is a coupling constant. Note that the coupling constant is a free parameter that is different for each of the three Standard Model gauge groups.

G^a_μ is the gluon gauge field and $G^a_{\mu\nu}$ is the gluon field strength tensor, where the index "a" labels the eight generators of SU(3), corresponding to eight gauge bosons (gluons). W^a_μ is the gauge field corresponding to SU(2), and $W^a_{\mu\nu}$ is the gauge field strength tensor, where "a" runs over the three generators of SU(2), corresponding to three gauge bosons. B_μ is the gauge field corresponding to U(1) and $B_{\mu\nu}$ is the gauge field strength tensor (here there is no need for a generator index, as U(1) has only one generator).

The three gauge fields, their degrees of freedom (given by the number of group generators) and their dynamics (determined by the group structure coefficients) are a result of requiring local SU(3)×SU(2)×U(1) gauge invariance on a relativistic quantum field. Due to the relationship between each symmetry group and the resulting physical dynamics, the Standard Model gauge group is sometimes labelled $SU_C(3) \times SU_W(2) \times U(1)_Y$, where "C" stands for color, "W" stands for weak, and "Y" stands for weak hypercharge. We will later see that the $SU_W(2) \times U(1)_Y$ gauge symmetry is *spontaneously broken* to $U(1)_{EM}$, where "EM" stands for "electromagnetic."

The next term in the Standard Model Lagrangian represents the interaction between the matter fields and the gauge fields. It is convenient to break the interaction term into two pieces:

$$\mathscr{L}_{int} \;=\; \mathscr{L}_{QCD} + \mathscr{L}_{EW} \tag{1.5}$$

QCD Sector

The quantum chromodynamics (QCD) sector describes the strong force, and $\mathscr{L}_{QCD}$ describes the interaction between matter fields called the quark fields and the gluon field, where the gluon field is a gauge field that arises from SU(3) gauge symmetry. The quark fields transform under the fundamental representation of SU(3) and can take on the values: red, green, and blue. The global symmetry under this transformation gives rise via Noether's theorem to eight conserved charges, which can be thought of as combinations of the three colors that act as sources for the gluon field. The local invariance of matter fields under SU(3) transformations requires the introduction of eight gauge fields. The corresponding gauge bosons are called gluons. The part of the QCD Lagrangian describing how the quark fields couple to the gluon fields is given by:

$$\mathscr{L}_{QCD} = i\overline{U}(\partial_\mu - ig_s G^a_\mu T^a)\gamma^\mu U + i\overline{D}(\partial_\mu - ig_s G^a_\mu T^a)\gamma^\mu D \tag{1.6}$$

where G^a_μ is the SU(3) gauge gluon field, T^a are the generators of SU(3), γ^μ are the Dirac matrices, D and U are the Dirac spinors associated with up- and down-type quarks, and g_s is the strong coupling constant.

Electroweak Sector

The global SU(2) symmetry gives rise via Noether's theorem to three conserved charges known as weak isospin, and the global SU(1) symmetry likewise gives rise to the conserved charge known as weak hypercharge. As we will soon see, not all of these charges will remain conserved after we introduce a mechanism that breaks the electroweak symmetry.

The electroweak sector describes the weak and electromagnetic forces unified into a single electroweak force that results from fields' invariance under SU(2)×U(1) gauge symmetry. It requires the introduction of three W_μ gauge fields and one B_μ gauge field. The part of the electroweak Lagrangian describing how matter couples to the B and W fields is given by:

$$\mathscr{L}_{\mathrm{EW}} = \sum_\psi \bar{\psi}\gamma^\mu \left(i\partial_\mu - g'\frac{1}{2}Y_{\mathrm{W}}B_\mu - g\frac{1}{2}\vec{\tau}_{\mathrm{L}}\vec{W}_\mu \right)\psi \tag{1.7}$$

where B_μ is the U(1) gauge field, Y_W is the generator of U(1) (the weak hypercharge), $\vec{W}_\mu$ is the three-component SU(2) gauge field, $\vec{\tau}_{\mathrm{L}}$ are the three generators of SU(2) (the Pauli matrices, or weak isospin) but which only act on left-handed fermions, and the "$g\prime$" and "g" are coupling constants.

The electroweak sector treats left- and right-handed fermions differently. Left-handed fermions transform under the fundamental representation of SU(2) while right-handed fermions transform under the trivial representation of SU(2). This is another way of saying that the right-handed fermions do not participate in the weak interaction. For this reason the symmetry group of the electroweak sector is often written as $SU(2)_L \times U(1)$, because only the left-handed fermions transform under a non-trivial representation of SU(2), and therefore only left-handed fermions are coupled to gauge bosons through the requirement of local invariance under SU(2). We say that left-handed fermions have weak isospin $I = \frac{1}{2}$ (they transform as a doublet) and right-handed fermions have weak isospin $I = 0$ (they transform as a singlet).

The Higgs Mechanism

The final piece of the Standard Model Lagrangian is $\mathscr{L}_{mass}$, which contains the mass terms of the matter and gauge fields. At this point, however, our construction of the Standard Model runs into a problem. It turns out that a mass term for any of the fermion or gauge fields would not be gauge invariant. Therefore all of the particles in the Standard Model must be massless. Gauge field mass terms contain the combination $A^{\mu}A_{\mu}$ which is just not gauge invariant under U(1) or SU(2) or SU(3). The fermion field mass terms are not gauge invariant for a more interesting reason. The fermion mass term can be decomposed into helicity states:

$$-m\bar{\psi}\psi = -m(\bar{\psi}_R + \bar{\psi}_L)(\psi_L + \psi_R) = -m(\bar{\psi}_R\psi_L + \bar{\psi}_L\psi_R) \tag{1.8}$$

Therefore the mass term acts as a coupling between left- and right-handed fermions. The reason these terms are not gauge invariant is because left-handed and right-handed fermions transform under different representations of SU(2). Left-handed fermions have weak isospin $I = \frac{1}{2}$ (they transform as a doublet) and right-handed fermions have weak isospin $I = 0$ (they transform as a singlet). Since all left-handed fermions in the Standard Model carry weak isospin charge, a mass term for any fermion in the Standard Model is forbidden.

Gluons, the quanta of the SU(3) gauge fields, have not empirically been found to have mass.

But some of the gauge fields we associate with the electroweak sector do appear to have mass. In fact it is the mass of gauge bosons in the electroweak sector that make the weak force *weak*; forces communicated by massive bosons are *short-ranged* because their exchange is energetically unfavorable. Therefore the problem of adding mass terms to the Standard Model Lagrangian is confined to the electroweak sector.

This problem is solved in the Standard Model by the introduction of a new bosonic, complex scalar field called the *Higgs field* transforming under $SU(2)_L$:

$$\phi = \frac{1}{\sqrt{2}} \begin{pmatrix} \phi^+ \\ \phi^0 \end{pmatrix} \tag{1.9}$$

The indices $+$ and 0 indicate the electric charge Q, defined as a combination of weak hyper charge and the third component of weak isospin:

$$Q = T_3 + \frac{Y_\mathrm{W}}{2} \tag{1.10}$$

which generates a copy of U(1) called $U(1)_{EM}$.

The idea is that this new Higgs field obtains a *vacuum expectation value* which breaks electroweak symmetry. To see conceptually how this works, consider a simple interacting classical scalar field theory with Lagrangian:

$$\mathscr{L} = \frac{1}{2}(\partial_\mu \phi)^2 - \frac{1}{2}m^2\phi^2 - \lambda\phi^4 \tag{1.11}$$

The $\frac{1}{2}(\partial_\mu \phi)^2 - \frac{1}{2}m^2\phi^2$ term describes a free scalar field with mass 'm', and the $\lambda\phi^4$ term describes how the field couples to itself. The field has a very simple discrete symmetry: it is invariant under the transformation $\phi \to -\phi$. Now consider what happens if we do something that seems at first bizarre: we replace the ordinarily positive m^2 mass term by $-\mu^2$. This might seem physically nonsensical (it implies the mass is imaginary) however we can regain a positive mass term by noting that by changing the ordinary m^2 mass term to $-\mu^2$ we have changed the classical potential from:

$$V(\phi) = \frac{1}{2}m^2\phi^2 + \lambda\phi^4 \tag{1.12}$$

for which the potential is minimized at $\phi = 0$, to:

$$V'(\phi) = -\frac{1}{2}\mu^2\phi^2 + \lambda\phi^4 \tag{1.13}$$

for which the potential is minimized at $\phi = \pm\sqrt{\frac{1}{4\lambda}}\mu$. Each potential is shown in Figure 1.2.

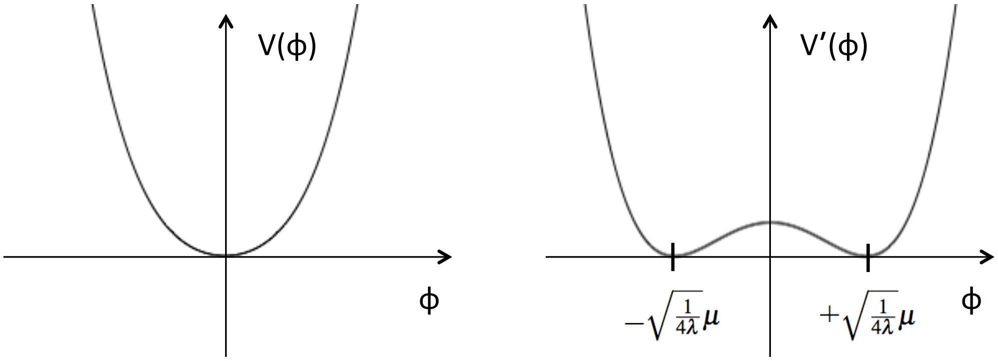

Figure 1.2: The potential given a positive mass term (left) and negative mass term (right).

We have thus altered the ground state, i.e. the *vacuum*, of our theory, such that the field's ground state is no longer zero. In order for the field to attain its ground state it must *spontaneously break the symmetry* of the Lagrangian by obtaining a non-zero *vacuum expectation value* $v = \pm\sqrt{\frac{1}{4\lambda}}\mu$. Since fluctuations of the field are with respect to its ground state $\phi = v$ rather than with respect to $\phi = 0$, we must re-write our Lagrangian in terms of field values with respect to v rather than 0. We can do this by simply redefining $\phi \to v + \phi$:

$$\mathscr{L} = \frac{1}{2}(\partial_\mu\phi)^2 - \frac{1}{2}(2\mu^2)\phi^2 - \sqrt{4\lambda}\mu\phi^3 - \lambda\phi^4 \tag{1.14}$$

With this redefinition we see that we have a new theory describing a scalar field of (non-imaginary) mass $\sqrt{2}\mu$ and with two types of self-interaction described by the ϕ^3 and ϕ^4 terms. The new Lagrangian is no longer invariant under the transformation $\phi \to -\phi$. The symmetry has been spontaneously broken by the field obtaining a non-zero vacuum expectation value in order to minimize the potential energy of the vacuum, in a similar way to how a pencil stood straight up on a table will fall sideways in order to minimize its potential energy despite its Lagrangian being rotationally invariant. Despite the symmetry of the Lagrangian the field or pencil is able to reach its asymmetric ground state due to quantum indeterminacy (sometimes referred to as a quantum "fluctuation"); this is the sense in which the breaking of symmetry is spontaneous.

The addition of the Higgs field to the Standard model serves the purpose of creating a vacuum whose ground state requires that the Higgs field attain a vacuum expectation value which breaks $SU(2) \times U(1)$ symmetry. It should be emphasized that the underlying theory is still invariant under $SU(2) \times U(1)$, just as in the pencil example above in which the underlying theory is rotationally invariant. Therefore the motivation of the gauge fields as enforcing local gauge invariance still holds; it is only after the Higgs field obtains a vacuum expectation value in order to minimize its ground state, *and after we have redefined the fields to accommodate that new ground state*, that the symmetry of the theory is no longer *manifest*.

The Higgs part of the Standard Model Lagrangian is:

$$\mathscr{L}_H = [(\partial_\mu - igW^a_\mu t^a - ig'Y_\phi B_\mu)\phi]^2 + \mu^2\phi^\dagger\phi - \lambda(\phi^\dagger\phi)^2 \tag{1.15}$$

This is in direct analogy with Equation 1.11; the main difference is that the first term is more complicated due to the requirement of gauge invariance (there is a general procedure for maintaining gauge invariance in which the derivative is replaced by the "covariant derivative" containing the gauge fields), and the mass and self-coupling terms are slightly different-looking because the Higgs field is complex rather than real-valued. As in the example, the mass term is imaginary, leading to spontaneous symmetry breaking. The Higgs field acquires a vacuum expectation value:

$$\phi = \frac{1}{\sqrt{2}} \begin{pmatrix} 0 \\ v \end{pmatrix} \tag{1.16}$$

with $v = \sqrt{\mu^2/\lambda}$. After redefinition of the field in terms of deviations from its vacuum expectation value, the Higgs mass is seen to be the (non-imaginary) $m_h = \sqrt{2}\mu = \sqrt{2\lambda}v$, and in addition the Higgs Lagrangian contains combinations of the three W_μ and one B_μ gauge fields that can be redefined as new fields associated with particles of definite mass and electric charge. The W^+ and W^- bosons are defined as $W^\pm_\mu = \frac{1}{\sqrt{2}}(W^1_\mu \mp iW^2_\mu)$ with masses $m_W = \frac{gv}{2}$ and electric charges ±1. The Z boson is defined as $Z^0_\mu = \frac{1}{\sqrt{g^2+g\prime^2}}(gW^3_\mu - g\prime B^2_\mu)$ with mass $m_Z = \sqrt{g^2+g\prime^2}\frac{v}{2}$ and zero electric charge. The photon is defined as $A^0_\mu = \frac{1}{\sqrt{g^2+g\prime^2}}(g\prime W^3_\mu + gB_\mu)$ with mass $m_\gamma = 0$ and zero electric charge.

The introduction of a field with a (gauge-dependent) nonzero ground state expectation value has resulted in a redefinition of our theory in which manifest electroweak symmetry has been (partially) broken, and as a reflection of that broken symmetry, the gauge fields which formally were required by gauge invariance to be massless, have mixed with each other and acquired mass. We say that $SU_W(2) \times U(1)_Y$ gauge symmetry has been spontaneously broken to $U(1)_{EM}$, because in our field redefinitions we find that only a single boson remains massless, the mixture of gauge bosons $\frac{1}{\sqrt{g^2+g\prime^2}}(g\prime W^3_\mu + gB_\mu)$ corresponding to the combination of gauge group generators $T_3 + \frac{Y_W}{2}$ which we find to be the only remaining conserved charge. Since $T_3 + \frac{Y_W}{2}$ generates a copy of U(1), and we expect a massless boson (the photon) to mediate the electromagnetic field, we define the electric charge $Q = T_3 + \frac{Y_W}{2}$ and call the U(1) symmetry remaining after electroweak symmetry breaking $U(1)_{EM}$.

The mixing between the W^3 and B gauge bosons that gives rise to the Z and γ boson mass eigenstates can be described by a rotation by an angle θ_w called the *weak mixing angle*:

$$\begin{pmatrix} \gamma \\ Z^0 \end{pmatrix} = \begin{pmatrix} \cos\theta_W & \sin\theta_W \\ -\sin\theta_W & \cos\theta_W \end{pmatrix} \begin{pmatrix} B \\ W^3 \end{pmatrix} \tag{1.17}$$

where $tan\theta_w = \frac{g\prime}{g}$. This mixing angle controls the mixing of the $W^\pm$ and B fields into Z and γ fields and the g and $g\prime$ SU(2) and U(1) coupling constants into the $W^\pm$, Z, and γ coupling constants. The electromagnetic and Z coupling constants can be identified with $g\sin\theta_w$ and $\frac{g}{\cos\theta_w}$, respectively, where $\frac{g}{\sqrt{2}}$ is the coupling constant of the $W^\pm$. Since g and $g\prime$ are related by θ_w, the mass of the $W^\pm$ is rotated with respect to the mass of the Z: $m_W = m_Z \cos\theta_w$. The existence of the $W^\pm$ and Z bosons with masses related by θ_w was predicted by this model of electroweak symmetry breaking before their discovery in 1983. The Higgs boson, the quanta of the Higgs field, appears to have been discovered in 2012, decaying to pairs of electroweak bosons, $\gamma\gamma$, WW, and ZZ at rates roughly consistent with those expected given the Higgs mechanism of electroweak symmetry breaking.

We are finally in a position to complete the Standard Model Lagrangian by adding mass terms for the fermions. Recall that the problem was that the mass term for any fermion field is not gauge invariant because left- and right-handed fermions transform under different representations of SU(2). Recall also that a fermion mass term can be interpreted as a coupling between left- and right-handed fermions. It turns out that while directly coupled left- and right-handed fermions mass terms are not gauge invariant, terms which couple the left- and right-handed fermion fields *to the Higgs field are* gauge-invariant:

$$\mathscr{L}_f = -\lambda_f \bar{\psi}_L \phi \psi_R \tag{1.18}$$

We have given just the Lagrangian mass term for a single fermion, represented by a coupling between the Higgs filed and the left- and right-handed fermion fields with coupling strength λ_f. When the Higgs acquires its vacuum expectation value v and the fields are redefined with respect to fluctuations about the ground state, terms of this form become fermion mass terms:

$$\mathscr{L}_f = -\frac{1}{\sqrt{2}}\lambda_f v \bar{\psi}_L \psi_R \tag{1.19}$$

The mass of the fermion can be seen to be $m_f = \sqrt{2}\lambda_f v$. For each fermion in the Standard Model, a new coupling constant between the Higgs field and the left- and right-handed fermion fields, λ_f, must be added to the theory, the strength of each coupling determining each fermion's mass. These are referred to as the "Yukawa" couplings. Thus our construction of the Standard Model is complete. The Higgs mechanism allows the Standard Model to be fully gauge-invariant; the non-zero ground state of the Higgs field breaks the appearance of electroweak symmetry and gives mass terms to the W and Z gauge bosons and the fermions.

Beyond the Standard Model

The Standard Model has been enormously successful in its predictive power, however it is an incomplete model. For example it provides no explanation for dark matter, which accounts for most of the matter in the universe (a more complete list of the SM's shortcomings can be found in Section 1.3.1). Efforts made to address the SM's shortcomings have resulted in numerous models containing beyond the Standard Model physics. In particular much effort has gone into the construction of models that include "hidden" or "dark" sectors, that is, groups of particles that, like neutrinos, interact only weakly with SM particles. Such hidden sectors may include dark matter candidates in addition to any number of particles which have so-far remained undetected due to their small coupling to SM particles. Section 1.3.1 contains an introduction to beyond-the-Standard-Model-physics and in particular an introduction to the hidden sector models that are the subject of this thesis.

1.2 QCD and Proton-Proton Collisions

1.2.1 Perturbation theory in Quantum Field Theory

We have so far discussed the SM Lagrangian, however we have only touched upon its experimental predictions. This leads to two challenges, one *interpretational*, and the other *calculational*. The interpretational challenge is that the SM consists of a collection of interacting quantum fields, and the mapping between those fields and particles is not always well-defined. If we consider, for example, a non-interacting theory, we may find that there exist stable ripples in these fields that we can label “particle X,” “particle Y,” and so on. However when we add interactions to the theory things are not so simple. The fields change their properties in the presence of forces, and since the forces between field excitations change with time, so do their properties. As ripples interact they become agitated, and their particle-like properties are no longer as clearly defined. They can become unstable, decomposing into ripples in other fields, which in turn affect each other and do the same. In such a situation reductionism breaks down, and the physical state would better be described as a holistic jumble of field excitations than by a neat and tidy set of “particles.” The way out of this difficulty is to hope that such situations only arise during *particle collisions* (as we will see in Section 1.2.1 this is not always true) in other words, to hope that unstable field configurations are empirically found to typically decompose with time into stable ones that are “far enough away” from each other that the strength of the interaction between them is small. They can then be treated as stable ripples and we can apply “particle” labels to them until another “collision” takes place. We are therefore lead to consider SM predictions of the form:

$$\text{Stable “in” States} \rightarrow \text{Collision} \rightarrow \text{Stable “out” States} \tag{1.20}$$

The *in* states are also called *initial states* and the *out* states are also called *final states* and the *collision* is also called the *scatter*. The probability amplitude for a given initial state to evolve into a given final state (the *scattering amplitude*) is given by the so called “Scattering Matrix” or *S-Matrix*. The corresponding experimentally measurable quantity is called the *cross-section*, which tells us the expected rate of scattering given two intersecting beams of particles. Deriving the S-Matrix in general amounts to computing an intractable integral involving the SM Lagrangian. This leads us to the second difficulty mentioned earlier, this one *calculational*.

In order to render the calculation of scattering amplitudes mathematically tractable, scattering amplitudes may be calculated, at sufficiently high energy, using the approximation framework known as *perturbation theory*. The basic principle is that the non-interacting SM Lagrangian[6] *is* mathematically tractable; we understand the properties of the "in" and "out" particles. We therefore expand the scattering amplitude in terms of the non-interacting fields, in other words the scattering amplitude is written as a power series expansion in powers of the coupling constants. Each term in the power series expansion represents a *perturbation* of the non-interacting Lagrangian, and, as long as the coupling constants are small, the higher-order terms contribute less and less to the overall amplitude. Each term in the perturbation expansion can be represented pictorially by *lines* describing the flow of momentum and quantum numbers of the non-interacting field basis states, and by *vertices* which represent the exchange of momentum and quantum numbers. These are called *Feynman Diagrams*.

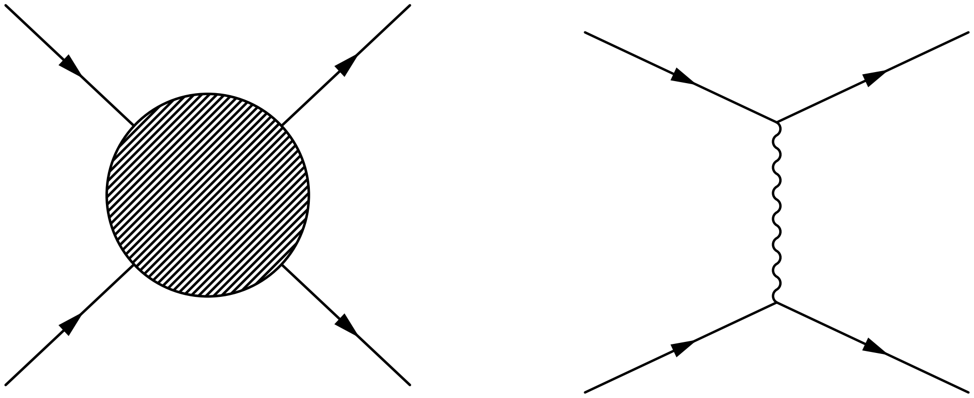

Figure 1.3: Left: Representation of non-perturbative real-life $ff \to ff$ scattering. Right: Example lowest-order Feynman diagram contributing to $ff \to ff$ scattering, pictorially describing two fermions transferring momentum through boson exchange. Fermions are generally drawn with solid lines, and gauge bosons with wiggly lines.

---

[6] The SM Lagrangian described in Section 1.1.4 where the values of the coupling constants g, $g\prime$, and g_s are taken to zero.

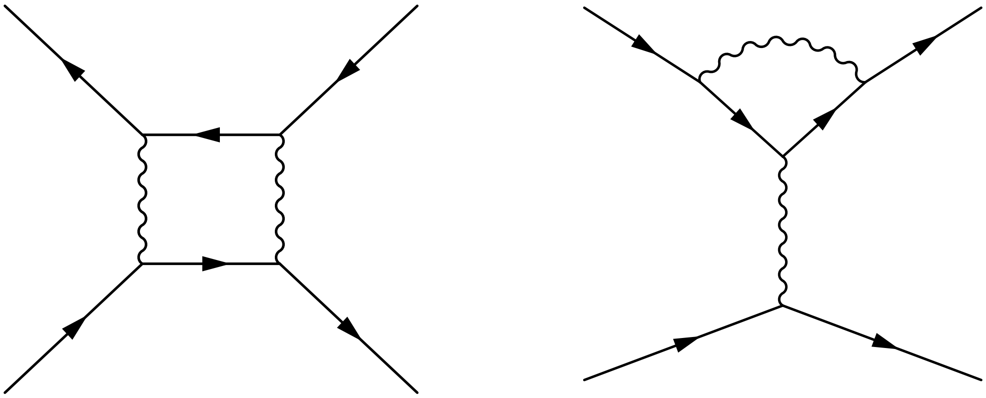

Figure 1.4: Example higher-order Feynman diagrams contributing to $ff \to ff$ scattering, pictorially describing two fermions transferring momentum through boson exchange.

For the example of $ff \to ff$ scattering, Figures 1.3 and 1.4 show Feynman diagrams that contribute to first- and second-order corrections (perturbations) to a non-interacting theory. When the perturbations up to a given order have been summed, the situation might best be described by an effective diagram looking like the one on the left in Figure 1.3.

This perturbative method works well in the electroweak sector of the SM, where the coupling constants are small. However in the QCD sector it turns out that the coupling may be large, and so perturbation theory may break down. There is a caveat to all of this, which is that the couplings that we *measure* are different from the g, g', and g_s in the SM Lagrangian. Naively these couplings determine the strength of the interaction between matter and gauge fields. But this is what is known as a "first-order" coupling; if a matter field can interact with a gauge field and a gauge field can interact with a matter field, then a matter field can interact with itself (at 'second-order"). An example of such a *self-interaction* can be seen on the right in Figure 1.4. Self-interactions result in fields that can be redefined with respect to how they behave after self-interactions have been taken into account. The *measured* couplings can be related to the measured scattering amplitude represented by the left diagram in Figure 1.3, whereas the *bare* or *unphysical* couplings are those that appear in each term in the perturbation expansion (associated with each vertex in the Feynman diagrams in Figures 1.3 and 1.4). As higher-order Feynman diagrams are added to a perturbation expansion, the *effective* coupling becomes *dressed* or *renormalized* by the corrections. In other words we can replace the bare couplings in our theory with effective or *renormalized* couplings, as seen in Figure 1.5.

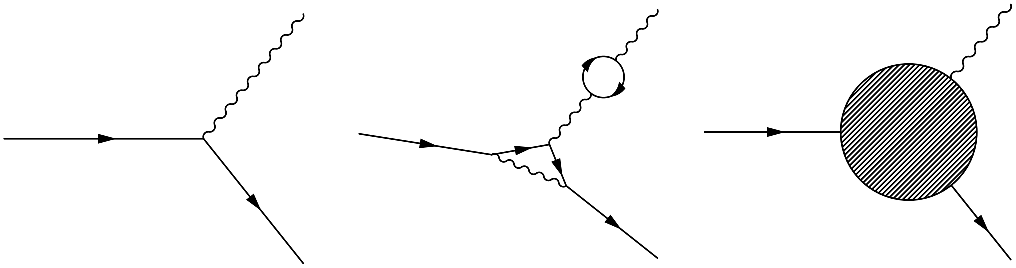

Figure 1.5: Left: First order coupling between a fermion and a boson. Middle: Example of a higher-order coupling. Right: Effective coupling that includes all higher-order terms.

It turns out that the degree to which a bare coupling differs from its physical renormalized counterpart depends on the momentum transfer of the collision. In quantum electrodynamics, for example, this can be understood physically as a result of vacuum polarization; if we place two charges into a vacuum, the vacuum becomes polarized and lowers the effective force between the two charges. Each charge can be thought of as being surrounded by a "cloud" of induced vacuum polarization, and the closer one charge gets to another, the deeper it penetrates this cloud (or *dress*) and therefore the less the polarization is able to *screen* the bare charge. Analogs of this effect hold true in the electroweak and strong sectors of the SM; the effective SM couplings depend on the energy scale of a collision (the momentum transfer Q). We therefore speak of *running couplings*, the renormalized couplings that depend on the *renormalization scale* μ. The point is that it is convenient to compare the couplings measured in scattering processes at momentum scale Q with those predicted at a renormalization scale μ that is near Q, because doing so minimizes the effect of higher-order terms on the effective coupling. For example, as the renormalization scale increases, the renormalized electromagnetic coupling *increases*. Physically this corresponds the the fact that the effective electromagnetic force increases with collision energy. Mathematically this corresponds to the fact that the inclusion of higher-order terms in the perturbation expansion becomes more and more important when comparing quantum electrodynamic theory to experiment at higher and higher

Q.

As mentioned earlier, perturbation theory may break down for QCD "because the QCD coupling may be large." The situation is actually not quite that simple, and now we are in a position to discuss this subject with greater clarity. The effective QCD coupling is dependent on the energy scale. The so-called strong force is *strong* only at low energy scales. Unlike the couplings in the electroweak sector, the effective QCD coupling *decreases* with energy. One of the defining characteristics of the QCD sector that separates it from the electroweak sector is this so-called *asymptotic freedom*; in high-energy collisions the strong force is *weak*, and therefore amenable to perturbation theory. The scale at which QCD becomes non-perturbative is $\Lambda_{QCD} \approx 200$ MeV. We can therefore predict scattering amplitudes for interactions between strongly-interacting particles for which $Q \gg 200$ MeV. But the fact that QCD is strongly-interacting at low-energy implies some very unusual phenomenology that cannot be predicted using perturbation theory.

Hadronization and Jet formation

The fact that the strong force increases with decreasing energy has an important implication: *color confinement*. In electrodynamics positive and negative charges form bound states; in QCD *color-singlets* form bound states. QCD is a more complicated non-abelian theory than electrodynamics, however an analogy can be made between the positive and negative electric charges of electrodynamics, and the red green and blue color charges of QCD. In electrodynamics bound states must have zero electric charge, while in QCD bound states must be color-neutral. A quark or a gluon alone is not color-neutral. Baryons are color neutral because they contain equal numbers of red, green and blue quarks. Mesons are color-neutral because they contain a quark of a given color and an anti-quark of the corresponding anti-color. QCD bound states, however, are different from electrodynamic bound states in another important respect: while the electric charges in in an electrodynamic bound state can in principle be separated from each other, the color charges in a hadronic bound state cannot. The quarks inside a hadron naturally engage each other in very limited exchanges of momentum; the effective QCD coupling is large. In fact the gluon self-coupling is so large that the gluon field forms a string-like flux tube between quarks (in contrast to the more isotropic behavior of, for example, the weakly self-coupled electromagnetic field). As a consequence the force between quarks does not decrease with distance as it does in electrodynamics, but remains constant independent of separation. As two quarks are pulled apart from each other the energy contained in the gluon field between them increases linearly until it becomes energetically favorable for the energy to be converted into quark-anti-quark pairs. Quarks that are pulled from the vacuum combine with each separated group of quarks until all states are color-neutral hadrons. This non-perturbative process, called *hadronization*, results in color confinement: it is *impossible* to isolate a single quark or gluon.

An important phenomenological consequence of confinement is that if a quark or gluon scatters out of a hadron the final state is not a single quark or gluon but a collinear spray of hadrons resulting from the *hadronization* of the out-going quark or gluon. This spray of hadrons is called a *jet*, where the sum of the four-momenta of the hadrons that comprise the jet is equal to the four-momentum of the initial quark or gluon. The initial stage of jet formation may involve energies well above Λ_{QCD} and so can be described perturbatively; quarks and gluons tend to emit collinear gluon radiation that results, even before hadronization, in a shower of quarks and gluons. During the final stage of jet evolution, however, after the energy of the initial outgoing quark or gluon has been divided among a shower of many quarks and gluons, the effective strong coupling becomes large and the evolution becomes non-perturbative. If one wishes to nonetheless conceptualize the final stages of jet evolution perturbatively, each parton's evolution is dominated by infinite numbers of higher and higher-order terms involving the Feynman diagram primitive vertices shown in Figure 1.6. Figure 1.7 gives a conceptual visualization of low-Q parton evolution within the perturbative framework.

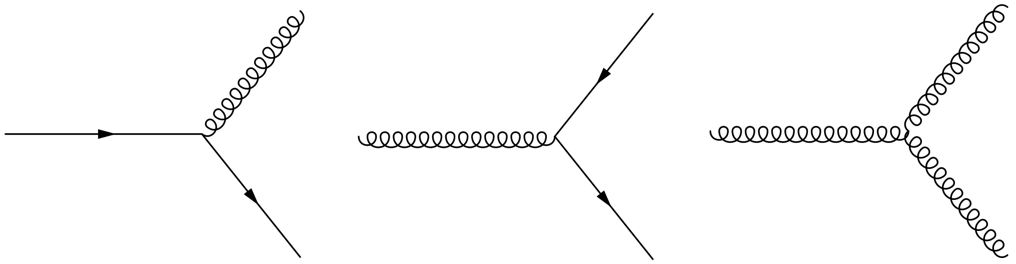

Figure 1.6: Left: Quark radiating a gluon. Middle: Gluon "splitting" into a quark-anti-quark pair. Right: Gluon radiating a gluon.

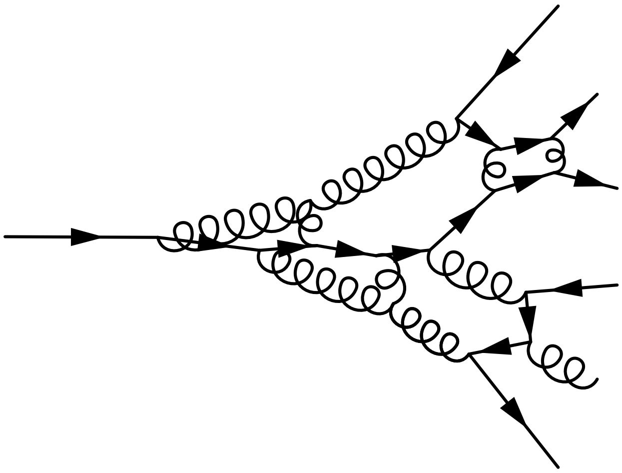

Figure 1.7: Attempt to perturbatively visualize the proliferation of quark-gluon and gluon-gluon vertices in the fundamentally non-perturbative process of low-Q parton evolution that occurs in jet formation.

The identification between quarks and gluons and the sprays of hadrons that originate from them is of critical significance because the proton's constituents, partons, are strongly interacting, and QCD processes vastly dominate over electroweak processes at the energy scales involved in proton-proton collisions at the LHC. As a consequence perturbation theory predicts that in proton-proton scattering, in cases where the momentum transfer is large enough to break the protons apart, that scattering amplitudes that include quarks and gluons in the final state are vastly dominant over others. The resulting "QCD jets" are the most common result and feature of inelastic proton-proton collisions. It should be noted, however, that jets can result not only from quarks and gluons that scatter out of the proton, but also from the decay of any particle produced in the proton-proton collision that decays into some final state that includes quarks or gluons. Higgs, Z, and W bosons, as well as the tau lepton, can all decay to final states that result in jets.

1.2.2 The Hard Scatter and Parton Distribution Functions

We have asymptotic freedom to thank for the fact that perturbation theory allows us to predict scattering amplitudes between quarks and gluons in high-energy collisions. But further than that, we can thank asymptotic freedom for the fact that in a high-energy *proton-proton* collision, only a single quark or gluon from each proton is likely to take part in each scattering process. This is important because while each proton contains only three *valence quarks*, a proton's internal dynamics are low-energy and therefore *strong*, and so cannot be so simply defined in terms of non-interacting "quark" and "gluon" basis-states. Since we nonetheless insist on describing the proton structure in terms of quarks and gluons (we have no better choice of basis states) the proton can be said to contain a "sea" of gluons and quark-anti-quark pairs whose structure cannot be predicted using perturbation theory. One could say that the previously described process of hadronization is in some sense *constantly occurring* inside a proton, with periodically stretched gluon fields generating quark-anti-quark pairs that briefly combine with the valence quarks before decaying back into excitations of the gluon field. Therefore when two protons collide, interactions can take place not only between two valence quarks but also between two sea quarks or two gluons, or between a valence quark and a sea quark, a valence quark and a gluon, or a sea quark and a gluon. And yet, because of asymptotic freedom, when any two such quarks or gluons scatter at high Q, we can largely ignore the forces between them and the rest of the proton's constituents, and treat the process as having two well-defined "in" states and use perturbation theory to predict the probability of observing possible "out" states. Such "in" states are called *partons*, and the high-Q interaction between them the *hard scatter*.

We can use perturbation theory to make statistical predictions regarding possible "out" states given any two parton "in" states, but cannot use perturbation theory to predict what the "in" states will be. We can, however, factorize the problem of finding the cross-section for a given hard scatter into two parts: the calculable part, and a *parton distribution function* (PDF). A PDF is an empirically-determined function representing the probability density for each parton to carry a fraction x of the proton's momentum at a given squared energy scale Q^2. While the x-dependence is determined empirically, the Q^2 dependence can be constrained perturbatively to some order in the Q^2-dependent strong coupling constant. Figure 1.8 shows two PDFs, one at a scale of $\mathrm{Q}^2 = 10\ \mathrm{GeV}^2$, and one at a scale of $\mathrm{Q}^2 = 10^4\ \mathrm{GeV}^2$.

The construction of PDFs requires piecing together measured cross-sections from various lepton-nucleon Deep Inelastic Scattering (DIS) experiments (many of which involve large experimental errors, especially for low momentum transfers), and then fitting the data points to fuctions that are theoretically constrained. Since this process involves some freedom of choice, there is no univer-

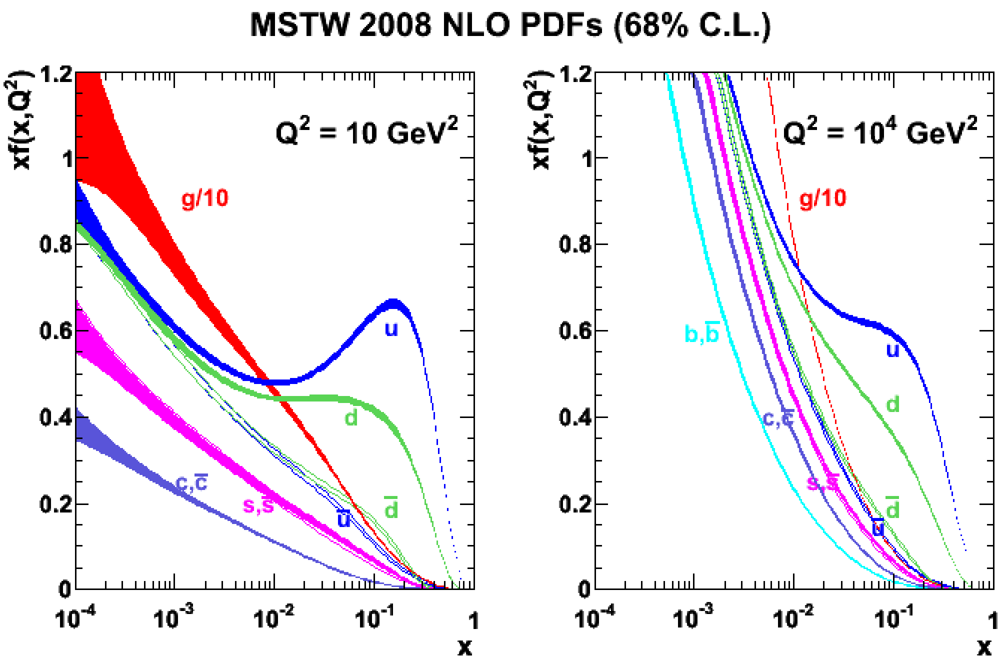

Figure 1.8: Next-to-leading order parton distribution functions for a momentum transfer of 10 GeV^2 (Left) and 10,000 GeV^2 (Right) [10].

sally agreed-upon set of PDFs. However some general features can be expected. Gluons dominate at low-x, and up-quarks (followed by down-quarks) dominate at high-x. Sea-quarks are relatively more common at high Q, and more massive sea-quarks are relatively rare. A particularly *hard* scatter is most likely to involve “q-q” as the initial state, the second most likely “q-g”, and the third most likely “g-g.” In contrast *soft* scatters are more likely to involve “g-g” in the initial state, second most likely to involve “q-g”, and the third most likely to involve “q-q.” Figure 1.9 shows two examples of proton-proton collisions with “q-q” final states; one in which the initial state partons are “q-q” and one in which the initial state partons are “g-g.”

1.2.3 The Scattering Cross Section

We are now in a position to return to the idea of the “cross-section” mentioned in Section 1.2.1 in its relation to the S-Matrix as an experimental observable. The cross-section, labelled σ, is a quantity directly related to the S-Matrix, defined for a given process ($qq \to qq$ for example) occurring at

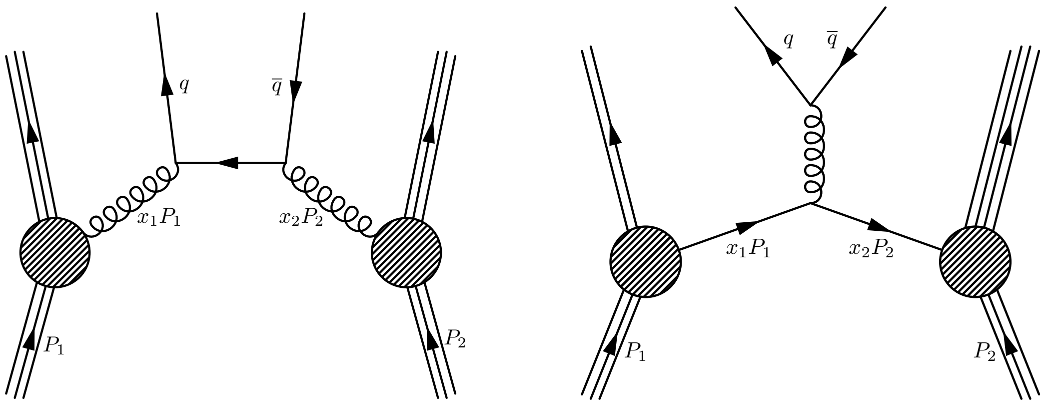

Figure 1.9: Examples of proton-proton collisions involving the hard scatter of two partons to a $q\bar{q}$ final state before hadronization. A lowest-order Feynman diagram is shown for the hard scatter, while the non-perturbative intra-proton dynamics and associated PDFs are represented by the shaded regions. Left: Gluon initial state partons. Right: Quark initial state partons.

a given center-of-mass (CM) energy. It is designed to predict the expected number of scattering events when two beams of particles of a given type (protons, for example) are made to collide. Given, for example, a collection (or *bunch*) of particles with a density of particles-per-unit-area ρ_1, and a bunch of particles moving in the opposite direction with a density of particles-per-unit-area ρ_2, we can ask how many particles we expect to scatter if the two collections simultaneously pass through an overlapping area A. This scenario is depicted in Figure 1.10. The expected number of scattering events is a result of a property of the particles defined by the S-Matrix: how likely they are to interact. An analogy one can make is that particles are more likely to interact in a certain way if they are large, that is, if they have a large cross-sectional area. The cross-section σ for a given type of scattering event indeed has the units of area, and in the example given can be expressed experimentally as:

$$\sigma = \frac{\text{Number of scattering events}}{\rho_1 \rho_2 A} \tag{1.21}$$

A cross-section can be specified for different processes, allowing us to measure the relative probability for different processes to occur. Cross sections are measured in units of barns, b, where 1 b = $10^{-28}m^2$. The total proton-proton cross section is on the order of 10^{-1} b, while many impor-

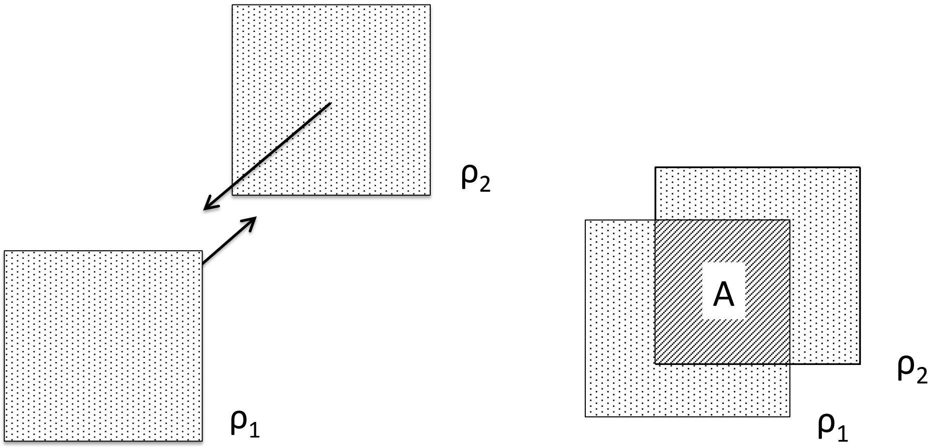

Figure 1.10: Left: Two bunches of particles, each with a particle density per-unit-area ρ, approach each other. Right: The two bunches pass through each other with an overlapping cross-sectional area A.

tant physics processes of interest have cross-sections on the order of 10^{-12} b, or a *picobarn*. Part of this huge disparity is due to the fact that in proton-proton collisions QCD processes naturally predominate over many interesting electroweak processes involving the Z, W, and Higgs bosons. But the main reason for the disparity is that the majority of the proton-proton cross-section comes from elastic scattering, $pp \to pp$, and *minimum bias* collisions. Minimum bias collisions involve a momentum transfer just large enough to produce particles that enter the acceptance region of the detectors, and therefore only minimally qualify as hard-enough scatters to be measurable by the experimental apparatus.

If the cross-section is a measure of the expected number of scattering events given the collision of two bunches of particles, the *luminosity* is a measure of how dense and frequent those bunches of particles are. The luminosity may change with time; in such a case we refer to the *instantaneous luminosity* L. The instantaneous luminosity depends on the number of protons per bunch N_b, the number of colliding bunches n_b, the frequency f_r with which bunches circulate, the beam's cross-sectional size and shape ε_n (called the transverse emittance), the relativistic gamma factor γ_r, the beam's focus at the collision point β^*, and the beam crossing angle, parametrized by F. The instantaneous luminosity can be defined [15] as:

$$\mathrm{L} = \frac{\mathrm{N}_b^2 \mathrm{n}_b f_r \gamma_r}{4\pi\varepsilon_n\beta^*} F \tag{1.22}$$

An experiment collects data over time; when the instantaneous luminosity is integrated over time the result is the *integrated luminosity*, measured in inverse barns. The total number of expected events N corresponding to a given process is directly proportional to its cross-section σ and the integrated luminosity $\mathscr{L}$:

$$\mathrm{N} = \mathscr{L}\sigma \tag{1.23}$$

1.2.4 Loose Ends

Initial and Final State Radiation

So far we have discussed "2 → 2" parton scattering, in which two initial state partons interact and result in two final state partons. We have emphasized that due to asymptotic freedom we only have to consider the interaction between two initial state partons. While this is true, it is possible for one or both of the initial state partons to radiate a gluon or photon before participating in the hard scatter. This is called *initial state radiation* (ISR). Similarly final state partons can radiate gluons or photons. This is called *final state radiation* (FSR). Partons are most likely to emit soft (non-energetic), collinear gluon radiation, which contributes during hadronization to the structure of a jet, but partons can also emit more energetic gluons which go on to form separate, additional jets. Examples of ISR and FSR are shown in Figure 1.11.

Multi-Parton Interactions

It is possible for two or more distinct hard parton scatterings to occur simultaneously in a single proton-proton collision. Such events contain multi-parton interactions (MPI). In general one scatter will be much harder than the other *secondary* interactions, which can resemble minimum bias events that exist simultaneously with the primary hard scatter event.

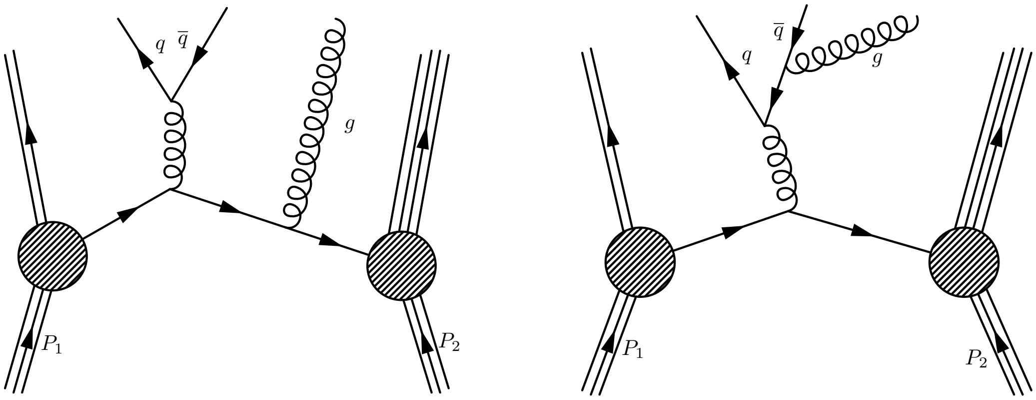

Figure 1.11: Examples of proton-proton collisions involving the hard scatter of $q\bar{q}$ to a $q\bar{q}g$ final state before hadronization. A lowest-order Feynman diagram is shown for the hard scatter, while the non-perturbative intra-proton dynamics and associated PDFs are represented by the shaded regions. Left: Initial state gluon radiation. Right: Final state gluon radiation.

Underlying Event

In Section 1.2.1 we discussed the role of hadronization and the fact that all colored objects must end up in color-neutral bound states (hadrons). We considered this in the context of out-going final state partons, however we didn't consider the fact that the hard-scatter can directly result in the removal or addition of a colored object to or from a proton, resulting not only in final state partons which must hadronize, but also unstable former protons or proton remnants which must hadronize as well. The right-hand diagram in Figure 1.9, though vastly simplified, illustrates the fact that the two quarks that participate in the hard scatter come at the price of the removal or addition of a quark from each of the protons, such that the former protons are no longer color-neutral. Furthermore, conservation of momentum implies that the proton's constituents must recoil to balance the momentum exchange. This recoil is crudely shown by the kink the the proton constituents' momentum lines in Figure 1.9, however in reality the momentum exchange does not affect all proton constituents equally. For example in the left-hand diagram in Figure 1.9 the proton remains color-neutral after the emittance of the gluon that participates in the hard scatter, however the gluon's momentum must ultimately result in recoil against one of the proton's constituent partons, which may cause a quark to scatter out of the proton, which again results in a disintegrating proton undergoing hadronization. Since x_1

and x_2 in Figure 1.9 are typically small, the hadronized proton remnants tend to follow the beam direction and do not always enter the acceptance of the detector.

The *underlying event* is generally defined to be everything except the hard scatter: minimum bias MPI, ISR and FSR, and beam remnant.

Coordinates and Kinematic Variables

The ATLAS coordinate system will be introduced in Section 2.2.3, however it is worth explaining a couple of important physical concepts that relate to how the angular coordinate system is defined and why in proton-proton collisions the transverse component of post-collision physics objects' momenta is generally more physically relevant than the longitudinal component.

The polar angle (the angle relative to the line between the origin at the center of the detector and the beam direction) is not typically measured in radians (the variable measured in radians is θ). Instead, the polar angle is measured in units of *pseudorapidity* η defined as a function of θ:

$$\eta = \text{-}\ln(\tan\frac{\theta}{2}) \tag{1.24}$$

A pseudorapidity of zero corresponds to $\theta = \frac{\pi}{2}$, in other words it constrains a vector to be tangential to the beam direction. A pseudorapidity of $\pm\infty$ corresponds to $\theta = 0$ or $\theta = \pi$; it constrains a vector to be parallel or anti-parallel to the beam direction. For angles that are near-parallel to the beam direction, very large changes in η correspond to very small changes in θ. The behavior of η as a function of θ can be seen in Figure 1.12.

Pseudorapidity η may seem like an odd choice of coordinate, however the pseudorapidity is the massless limit of a variable which is additive under boosts in the z-direction (the beam direction), the longitudinal rapidity y:

$$\text{y} = \frac{1}{2}\ln(\frac{E + p_z c}{E - p_z c}) \tag{1.25}$$

By noting that the energy of a particle is related to its momentum and mass by the relation $E = c\sqrt{p^2 + (mc)^2}$, the pseudorapidity can be seen to be equal to the longitudinal rapidity in the limit $|\vec{p}| \gg mc$.

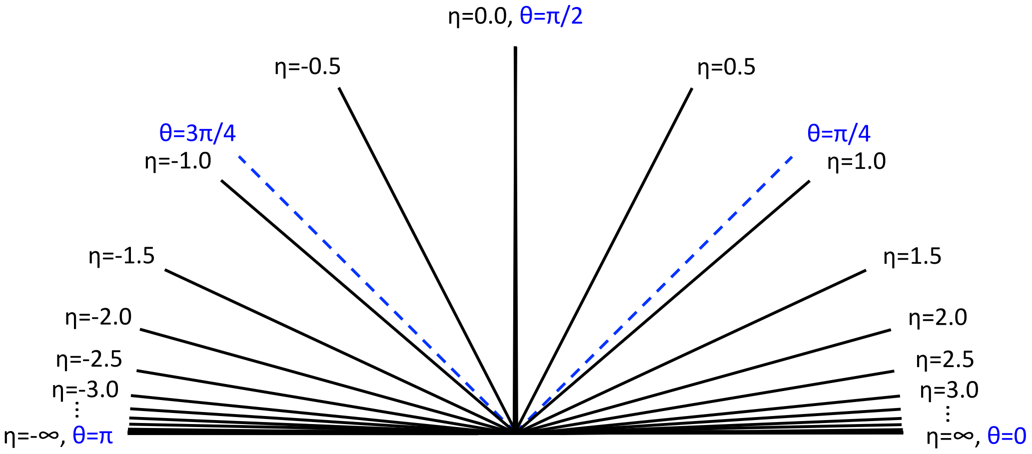

Figure 1.12: Various values of η (in solid black) and θ (in dotted blue) in a polar coordinate system with the beam line along the horizontal axis.

The momentum of a particle is related to its speed by the relation $p = \gamma\beta mc$, where β is the particle's speed in units of the speed of light, and γ is the relativistic gamma factor $\gamma = 1/\sqrt{1-\beta^2}$. Therefore $|\vec{p}| \gg mc$ implies that $\gamma\beta \gg 1$, in other words that the particle is moving close to the speed of light. This is a characteristic almost universally true for lighter particles emerging from high-energy collisions for which $Q^2 \gg (mc)^2$ (the notable exceptions are: the W, Z, and Higgs bosons, and the top quark, whose masses are not small compared to typical Q^2 at the LHC[7]). Therefore the assumption that η is additive under boosts in the beam direction is generally approximately valid for most particles emerging from the hard scatter.

The reason a coordinate that is additive under boosts in the beam direction is preferred is due to a feature of proton-proton collisions we have thus far discussed only tangentially. Conservation of momentum would guarantee us that the momentum of the final state particles exiting a proton-proton collision is conserved. However, only the momentum in the transverse plane (the momentum orthogonal to the beam direction) must sum to zero, since the initial state particles move parallel along the beam direction and thus have a transverse momentum of zero; their momentum is entirely *longitudinal*, or along the beam direction. As the PDFs tell us, and as can be seen in Figure 1.9, each

---

[7] Note, however, that these particles rapidly decay into lighter particles which do typically travel at close to the speed of light.

initial state parton carries a fraction x of the proton's *entirely longitudinal* momentum. Therefore while the transverse momentum of the outgoing partons must sum to zero, the sum of the longitudinal momentum is in general random, depending on the difference between the unknown x_1 and x_2 parton momentum fractions, experimental evidence for which is carried down the beam line in the underlying event. Therefore we will most often speak only of the transverse momentum of particles and jets, written as p_T, and in general we will be concerned only with the transverse component of any quantity with units of energy or momentum.

The pseudorapidity η is preferred over θ for precisely the same reason that p_T is preferred over p: because in proton-proton collisions the final state particles are subjected to arbitrary boosts along the beam direction. Because η is approximately additive under boosts along the beam direction, and because final state particles scatter roughly isotropically in the hard-scatter's rest frame, particle production is (generally speaking) roughly constant in η. In fact, the density of lines portrayed in Figure 1.12 roughly corresponds to the density of particles expected in collision events. It should be emphasized, however, that this is an approximation that is valid only near $\eta = 0$, because the distribution of boosts along the beam direction depends on the PDF's and is not a constant function. In particular there is a maximum possible boost along the beam direction corresponding to the initial rapidity of each proton in the beam.

The fact that the pseudorapidity η is additive under boosts along the beam direction has another important and useful implication: differences in pseudorapidity ($\Delta\eta$) between particles produced in the same hard scatter are invariant under boosts in the beam direction. This is because all particles produced from a given hard scatter are subject to the same longitudinal boost, and therefore the η of each particle in the event is shifted by the same constant value.

Because the speed of light, c, appears so frequently in formulae used in high-energy physics (see above), it is common for convenience to adopt a convention in which $c = 1$, and therefore in which both p and E are measured in the same units: electron volts (eV). As will be seen in Section 2.2.3, this is the convention adopted by ATLAS. Furthermore in cases where a particle is moving close to the speed of light, $p \gg mc$ implies that $E \approx p$. In other words either the momentum or the energy of a particle can be an equally valid description of either its momentum or its energy. As noted above, this may not be true for massive particles like the W, Z, and Higgs bosons or the top quark, however it is generally true for their much lighter decay products.

1.3 Hidden Valley Models

1.3.1 Invitation: Beyond the Standard Model

One may ask, given the compelling nature of the seeming *principle of fecundity* proposed in Section 1.1.2, why the $SU(3) \times SU(2) \times U(1)$ Standard Model does not include further gauge groups, such as SU(4) or SU(5). One might go further and ask why there are not multiple copies of the Standard Model gauge group each with different values of the Standard Model's 19 free parameters. As to the first question, one reason why *extending* the SM by larger SU(N) gauge groups may not be so useful is because larger gauge groups are large enough to already redundantly contain the SM gauge groups as subgroups. Moreover, just as magnetic and electric forces have been unified under the electromagnetic force, and the U(1) electromagnetic and SU(2) weak forces have been unified under the $SU(2) \times U(1)$ electroweak force, physicists seek to unify the strong and electroweak forces in a so-called *grand-unified theory* (GUT). Such a unification (in the context of gauge theory) would take the form of the SM gauge group being embedded in some larger gauge group. There have been a number of famous attempts to unify the three SM gauge groups under the umbrella of larger gauge groups. In the the Pati-Salam model [2] $SU(4) \times SU(2)_L \times SU(2)_R$ is spontaneously broken into copies of the SM gauge groups, and in the Georgi-Glashow model [3] SU(5) is spontaneously broken to copies of the SM gauge groups. Both the Pati-Salam and Georgi-Glashow models can be embedded in SO(10), the gauge group of yet another GUT. Unfortunately many of these kinds of models have so far been unsuccessful due in part to predicting unobserved phenomena such as monopoles or proton decay. Nonetheless the search is on for *Beyond the Standard model* (BSM) gauge groups, and since most such models predict additional physics beyond the SM, the search is on for BSM physics.

As to the second question of why there are not further copies of the Standard Model, it is worth pointing out that the Standard Model contains three copies of the fermion fields (the corresponding particles are referred to as three *generations* of matter) each of which respects $SU(3) \times SU(2) \times U(1)$ symmetry and interacts with the same corresponding gauge fields. The three generations of matter are nearly identical, differing only in flavor quantum numbers and mass. One may well ask why there are not more such copies, and moreover why there are not a wide variety of copies featuring myriad different values of the SM's free parameters. Additional gauge group factors, such as $U(1)'$ or $SU(2)'$, would correspond to additional, not currently known, interactions (although those interactions might be very similar to those in the SM). One can always ask: why not $SU(3) \times SU(2) \times U(1) \times U(1)'$? Why not $SU(3) \times SU(2) \times U(1) \times SU(2)'$? And so forth.

Such questions do not appear to be answerable within the gauge theory framework, because it does not provide a recipe for selecting which or how many gauge symmetries are respected by which or how many matter fields. In fact searches for evidence of additional matter fields or evidence of $U(1)'$ and $SU(2)'$ gauge groups (in the form of massive W' and Z' gauge bosons) are, for example, at the fore of BSM physics searches. There is, however, a different kind of BSM theory that may hold the answers to some of these questions: *String Theory*. String theory is a departure from gauge theory that goes much further, attempting to explain all of the particles and fundamental forces of nature as a consequence of the vibration of tiny strings. Remarkably, string theory may be deeply connected with gauge theory through *holographic dualities* (of which the famous AdS/CFT correspondence is an example), in which a string theory in a volume of space can be mapped to a gauge theory defined on the boundary of that space.

String theory is arguably the most promising quantum theory of gravity, however it is criticized for not being falsifiable at experimentally accessible energy scales. This is a consequence of string theory's main shortcoming, which is that, though it has no adjustable parameters, it has an enormous number of possible stable, and metastable, vacua. The many possible vacua come about as a result of the fact that string theory must be defined in more than 3 dimensions, and so the geometry of space-time must be such that all but 3 of these dimensions are "curled-up" small enough to not be observable at presently-accessible energy scales. Such dimensions are said to be *compactified* (one can imagine an ant moving only left or right along a piece of wire, its thickness a dimension largely "hidden" to the ant). There is no known unique compactification; many possible space-time geometries (and topologies) are consistent with the rules of string theory, and after the big-bang the universe could have settled into any number of possible vacua. This is a reflection of the fact that the vacuum structure of space-time is *complicated*; many geometrical (and topological) configurations locally minimize the potential energy of the universe in such a way that a transition to the true vacuum would first require moving through energetically unfavorable configurations.

The set of possible vacua in string theory is called the *landscape*. If the string theory landscape included only a few million, or even a few trillion possible vacua, we could perhaps catalog and search through the possible vacua and identify the unique vacuum that gives rise to the Standard Model and observed cosmology, therefore turning string theory into a predictive Theory of Everything (ToE). However it is estimated that there are $10^{hundreds}$ of possible vacua, making such a search rather computationally intensive.

The dynamics within string theory vacua at low energies can be described by effective Lagrangians, and gauge groups are common in such effective field theory descriptions. In fact it may be generic that such effective Lagrangians are constrained to be invariant [5] [6] under various SU(N) gauge groups. The landscape of vacua in string theory therefore provides a basis for a response to the critique that the SM gauge group is arbitrary: there exist an ensemble of effective Lagrangians that each may describe our region of space-time (different regions of the universe may settle into different vacua), and we simply happen to find ourselves in a vacuum that supports life.

Therefore there may very well be *additional* gauge group sectors that extend the Standard Model's QCD and electroweak sectors (discussed in Section 1.1.4). Such sectors may simply be "hidden" from us due to residing at higher energy scales or due to being only weakly coupled to SM particles. Such *hidden sectors* appear not only in "Landscape-aware" string theory constructions [4] but also generically in string theory [7] [8] [9] vacua whose effective field theory description contains the SM gauge groups, and also in supersymmetry (which will be discussed in Section 1.3.2). This thesis concerns itself with a class of hidden sector models (*Hidden Valley* models, discussed in Section 1.3.3) whose phenomenology can give rise to striking experimental signatures and which therefore may be experimentally accessible in early LHC data.

Canonical Failures of the Standard Model

I would like to end this introduction by listing some of the canonical ways in which the Standard Model is considered incomplete. The Standard Model assumes that the neutrinos are massless, but experiments measuring neutrino oscillation indicate otherwise[8]; the Standard Model cannot account for the apparent existence of the "dark matter" and "dark energy" required to make sense of astronomical observations; various parameters in the Standard Model must be tuned extremely finely

---

[8] It should be noted that this is only a mild failure of the SM: while neutrino masses are non-zero they are nonetheless extremely tiny ($<\sim$1 eV). Incorporating neutrino masses into the SM can be straightforward, however multiple scenarios are possible, and so the neutrino-sector of the SM remains incomplete.

to account for the strength of the weak force, to account for the lack of CP-violation in the strong-interaction, and to account for the small value of the cosmological constant; the Standard Model cannot explain the values of its various arbitrary parameters, to unify the strong and electroweak forces, or to model the gravitational interaction or incorporate General Relativity.

The Standard Model, it can rightly be said, is a good approximation to nature up to the energies we have so far probed, but it is not the final word; there is hope that concrete examples of new physics may appear given the high energies accessible at the LHC.

1.3.2 Supersymmetry

One extension of the Standard Model that is capable of addressing some of the above concerns is Supersymmetry. Supersymmetry proposes that the space-time symmetries of ordinary quantum field theory be extended to include a transformation between fermions and bosons. This expanded symmetry predicts the existence of a fermion *superpartner* to each Standard Model boson, and a boson superpartner to each Standard Model fermion. The name of a superpartner of a boson incorporates an " - ino " suffix (gluon → gluino, photon → photino). The Superpartner of a fermion is given an " s - " prefix (electrion → selectron, quark → squark). If Supersymmetry is manifest, then the superpartners are predicted to have the same mass as their Standard Model counterparts, but, since no superpartners have been detected, Supersymmetry is assumed to be "broken" (perhaps in a manner analogous to how electroweak symmetry is broken, which was described in Section 1.1.4), causing superpartners to be much heavier than Standard Model particles. While many different schemes have been developed to describe how the symmetry breaking could occur spontaneously, explicit supersymmetry-breaking terms can be added to the Lagrangian as an effective approximation for some more detailed supersymmetry-breaking mechanism.

In addition to being mathematically compelling as an elegant and fairly unique extension of the group of space-time symmetries, Supersymmetry has a number of other things going for it: it provides a framework for unifying particle physics and gravity; it can explain the strength of the weak force relative to the gravitational force without requiring unnatural fine-tuning; it makes possible the unification of the three gauge couplings close to the Plank scale; it is a symmetry of all well-behaved superstring theories, which arguably offer the best hope for a description of quantum gravity and the unification of all four forces; finally, it generally predicts a particle that may very well account for dark matter – the lightest supersymmetric partner, or LSP. Because most of the above motivations are maintained most naturally for models containing superpartners with masses near 1 TeV, it is hoped that Supersymmetry might be discovered at the LHC.

There are many possible extensions to the Standard Model involving Supersymmetry. The minimal supersymmetric extension of the Standard Model (MSSM) is the supersymmetric Standard Model but with two Higgs-like scalar fields (necessary to give mass to both "up"- and "down"-type quarks). This minimal model brings with it over 100 free parameters (the masses of the superpartners, mixing angles, and phases), making for a rich set of possibilities for supersymmetric phenomenology. Much of this phenomenology is governed by the spectrum of mass-eigenstates of the superpartners, which in general are mixtures of the flavor states. For example, the mixing between charged gauginos and higgsinos results in two mass eigenstates: *charginos* $\tilde{\chi}_1^\pm$ and $\tilde{\chi}_2^\pm$, in order of increasing mass. Likewise, the mixing between the neutral gauginos and higgsinos gives rise to four *neutralinos* $\tilde{\chi}_1^0$, $\tilde{\chi}_2^0$, $\tilde{\chi}_3^0$, and $\tilde{\chi}_4^0$.

An important constraint on supersymmetric phenomenology is a symmetry of the supersymmetric Lagrangian that leads to the conservation of *R-parity*. All Standard Model particles have even R-parity, whereas all superpartners have odd R-parity. R-parity-violating terms can be artificially added to the Lagrangian, but fine-tuning is required to prevent the rapid decay of the proton, so R-parity is generally assumed to be conserved. Conservation of R-parity implies that superpartners must be produced in pairs from collisions of Standard Model particles, and that their decay products must contain an odd number of superpartners. Thus a general Supersymmetry event is expected to consist of the production of a pair of heavy superpartners, which decay to Standard Model particles and lighter superpartners, which in turn decay until the lightest superpartners (LSP's) are reached. The LSP's cannot decay due to conservation of R-parity, so end products of the event are an even number of stable LSP's. The LSP may interact only weakly, and therefore represents a compelling candidate for dark matter. Dark matter candidate LSP's include the lightest neutralino ($\tilde{\chi}_1^0$), the lightest sneutrino, or in the case of "supergravity", in which Supersymmetry is promoted from a global to a local symmetry, the gravitino (the superpartner to the graviton). The neutralino is favored to be the LSP because cosmological and direct experimental constraints indicate that neither the gravitino nor the sneutrino can alone account for the observed abundance of dark matter in the universe.

Because the LSP's are electrically neutral, stable particles, they do not interact with a detector; the generic experimental signature of Supersymmetry is "missing energy" caused by LSP's sneaking energy from the collision out of the detector.

Supersymmetry, if it exists, must be a broken symmetry, and there are many different models for how supersymmetry-breaking might arise spontaneously (without explicitly adding symmetry-breaking terms to the Lagrangian). Most realistic scenarios of spontaneously-broken-supersymmetry require Supersymmetry to be broken in a "hidden" sector of particles completely neutral with respect to the Standard Model, and then transmitted to the "visible" sector (all Standard Model particles and their superpartners) by some *mediator* connecting the two sectors. Supersymmetry is therefore an important motivator for the possible existence of a hidden sector of matter.

1.3.3 Hidden Valley Models and Long-Lived Neutral Particles

While the existence of a hidden sector is well-motivated by supersymmetry in particular, hidden sectors can arise within a wide variety of models, such as the string theory and GUT models discussed in Section 1.3.1. The name *Hidden Valley* indicates any model in which the Standard Model gauge group G_{SM} has been extended by a non-abelian gauge group G_v under which all Standard Model particles are neutral, and in which there are new *valley particles* ("v-particles") that are neutral under the Standard Model gauge group but charged under the "valley" gauge group. If the dynamics of the *valley sector* ("v-sector") are confining as in Standard Model QCD, then the v-particles hadronize into *v-hadrons*. The hidden and visible sectors are connected by a neutral massive mediator such as a new massive gauge boson Z', Higgs bosons, neutralinos, or a loop of massive particles carrying both G_{SM} and G_v charges; if the energy of the LHC is high enough to produce such mediators, a "hidden" v-sector may not remain hidden for long.

The high mass of the mediator represents an energetic barrier that explains why such a hidden sector may be discovered at the LHC but not at prior, lower energy experiments. The high mass of the mediator also represents an energetic barrier that prevents otherwise stable v-hadrons from quickly decaying back to SM particles. Therefore it is natural for v-hadrons to exhibit long lifetimes when decaying (through the off-shell mediator) back to SM particles. Figure 1.13 shows a visual depiction of the SM and Hidden Valley sectors separated by an energetic barrier that is traversed at the LHC. Hidden Valley models are examples of models that predict long-lived neutral particles that could theoretically decay anywhere inside the detectors at the LHC. Such features imply the possible existence of discovery channels for rare decays of the Higgs boson that result in signals uniquely different from those expected within the Standard Model.

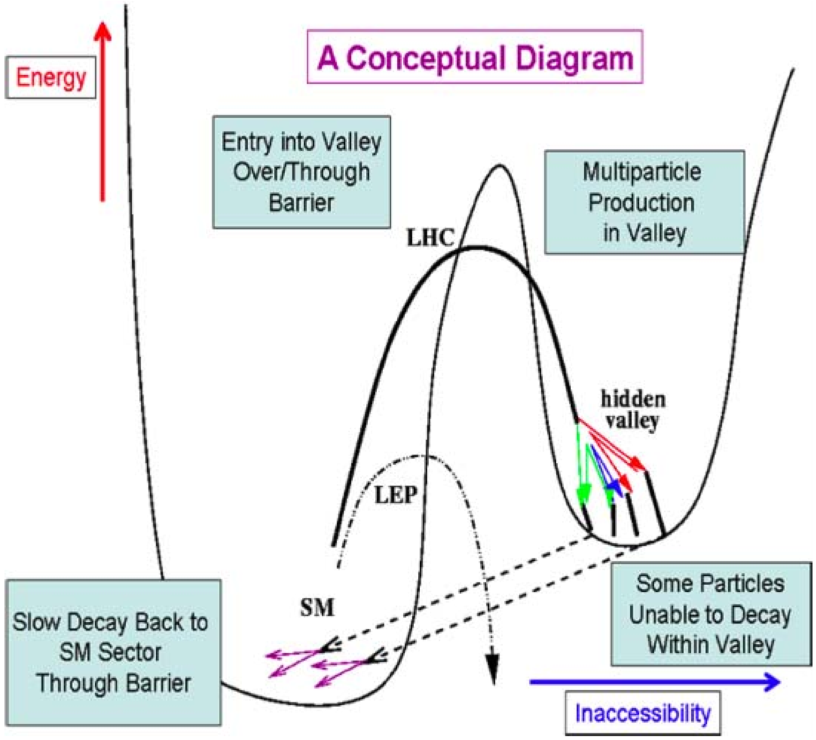

Figure 1.13: Conceptual depiction of the production and decay of v-hadrons. The SM sector is separated from the v-sector by an energetic barrier. Prior, lower energy particle accelerators such as LEP were unable to penetrate the barrier separating the sectors, but the LHC may be able to produce v-particles that hadronize and then decay back to SM particles by tunneling through the energetic barrier. [Taken from Matthew J. Strassler [39]]

There are many extensions to the Standard Model that could involve long-lived neutral particles with signatures similar to those found in Hidden Valley models. Examples include gauge-mediated supersymmetry extensions of the MSSM [11], MSSM with R-parity violation [12], and inelastic dark matter [13]. In this sense a focus on long-lived neutral particle phenomenology is fairly model-independent. On the other hand choosing a particular benchmark model allows specific predictions that can be studied using Monte Carlo data, and compared to the results of an experimental search. The hidden valley scenario, a generic class of models containing long-lived neutral particles, has been chosen in order to model the signatures of long-lived neutral particles.

1.3.4 A Specific Hidden Valley Model

There are many possible manifestations of hidden valley models. In general the SM gauge group G_{SM} is extended by a non abelian group G_V (the hidden sector). All SM particles are neutral under G_V, but typically v-particles are charged under G_V and neutral under G_{SM}. Interactions between the two sectors are made possible through higher dimension operators at the TeV scale, induced by a communicator as previously described. In a QCD-like scenario, the hidden sector is given a particle content to mirror the SM flavour structure, with v-particles assembled into G_V-neutral v-hadrons and QCD-like hadronization generating valley pions π_v. The decay of v-hadrons into SM particles, with observable lifetimes and significant branching ratio, is predicted by these models.

A specific benchmark model was chosen for this analysis in which a new Z' boson and the Higgs boson are mediators between the SM- and v-sectors, producing electrically neutral v-hadrons which can decay back to the SM with long lifetimes. It is desirable for the long-lived neutral particle search to be as model-independent as possible. Therefore the model considered is one of the simplest Hidden Valley sector examples [39]. The v-sector gauge group G_v is chosen to be $SU(3)_v \times U(1)'$, so that the SM is extended to be:

$$G_{SM} \times G_v = [SU(3) \times SU(2) \times U(1)]_{SM} \times SU(3)_v \times U(1)' \tag{1.26}$$

The hidden sector therefore contains eight gluon-like gauge fields just like SM QCD, and one photon-like neutral gauge Z' boson. The hidden sector is given two light U and D "v-quarks", given mass through the addition of a scalar field ϕ, whose vacuum expectation value spontaneously breaks the $U(1)'$ symmetry, giving the Z' gauge boson a mass of 1-6 TeV. This is an example of the Higgs mechanism discussed in Section 1.1.4. Both the SM fermions and v-quarks carry some charge under $U(1)'$, allowing the Z' to serve as a communicator between the two sectors. The $SU(3)_v$ group confines at an energy scale $1 \text{ GeV} < \Lambda_v < 1 \text{ TeV}$, much larger than the v-quark masses, such that they hadronize to form v-hadrons, combinations of U and D v-quarks. There are three v-pions

($\pi_v^{\pm}$,π_v^0) formed from U and D v-quarks in analogy to the three pions ($\pi^{\pm}$,π^0) in SM QCD formed from up and down quarks. It is important to note that both the π_v^0 and the $\pi_v^{\pm}$ are neutral under the SM and therefore invisible; the ± indicate charge under $U(1)'$, not $U(1)_{EM}$. Conservation of v-isospin implies that the $\pi_v^{\pm}$ cannot decay to SM particles not charged under $U(1)'$, and therefore the $\pi_v^{\pm}$ are stable (and therefore a dark-matter candidate). The π_v^0 is neutral and therefore can decay to SM charges via $\bar{Q}Q \to Z' \to \bar{f}f$, where f is any SM fermion. Due to the large Z' mass and small Z' coupling $g\prime$, the π_v^0 is long-lived.

The π_v^0 prefers to decay to more massive particles due to the same helicity-suppression that enhances $\mu^+\nu$ in usual π^+ decay. Helicity suppression is the result of the fact that while a spin-0 particle must decay to particles of opposite helicity in its own rest frame, as discussed in Section 1.1.4 only left-handed particles participate in the weak interaction. This might lead one to suspect that the weak decay of a spin-0 particle is impossible, however as described is Section 1.1.4 left- and right-handed particles are coupled by the Higgs mechanism with a coupling proportional to their mass. If the mass of the π_v^0 is less than the top quark mass but greater than twice the bottom quark mass, its dominant decay mode is $\pi_v^0 \to b\bar{b}$, and the π_v^0 branching ratios are ~85:8:5 for $b\bar{b}$, $\tau^+\tau^-$, and $c\bar{c}$, respectively. For $m_{\pi_v} \ll m_Z$, the decay width to $b\bar{b}$ is given by:

$$\Gamma_{\pi^0 \to \bar{b}b} \sim 10^9 s^{-1} \frac{f_{\pi_v}^2 m_{\pi_v}{}^5}{(20\ \mathrm{GeV})^7} \left(\frac{10\ \mathrm{TeV}}{m_{Z'}/g'}\right)^4 \tag{1.27}$$

where f_{π_v} is the π_v decay constant analogous to the SM pion decay constant, and the parameters $m_{Z'}$, $g\prime$ and f_{π_v} are unknown and may vary widely. The π_v^0 may therefore decay promptly or travel macroscopic distances.

Since we are primarily concerned with the π_v^0 we will hereafter drop the superscript and, excepting cases of possible ambiguity, will refer to it simply as the π_v . One mechanism for producing v-particles is through a Z' mediator. The large mass of the Z' results in high-multiplicity π_v final states. Z' production, hadronization, and decay of v-particles is depicted in Figure 1.14.

An alternative production mechanism is through the effect of mixing between the SM higgs, H, and the v-Higgs, ϕ, via the inclusion of a gauge-invariant $|h|^2|\phi|^2$ coupling term in the Lagrangian. Since the SM Higgs is light, v-particle production will be less abundant. This thesis focuses on the Higgs boson decay to two π_v's, $h \to \pi_v\pi_v$, where each π_v decays to a highly-displaced $b\bar{b}$ pair, a process depicted in Figure 1.15. We focus in particular on the gluon fusion process of Higgs boson production (Higgs production mechanisms will be briefly described in Section 1.3.5). A Feynman diagram depicting the Higgs production process is shown in Figure 1.16.

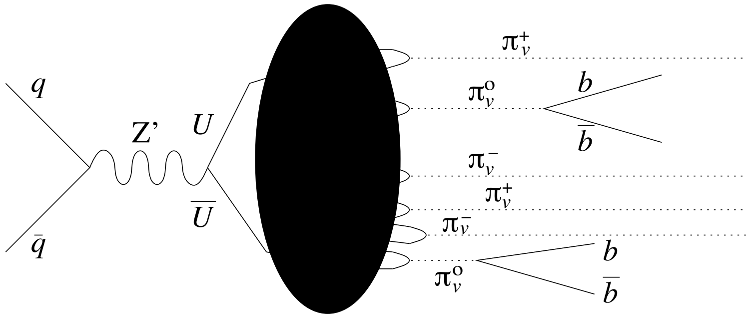

Figure 1.14: The Z' production mechanism, showing v-particle production, hadronization, and decay. Note that the $\pi_v^\pm$ is electrically neutral and invisible. [Taken from Matthew J. Strassler [39]]

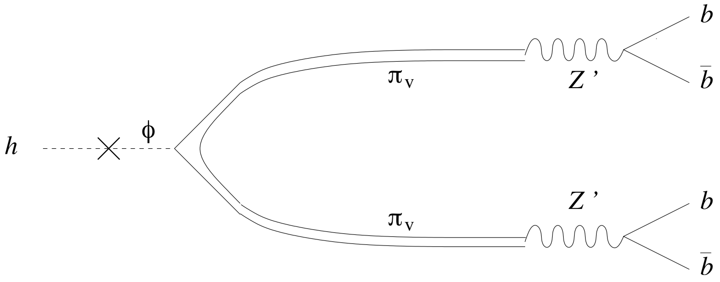

Figure 1.15: Higgs decay to π_v's, each of which decays to $b\bar{b}$. [Taken from Matthew J. Strassler [39]]

ATLAS has already published a search of this production and decay on 1.94 fb^{-1} of data [45]. That analysis focused on π_v decays in the muon spectrometer. This analysis uses 20.8 fb^{-1} of 2012 data, and is focused on searches for decays near the outer radius of the calorimeter. Figure 1.17 shows a simulated event with a π_v decaying in the calorimeter and the muon spectrometer. The prior analysis was designed to be sensitive to decays in the muon spectrometer; the analysis presented in

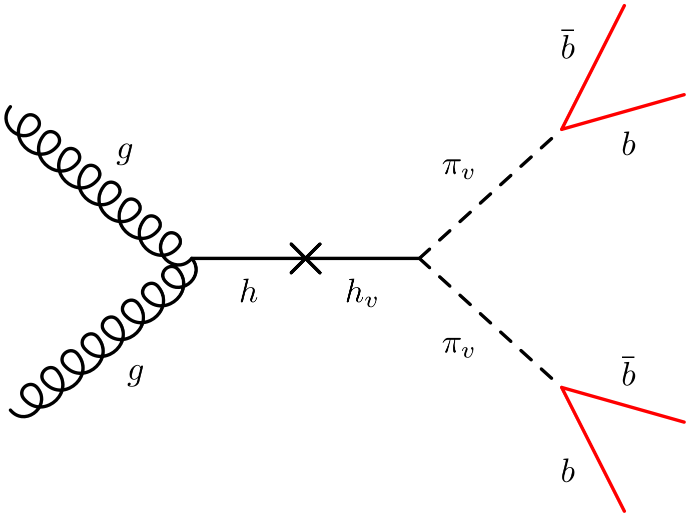

Figure 1.16: Gluon fusion Higgs production and decay to two neutral π_v's, each of which decays to a $b\bar{b}$ pair.

this thesis is designed to be sensitive to decays in the calorimeter.

1.3.5 Higgs Production Mechanisms

As discussed in Section 1.1.4, the Higgs boson couples to all massive particles in the SM, with a coupling strength proportional to their mass. Therefore the dominant Higgs production mechanisms in proton-proton collisions are not those in which partons couple directly to the Higgs (like if the gluon produced in the right hand diagram in Figure 1.9 were instead a Higgs), but rather involve the production and exchange of the most massive particles in the SM: the top quark and the W and Z bosons. Various possibilities are shown in Figure 1.18, which happens to show the four dominant Higgs production mechanisms in proton-proton collisions. The so-called “gluon fusion” production mechanism, the dominant contribution to which is represented by the upper-left diagram in Figure 1.18, has the largest cross section by far. This is both a consequence of the PDF’s (Figure 1.8), in which gluons make a strong showing, but also the fact that the top quark is too massive. Similar diagrams, but in which the top quark loop is replaced by loops of lower-mass fermions, also con-

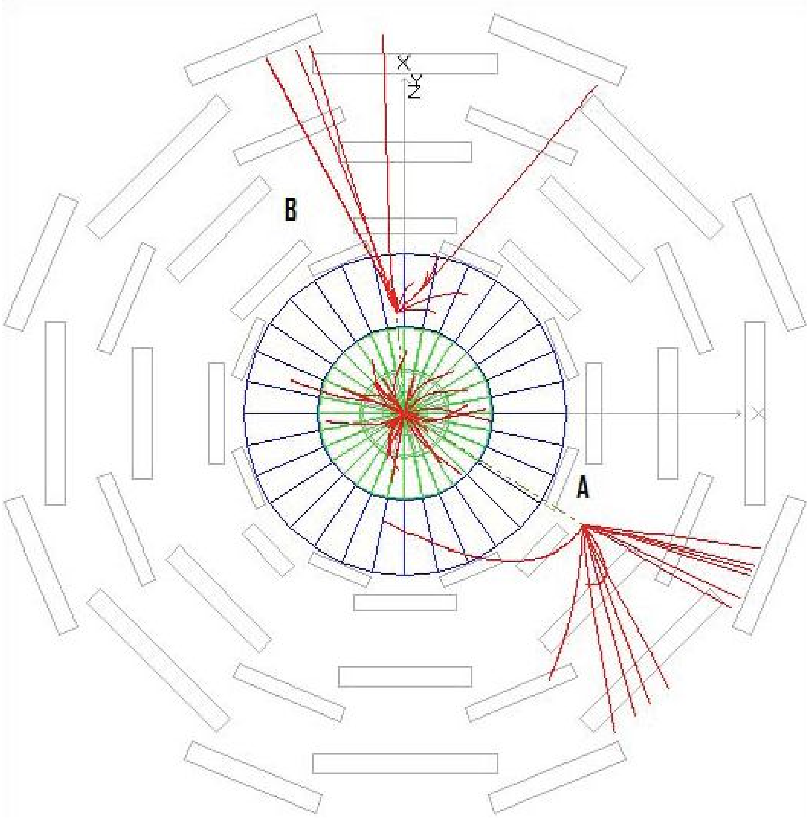

Figure 1.17: A simulated event showing the production and decay of two π_v's via $h^0 \rightarrow \pi_v\pi_v$, where one π_v decays in the calorimeter and the other decays in the muon spectrometer. This analysis is focused on identifying decays in the calorimeter.

tribute to the gluon fusion process, however the loop involving the massive top quark is by far the dominant contribution to the process. The lower-left diagram in Figure 1.18 is not a strong contender because it involves the energetically less-favorable production of not only the Higgs boson but also two massive top quarks.

Because of the large gluon fusion Higgs production cross section, it is favorable to search for Higgs produced through this mechanism. One big disadvantage, however, is that while many Higgs are produced, many may be lost if their experimental signature is not unique enough to be routinely accepted by the ATLAS trigger system[9]. This subject will be discussed in more detail in Section 2.8,

---

[9] So many collisions are produced at ATLAS that not all can be saved for analysis. The ATLAS trigger system selects only a small fraction ($\sim$0005%) of interesting collision events to save to disk. More background on this subject can be

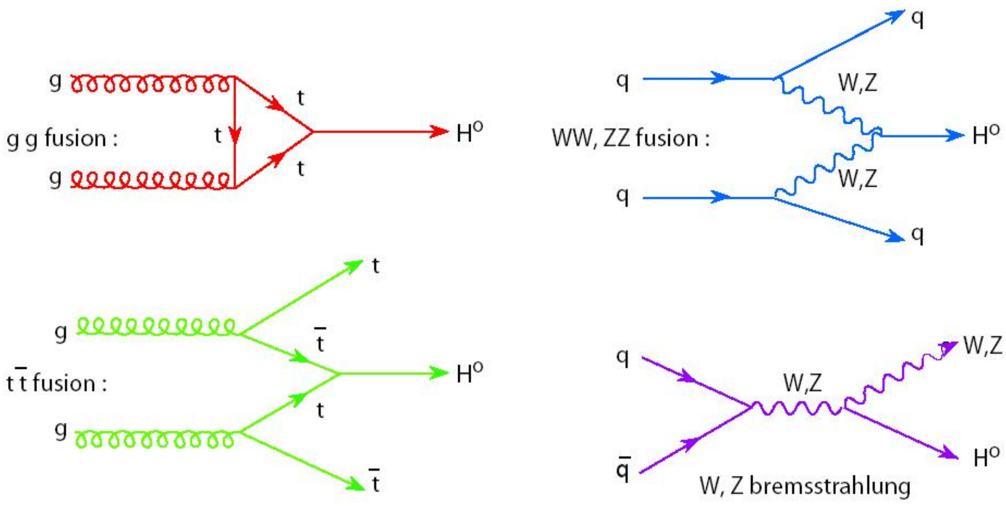

Figure 1.18: The four mechanisms for the Higgs boson production which have the highest production cross-section in TeV-scale proton-proton collisions.

however let us briefly consider a back-of-the-envelope comparison between the gluon fusion Higgs production cross section to the cross section for the production of QCD dijets (Feynman diagrams for which are shown in Figure 1.9) whose invariant mass is near the Higgs mass of 125 GeV. This is a valid comparison because, for a SM Higgs near 125 GeV, the Higgs decays predominantly to $b\bar{b}$, in other words: dijets. This, incidentally, is again a result of the fact that the Higgs coupling to matter fields is proportional to their mass; a pair of bottom quarks is the most massive pair of SM particles a 125 GeV Higgs can decay to.

For a Higgs mass near 125 GeV and for a proton-proton collision CM energy of 8 TeV, the gluon fusion Higgs production cross section is about 20 pb [44]. Cross sections and their relation to the number of observed events in proton-proton collisions were discussed in Section 1.2. In 2012 the LHC accumulated about 20fb^{-1} of integrated luminosity. The total number of expected Higgs events resulting from the gluon fusion process is therefore about $(20 \times 10^{-12}b) \times (20 \times 10^{15}b^{-1}) = 4 \times 10^5$. In contrast, consider that the QCD production cross section for dijets with an invariant mass near the higgs mass is on the order of 10^9pb. This implies that we expect about $(10^9 \times 10^{-12}b) \times (20 \times 10^{15}b^{-1}) = 2 \times 10^{13}$ such dijet events to have been produced in 2012. Considering

---

found in Section 2.8

that each event requires that about a megabyte be stored in some form of digital memory, storing this many events for an analysis would require more than 10^7 terabytes of disk space (as we will see in Section sec:trig, this is actually a far easier proposition than if we wanted to store *all* proton-proton events). Given that storing all these Higgs candidate events is completely unfeasible with current technology, some *filter* is necessary. Such a filter is called the *trigger*, and it is the trigger's job to reject events that are too common and *select* events that have some unique identifying characteristic.

Therefore let us return to the Higgs production mechanism. While the gluon fusion mechanism has the highest cross section, it does not typically produce events with particularly unique identifying characteristics. For this reason one might wish to study Higgs production via processes that have somewhat more identifiable characteristics. The gluon fusion alternatives in Figure 1.18 include, for example, cases in which the Higgs is accompanied by top quarks or W or Z bosons in the final state, which can decay to high-p_T leptons and additional jets. The choice of studying a Hidden Valley model in which the Higgs communicator to the hidden sector is produced via the gluon fusion process is crucially dependent on the experimental signature being uniquely identifiable. The Hidden Valley Higgs decay to long-lived neutral particles described in Section 1.3.3 is emphatically unique, however its unique characteristics must be identifiable by a trigger in order for such events to not be accidentally thrown away.

1.3.6 The unique characteristics of Hidden Valley Higgs decays

The unique characteristic of the Hidden Valley Higgs events under study, the process for which is shown in Figure 1.16, is the displaced decay of two neutral π_v's, which each produce a jet whose origin is far from the proton-proton collision interaction point (IP) and associated *primary vertex* (PV). This is distinct from most SM jets, which originate from the hadronization of outgoing final state partons emerging from the proton-proton collision. The hadronization time scale Λ_{QCD}^{-1} is roughly $\frac{1}{200\,\mathrm{MeV}}$ or $10^{-23}s$, which corresponds to an up quark (mass $\sim$2 MeV) and momentum 100 GeV traveling a distance of about 10^{-10}m, or 1 fm, which is not very far from the IP. On the other hand the most massive SM quark, the top quark, has a much higher mass ($\sim$173 GeV) and with a momentum of 100 GeV will travel only about 10^{-5} femtometers before hadronizing due to its smaller Lorentz factor. However, the top quark is highly unstable and decays in roughly 10^{-25} s, before it would have ever had a chance to hadronize (it is unique in this respect). The point is that either hadronization or decay of quarks and gluons occurs extremely close to the IP. This is true even for quarks and gluons indirectly produced through the decay of W or Z bosons, which have a lifetime roughly similar to that of the top quark. On the other hand many of the hadrons produced during the rapid hadronization of the quarks and gluons have significantly longer lifetimes.

SM jets are primarily composed of combinations of neutral and charged pions. Neutral pions decay immediately to photons, and charged pions are relatively stable[10], so jets are primarily seen as a combination of photons and charged pions originating from the IP. Jets also sometimes contain charged and neutral kaons, protons, and neutrons. While protons and neutrons are stable, and most kaons are relatively stable, the K_S^0 can sometimes decay macroscopically to charged or neutral pions (the K_L^0 has a much longer lifetime and rarely decays inside a typical detector volume). Thus ultimately a typical jet is composed of some combination of charged and neutral particles, almost all of which originate at the IP, but some small fraction of which originate some distance from the IP.

Less typically a SM jet may contain a bottom quark, which is relatively massive and therefore may carry a sizable fraction of the jet's energy. In such cases hadronization will lead to a hadron (containing the bottom quark) which carries a large fraction of the jet's energy, and whose decay will therefore largely define the jet's composition. Hadrons containing bottom quarks, *B-hadrons*, have lifetimes such that they typically decay on the order of millimeters or even centimeters from the IP (this is a result of the fact that the bottom quarks decay via the weak interaction). They therefore result in jets that largely originate from a *secondary vertex*, a point some distance from the primary vertex (and associated IP). Such secondary vertices, however, are never found beyond a few centimeters away from the IP.

It is extraordinarily rare, within the SM, for any high-energy jet to originate from anywhere other than within a few centimeters from the IP. Even in cases where some fraction of a jet's energy is carried by long-lived particles like the K_S^0, the jet is largely defined by the more dominant contribution from photons and charged pions originating from the IP. The long-lived decay of two π_v's, each of which decays on the order of a meter from the IP, is therefore a spectacular signature that cannot be easily confused with SM physics. The key difficulty, as will be seen in Section sec:Trigger, is

---

[10] Here by "relatively stable" I mean: stable enough that it is unlikely to decay within the volume of a typical detector (although it may be stopped or absorbed through its interaction with matter).

exploiting the capabilities of an experimental apparatus that was not designed primarily with the discovery of such decays in mind.

Chapter 2

EXPERIMENTAL APPARATUS

This section describes the particle accelerator used to produce proton-proton collisions (the LHC) and the detector used to identify particles emerging from the collisions (ATLAS). Each subcomponent of the ATLAS detector will be described, however the two components most important to this analysis are the Inner Detector and the Calorimeters, described in Sections 2.3 and 2.4, respectively.

2.1 The Large Hadron Collider

2.1.1 Motivation and Philosophy

Particle accelerators have been described as ‘the world’s most powerful microscopes.’ Such a description may sound clumsy, but it is in fact surprisingly apt. The operating principle of a microscope can be summarized as follows: probe particles strike a target and the particles that emerge from the resulting collisions are collected and studied in an effort to gain information about the target.

In an optical microscope the probe particles are photons. The particles that emerge from collisions with the target are also photons, and are recorded by the detector elements in our eyes. The energies of the detected photons (which we see as a range of colors) tell us something about the chemical properties of the target; the angular distribution of the photons tell us about its shape. This works for relatively large objects, but the photons of visible light are big – their low energy makes their wavelength about the size of a bacteria. Smaller probes are needed to resolve objects down to the atomic or subatomic scale. Electrons or protons are often used because their mass gives them a large intrinsic energy which corresponds to a short wavelength via the de Broglie relation. Electrons and protons also have the advantage of being electrically charged, which allows them to be accelerated and controlled using electromagnetic fields. A particle accelerator is a form of microscope that accelerates charged probe particles to near the speed of light in order to study objects at very short distance scales.

Probes of high enough energy do not merely scatter off the surface of atoms, but can be penetrating enough to reveal the atoms' internal structure: each atom consists of a small positively charged *nucleus* that is surrounded by a "cloud" of electrons. Probes of even higher energy can penetrate the nucleus, breaking it apart to reveal its constituents: protons and neutrons. At higher energies still, protons and neutrons can be broken apart and found to contain quarks. At the present day, using probes of the highest achievable energy, quarks and electrons appear to be *elementary*: they are not composed of smaller particles. However if higher energies are achieved it remains possible that they may be broken apart and found to be composed of smaller elementary particles that we have yet to discover.

Higher and higher energies are necessary not only to study the structure of matter at smaller and smaller distance scales, but also the forces that act between matter. Some forces operate at very short distance scales, and therefore can only be studied through high-enough energy collisions. Higher energy collisions may yet reveal forces we have yet to discover, forces which operate at smaller distance scales than we are currently able to probe.

A key difference between, for example, the use of optical microscopes and the use of particle accelerators, is the way in which the "images" that result from collisions are studied. The images that result from optical microscopes are often studied qualitatively, the eye discerning colors and shapes, each image the result of an average over countless collisions. The ability of perturbation theory (Section 1.2.1) to make quantitative predictions about high energy collisions, however, has resulted in a decidedly different paradigm. The predictions take the form of probabilities of observing types of collision events involving various "in" and "out" states. Thus particle accelerators, the providers of the "in" states, are designed to produce collisions that can be studied individually and categorized based on observed "out" states. Particle accelerators are therefore designed to produce collisions at discrete intervals, and an "image" must be taken of each collision event. Once many collisions have been individually categorized, the statistical predictions of the Standard Model can be compared to experiment. Experimental evidence of new forces or new particles manifests itself as the deviation of measured cross sections from those predicted by the Standard Model. The Standard Model, for example, predicts a cross section of zero for processes in which a massive neutral particle decays to $b\bar{b}$ pairs significantly away from the interaction point. The unambiguous observation of even a single such event would prove the Standard Model's prediction to be wrong.

The Large Hadron Collider (LHC) is a particle accelerator designed to accelerate and collide two beams of protons[1] moving in opposite directions at ∼99.999999% the speed of light. Protons (and their constituents) are therefore simultaneously the probe and target particles. In order to accelerate protons to the highest possible energy, the LHC is a circular accelerator of enormous size. Its circumference is dictated by the strength of the magnets used to bend the trajectory of the protons. The LHC was designed to accelerate protons to 7 TeV, resulting in a CM energy of 14 TeV. Higher proton speeds (and thus higher collision energies) require magnets more powerful than are currently available. Due to problems maintaining magnetic fields of high-enough intensity, the LHC has not yet achieved its design energy, instead operating at a CM energy of 8 TeV in 2012. This represents a fourfold increase in CM energy with respect to the previously most powerful particle accelerator, the Tevatron, which stopped operation in 2012.

2.1.2 The LHC and the CERN Accelerator Complex

The Large Hadron Collider (LHC) is a hadron accelerator designed to accelerate and collide two counter-rotating beams of hadrons. It is the largest and highest-energy collider in the world, located in a 27 km circular tunnel roughly 100m underground, at The European Organization for Nuclear Research (CERN), in Switzerland. The LHC was designed to collide protons at a CM energy of 14 TeV and with an instantaneous luminosity of $10^{34} cm^{-2} s^{-2}$. The acceleration of protons does not begin at the LHC, but occurs in many stages, in smaller particle accelerators which historically preceded the LHC. The LHC is fed by a succession of particle accelerators that, together with the LHC, make up the CERN accelerator complex (Figure 2.1).

The protons are initially obtained from a duoplasmatron source, which ionizes hydrogen atoms and uses electric fields to accelerate the protons away from the electrons, resulting in a 92 keV proton beam. The protons are then formed into bunches and injected into the LINAC (linear particle accelerator) where they are accelerated to 50 MeV before being fed into the first circular accelerator in the chain, the Proton Synchrotron Booster (PSB). The PSB accelerates the protons to 1.4 GeV and injects them into the Proton Synchrotron (PS), which accelerates the protons to 25 GeV before injection to the Super Proton Synchrotron (SPS), which accelerates the protons to 450 GeV. The 450

---

[1] The LHC will also be intermittently used to collide lead ions.

GeV protons are finally injected into the LHC, which in 2012 accelerated each beam of protons to 4 TeV, resulting in a collision CM energy of 8 TeV.

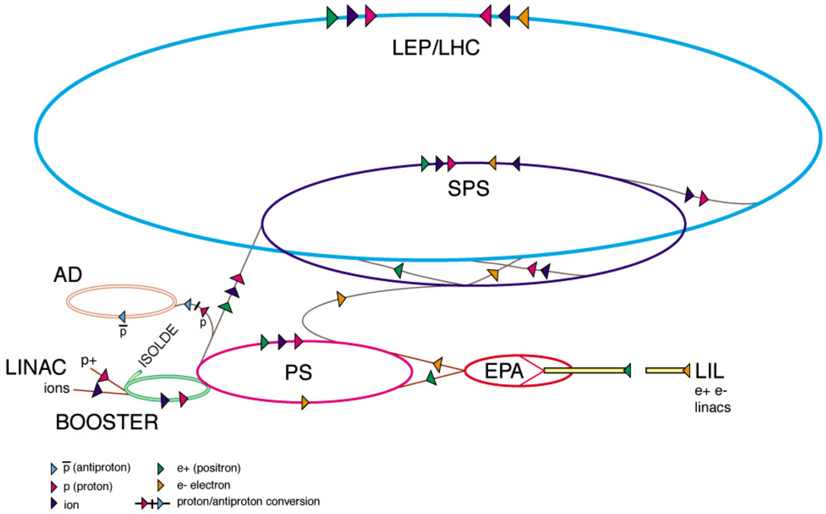

Figure 2.1: The CERN accelerator complex. The largest blue ring represents the Large Hadron Collider (LHC, preceded by LEP, the Large Electron-Positron Collider). Continuing in order from largest to smallest, the purple ring represents the Super Proton Synchrotron (SPS), the pink ring the Proton Synchrotron (PS), and the green ring the Proton Synchrotron Booster (PSB), which is fed by the linear particle accelerator (LINAC). The red and beige rings are not used by the LHC. The red ring represents the electron-positron accumulator (EPA) previously used by LEP, which was fed by the LINAC Injector for LEP (LIL). The beige ring represents the Anti-proton Decelerator (AD) used for anti-matter experiments.

2.1.3 The LHC

The layout of the LHC ring is shown in Figure 2.2. There are eight straight sections each approximately 528 m in length, labelled “Point 1” through “Point 8.” The proton beams are injected near Point 1, and accelerated by the RF-cavities at Point 4. Collisions occur at Points 1, 2, 5, and 8, where the four experiments are located (ATLAS, ALICE, CMS, LHCb, respectively). The beam is collimated at Points 3 and 7, and dumped at Point 6. A total of 1232 superconducting dipole magnets distributed among the eight arc sections are used to bend the beam into its circular trajectory.

The protons in the LHC do not come in a continuous stream, but are organized into *bunches*.

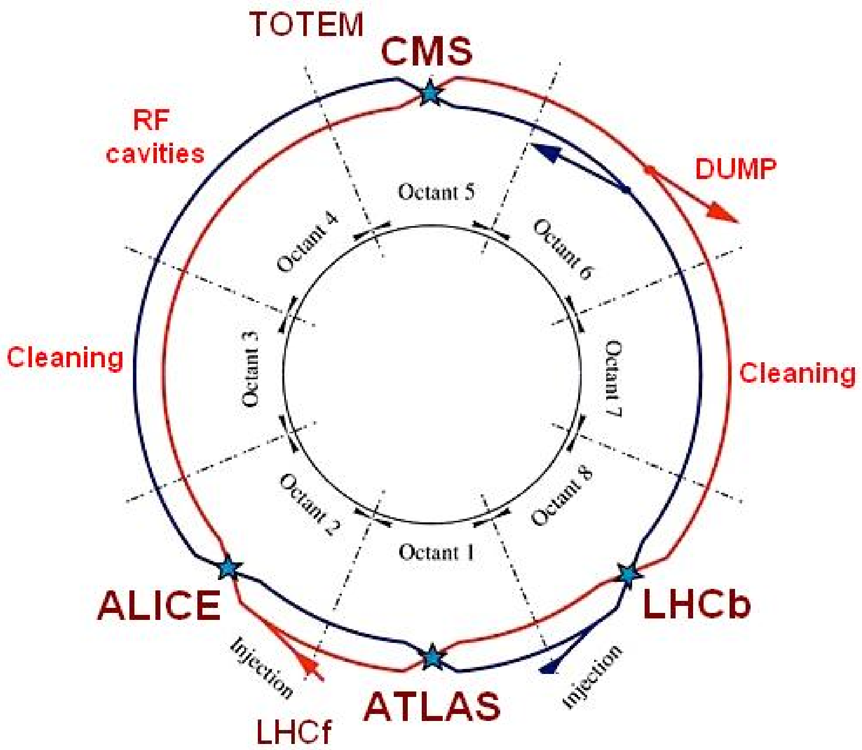

Figure 2.2: Schematic of the LHC ring showing the four interaction points.

This is a result of the fact that the radio frequency (RF) cavities used to accelerate the beams operate at about 400 MHz, which corresponds to 35640 potential wells (referred to as *buckets*) in the RF field where the bunches can be located. This corresponds to a bunch spacing of 2.5 ns, approximately the time it takes for light to travel three quarters of a meter. The LHC is designed to fill approximately only one out of every ten RF buckets, resulting in a bunch spacing of 25 ns, and 3564 possible bunch locations within each beam. This results in 3564 possible *bunch-crossings* per revolution of the beams. As the accelerators in the chain leading up to the LHC grow larger in circumference, the storage rings can hold larger numbers of fills coming from the previous stages, each separated by *injection gaps*. The *bunch pattern* is the sequence of filled and un-filled bunches that results from the various stages of the accelerator chain leading up to the LHC. Additionally, a long *abort gap* of unfilled bunches is necessary in case poor beam quality requires that the beams be removed from the ring (*dumped*) by “kicker” magnets which require 3 μs to reach full field strength. If the abort gap were not present in order to allow the kicker magnets to reach their full field strength, bunches of protons not fully diverted by hte kicker magnets could be sprayed into the superconducting magnets situated downstream. In general the deposition of energy from stray particles entering the superconducting magnets that surround the beam is a problem because it can cause them to "quench" (become non-superconducting), which requires that the magnets quickly dump their stored energy in order to avoid catastrophic thermal runaway. Because the magnets take hours to cool back down to operating temperatures before they can return to operation, the LHC strives to minimize the rate of magnet quenches in order to operate at as efficiently as possible.

Given the injection and abort gaps, each of the two beams in the LHC are designed to consist of up to 2808 proton bunches (out of 3564 possible bunch locations), each spaced 25 ns apart. Each bunch is a few cm long in the longitudinal direction, $\sim$1 mm in the transverse direction, and initially consists of $\sim 10^{11}$ protons. During the 2012 data taking period the LHC operated with a larger 50 ns spacing between bunches, resulting in 1380 bunches per beam.

2.1.4 Luminosity Production

The integrated luminosity (defined in Section 1.2.3) delivered by the LHC is proportional to the total number scattering events, and therefore one of the primary goals of the LHC is to deliver as much luminosity as possible to each experiment. The particle density at the interaction point of each experiment is therefore increased by squeezing the cross-sectional area of the beam at the collision point (β^*) to as small as possible (with a design radius of 16 μm) using quadrupole magnet pairs at each interaction point. The proton flux is likewise made as large as possible, however difficulties with beam confinement[2] limit the proton flux to approximately 10^{11} protons per bunch, and in 2012 beam stability issues limited the number of bunches per beam to 1380 (corresponding to a 50 ns bunch spacing). As described in Section 1.2.3, the instantaneous luminosity can additionally be increased by reducing the beam's transverse emittance ε_n and beam crossing angle F. The LHC delivered a peak instantaneous luminosity of approximately $8 \times 10^{33} cm^{-2} s^{-2}$ in 2012; the delivered instantaneous luminosity as a function of time in 2012 is shown in Figure 2.3. The total integrated luminosity delivered to ATLAS and recorded by ATLAS, as a function of time during the 2012

---

[2] Protons electrically repel each other and are confined using quadrupole, octupole, and sextupole magnets located in the eight straight sections of the LHC.

proton-proton run, is shown in Figure 2.3.

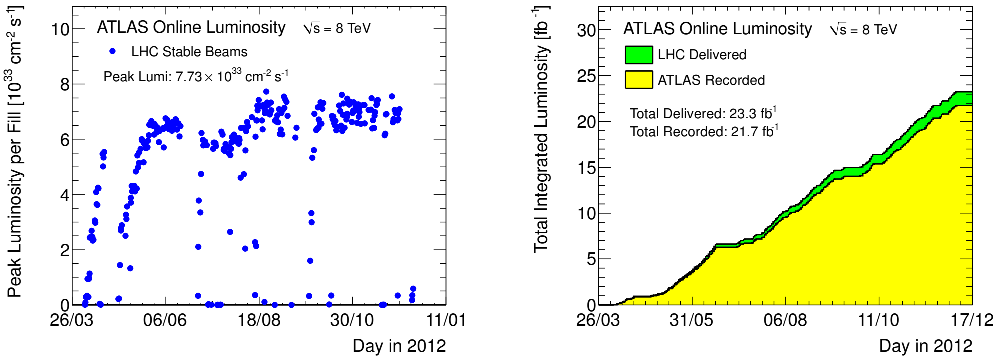

Figure 2.3: Left: Peak instantaneous luminosity per LHC fill as a function of time in 2012. Right: Integrated luminosity as a function of time in 2012.

While high instantaneous luminosities are desirable due to the resulting high number of scattering events, they come with corresponding challenges. Each bunch crossing typically produces multiple low-p_T proton-proton interactions known as *pileup* whose resulting jets and tracks overlay those resulting from the rarer and more interesting high-p_T scattering events. As is shown in Figure 2.4, bunch crossings in 2012 resulted in as many as 40 pileup proton-proton interactions. High pileup results in a large amount of tracks, primary vertices, and energy in each bunch crossing (in addition to that which is produced by the hard-scatter), which not only presents a challenge to detector performance, but also presents a challenge to the identification of tracks, vertices, and jets coming from the primary collision, and can therefore introduce systematic errors into physics measurements.

2.2 The ATLAS Detector

2.2.1 Motivation and Philosophy

The goal of a general purpose detector at a particle accelerator is to characterize a given scattering event as fully and accurately as possible. This means determining the energy of the particles emerging from the collision, as well as their charge and momentum and direction. The also means identifying individual particles when possible, as well as associating groups of particles with jets.

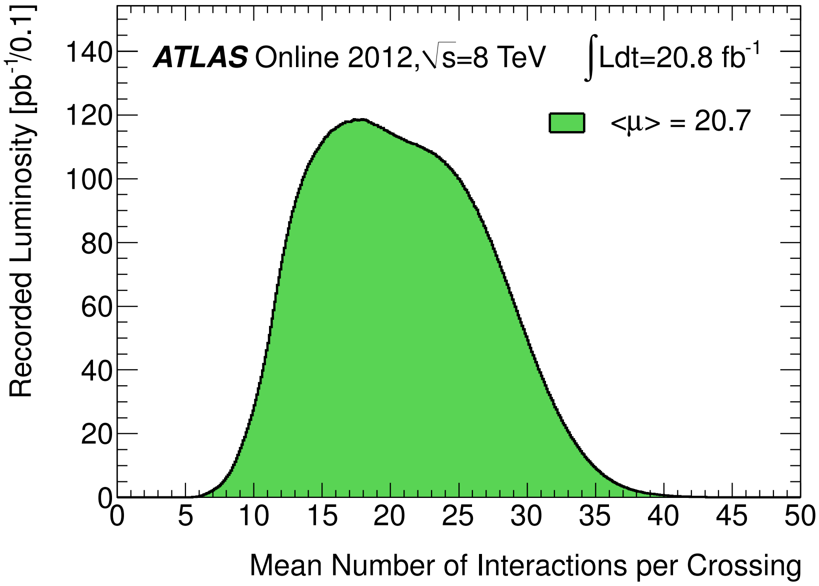

Figure 2.4: The luminosity-weighted distribution of the average number of interactions per bunch crossing in 2012.

Since particles can emerge from a collision in all directions, the detector is generally built in a radially-symmetric cylindrical shape surrounding the beam line, with its center at the collision point. Generally the detector consists of a "Barrel" section whose detector elements are placed parallel to the beam direction in order to detect particles emerging in directions roughly orthogonal to the beam line, and "Endcap" sections (one on either side of the barrel) whose detector elements are placed orthogonal to the beam direction in order to detect particles emerging in directions roughly parallel to the beam line.

The particles that emerge from a scattering event come in a variety of SM charges: some may be electrically charged or neutral; some may or may not interact via the strong interaction; some may only interact through the weak interaction. Therefore a number of particle detection methods must be employed.

Electrically charged particles ionize mediums through which they traverse, and can therefore be *tracked*. When subjected to a magnetic field perpendicular to their direction of motion, charged particles travel along a helical arc, clockwise or counterclockwise, depending on whether they are negatively or positively charged. If the magnetic field is roughly constant and if the particles' momenta are high enough that their ionization energy loss is small, then the radius of their helical path is roughly constant and proportional to the particle's momentum. In such cases each electrically charged particle's trajectory can be *reconstructed* by identifying at least three points along its path where it has passed through a detector element and left an ionization signature.

Therefore an important feature of a detector is its particle *tracker* and the surrounding magnetic field. The tracker is placed at the center of the detector, closest to the IP, in order to minimize the amount of material the particles must pass through before reaching the tracking detector elements. This ensures that by the time the particles' tracks are reconstructed there has been minimal ionization energy loss or multiple scattering, and that therefore each particle's reconstructed momentum is faithful to its value when it first emerged from the IP. The location of the tracking elements close to the IP is correspondingly important for the precise reconstruction of primary and secondary vertices close to the IP. The tracker is enclosed in a powerful superconducting magnet that generates a magnetic field running parallel to the beam pipe, in order to produce the bending of charged particles that is necessary for momentum determination. Due to the very high momentum possessed by some particles, a very powerful magnetic field is required to produce identifiable radii of curvature.

Since many particles are not electrically charged and therefore cannot be tracked, much of the energy coming from a collision would be invisible to a detector that only included a particle tracker. Therefore it is important that a different kind of detector surround the tracker, one that is capable of stopping, absorbing, and measuring the energy of the majority of SM particles. This is called a *calorimeter*. Generally two types of calorimeter are employed in sequence, one closer to the IP which is better at stopping electrons and photons, and a second that is best at stopping the hadrons that make it past the first calorimeter. In this way electrons and photons are more easily identified.

Two types of SM particles are not stopped by the calorimeters: muons and neutrinos. Muons are massive enough that they do not lose much energy passing through the calorimeters (they only interact through the electromagnetic and weak interactions), while neutrinos only interact weakly, and cannot be detected at all. Muons are therefore identified by placing tracking elements outside of the calorimeters; any charged particle passing through these detector elements is likely to be a muon. Neutrinos are identified indirectly, by the fact that they escape the detector and therefore result in a vector sum of transverse momenta in a collision event that does not sum to zero. Since the total transverse momentum before a collision is zero, momentum conservation ensures that the vector sum of the transverse momenta in an event should be zero. If it is not, the presence of a neutrino (or other neutral non-SM particle) can be inferred to carry away the momentum necessary for the total momenta to sum to zero.

2.2.2 ATLAS Overview

ATLAS ("**A** **T**ovoidal **L**HC **A**pparatu**S**") is a general purpose detector located at the collision Point 1 of the LHC. ATLAS is one of two general purpose detectors on the LHC ring; the other is CMS (the **C**ompact **M**uon **S**olenoid). ATLAS is large; its overall dimensions are roughly 45 meters long and 25 metres in diameter, with a weight of about 7,000 tons. The ATLAS collaboration consists of approximately 3000 physicists from 175 institutions in 38 countries.

A cutaway view of ATLAS indicating its various detector components is shown in Figure2.5. Moving outward from the IP is the *inner detector*, the *calorimeters*, and the *muon system*. Broadly speaking the inner detector identifies positively or negatively charged tracks and measures their momenta, the calorimeters capture and measure the energy and direction of all SM particles apart from muons and neutrinos, and the muon system identifies muons and measures their momenta.

The inner detector is composed of three particle tracking technologies: the silicon pixel tracker, the silicon strip tracker, and the transition radiation tracker, each designed to measure the trajectory and momentum of charged particles. The inner detector is surrounded by a superconducting solenoid magnet which produces a roughly 2 Tesla magnetic field in the inner detector.

The calorimeters surround the inner detector and solenoid magnet, and consist of two subdetectors in sequence: the electromagnetic calorimeter and the hadronic calorimeter. Together the electromagnetic and hadronic calorimeters measure the energies and directions of electrons, photons, and hadrons.

The calorimeters are surrounded by the muon spectrometer and superconducting toroid magnets which generate a roughly 0.5 Tesla magnetic field in the muon system for momentum-determination. The muon spectrometer is a tracking system composed primarily of drift tubes that is designed to measure the trajectory and momentum of the muons which typically escape the calorimeters.

Figure 2.6 shows examples of several different types of particles interacting with the various

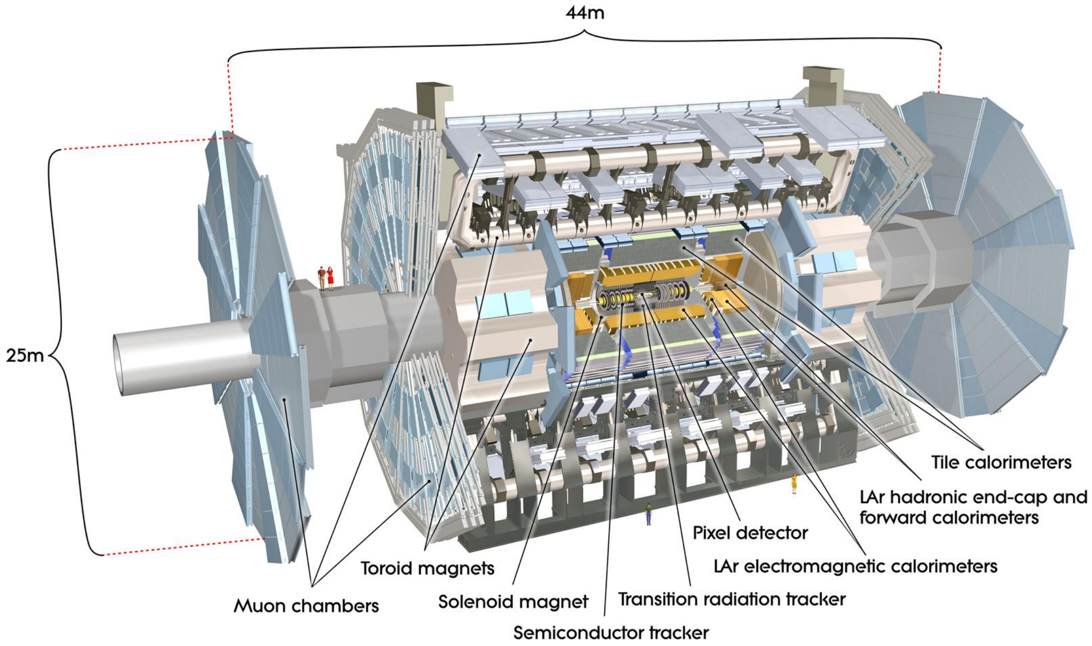

Figure 2.5: Three dimensional cut-away view of the ATLAS detector.

ATLAS detector subsystems. Muons, electrons, and charged hadrons leave tracks in the inner detector. Photons and electrons deposit most the their energy in the electromagnetic calorimeter, while hadrons like protons and neutrons deposit most of their energy in the hadronic calorimeter. Muons and neutrinos escape the calorimeter, but only muons are tracked by the muon system.

2.2.3 ATLAS Coordinate System and Conventions

ATLAS primarily uses two coordinate systems, both of which share an origin at the center of the ATLAS detector. A right-handed cartesian (x,y,z) coordinate system is defined with the z-axis pointing along the beam pipe in the counterclockwise direction as seen from above. The x-axis points towards the center of the LHC ring, and the y-axis points skyward. The other, more commonly used coordinate system (R,ϕ,η) uses polar coordinates (R,ϕ) to describe the transverse plane, where ϕ is the azimuthal angle around the beam pipe with $\phi = 0$ defined to point along the x-axis. The coordinate η was introduced in Section 1.2.4, and is defined in terms of the polar angle θ, the an-

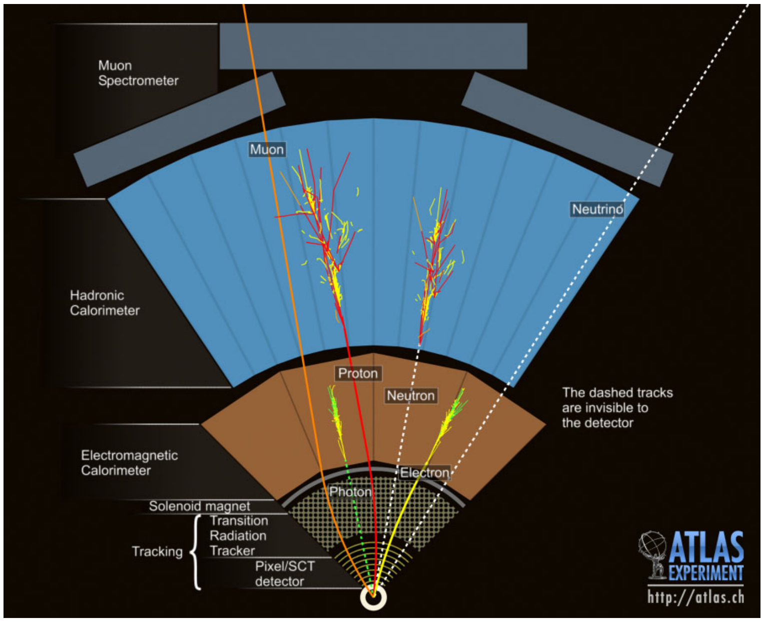

Figure 2.6: Examples of particle interactions with the ATLAS detector subsystems.

gle from the beam axis. Since differences in η are approximately invariant under boosts along the z-direction, it is the preferred parametrization of polar angle. Distances in θ-ϕ space (which define solid angles, for example) are likewise preferred to be invariant under boosts along the z-direction. Angular distances are therefore generally measured in terms of "ΔR":

$$\Delta R = \sqrt{\Delta\eta^2 + \Delta\phi^2} \tag{2.1}$$

As discussed in Section 1.2.4, the use of η is related to the fact that the partons that particpate in a hard scatter have zero momentum in the transverse plane, but have an unknown longitudinal fraction of the proton's momentum. Due to conservation of momentum, the total momentum in the transverse plane must sum to zero. Therefore variables are frequently projected onto the transverse plane. For example the transverse momentum vector is defined as $\vec{p}_T = (p_x, p_y)$, and the transverse energy is defined as $E_T = Esin(\theta)$.

ATLAS uses natural units with the speed of light, c, set equal to one. As a consequence, mass, energy, and momentum are all measured in GeV. Likewise both the proper lifetime (τ) and the proper decay length (cτ) of particles are measured in meters.

2.3 Inner Detector

The ATLAS inner detector is designed to be able to precisely measure the momentum and direction of the over 1000 charged particles with $|\eta| < 2.5$ expected to emerge from the collision point every 25 ns at the design luminosity of $10^{34} cm^{-2} s^{-1}$. A cutway view of the inner detector is shown in Figure 2.7, and a more detailed schematic layour is shown in Figure 2.8.

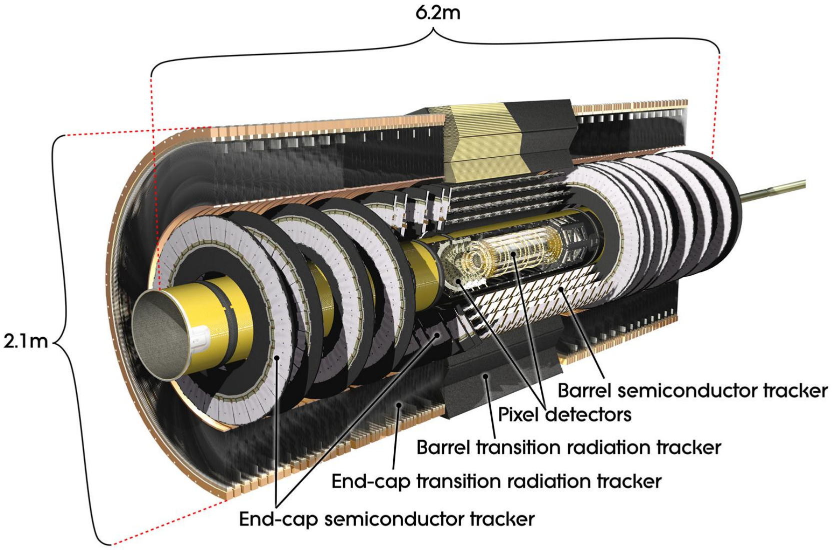

Figure 2.7: Cutaway view of the ATLAS inner detector.

The inner detector is composed of three main subdetectors: the pixel detector, the silicon microstrip (SCT) detector, and the transition radiation tracker (TRT). Together, by measuring typically $\sim$37 space-points or *hits* along tracks, they are able to precisely measure the trajectories of charged particles with $|\eta| < 2.5$ and $p_T > 0.5$ GeV.

2.3.1 Pixel Detector

The pixel detector is a technology consisting of millions of tiny silicon pixel sensors. The pixel detector is closest to the beam pipe, and consists of three concentric cylindrical layers of pixels in the barrel (starting at R = 51 mm) and three consecutive disk-shaped layers in the endcaps (starting at $|z|$ = 495 mm). Typically three pixel layers are traversed by each track, and each space point

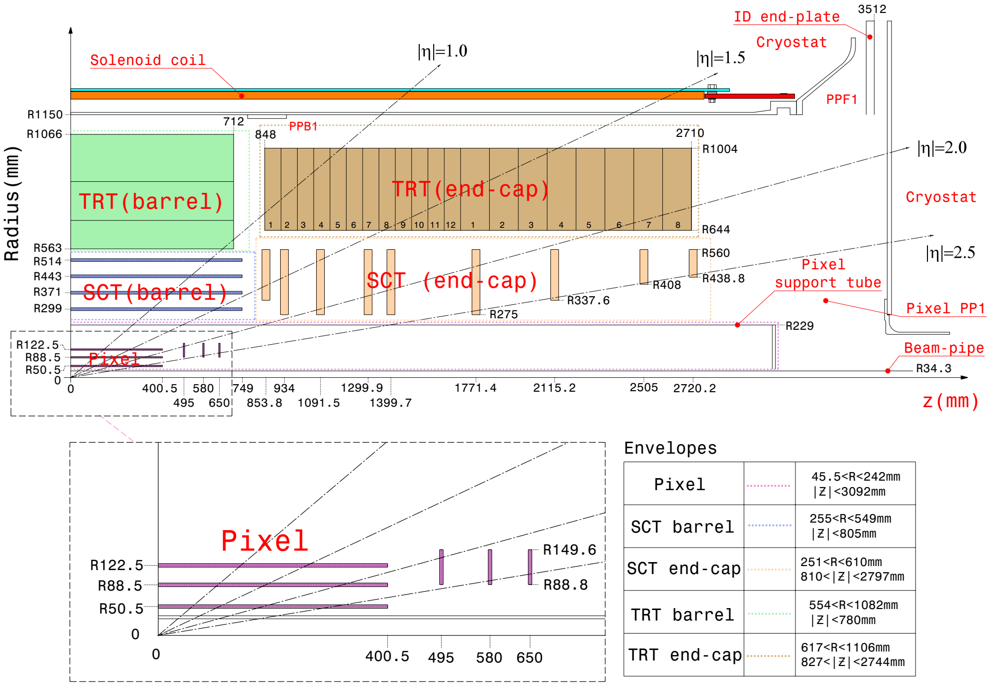

Pixel	⋯	45.5<R<242mm |Z|<3092mm
SCT barrel	⋯	255<R<549mm |Z|<805mm
SCT end-cap	⋯	251<R<610mm 810<|Z|<2797mm
TRT barrel	⋯	554<R<1082mm |Z|<780mm
TRT end-cap	⋯	617<R<1106mm 827<|Z|<2744mm

Figure 2.8: Quarter-section of the ATLAS inner detector showing each of the main components and their dimensions.

is measured with an intrinsic accuracy of 10 μm in (R-ϕ) and 115 μm in z in the barrel (with an alignment tolerance of 10-20 μm in R), and 10 μm in (R-ϕ) and 115 μm in R in the end cap (with an alignment tolerance of 100 μm in z). The pixel detector is closest to the IP where the track density is highest and where precision measurements are crucial for constraining the location of primary vertices. It is therefore the highest-granularity detector in ATLAS, with approximately 80.4 million readout channels.

2.3.2 *Semiconductor Tracker*

The SCT is a technology consisting of millions of silicon microstrip sensors. In the barrel the strips lay parallel to the beam direction, and each strip only measures the R-coordinate, however strips are displaced from each other by small angles such that the R-coordinate information from a pair of strips gives the (R-ϕ) coordinate of a single space point. A similar technique is used in the endcaps, where the strips are organized radially. The SCT consts of 4 concentric cylindrical barrel modules and 9 consecutive end cap modules, providing up to 4 space points in the barrel and 9 space points in each end cap. Barrel hits have an intrinsic accuracy of 17 μm in (R-ϕ) and 580 μm in z (with an alignment tolerance of 100 μm in R), and endcap hits have an intrinsic accuracy of 17 μm in (R-ϕ) and 580 μm in R (with an alignment tolerance of 200 μm in z).

2.3.3 Transition Radiation Tracker

The TRT is a technology based on hundreds of thousands of 4 mm diameter straw tubes each containing a Xe-based gas mixture and a central wire held at 1560V for the colleciton of ionization electrons. The straw tubes are 144 cm long and arranged in up to 73 concentric layers parallel to the beam pipe in the barrel, and 37 cm long and arranged radially in 160 layers in wheel modules in the end caps. Due to the length of the straw tubes the TRT provides only R-ϕ information in the barrel and Z-ϕ information in the endcaps, with an intrinsic accurancy of 130 μm per straw. The many layers of straw tubes provide on average 30 hits per track; the lower precision per space point is compensated by a large number of measurements along a longer track length as compared to the silicon-based detectors, and so the TRT contributes significantly to the overall track momentum measurement. Additionally, the TRT exploits the fact that more charge is deposited in straw tubes by electrons (due to their radiation of transition radiation photons) than by heavier (and therefore slower) charged particles such as muons or pions. Such “high threshold” hits along tracks are used to identify electrons and distinguish them from other charged particles.

2.4 Calorimetry

The primary objective of the calorimeter system is to stop all particles (except muons and neutrinos), and measure their position and energy. Particles are stopped using a dense absorber material which causes the particles to *shower*. A particle shower results when a particle interacts with a material and produces secondary particles which do the same, leading to a cascade. Electromagnetic showers involve photon pair production and electron bremsstrahlung (radiation of photons) as a result of electrons’ or photons’ interaction with atomic electrons and nuclei. Hadronic showers result from hadrons interacting with nuclei to produce mainly charged and neutral pions, some of which interact with further nuclei, and some of which decay to muons, neutrinos, electrons, and photons, where the electrons and photons shower electromagnetically.

The ATLAS calorimeter system is designed to separate electromagnetic from hadronic showers using two different detector technologies. The electromagnetic calorimeter is designed to initiate electromagnetic showers and measure their energy content, while the hadronic calorimeter is designed to initiate hadronic showers and measure their energy content. Therefore the electromangetic calorimeter is optimized to stop and measure particles that interact electromagnetically (primarily electrons and photons), while the hadronic calorimeter is optimized to stop and measure particles that interact via the strong nuclear force (hadrons). The calorimeters are shown in Figure 2.9.

Both the electromagnetic and hadronic calorimeters are sampling calorimeters in which layers of dense materials that produce particle showers and layers of active detector mediums are interleaved. Two primary technologies are employed in the two different calorimeter systems: the electromagnetic calorimeter employs lead absorber plates interleaved with an active liquid argon (LAr) ionization medium, while the hadronic calorimeter primarily uses iron absorber tiles interleaved with plastic scintillator tiles. When a charged particle passes through LAr, ionization electrons are released and collected at a charged anode to produce a signal amplitude; when a charged particle passes through a scintillator tile, ionization results in luminescence whose intensity represents a signal amplitude. The electromagnetic calorimeter has a fine granularity for the precise measurement of electrons and photons, while the hadronic calorimeter has a coarser granularity that is sufficient for the identification of jets and missing transverse energy. The two calorimeters work in concert, as typical jets include some energy deposition in both the electromagnetic and the hadronic calorimeters (on average about $\sim$70% and $\sim$30%, respectively).

Since the missing transverse energy is an important variable in many physics analysis, it is necessary that the calorimeters' energy measurement cover as large a region in η as possible, and that the calorimeters are deep enough to contain both electromagnetic and hadronic showers. The ATLAS calorimeters are hermetic in ϕ and cover $|\eta| < 4.9$.

2.4.1 The Electromagnetic Calorimeter

The electromagnetic calorimeter (ECal) primarily consists of a lead/LAr sampling calorimeter divided into a barrel and two endcap sections. The barrel provides coverage up to $|\eta| < 1.475$, and

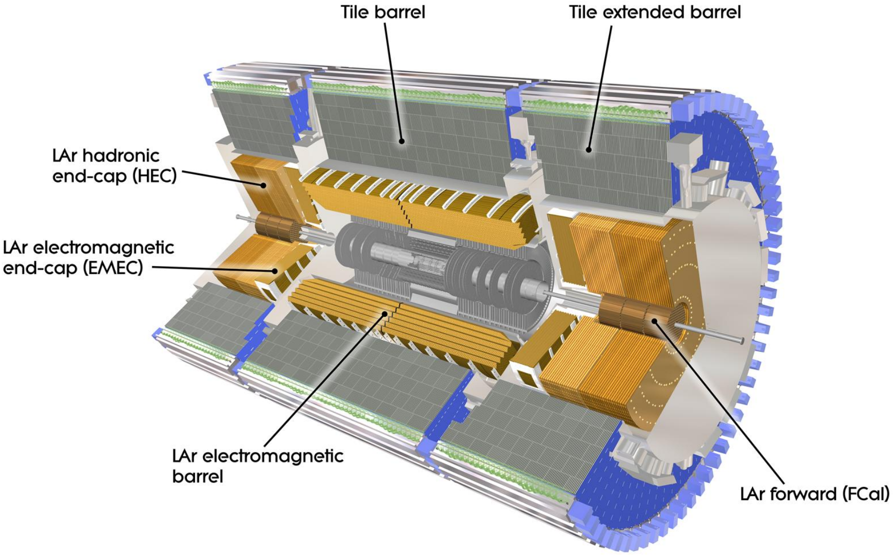

Figure 2.9: The ATLAS calorimeters.

the endcaps cover $1.375 < \eta < 3.2$. Additional coverage in the forward region ($3.1 < |\eta| < 4.9$) is provided by a tungsten/LAr calorimeter (part of the "FCal"). The barrel of the ECal resides just after the solenoid magnet and shares its cryostat in order to reduce the amount of material in front of the calorimeters, while the endcaps reside in their own cryostats. The barrel is 6.4 m in length with an inner and outer radius of 2.8 m and 4 m, while the endcap sections are 0.6 m in length with inner and outer radii of 0.3 m and 2.1 m.

Figure 2.10 shows the segmentation of cells in a barrel ECal module, as well as the accordion geometry of the alternating lead and LAr/electrode layers which allows for hermetic coverage in ϕ while simultaneously allowing electronic readout at the inner and outer radii (this has the advantage of eliminating gaps in ϕ that would otherwise be necessary for electronic readout). Cells are segmented in η and ϕ, and the depth of each of the three layers are shown in terms of electromagnetic radiation lengths, X_0. The radiation length is the mean distance over which an electron loses $1/e$ of its energy due to bremsstrahlung. The first layer has a granularity in $\Delta\eta \times \Delta\phi$ of 0.003×0.1, the second layer a granularity of 0.025×0.025, and the third layer a granularity of 0.05×0.025.

The first layer of the ECal is shallow in depth but very finely grained in η (less so in ϕ to account for electrons bending in ϕ due to the magnetic field) in order to produce precise electron and photon direction measurements, and to aid in the detection of photon conversions and in the discrimination between pions and photons. The second layer has the largest material depth and so contains the majority of the shower's energy, and is finely grained in order to aid in the analysis of electromagnetic shower shape. The third layer, shallow in depth and more coarsely grained, measures the tails the elecromagnetic shower. The region $|\eta| < 1.8$ before the first layer additionally includes a thin "presampler" LAr layer which identifies showers that have begun in the 2-6 radiation lengths worth of infrastructure and detector material before reaching the calorimeters, and which therefore aids in the correction for energy loss in pre-calorimeter material.

The ECal exceeds 22 radiation lengths in the barrel and 24 radiation lengths in the endcaps, sufficient to almost always fully contain electromagnetic showers from electrons or photons. The number of radiation lengths in the active material is at its minimum in the region of transition between the barrel and endcaps ($1.37 < |\eta| < 1.52$), where there is also up to 7 radiation lengths of inactive material, and for this reason the transition region is sometimes excluded from analyses. The cumulative amount of material in the electromagnetic calorimeter in terms of the radiation length is shown in Figure 2.11.

The ECal represents about 2.3 nuclear interaction lengths, λ. The nuclear interaction length is the mean distance traveled by a hadron before interacting inelastically with a nucleus. Therefore hadronic showers often begin in the ECal, and can even sometimes be entirely contained in the ECal. The cumulative amount of material in the ATLAS calorimeter system in terms of the nuclear interaction length is shown in Figure 2.14.

The fractional energy resolution of the ECal has been measured using an electron beam calibrated to various energies and angles. The experimental data is fitted to the expression

$$\frac{\sigma_E}{E} = \frac{a}{\sqrt{E}} \oplus b \tag{2.2}$$

where "a" is the stochastic term due to statistical fluctuations in the energy deposits, and "b" the constant term due to local non-uniformities in the response of the calorimeter. The result, for various electron energies between 10 and 245 GeV and at various η values in the barrel and endcaps, is a fractional energy resolution that does not exceed $\frac{10\%\sqrt{GeV}}{\sqrt{E}} \oplus 0.7\%$.

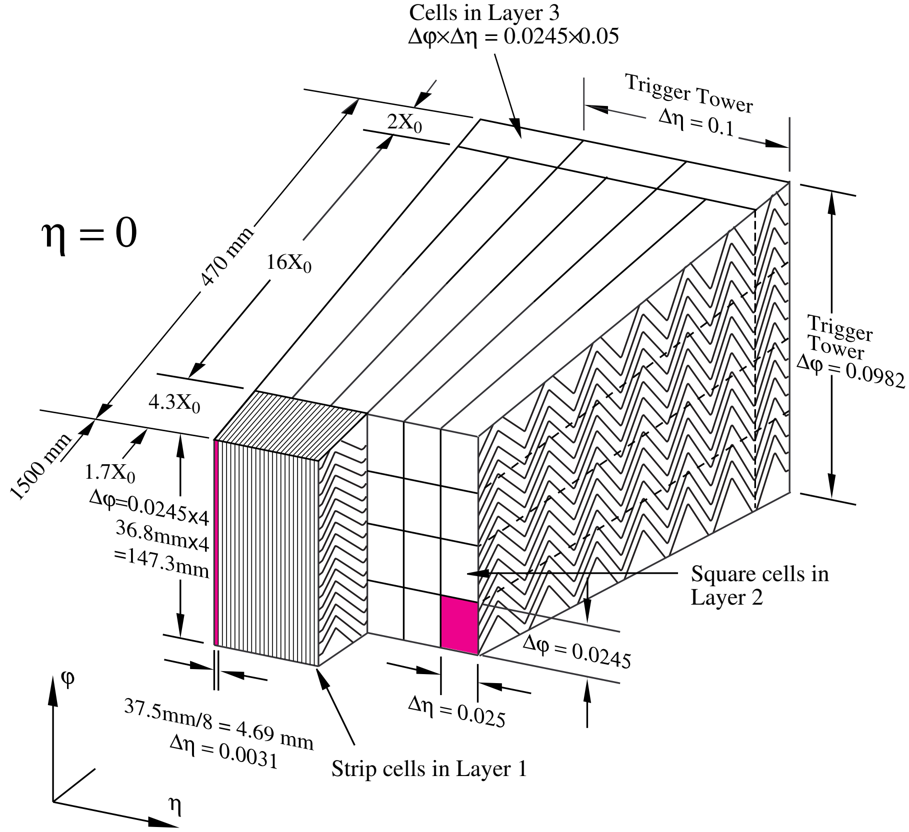

Figure 2.10: The layout of an electromagnetic calorimeter module in the barrel. A single cell in the second layer of the calorimeter (which represents the majority of the ECal's depth) is colored in purple.

The time resolution of the ECal was also studied using test beams. The time resolution of a typical calorimeter cell is about 0.1 nanoseconds.

2.4.2 The Hadronic Calorimeter

The hadronic calorimeter (HCal) consists of barrel and endcap components which utilize different sampling calorimeter technologies. The barrel ($|\eta| < 1.7$) uses iron tiles interleaved with plastic scintillator tiles, while the endcaps ($1.5 < |\eta| < 3.2$) use copper interleaved with active layers of LAr, similar to the ECal. Additional coverage in the forward region ($3.1 < |\eta| < 4.9$) is provided by a tungsten/LAr calorimeter (part of the "FCal"). The barrel of the HCal extends from and inner

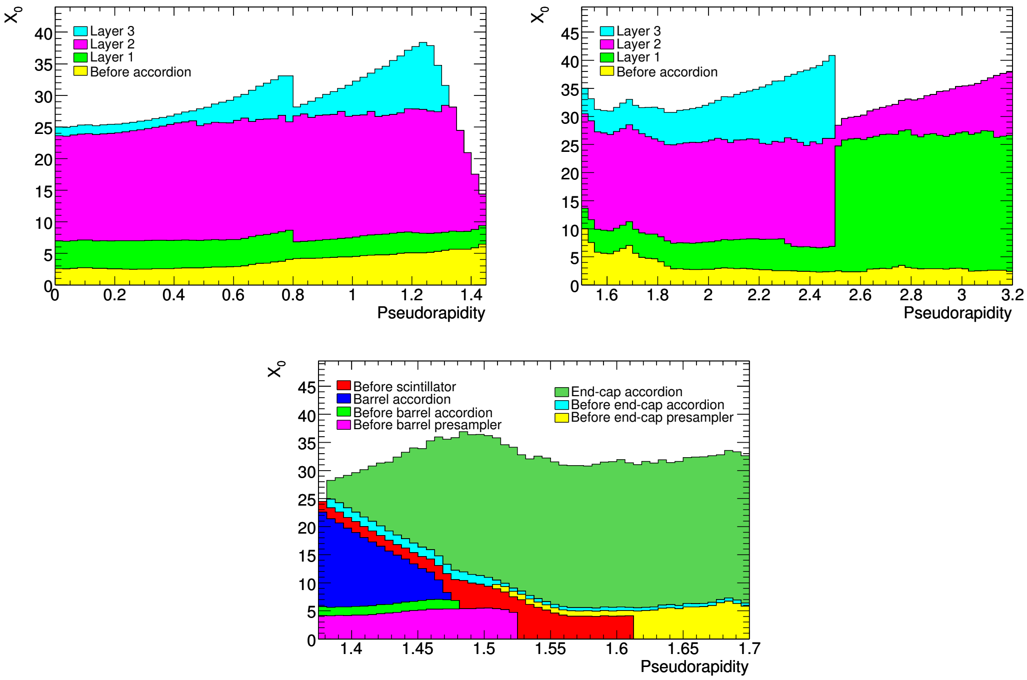

Figure 2.11: The cumulative amount of material in the electromagnetic calorimeter in units of electromagnetic radiation length X_0. The two top plots show separately for the barrel (left) and end-cap (right), the thicknesses of each calorimeter layer as well as the amount of material before the first active layer. The bottom plot shows the details of the crack region between the barrel and endcap cryostats, both in terms of material in front of the active layers as well as the total thickness of the active calorimeter.

radius of 2.3 m to an outer radius of 4.3 m, and the endcaps extend from an inner radius of 0.4 m to and outer radius of 2.0 m.

The barrel of the HCal consists of two sections: the central barrel ($|\eta| < 0.8$) that is 5.8 m in length and extended barrels ($0.8 < |\eta| < 1.7$) each 2.6 m in length. The cracks between the barrel and extended barrels are used for services. The tiles are oriented radially about the beam axis and grouped into wedge-shaped modules (Figure 2.12) of size $\Delta\phi \sim 0.1$, 64 of which make up each barrel and extended barrel section. The scintillator tiles are read out by optical fibers into photomultiplier tubes. The tiles within each module are arranged into cells which form three sampling layers oriented parallel to the beam pipe, and towers in η which point toward the center of the detector (Figure 2.13). The first two layers have a granularity in $\Delta\eta \times \Delta\phi$ of 0.1×0.1; the third layer has a granularity of 0.2×0.1.

Each endcap of the HCal consists of two independent wheels. Each wheel is composed of 32 wedge-shaped modules each containing two sampling layers arranged parallel to the beam pipe. The low-η layers have a granularity in $\Delta\eta \times \Delta\phi$ of 0.1×0.1 and the high-η layers have a granularity of 0.2×0.2.

While the granularity of the HCal is less fine than the granularity of the ECal, it is sufficient for the measurement of jet direction and energy, and is fine enough to allow some measurement of the shower shape development. The radial thickness of the barrel HCal is approximately 7 hadronic interaction lengths; the thickness of the endcap HCal is aproximatelly 10 interaction lengths. The calorimeter as a whole, including both the ECal and the HCal consitutes a total of 11-19 interaction lengths, depending on η. The cumulative amount of material in the ATLAS calorimeters in units of interaction length is shown in Figure 2.14.

There is a transition region between the central and extended barrels as well as between the extended barrels and endcaps, covering about $1.0 < |\eta| < 1.6$, which includes inactive material including services and the cryostat walls. Extra scintillators are installed (modules E1-E4 in Figure 2.14) to partially recover energy lost in the inactive material, however there is nonetheless a poorer energy resolution in this region.

While the thickness of the HCal is optimized to contain hadronic showers, it is possible for the shower development of very high energy jets to not be entirely contained within the HCal. This results in "punch-through", in which particles emerge from the HCal and produce activity in the muon system.

The HCal modules have been calibrated using electron beams with energies between 10 and 180 GeV in order to set the energy conversion scale to be consistent with the ECal electron response. Beams of charged pions at various energies and angles were used to measure the fractional energy resolution of the HCal. The data was parametrized by Equation 2.2 and the average fractional energy resolution in the barrel was found to be about $\frac{56\%\sqrt{GeV}}{\sqrt{E}} \oplus 6\%$, although significant η-dependence was observed.

The time resolution of the HCal was also studied using test beams. The time resolution of a given cell depends on the amount of energy deposited, and ranges from 0.2 to 1.5 nanoseconds.

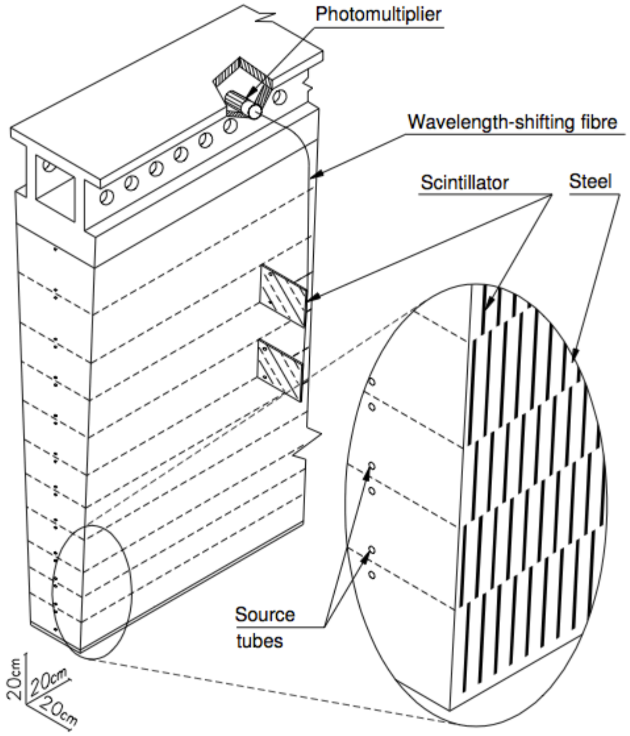

Figure 2.12: An illustration showing the integration of tiles into a single module in the hadronic calorimeter.

2.5 Muon Spectrometer

The muon spectrometer (MS) is the outer-most part of the ATLAS detector, designed to identify muons and measure their momenta. Muons are identified with tracks in the muon spectrometer because they are the only charged Standard Model particle likely to escape the calorimeters. The bending of the muon trajectory required for momentum determination is accomplished using superconducting barrel and endcap air-core toroid magnets, around which the MS is built. The MS is composed of barrrel and endcap sections which together cover the pseudorapidity range $|\eta| < 2.7$, and is comprised of four different detector technologies. The Monitored Drift Tube chambers (MDT's) and Cathode-Strip Chambers (CSC's) provide precision tracking measurements in the respective eta ranges $|\eta| < 2.7$ and $2.0 < |\eta| < 2.7$, and the Resistive Plate Chambers (RPC's) and

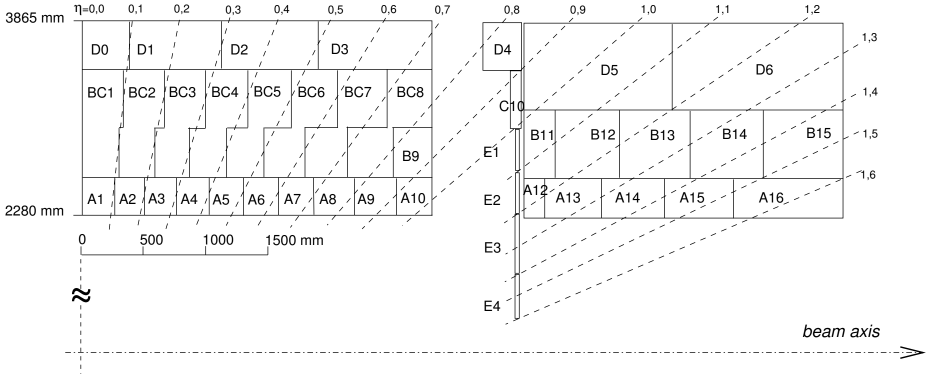

Figure 2.13: An illustration showing a module in the barrel (left) and extended barrel (right) of the hadronic calorimeter, showing the arrangement of the tile cells into towers in η and layers parallel to the beam pipe.

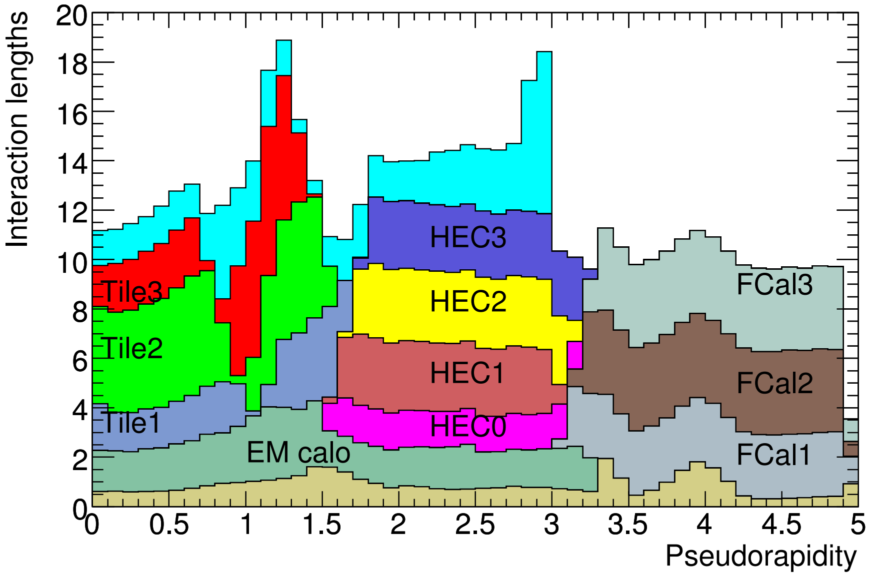

Figure 2.14: The cumulative amount of material in the various calorimeter systems in units of nuclear interaction length, as a function of η. The unlabeled material on the bottom represents the total amount of material in front of the electromagnetic calorimeters, and the unlabeled material on top represents the total amount of material in front of the first active layer of the muon spectrometer.

Thin Gap Chambers (TGC's) are designed for triggering on muons in the respective eta ranges $|\eta| < 1.05$ and $1.5 < |\eta| < 2.4$.

The barrel chambers are arranged in three concentric cylindrical layers at radii 5 m, 7.5 m, and 10m. The endcap chambers are arranged in wheels perpindicular to the beam pipe, located at distances $|z| \approx 7.4$ m, 10.8 m, 14 m, and 21.5 m. Both the barrel layers and endcap wheels consist of eight octants, each containing two overlapping sets of chambers to ensure hermetic coverage in ϕ. Figures 2.15 and 2.16 show the layout of the ATLAS muon system.

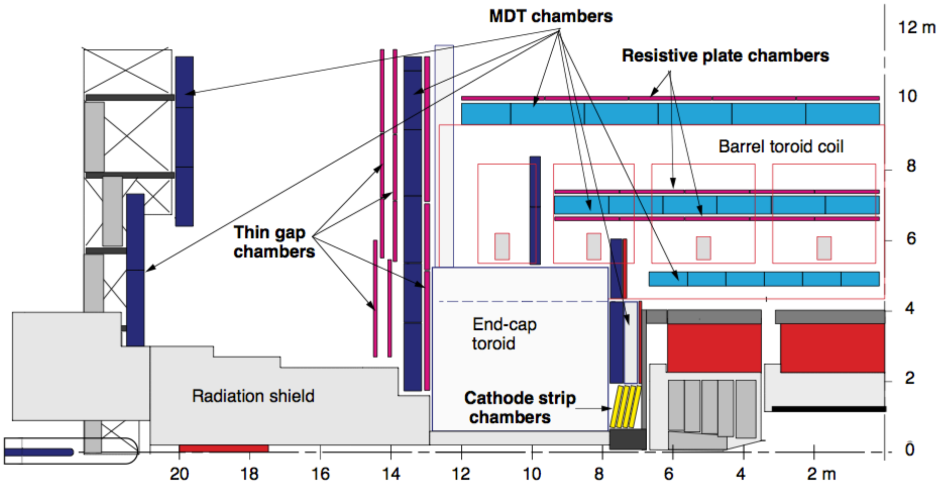

Figure 2.15: Quarter section side-view of the ATLAS muon spectrometer. The barrel MDT chambers are shown in light blue, the endcap MDT chambers are shown in dark blue, and the trigger chambers are shown in purple.

All of the technologies in the muon system are based on the same principle: a passing muon ionizes a gas mixture and the resulting deposition of charge at a charged anode or cathode is detected. The CSC and TGC are both multiwire proportional chambers where each space point is determined by the amount of charge deposited on neighboring anodes/cathodes, while the RPC employs parallel plates held at a voltage, and the drift motion of avalanche electrons induces readout signals on layers of capacitive strips.

The bulk of the volume of the MS is taken up by the over 350,000 MDT's, each ~30 mm in diameter and between 0.8 m and 5.7 m in length. Each MDT chamber consists of an arrangement of 6-8 layers of drift tubes. Though each drift tube is 30 mm in diameter, the electron drift time to the central-wire anode is used to constrain the drift radius in each tube to within ~80 μm, providing

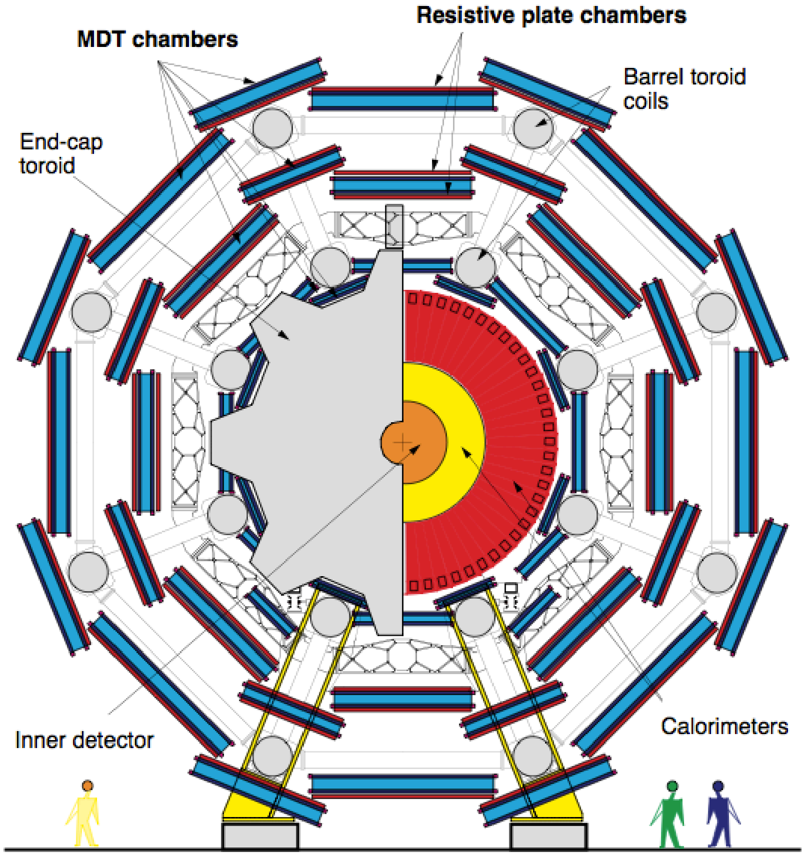

Figure 2.16: Transverse view of The ATLAS muon spectrometer, showing the barrel chambers and toroid magnets.

precision tracking measurements. The MDT's are oriented azimuthally about the beam direction because the magnetic field produces bending in η; therefore while the MDT's provide precision tracking in the bending-plane, they do not provide ϕ coordinate measurements. Both both η and ϕ coordinates are provided by the RPC's and TGC's, whose fast response times additionally allow them to trigger on muons and identify bunch crossings. The CSC's compliment the MDT's by providing additional precision measurements in the inner-most forward region where the higher particle densities require finer granularity and faster response times.

2.6 Magnet System

The ATLAS magnet system is designed to produce bending of tracks in the R-ϕ plane in the inner detector and in the R-z plane in the muon system. The helical trajectories induced by the magnetic fields are used to determine the momenta of charged particles and the sign of their charge. A schematic of the magnet system is shown in Figure 2.17. The central cylindral object depicted is the calorimeter system, which forms a return yoke for the solenoid field and shares a cryostat with the superconducting solenoid, which is located just inside the inner-most layer of the calorimeter system. The solenoid produces a 2 Tesla magnetic field inside the inner detector. Outside of the calorimeter system are the barrel and endcap superconducting air-core toroid magnets, each built out of eight coils arranged radially about the beam axis. The barrel toroid produces a $\sim$0.5 Tesla magnetic field in the barrel muon system, and the endcap toroids produce a $\sim$1 Tesla magnet field in the muon system's endcaps. The ATLAS barrel toroid is the largest superconducting magnet ever built.

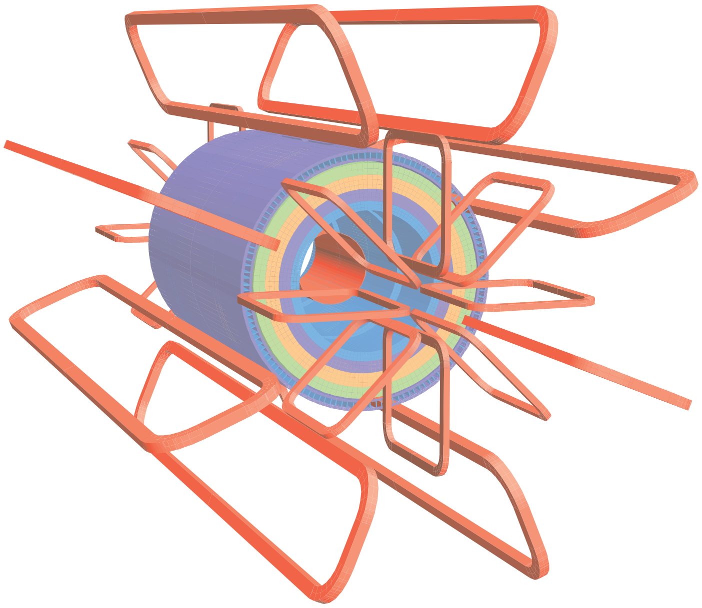

Figure 2.17: ATLAS magnet system. The solenoid lies at the innermost radius of the calorimeter system, and the HCal's iron tiles act as a return yoke for the solenoid's field. The eight barrel toroid coils are interleaved with the two endcap toroid coils.

2.7 Luminosity Detectors

As discussed in Sections 1.2.3 and 2.1.4, knowledge of the instantaneous and integrated luminosities is critical for understanding pileup and the expected number of scattering events, respectively. The primary detectors used for luminosity determination in ATLAS are LUCID and BCM.

LUCID (**Lu**minosity measurement using **C**erenkov **I**ntegrating **D**etector) is designed solely for the purpose of luminosity measurement. LUCID is a Cerenkov detector, consisting of two stations positioned in the ATLAS endcap regions at z = ±17 m. Each station consists of 20 aluminum tubes pointing towards the IP and arranged to surround the beam line at a radial distance of 10 cm, or $|\eta| \approx 5.8$. The tubes, 1.5 m long and with a diameter of 15 mm, are filled with a low refractive index gas in which charged particles of sufficient velocity emit Cerenkov radiation that is detected by photomultiplier tubes. A hit is registered when the number of charged particles passing through a tube is high enough that the intensity of detected Cerenkov radiation exceeds a set threshold.

The BCM (**B**eam **C**ondition **M**onitor) is designed to measure hit rates for the monitoring of beam background and for sending beam dump requests in cases that the beam might damage the detector, and it is also capable of luminosity measurement. The BCM consists of two stations at z = ±184 cm, each with 4 diamond sensors arranged in horizontal and vertical pairs and placed only 5.5 cm from the beam line. The BCM sensors have very precise timing which is used to distinguish particles emerging from the IP (which produce hits in both stations simultaneously) from background particles (which produce a hit in one station before reaching the other), and are sensitive to the passage of even a single minimum ionizing particle.

Both LUCID and BCM are capable of providing particle flux measurements for each individual LHC bunch. Since the number of inelastic interactions per bunch crossing is proportional to the instantaneous luminosity, the measurements from LUCID and BCM are used to determine the instantaneous luminosity at ATLAS on a bunch-by-bunch basis. The total integrated luminosity is then the instantaneous luminosity integrated over all bunch crossings.

2.8 Trigger System

In Section 1.3.5 we discussed[3] the number of Higgs-like scattering events expected in a single year of LHC data taking is so large that to store them electronically would require more than 10^7 terabytes of disk space. Higgs-like processes, however, are not the only type of scattering events expected at the LHC. In fact, the *total* inelastic scattering cross section at the LHC is about two orders of magnitude higher, corresponding to roughly 2×10^{15} events per year, enough to require over 10^9 terabytes of disk space. The ultimate amount of storage is not the only problem; there is also the problem of *recording* the data in real time. If every inelastic collision event were to be recorded in real time, it would be necessary to record more than 300 terabytes of data per second.

The bunch-crossing frequency in the LHC is roughly 40 MHz, and with the luminosity reached in 2012 each bunch-crossing results in an average of 20 proton-proton collisions. It is simply not possible to record each event that results from each bunch-crossing. It was ultimately decided that a technologically feasable compromise is to limit the events recorded per second to roughly 200 Hz, corresponding to roughly 300 megabytes of data being recorded per second, and ultimately 3000 terabytes of data recorded per year. The reduction of the event rate from 40 MHz down to 200 Hz represents the necessary rejection of $\sim$200,000 events for every single event that is recorded.

The ATLAS trigger system is designed to quickly and roughly discriminate between events with more or less physics potential in order to decide which events to keep and which events to reject. In general events of interest to ATLAS are characterized by multiple high-p_T jets and/or leptons, and/or a large total transverse energy (E_T) or large missing transverse energy (E_T^{miss}). Therefore the triggers primarily attempt to identify combinations of jets, leptons, E_T, and E_T^{miss} which exceed certain thresholds. Each requirement that an event can satisfy in order to be selected by the trigger is called a *trigger item*. Trigger items exist which require, for example: a single low- or high-p_T jet; multiple low- or high-p_T jets; 2 high-p_T muons; and so on. The *trigger menu* is the set of all trigger items that an event can satisfy in order to be selected by the trigger. The sum total rate of all events selected by the various trigger items within the trigger menu must be roughly limited to $\sim$200 Hz.

Since most trigger items within the trigger menu would otherwise consistently comsume too

---

[3] There we discussed Standard Model QCD events with a similar event topology to the most prolific category of Higgs decay events at the LHC: events in which a Higgs produced via gluon-fusion decays to $b\bar{b}$.

large a fraction of the allowed rate, most trigger items must be *prescaled*: their request to select an event is periodically ignored. A trigger item's prescale value is a rejection factor that represents, for every event that is selected by the trigger, the number of events that would otherwise be selected by the trigger but which are deliberately ignored. The trigger prescales are chosen to not only ensure that the total trigger rate is not exceeded, but also to ensure that each of the many physics analyses at ATLAS are able to obtain a useful number of events that are relevant to their respective analyses.

The trigger system consists of three successive tiers: Level-1, Level-2, and the Event Filter. The Level-2 and Event Filter are together referred to as the High-Level Trigger (HLT). The Level-1 trigger is hardware-based using custom-designed electronics, while the HLT is software-based and uses commercially available computers and networking hardware. A schematic representation of the ATLAS trigger system is shown in Figure 2.18.

The analysis presented in Section 5 makes use of a dedicated, unprescaled trigger (described in Section 5.2) in order to select and save permanently events containing indications of physics that are of interest to this analysis.

2.8.1 The ATLAS Trigger

The Level-1 (L1) trigger is a hardware-based trigger designed to rapidly reject events or accept them for further analysis. Given the $\sim$40 million events that must be processed per second, the L1 trigger must reach a decision in only 2 μs[4] in order for the pipeline of events to be analyzed to not exceed the amount of memory available for temporary event storage. Such a rapid decision is acheived by considering only a subset of ATLAS detector data, quickly examining reduced-granularity information from the calorimeters and the muon system trigger chambers, and searching for high-p_T jets/electron/photons/τ-leptons (all of which produce calorimeter activity), muons, and constructing an approximate sum of jet energy ΣE_T, and E_T^{miss}.

The identification of jets/electrons/photons/τ-leptons is accomplished by considering only the sum of calorimeter signals in 0.1$\times$0.1 $\eta \times \phi$ regions, called *trigger towers*, that exceed certain thresholds. The identification of muons is similarly accomplished by considering only coincidences between RPC or TGC stations that are found in $\eta \times \phi$ regions called *roads*, and the muon p_T is

---

[4] This includes the 1 μs it takes for signals from the detectors to travel along cables and reach the central trigger processor.

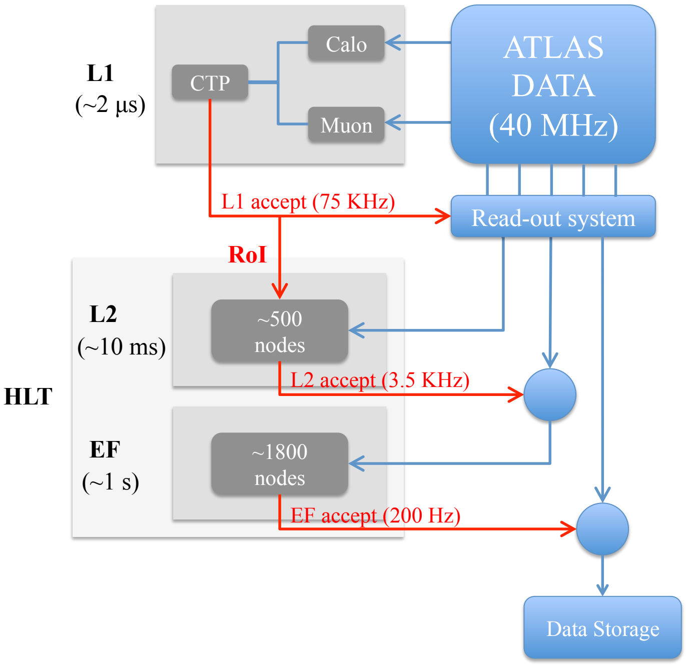

Figure 2.18: Schematic of the three-tiered ATLAS trigger system. Data flow is shown in blue. Trigger decisions are shown in red.

quickly estimated from the degree of deviation of RPC or TGC hits from a non-curved trajectory.

The L1 trigger identifies $\eta \times \phi$ Regions of Interest (RoI's) associated with calorimeter towers or muon roads, and the Central Trigger Processor (CTP) implements the L1 trigger menu. The L1 trigger menu contains trigger items which accept or reject events based on the ΣE_T, E_T^{miss}, and/or the requirement that the one or more jet/electron/photon/τ-lepton RoI's meet various p_T thresholds.

The ATLAS detector produces an enormous amount of data, and the L1 trigger only basis its decision on a small portion of it. The L1 trigger does not at all consider data from the inner detector or from precision tracking in the muon system, for example. Limitations of the detector read-out systems require that in order for the full set of data to be passed on to the HLT, the L1 trigger must reduce the event rate to a maximum of 75 KHz. The L1 trigger thus reduces the event rate by a factor of $\sim$500.

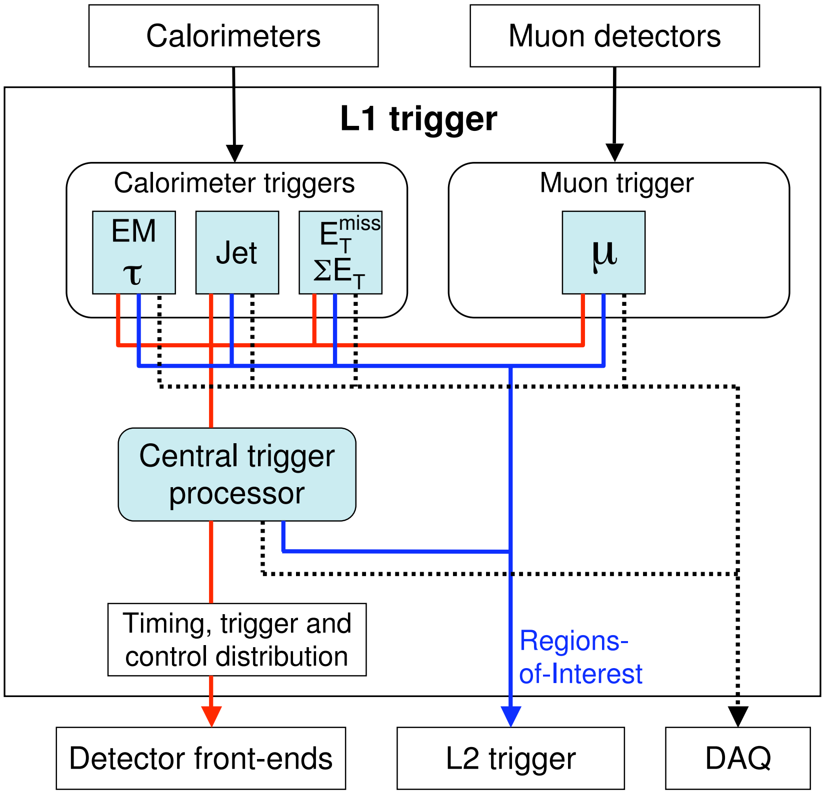

Figure 2.19: Schematic of the Level-1 trigger system.

2.8.2 The Level 2 Trigger

The Level-2 (L2) trigger is entirely software-based running on ∼500 computing nodes, and is able to refine the event selection using the full granularity of the ATLAS detector data. However due to processing speed and bandwidth limitations this can only be achieved by restricting the amount of data considered by the L2 trigger. Therefore the L2 trigger is "seeded" by the L1 RoI; only data is retrieved within the $\eta \times \phi$ coordinates specified by the RoI. With access to the full detector data within the RoI the L2 trigger is able to consider the full granularity of data from the calorimeter and muon systems. In addition the L2 trigger is able to include data from the inner detector in its trigger decision. The L2 trigger menu includes trigger items that that not only make use of refined jet/electron/photon/τ-lepton/muon identification and energy measurements, but also the identification and momentum measurement of inner detector tracks. The L2 trigger reduces the event rate to

$\sim$3.5 KHz (a rejection factor of $\sim$20).

2.8.3 The Event Filter

The final trigger is the Event Filter (EF) trigger, which is entirely software-based, running on $\sim$1800 computing nodes. The Event Filter uses the complete set of ATLAS data at full granularity coming from all ATLAS sub-detectors and reconstructs physics objects and analyzes the event using software algorithms similar to those used "offline"[5]. The Event Filter accepts approximately 1 out of 10 events, reducing the event rate to $\sim$200-300 Hz.

---

[5] "Offline" refers to the processing of data after it has been selected by the trigger and saved to premanent storage.

Chapter 3

RECONSTRUCTION

The data from the various ATLAS sub-detectors is combined and used to *reconstruct* physics objects: inner detector hits are used to reconstruct tracks; energy deposits in the calorimeters are used to reconstruct jets; hits in the muon system are used to reconstruct muons. Higher-level physics objects such as primary vertices are reconstructed by considering combinations of reconstructed tracks; electrons and photons are reconstructed by considering the properties of reconstructed tracks and their association with energy deposits in the ECal; E_T^{miss} is reconstructed by considering the energies and momentum vectors of all reconstructed objects in the event. In this section the recon-struciton of each of these types of physics objects will in turn be described, with special focus on jets and tracks, which are important to this analysis. In addition, the reconstruction of the luminosity will be described, and the section will end with a description of the assessment of the quality of the data reconstructed by the ATLAS detector.

The full output of reconstruction, along with low-level detector information used in the reconstruction process, is saved in the Event Summary Data (ESD) data format. In order to save disk space the Analysis Object Data (AOD) format is commonly used. Data stored in AOD format is derived from ESD data, and is less complete and primarily contains only high-level reconstructed objects.

Figure 3.1 shows a pizza-slice-shaped cross-section of the barrel of the ATLAS detector, showing particles passing through detector elements and depositing energy, and showing some of the corresponding objects that are reconstructed.

3.1 Track and Primary Vertex Reconstruction

Charged particles that travel through the inner detector leave "hits" in the Pixel, SCT, and TRT tracking detectors. The spatial information derived from hits is used to reconstruct tracks for which the hits lie on a helical trajectory. The radius of the helical trajectory is used to determine the

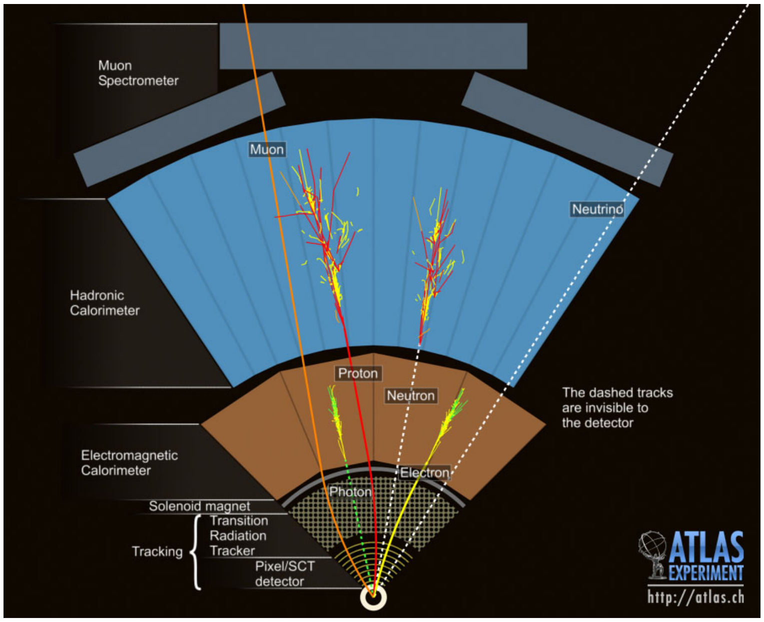

Figure 3.1: Examples of particle interactions with the ATLAS detector subsystems, and some corresponding reconstructed objects. Particles emerge from the collision at the IP (located at the bottom of the picture) and travel through the detector away from the IP (towards the top of the picture). Particles first travel through the Inner Detector, where charged particles leave energy deposits that are reconstructed as tracks. Calorimeters are then positioned outside the Inner Detector in order to stop and capture the energy of both charged and neutral particles. Electrons and photons are reconstructed using energy deposits in the first section of the calorimeter (the electromagnetic calorimeter), and jets are reconstructed using energy deposits in both the electromagnetic and the hadronic calorimeters. Charged particles that emerge from the calorimeters pass through the muon spectrometer and leave tracks which are reconstructed. Neutrinos do not interact with the ATLAS detector, but their presence can be inferred from the reconstruction of an overall momentum imbalance in the event.

momentum of the particle. Primary vertices are derived from the intersection of two or more tracks near the beam line.

3.1.1 Reconstruction of Space Points

In order to reconstruct a particle's trajectory, at least three space points (three-dimensional coordinates) are required. Each pixel hit measures a space point, however each SCT hit measures only two out of the three necessary coordinates for a space point. This is because the SCT is designed to reconstruct each space point using two measurements from neighboring SCT layers; each SCT measurement comes from a strip determining two spacial coordinates (rather than a pixel which determines three), and the strips in neighboring layers are oriented at an angle such that the third spactial coordinate can be reconstructed stereoscopically. Hits in the TRT similarly do not individually measure space points. Each TRT hit measures the time it takes for ionization electrons to drift to the wire anode at the center of each straw tube. This *drift time* is then converted into a radius measurement. Each radii measurement offers only a constraint on the spatial coordinate; multiple TRT hits must be combined in order to resolve left-right ambiguities. Since each straw tube is dozens of centimeters long, each TRT hit constrains only two out of three spatial coordinates in the magnetic-field bending plane, and is therefore most useful in further constraining the helical radii of tracks already identified using pixel and SCT space points.

A particle in the barrel typically traverses 3 pixel layers (resulting in 3 measured space points) and 8 SCT layers (resulting in 4 measured space points), generating a total of 7 measured space points. A particle will on average generate an additional 30 hits in the TRT, resulting in additional constraints in the track's bending plane.

3.1.2 Track-finding

Reconstructed space points in the three pixel layers and in the first SCT layer are used to seed the inside-out track-finding algorithms [16, 17], algorithms which search for tracks starting from hits in the inner-most layers of the inner detector. The seeds are used to form an initial candidate tracks, which are extended outward through the SCT to incorporate hits found along the projected trajectories. Each candidate track is then fit using the hits found along its trajectory, outliers are removed (hits whose inclusion in the track fit result in a large χ^2), and quality cuts are applied to remove "fake" tracks. Quality cuts include requirements on the mimimum number of space points used, and limits on the number of "holes" along tracks (traversed detector elements that did not record a hit). Tracks are then extended into the TRT and re-fitted, incorporating the constraints imposed by the TRT hits, and outlier TRT hits are discarded.

Once the inside-out track-finding is complete, the outside-in ("back-tracking") track-finding algorithms are run. The outside-in track-finding algorithms are complementary to the inside-out tracking algorithms, increasing the efficiency for reconstructing secondary tracks from photon conversions or decays of long-lived particles such as the K_S^0. These algorithms search for unused track segments in the TRT by first removing all hits used by the inside-out tracking algorithms, and then running a track-finding algorithm using only TRT hits. Found TRT track segments are then extended back toward the IP, incorporating unused hits from the pixel and SCT detectors, and re-fit, again discarding fake tracks and outlier hits.

3.1.3 Primary Vertex finding

Each proton-proton collision produces a *primary vertex* (PV), a point from which two or more tracks emerge. Primary vertices are reconstructed [18] starting with seeds obtained from the z-position at the beamline of the reconstructed tracks, the z_0. All tracks are required to have 9 space points, no holes, and $p_T > 400$ MeV. Additionally tracks are required to have $|d_0| < 4$ mm, where d_0 is the track's reconstructed distance-of-closest-approach to the beam line, such that primary vertices can only be found inside the beam pipe.

Primary vertices are reconstructed by combining seed tracks with nearby tracks and minimizing a χ^2 fit on the reconstructed vertex position, iteratively removing outlier tracks and re-fitting until no nearby tracks remain. Unused tracks are used to seed the reconstruction of other primary vertices, and this process continues until no additional vertices are found. The primary vertex with the highest average track p_{T} is identified with the position of the hard scatter and the other vertices are identified with pileup. The number of reconstructed primary vertices in each event averaged between $\sim$10 and $\sim$15 in 2012 running.

3.2 Electron and Photon Reconstruction

Electrons and photons both generate electromagnetic showers that are generally contained entirely in the ECal. Photon-initiated showers are very narrow and tend to be isolated from tracks (photons do not leave tracks in the inner detector), while electron-initiated showers tend to be wider due to the electron's curved trajectory in the magnetic field, and can be matched to the track produced by the electron in the inner detector. Reconstructed electrons or photons are not used in this analysis.

3.2.1 Photon Reconstruction

Photons are primarily identified by searching for narrow energy deposits contained entirely in the ECal. However before reaching the ECal photons can interact with material in the inner detector and convert to electron-positron pairs. These photon conversions are identified [17] as pairs of oppositely-charged tracks with a common vertex, and which can be matched to clusters of energy in the ECal. Additionally, since the photon is massless, the invariant mass[1] of the track pair must be zero; the angle between the two tracks' momenta vectors at the vertex must be zero. The identification of photon conversions increases the overall efficiency of photon identification as well as additionally providing a tool for discrimating between single photons and π^0 decays to photon pairs in which one of the two photons has undergone conversion.

Calorimeter-based photon reconstruction [19, 20] is seeded by energy clusters in the second layer of the ECal[2] found to contain $E_T > 3$ GeV. Backgrounds from electrons and other charged particles are removed by requiring that the energy clusters in the ECal be isolated from ID tracks other than those associated with photon conversions. Such photon candidates and are then required to have less than 2% of their energy deposition contained in the first layer of the HCal, in order to remove backgrounds from hadrons whose showers are not contained entirely within the ECal. Backgrounds from electrons and jets are further removed by exploiting the narrow shower shape of photons, rejecting photon candidates whose energy deposition in the ECal is not contained in a $\Delta\eta \times \Delta\phi$ window of 3×7 cells in the second layer of the ECal. While the second layer of the ECal represents the majority of the ECal's depth in radiation lengths, the first layer of the ECal is finely grained and provides discrimination between single photons and the photon pairs that result from π^0 decays. Photon objects are required to have only a single local maxima of energy deposition in the first layer of the ECal in order to remove backgrounds from π^0's and jets containing multiple hadrons.

---

[1] The invariant mass of a system of particles is a relativistically invariant quantity. It is calculated as the square of the sum of the particles' momenta subtracted from the square of the sum of the particles' energies. In the case of a single particle the invariant mass is the particle's rest mass.

[2] The second layer of the ECal consistutes the majority of the ECal's depth in radiation lengths. See Section 2.4.1.

3.2.2 Electron Reconstruction

The experimental signature of an electron is similar to that of a photon but with a matching ID track. As with photons, electron reconstruction [19, 21] is seeded by energy clusters in the second layer of the ECal found to contain $E_T > 3$ GeV. A matching ID track is then searched for, with the requirement that the track has not been flagged as belonging to a photon-conversion electron pair. If a matching track is not found the electron candidate is rejected. Energy clusters with a matching track are then required to satisfy shower shape cuts similar similar to those applied to photon candidates in order to reject hadron backgrounds: minimal energy deposition in the HCal; narrow width; single local maxima in the first layer of the ECal. Due to the small mass of the electron it's energy E is roughly equal to its momentum p; in order to additionally purify the sample of electron candidates a cut can be made on the ratio E/p of the energy of the cluster to the momentum of the track. Electron candidates can be further purified by requiring that the track contain a minimum number of high-threshold TRT hits (see Section 2.3.3).

3.3 Jet Reconstruction

As described in Section 1.2.1, a jet is a roughly collinear spray of hadrons that originates from a high-p_T quark or gluon emerging from the hard scatter. Since QCD processes are dominant in proton-proton collisions, the reconstruction of jets associated with high-p_T quarks and gluons is essential. Furthermore jets can result from Higgs, W, and Z bosons, whose decay products can include quarks. Since jets consist of a spray of hadrons, and some fraction of those hadrons are charged, jets are generally associated with a cluster of tracks. However jets also include some fraction of neutral hadrons which do not produce tracks, and, since all hadrons deposit most of their energy in the calorimeters, the primary signature of a jet is a large deposition of energy in the calorimeters which is in rough correspondence with the energy of the parton that originated the jet. Therefore in ATLAS any large deposition of energy in the calorimeters will be reconstructed as one or more jets. In this analysis, the decay of π_v's in the HCal results in large amounts of energy deposition in the HCal, thus resulting in the reconstruction of jets.

A jet generally consists of a combination of high- and low-p_T particles, distributed non-uniformilly but vaguelly in the shape of a cone. The number of particles, the shape and densities of their angular distributions, the fraction of charged and neutral particles, their distribution in p_T, and their ultimate shower development, are all partially stochastic. Therefore the reconstruction of a jet requires an algorithm which is insensitive to many of these variations, being able to, regardless of the composition and distribution of the particles that make up the jet, nonetheless associate clusters of calorimeter energy in such a way that the reconstructed jet energy is close to the energy of the quarks or gluons that initiated the jet. It is additionally desrable for a jet-finding algorithm to be robust against not only the presence of variable numbers of collinear soft particles produced during the formation of the jet itself, but also robust against the overlapping backgrounds of soft particles originating from the hard scatter (but not associated with the jet), and pileup. Two particularly desirable attributes of a jet-finding algorithhm is *infrared* and *collinear safety*. A jet-finding algorithm is infrared safe if the presence or absence of additional soft particles between any two particles in a jet does not affect the recombination of those particles into a single reconstructed jet. A jet-finding algorithm is collinear safe if the jet reconstruction is unaffected by whether or not the momentum carried by its high-p_T constituents is split among multiple lower-p_T collinear particles.

The main jet-finding algorithm at ATLAS [23, 24], and the one used in this analysis, is the *anti-k_T* algorithm [25] with a jet-cone radius parameter R = 0.4. The anti-k_T jet-finding algorithm is both infrared and collinear safe, and produces cone-shaped jets with approximate radii of $\Delta R = \sim 0.4$.

The anti-k_T algorithm used in this analysis represents calorimeter signals using topological clusters (“topoclusters”) in the calorimeter, which represent an attempt to reconstruct the three-dimensional local pockets of energy density corresponding to the shower development of each separate particle entering the calorimeter. The topoclusters are seeded by calorimeter cells with a high signal-to-electronic-noise ratio, $E_{cell}/\sigma_{noise} > 4$, and the topological clustering proceeds by collecting all neighboring cells in all three dimensions into each topocluster. Neighbor cells of neighboring cells are then iteratively added to the topocluster as long as they satisfy a signal-to-noise ratio rquirement of $E_{cell}/\sigma_{noise} > 2$. Once this process is complete a final layer of neighboring “guard” cells are added to the topocluster as long as they satisfy $E_{cell}/\sigma_{noise} > 0$. Once each initial topocluster has been constructed, it is analyzed for multiple local maxima; topoclusters containing multiple local maxima are spit into multiple independent topoclusters.

The anti-k$_T$ algorithm is an iterative sorting algorithm applied to the collection of topoclusters, designed to associate “nearby” topoclusters into jets using an abstract definition of distance that depends not only on the angular ΔR distance between topoclusters but also their relative energies. The anti-k$_T$ algorithm defines two abstract distances when considering any two topoclusters ‘i’ and ‘j’:

$$d_{ij} = \min(\frac{1}{p_{T,i}^2}, \frac{1}{p_{T,j}^2}) \frac{\Delta R_{ij}^2}{R^2} \tag{3.1}$$

$$d_{i\mathrm{B}} = \frac{1}{p_{T,i}^2} \tag{3.2}$$

d_{ij} is the abstract distance between the two topoclusters as a function of the p_T of the higher-energy topocluster and the $\eta - \phi$ distance ΔR_{ij} between the two topoclusters. d_{iB} is the abstract distance between topocluster ‘i’ and the beam line, depending only on the p_T of the topocluster. R is the distance parameter, which is set to 0.4. The algorithm begins by considering the set of all topoclusters and calculates the list of all distances d_{ij} and $d_{i\mathrm{B}}$. The list is then sorted by distance. If the smallest distance is found to be a d_{ij} between two topoclusters then those two topoclusters are combined to form a larger topocluster: their four-momenta are summed, the distances are recalculated, and the iterative process continues. If the smallest distance is found to be a d_{iB} between a topocluster and the beam line, then that topocluster is called a jet and removed from the topocluster collection, the list of distances is updated, and the iterative process continues. In this way, the initial list of topoclusters are sorted into larger topoclusters, which are eventually promoted to jets and removed from the list, until no more topoclusters remain.

The particular abstract distance measure chosen ensures that pairs of soft particles are “further away” from each other than similarly angularly separated hard particles, that soft particles are “far away” from the beam line, and that pairs of particles will combine as long as one of them is hard and as long as they are not separated angularly by more than R. This distance measure therefore ensures that hard particles are combined first, that soft particles will tend to cluster with hard particles long before they cluster amongst themselves, and that separate jets will be minimally separated by a distance $\Delta R_{ij} = $ R. Jets with no neighboring jets within a radius of 2R will be perfectly conical, whereas neighboring jets separated by less than $\Delta R_{ij} = $ 2R must compete for the topoclusters between them. The division of topoclusters between neighboring jets is not equal: topoclusters are combined with the higher p_T jet, which is always perfectly conical at the expense of its lower p_T

neighbors.

The choice of the distance parameter $R = 0.4$ is a compromise between the occasional underestimation of the lateral width of a jet (R too small), resulting in an understimation of its energy, and the occasional overestimation of the lateral width of a jet (R too large), resulting in an overestimation of its energy. Most high-p_T jets studied at ATLAS are narrow enough to be well-contained using the distance parameter $R = 0.4$, however some analyses which involve particularly clean events (in low-luminosity data with low pileup, for example) containing few well-separated jets may choose to use jets reconstructed with a larger distance parameter in order to maximize their jet energy resolution by ensuring that all of the jet's energy is contained inside the jet cone. This analysis searches for jets which are relatively narrow in width, so a distance parameter of $R = 0.4$ is used.

Once the anti-k$_T$ algorithm has completed the association between topoclusters and jets, the momentum four-vector associated with each jet is computed as the sum of each topocluster's momentum four-vector, where each topocluster is treated as a massless pseudo-particle with four-momentum (E,$\vec{p}$). The four-momentum components of each topocluster are derived from its energy-weighted $\eta - \phi$ barycenter, and are defined as:

$$\begin{aligned} E &= |\vec{p}| = \sqrt{p_x^2 + p_y^2 + p_z^2} && (3.3) \\ p_x &= p \cdot \frac{\cos\phi}{\cosh\eta} && (3.4) \\ p_x &= p \cdot \frac{\sin\phi}{\cosh\eta} && (3.5) \\ p_x &= p \cdot \tanh\eta && (3.6) \end{aligned}$$

3.3.1 Jet Quality Definition

Backgrounds to jets include electronic noise in the calorimeters, deposition of energy from beam halo muons, and cosmic rays. There are a number of variables used as quality cuts to distinguish such "bad" reconstructed jets from those actually arising as a result of the hard scatter. Additionally, jets may be labelled as questonable or "ugly" due to being reconstructed in the transition/crack region between the barrel and endcap calorimeters, or due to being built out of too large a fraction of calorimeter cells determined to be dead or questionable by data quality experts. The list of variables considered in the flagging of a jet as “ugly” or “bad” are:

- EMf: The fraction of the jet’s energy which is contained in the ECal.
- FMax: The largest fraction of energy contained in a single calorimeter layer.
- HECf: The fraction of the jet’s energy which is contained in the HEC.
- LArQ: The fraction of LAr cells with a Q-factor[3] greater than 4000.
- HECQ: The fraction of HEC cells with a Q-factor greater than 4000.
- NegativeE: The total amount of negative energy[4] contained in the jet.
- Timing: The average timing[5] of all cells contained in the jet, weighted by the cell energy.
- η: The η of the jet.
- CHf: The jet charge fraction; the ratio of the sum of track p_T’s associated with the jet to the calibrated jet p_T.
- TileGap3 fraction: The fraction of jet energy contained in the TileGap3[6]
- Dead fraction: The fraction of the jet’s energy that has been extrapolated into known dead cells (using the average of the surrounding cells’ energies), or which is contained in cells flagged by data quality experts as problematic.

A jet is flagged as “bad” if it satisfies any of the following criteria:

---

[3] The cell Q-factor is a measure of the difference between the predicted and measured signal pulse shapes used to reconstruct the cell energy.

[4] A calorimeter cell can contribute a negative energy signal due to the application of a noise-suppression technique which shifts the zero-point energy to correspond to an average over calorimeter cells.

[5] The cell time is the time of the calorimeter signal relative to the bunch-crossing.

[6] TileGap3 is a component of the ATLAS calorimeter system which covers the transition between the barrel and endcap calorimeters. It can be seen as elements E1-E4 in Figure 2.13.

- HECf > 0.50 and HECQ > 0.50
- HECf $> 1-HECQ$
- NegativeE > 60 GeV
- Timing > 10 ns
- EMf > 0.90 and LArQ > 0.80 and $|\eta| < 2.8$
- FMax > 0.99 and $|\eta| < 2.0$
- EMf > 0.95 and CHf < 0.05 and $|\eta| < 2.0$
- EMf < 0.05 and CHf < 0.10 and $|\eta| < 2.0$
- EMf < 0.05 and $|\eta| > 2.0$

A jet is flagged as “ugly” if it satisfies any of the following criteria:

- TileGap3 fraction $> 50\%$ of the total jet energy
- Dead fraction $> 50\%$ of the total jet energy.

Finally, a jet is flagged as “good” if it is neither “bad” nor “ugly”.

The standard “good jet” criteria are designed to reject reconstructed jets whose properties are inconsistent with what is expected from actual Standard Model jets. For instance, Standard Model jets originate at the IP and contain some fraction of charged particles which generate tracks in the Inner Detector that are associated with the jet and represent a considerable fraction of the jet’s energy. Furthermore, the hadrons that make up Standard Model jets typically begin to shower in the ECal; on average greater than 50% of the energy of a Standard Model jet is expected to be contained in the ECal. Therefore the cuts on very low EMf and CHf in the “bad jet” definition are reasonable for Standard Model jets: jets with few tracks and very low EMf are extremely rare in the

Standard Model, and are likely candidates for being the result of calorimeter noise or some kind of non-collision background. However this analysis is specifically interested in non-SM jets that may result from the decay of a neutral particle inside the HCal, jets that are expected to be both trackless and have a very low EMf. Therefore the "good jet" definition used in this analysis is slightly looser than the standard definition: the last two cuts in the "bad jet" definition listed above are not applied.

3.3.2 Jet Energy Scale

Jet reconstruction initially takes place at the *electromagnetic (EM) scale*, that is, the signals recorded in the calorimeter cells (both in the ECal and HCal) have been calibrated with respect to electron test beams, which produce electromagnetic showers. Jets in general are composed of charged pions, photons from the decay of neutral pions, kaons, and protons and neutrons. Charged pions on average carry $\sim$40% of a jet's energy, photons $\sim$25%, kaons $\sim$20%, and protons and neutrons $\sim$10%. Therefore only about $\sim$25% of a jet's energy is the direct result of electromagnetic showers. The remaining $\sim$75% of a jet's energy is due to hadronic showers, in which hadron-nuclei interactions result in the production of charged and neutral pions. Neutral pions decay to photons which shower electromagnetically, while charged pions produce a systematically different calorimeter response compared to electrons or photons. In general a hadronic shower produces a complicated and stochastic combination of electromagnetic showers, charged pions, and muons and neutrinos, and results in a calorimeter response that is systematically lower compared to the pure electromagnetic showers that result from electrons or photons. The response is lower due in part due to invisible processes including the production of muons and neutrinos in the hadronic shower, as well as energy stored in nuclear excitations.

In addition to the differences in calorimeter response between electromagnetic and hadronic showers, the calorimeter response is non-linear with hadron energy, and energy is lost in dead material and cracks and gaps in the calorimeters. Therefore a jet's energy is corrected from the initial measurement in order to correctly reproduce the *particle-level* jet energy: the total energy of all particles associated with the jet that enter the calorimeter. This correction produces a jet energy that at ATLAS is referred to as being at the *hadronic scale*.

An initial jet energy calibration at the hadronic scale is acheived by weighting the energy of topoclusters based on their shape. Topoclusters are classified as either electromagnetic, hadronic, or unknown, based on their energy (at the EM scale), depth in the calorimeter, average cell energy density, and $|\eta|$. The classification is based on predictions from GEANT4 detector simulations using Monte Carlo data in which charged and neutral pions are identified with topoclusters, and each pion's true energy is compared with the simulated detector response. Additional corrections are applied to account for energy deposits not included in topoclusters due to noise thresholds applied during the cluster formation, and corrections are also applied to account for energy deposits in materials before and between the calorimeters. This is accomplished using the calorimeter presampler to determine whether a shower has developed before entering the calorimeter, and by comparting samplings taken just before and beyond the cryostat walls that separate the ECal and HCal. Corrections are applied both on a jet-by-jet basis (presampler measurements and noise thresholds are taken into account) and also using average corrections applied to jets as a funciton of their p_T and η.

While jets at particle-level (hadronic scale) are calibrated with respect to the energy of the particles entering the calorimeter inside a cone of radius 0.4, they do not necessarily reflect the energy of the parton that initiated the jet. This is due to physics effects such as ISR and FSR, the underlying event, pile-up, as well as the fact that the magnetic field bends some fraction of a jet's low-energy charged constituents outside of the jet cone. These effects have the potential to overlay particles inside of the jet cone which are not daughters of the jet-initiating parton, or remove particles from the jet cone which are daughters of the jet-initiating parton. They therefore result in reconstructed jets that do not reflect the energies or directions of the single partons scattered in the underlying physics process. Therefore further calibration steps are needed to bring the jet energies and directions to *parton-level*, or *final jet energy scale* (EM+JES).

The calibration to the EM+JES is acheived using two calibration strategies [32], one using Monte Carlo simulated QCD data, and one using collision data. Monte Carlo data is used to calibrate the reconstructed jet energy to the energy of the parton that initiated the jet. This can be accomplished in Monte Carlo data because the "truth-level" particle information can be accessed and matched to each reconstructed jet. A correction for pile-up is obtained by measuring the average addition of energy to a jet as a function of η that results from a given instantaneous luminosity measured in collision data; the average energy density ρ in the event is multiplied by the jet's transverse area and subtracted from the jet's energy. Finally, collision data is used to measure a residual correction factor that is applied only to collision data. This correction factor is derived by identifying γ+jet and Z+jet events in which a photon or Z-boson is produced in the hard scatter and recoils against a quark or gluon. In such events conservation of momentum dictates that the jet's transverse momentum must be equal to the transverse momentum of the photon or Z. Since photon energies can be measured at EM-scale, and the energies of Z-bosons that decay leptonically can be precisely reconstructed from the invariant mass of electron or muon pairs, the jet's energy can be calibrated against the energy of its recoiling partner. Though less precise due to the lack of a photon or Z-boson, QCD dijets are used for this purpose as well, since they offer an independent dataset from which to measure relative changes in jet response as a function of η. Such "p_T-balance" techniques are used not only to derive the final JES calibration on data, but also to measure the final jet energy uncertainty and resolution.

The JES calibration, uncertainty, and resolution depend on a jet's 4-momentum (measured at EM-scale) and area, as well as the event's ρ, μ, and the number of PV's. Though depending on many variables, the average jet energy is corrected (EM-scale to EM+JES scale) upwards by $\sim$60-120%, and the jet energy uncertainty and resolution for QCD jets with $p_T > 30$ GeV is 1-2%, and 10-30%, respectively [33].

The signal jets considered in this analyses are not SM QCD jets, and therefore may require a different JES calibration scheme from those which are by default provided by ATLAS. This issue will be discussed in Section 5.6.2.

3.4 Muon Reconstruction

Muons are reconstructed [22] as tracks in the muon system (*standalone*), as ID tracks that are matched to hits in the muon system (*tagged*), or as tracks reconstructed from combined measurements in the ID and MS (*combined*). Reconstructed muons are not used in this analysis.

Standalone muon reconstruction uses hits in the MS to reconstruct tracks without the use of ID space points. The standalone muon reconstruction algorithm begins by building straight-line track segments in each of the three muon stations. The precision MDT and CSC chambers provide the η-coordinate measurements while the RPC (barrel) and TGC (endcap) chambers provide the ϕ-coordinate measurements. Muon segments are constrained to point toward the origin of the ATLAS detector. Two or more muon segments are then combined to form three-dimensional tracks which are extrapolated back to the PV after accounting for the average energy a muon loses when traversing the calorimeters ($\sim$3 GeV).

Tagged muon reconstruction propagates ID tracks of sufficient momentum into the first station of the MS. If a reconstructred muon segment is found to be sufficiently close to the extrapolated ID track position then the ID track is tagged as a muon. Though providing a lower muon reconstruction efficiency and higher fake-rate compared to standalone muon recontruction when considering high-p_T muons, tagged muon reconstruction is complementary to standalone muon reconstruction in cases where the muon p_T is too low ($p_T < 6$ GeV) to be consistently reconstructed in the MS due to the high curvature of its trajectory.

Combined muons are formed by pairing nearby standalone MS tracks with ID tracks, and performing a χ^2 test on the difference between the reconstructed track parameters. Consistent track pairs are combined into single tracks by re-fitting all of the hits found along both tracks or by statistically combining the track parameters from each. Combined muon reconstruction has a slightly lower average efficiency and similar fake-rate compared to standalone muon reconstruction, however it provides a better muon momentum fit, resulting in an average p_T resolution of $\sim$3% (compared to $\sim$4% for standalone muon reconstruction).

3.5 Missing Energy

The protons in the LHC move along the beam line (the z-axis in the ATLAS coordinate system), with very little transverse momentum p_T before taking part in a collision. Therefore by conservation of momentum the sum of the transverse momentum of all particles scattered in a proton-proton collision must be equal to zero: there should be no transverse momentum imbalance. Since the ATLAS detector cannot measure the transverse momentum of all particles scattered in a proton-proton collision (many particles are neutral, and even for charged particles the tracking efficiency is not 100%), it must rely primarily on its nearly hermetic calorimeters, which measure energy deposition. Therefore when describing an overall transverse momentum imbalance in events measured by the ATLAS detector, the term *missing transverse energy* (E_T^{miss}) is used rather than *missing transverse momentum*. While energy itself is a directionless quantity, the energy deposition associated with particles entering a calorimeter is not; energy depositions in the calorimeter are associated with particles which have a direction of motion, and their direction of motion is reflected by the location of their energy deposition in the calorimeter. Since the energies of Standard Model particles entering the calorimeters are dominated by their momenta (their mass energies are negigable compared to their kinetic energies), the missing transverse energy in an event is approximately equal to the missing transverse momentum. Therefore the E_T^{miss}, the sum of the transverse energies[7] or momenta of all particles scattered in an event must be equal to zero.

The E_T^{miss} *measured* by the ATLAS detector, on the other hand, is not always zero. One SM particle, the neutrino, escapes the ATLAS detector without leaving any direct indication of its presence: it leaves no track and it does not deposit energy in the calorimeters. Therefore collisions that produce one or more high-p_T neutrinos will in general result in an experimental signature that includes E_T^{miss}. If a single neutrino is responsible for the bulk of the E_T^{miss} (as is often the case in $t\bar{t}$ events where one top quark decays semileptonically, for example), its energy and direction can be reconstructed as that which balances the E_T^{miss} to zero. This can additionally allow for a more accurate reconstruction of the energy of the particle whose decay produced the neutrino.

E_T^{miss} has uses which go beyond the indirect identification of neutrinos and the reconstruction of their momenta. There are hypothetical non-SM particles, such the LSP's that appear in supersymmetric theories, or the long-lived neutral particles considered in this analysis, which like neutrinos would not interact with the ATLAS detector, and would therefore produce E_T^{miss}. E_T^{miss} is therefore an important potential signature of beyond-the-SM physics. This analysis, however, is not concerned with particles that are so long-lived that they escape the ATLAS detector before decaying. Nor do the long-lived particles considered in this analysis produce high-p_T nuetrinos when they decay. Therefore the experimental signature searched-for in this analysis does not include large E_T^{miss}. One of the important uses of E_T^{miss} that is relevant to this analysis is the rejection of backgrounds such as cosmic rays, beam halo muons, noisy calorimeter cells, or other non-proton-proton-collision backgrounds which, not being constrained by the protons' initial lack of transverse momenta, do not in general result in zero E_T^{miss}.

The E_T^{miss} [27] is calculated by summing the total transverse energy in the calorimeters, and,

---

[7] The transverse energy of a particle whose momentum is directed along θ is defined as $E \cdot \sin\theta$. It is the projection of the particle's energy, oriented by its direction of motion, into the transverse plane.

because muons escape the calorimeters, additionally summing the transverse momentum of all reconstructed muons:

$$\mathrm{E}_{x(y)}^{miss} = \mathrm{E}_{x(y)}^{miss,calo} + \mathrm{E}_{x(y)}^{miss,muon} \tag{3.7}$$

Then the E_T^{miss} and its direction ϕ^{miss} are calculated as:

$$\mathrm{E}_T^{miss} = \sqrt{(\mathrm{E}_x^{miss})^2 + (\mathrm{E}_y^{miss})^2} \tag{3.8}$$

$$\phi^{miss} = \arctan(\mathrm{E}_y^{miss}/\mathrm{E}_x^{miss}) \tag{3.9}$$

The missing energy in the calorimeter, $\mathrm{E}_{x(y)}^{miss,calo}$, is found by summing the transverse energy of all of the reconstructed calorimeter-based objects in the event, and then adding the transverse energy corresponding to all calorimeter cells not reconstructed as part of a physics object. This technique allows for the energy scale of the calorimeter cells belonging to each physics object to be calibrated separately. The $\mathrm{E}_{x(y)}^{miss,calo}$ is calculated as:

$$\mathrm{E}_x^{miss,calo} = -\sum_{i\in cells} E_i \sin\theta_i \cos\phi_i \tag{3.10}$$

$$\mathrm{E}_x^{miss,calo} = -\sum_{i\in cells} E_i \sin\theta_i \sin\phi_i \tag{3.11}$$

The missing energy associated with muons is calculated using combined muons for $\mid \eta \mid < 2.5$, and standalone muons for $2.5 < \mid \eta \mid < 2.7$, where ID tracking is no longer efficient. The missing energy contribution is calculated as the sum of all reconstructed muon momenta:

$$\mathrm{E}_{x(y)}^{miss,muon} = -\sum_{RecMuons} p_{x(y)} \tag{3.12}$$

Since muon energy loss in the calorimeter is already included in $\mathrm{E}_T^{miss,calo}$, muon momenta are calculated using the standalone MS and not extrapolated back to the ID, in order to avoid double-counting. It is important to also mention that the JES described in Section 3.3.2 plays an important role in compensating for features of the ATLAS detector that might otherwise, through the mismeasurement of energy, lead to large non-zero values of E_T^{miss}.

3.6 Luminosity Measurement

The determination of the instantaneous luminosity is of crucial importance for the understanding of pileup, and the corresponding integrated luminosity (the instantaneous luminosity integrated over time) is crucial for the understanding of the expected number of scattering events (and thus the measured cross-section) for a given physics process. As described in Section 2.7 ATLAS has several detectors designed to measure event rates for luminosity determination. Event rates can be used to estimate the average number of inelastic proton-proton collisions per bunch-crossing, which is related to the luminosity:

$$\mathrm{L} = \frac{R_{inel}}{\sigma_{inel}} = \frac{\mu n_b f_r}{\sigma_{inel}} \tag{3.13}$$

where on the left-side of the equality R_{inel} is the rate of inelastic collisions and σ_{inel} is the inelastic proton-proton cross-section. On the right-side of the equality R_{inel} has been expressed in terms of more fundamental parameters: μ is the average number of interactions per bunch-crossing, n_b is the number of bunches in each beam, and f_r is the rotational frequency of the protons in the LHC. Since n_b and f_r are known machine parameters, and σ_{inel} is a measured constant, the instantaneous luminosity can be determined from knowledge of either R_{inel} or μ. ATLAS chooses to parametrize its knowledge of L in terms of μ. It is not possible to measure μ directly, because the detectors are neither hermetic nor 100% efficient. Therefore, the measured number of interactions, μ^{meas} is related to the true μ by a coefficent ε that accounts for the acceptance and efficiency of the luminosity detectors. If the same luminosity detectors that measure μ are used to measure σ then the measured cross-section σ_{vis} is related to the true σ by the same efficiency coefficient ε, and equation 3.13 can be written as:

$$\mathrm{L} = \frac{\varepsilon \mu^{meas} n_b f_r}{\varepsilon \sigma_{vis}} = \frac{\mu^{meas} n_b f_r}{\sigma_{vis}} \tag{3.14}$$

μ^{meas} is measured at ATLAS [28] by measuring the fraction of bunch-crossings that register a hit above a given threshold in the luminosity detectors, and μ^{meas} is extrapolated using Poisson statistics. Without knowledge of σ_{vis}, μ^{meas} determines relative changes in instantaneous luminosity. An absolute measurement of the luminosity requires the calibration of the luminosity scale through measurement of σ_{vis}. This is acheived by inferring the absolute luminosity from measured machine parameters [29]:

$$\mathrm{L} = \frac{n_b f_r n_1 n_2}{2\pi\Sigma_x\Sigma_y} \tag{3.15}$$

where n$_1$ and n$_2$ are the number of protons in each colliding bunch, and Σ_x and Σ_y are related to the horizontal and vertical widths of the profile of the overlap between the colliding beams. Beam-separation scans [30] (also called Van der Meer scans) are used to determine Σ_x and Σ_y through the measurement of event rates as a function the horizontal and vertical distances between the centers of the two colliding beams (the center can be located by finding the location of maximum event rate). Then by combining equation 3.14 with equation 3.15, σ_{vis} can be measured as a function of the peak average interaction rate μ^{meas}_{MAX} and the corresponding beam currents $(n_1 n_2)^{max}$ measured during the beam-separation scans:

$$\sigma_{vis} = \mu^{meas}_{MAX} \frac{2\pi\Sigma_x\Sigma_y}{(n_1 n_2)^{max}} \tag{3.16}$$

3.7 Data Quality

The ATLAS detector consists of a large collection of sub-detectors, each of which is individually a complicated piece of machinery and which can, for example, suffer from gas leaks, high-voltage loss, power trips, noise bursts, software-control glitches, and operator error. In such cases the quality of the data read-out from some components of various ATLAS sub-detectors may be in question at various times during a physics run. For example a part of a detector may be offline or be operating below peak efficiency for a few hours, or on the other hand a part of a detector may be periodically producing noise bursts. In order to account for such problems ATLAS maintains a database of every lumiblock[8] of each physics run. Each sub-detector has its own set of common Data Quality tools and automated mechanisms for the flagging of potential problems, and in addition expert Data Quality shifters are responsible for assessing the quality of data coming from the various ATLAS subdetectors. Each individual lumiblock in each physics run is marked as either “good,”

---

[8] Each LB corresponds to roughly 2 minutes of data taking, but this can vary depending on run conditions and other operational issues.

"recoverable,"[9] "unknown," or "bad", depending on the available statistics and on the percentage of the ATLAS detector affected by data quality problems. GoodRunsLists are then created which collect all of the ranges of lumiblocks from runs which are marked "good," so that physics analyses can run only over data vetted by data quality shifters.

---

[9] The data may be salvagable if corrections are applied.

Chapter 4

MONTE CARLO

Simulated data is necessary in order to study the predicted experimental signatures of physics processes that have not yet been observed in nature. Simulated data is also sometimes used to isolate and study SM processes that cannot be cleanly separated from other physics processes or backgrounds. Data that is simulated is referred to as "Monte Carlo" data because it is produced using Monte Carlo (MC) methods: the simulation is partly acheived through the random sampling of theoretical and empirical probability distributions. MC data is produced in three consecutive steps: event generation, event simulation, and event digitization. That is, the hard-scatter from a proton-proton collision is simulated; particles' trajectories through, and interaction with, the magnetic field and detector material is simulated; and the detectors' response and digital readout is simulated. The final step produces an event whose digital signature is in the same format as would be recorded by the ATLAS data aquisition system for a real collision event. The exact same reconstruction algorithms that are applied to real data events can therefore be applied to MC data.

This chapter begins with a description of the event generation, detector simulation, and digitization steps, and ends with a description of the Monte Carlo samples used in this analysis. Particular attention is given to the signal Monte Carlo samples that model the production and decay of the long-lived neutral particles that are the focus of this analysis.

4.1 Monte Carlo production

The production of Monte Carlo simulated data proceeds in three stages: event generation, detector simulation, and event digitization. Each step is described below.

4.1.1 Event Generation

Event generation is the simulation of the hard scatter in proton-proton collisions. The initial state particles and their momenta are determined from a random sampling of the PDF's (described in

Section 1.2.2), while the final state particles and their momenta are determined from a random sampling of the theoretical differential cross-section (described in Section 1.2.3) of the physics process of interest. Event generation is done separately for the production of QCD dijets, Higgs bosons, W and Z bosons, and other SM physics processes, as well as beyond-the-SM physics processes such as the production of Hidden Valley long-lived neutral particles.

The event generator not only produces out-going final-state particles from the hard scatter, but also simulates parton showers and their hadronization, and handles the decay of unstable particles according to their lifetimes until all particles are either stable or outside the beam pipe[1]. The event generator also simulates the underlying event and MPI (discussed in Section 1.2.4), but does not simulate pileup: the simulation of hard scatters in the presence of pileup is acheived by overlaying real minimum bias events taken directly from data on top of the MC generated events (the insertion of pileup into the event occurs during the digitization step described below).

PYTHIA [47] is the event generator used in this analysis. Its library of hard-scatter processes is based on leading-order cross-section calculations, but it approximates higher-order processes through the modeling of ISR and FSR parton showers and gluon-string fragmentation.

Generation of Hidden Valley events

The process described in Section 1.3.4 is not included in PYTHIA's default library of physics processes; a custom process is defined by piggy-backing on processes that are aleady modeled by PYTHIA. The Minimal Supersymmetric extension of Standard Model (MSSM) requires the introduction of two higgs doublets and results in 5 Higgs bosons, two of which (h^0, H^0) are similar to the SM higgs, and one of which is a neutral pseudo-scalar with properties that make it a natural surrogate for the π_v^0. PYTHIA models MSSM processes in which the H^0 is naturally coupled to the A^0, and in which A^0 naturally decays predominantly to heavy fermions. It is therefore convenient to define the π_v^0 as the A^0 particle, and the SM higgs boson as the H^0, so that the process $h \to \pi_v \pi_v \to f\bar{f}$ is modeled in PYTHIA as the process $H^0 \to A^0 A^0 \to f\bar{f}$, where all other decays of the H^0 are suppressed, and where the masses of the H^0 and A^0 and the lifetime of the A^0 are set manually as desired. The Higgs and π_v^0 masses and lifetimes chosen for this analysis are described

---

[1] Particles that are unknown to GEANT (he next step in the simulation process, see Section 4.1.2), such as π_v's, are decayed by PYTHIA regardless of their lifetime.

in Section 4.2.

4.1.2 Detector Simulation

Each generated event is handed off to a full detector simulation within GEANT4 [31], in which the entire ATLAS detector (described in Section 2.2.2) is modeled using over 300,000 three-dimensional shapes and corresponding material descriptions. GEANT4 has been extensively calibrated with real data and models many material processes involving the passage of particles through matter at a fairly low level. Particles produced in the event generation step are propagated through a map of the ATLAS magnetic field and through the simulated ATLAS materials, where at each step of the simulation particles are given a probability to interact with a given detector material or decay. The energy-loss of particles moving through ATLAS is therefore modeled, including the secondary particles that are created during the particle-material interactions, and the corresponding energy depositions in active detector elements, or "hits", are recorded. The simulation relies heavily on a modelling of not only the detector geometry and material and alignment, but also the operating conditions such as temperature, gas pressures, and voltages. In a typical event over a million computational steps are required to adequately simulate the passage of particles through each of the ATLAS sub-detectors. In particular the simulation of the many particle-material interactions which lead to electromagnetic and hadronic showers in the calorimeters is the most computationally intensive step in the entire process of MC production. The GEANT4-based simulation has been extensively tested against data to ensure that the simulation is able to faithfully describe the particle-detector interactions that occur given a broad range of possible event topologies.

4.1.3 Event Digitization

Once particle-material interactions and their resulting energy depositions in the various detector electronics have been simulated by the detector simulation step, the electronic readout of the various ATLAS detectors and the digitization of their signals must be simulated. The event digitization step converts recorded detector hits into digital electronic readout signals, producing digits[2] when simulated signal voltages and currents from readout electronics exceed thresholds within in a timing

---

[2] A digitization, or digit, represents a detector output, such as a voltage, current, or time-over-threshold.

window. The simulation of electronic signals includes a simulation of electronic noise, and also includes a simulation of the hardware-based L1 trigger. Event digitization results in data stored as “Raw Data Objects” (RDO’s), which is formatted identically to what is produced in real data collisions. The same software reconstruction algorithms (see Section 3) are therefore applied to MC data as are applied to real collison data.

4.2 The Hidden Valley Monte Carlo signal samples

The signal Monte Carlo samples are generated using PYTHIA 8.165 [47] to simulate gluon fusion $gg \to h^0$ and the Higgs decay $h^0 \to \pi_v \pi_v$. Eight samples with 300000 events each were generated for different Higgs and π_v masses at E_{cm}= 8 TeV as part of the 2012 ATLAS Monte Carlo production run.

The lifetimes were chosen such that the π_v decays populate the entire volume of ATLAS. While the simulation allows the $\pi_v^0 \to f\overline{f}$ decay to all possible fermions, the dominant decay mode is to $b\overline{b}$ pairs. Other decay modes occur, and as discussed in Section 1.3.4, their relative abundance is in proportion to the squared mass of the fermion decay products, and therefore tau and charm-quark pairs are the second and third most-likely π_v^0 decay products. Table 4.1 summarizes all the parameters for the dataset production, together with branching ratios for π_v major decay channels. The $pp \to gg \to H$ production cross sections at $\sqrt{s}$ = 8 TeV are taken from reference [44].

Each event in each signal sample is weighted in order to account for the difference between the simulated pile-up conditions and the amount of pile-up present during actual data-taking.

4.2.1 The kinematics of the signal sample

In order to understand the main characteristics of the signal sample that will define our analysis strategy, a set of plots are provided at the generator level of the most relevant kinematic variables for each of the eight signal datasets.

The main driver of the kinematic differences between the samples is the difference between the Higgs and π_v masses. The Higgs is generally produced with low p_T (shown in Figure 4.3) and so its π_v decay products aqcuire a substantial fraction of their transverse momentum as a result of the energy difference: $m_h - 2\, m_{\pi_v}$. Samples in which the energy difference is larger tend to feature π_v’s

Dataset Number	Higgs Mass (GeV/c^2)	π_v Mass GeV/c^2	π_v lifetime (mm)	cross section (pb)	$b\bar{b}$ (%)	$\tau^+\tau^-$ (%)	$c\bar{c}$ (%)
159220	100	10	450	30.12	67.3	15.8	12.9
159221	100	25	1250	30.12	85.5	8.0	5.2
159222	126	10	350	19.22	67.3	15.8	12.9
159223	126	25	900	19.22	85.6	8.0	5.2
159224	126	40	1850	19.22	84.5	8.4	4.9
159225	140	10	275	15.63	67.3	15.8	12.9
158346	140	20	630	15.63	85.3	8.0	5.5
159226	140	40	1500	15.63	84.6	8.3	4.9

Table 4.1: Hidden Valley signal Monte Carlo parameters.

with higher transverse momentum and higher beta and gamma factors, while samples in which the energy difference is smaller tend to feature π_v's with lower transverse momentum and lower beta and gamma factors.

Higgs

The Higgs η and ϕ distributions are shown in Figure 4.1. The gluon-fusion Higgs production mechanism results in the Higgs' η distribution featuring a "double-hump" structure indicating that Higgs production in the forward direction is slightly preferred. This feature is accentuated by the fact that, as described in Section 1.2.4, the variable η is additive under boosts along the beam direction only under the condition that a particle's momentum is large compared to its mass, an assumption which does not always hold for a particle as massive as the Higgs boson. The β and γ factors of the Higgs are shown in Figure 4.2. The large mass of the Higgs results in a lower speed than is typical of lighter particles produced in collision events. Figure 4.3 shows the transverse (left) and longitudinal (right) components of the Higgs momentum. The Higgs boson is typically produced with low p_T. This is due in part to its large mass, but in addition it is due to its production mechanism: the Higgs does not have a partner to recoil against, and so is produced roughly at rest in the transverse

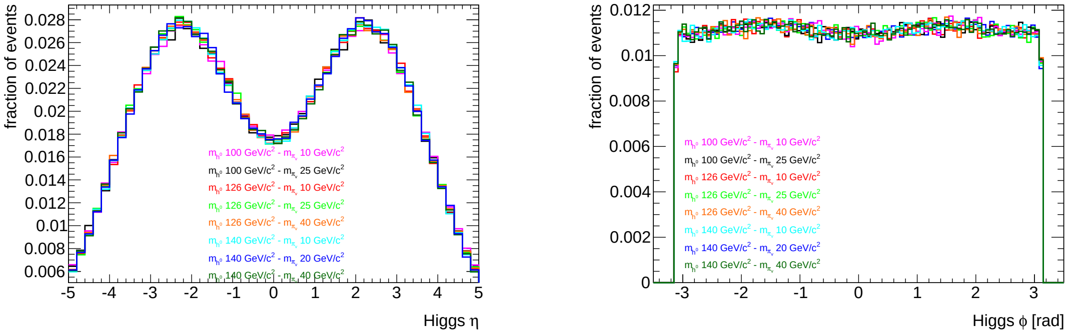

Figure 4.1: η (left) and ϕ (right) of the Higgs for the eight signal samples.

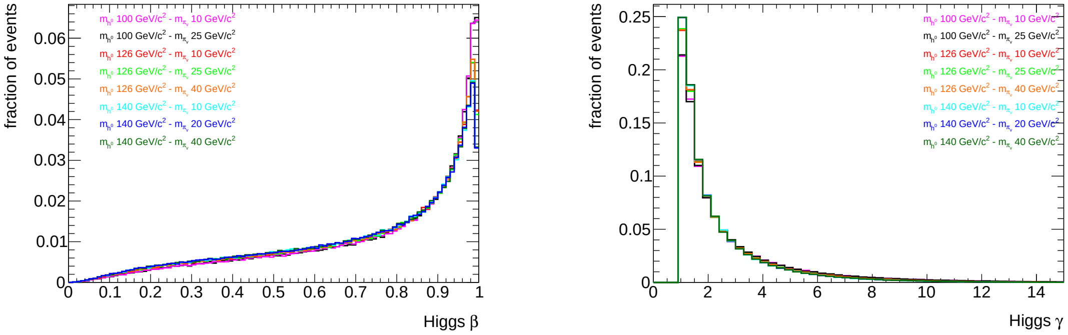

Figure 4.2: β (left) and γ (right) factor of the Higgs for the eight signal samples.

plane. The Higgs attains non-zero p_T due to higher-order corrections to the gluon-fusion production mechanism shown in Figure 1.18.

v-pion (π_v)

For each generated signal sample the π_v η and ϕ distributions are shown in Figure 4.4. For samples with large Higgs-π_v mass differences the "double-hump" structure of the parent Higgs' η distribution is no longer apparent. This is because the Higgs decays to π_v's isotropically in its own rest frame and large Higgs-π_v mass differences result in π_v momenta that overcome the boost provided by the Higgs' direction of motion. Figure 4.5 shows the $\Delta\phi$ (left) and ΔR (right) between the two π_v's produced in each event. The two π_v's are mostly produced back-to-back. Figure 4.6 and Figure 4.7 show the β (left) and gamma (right) factors for π_v's decaying in the ATLAS barrel or endcaps.

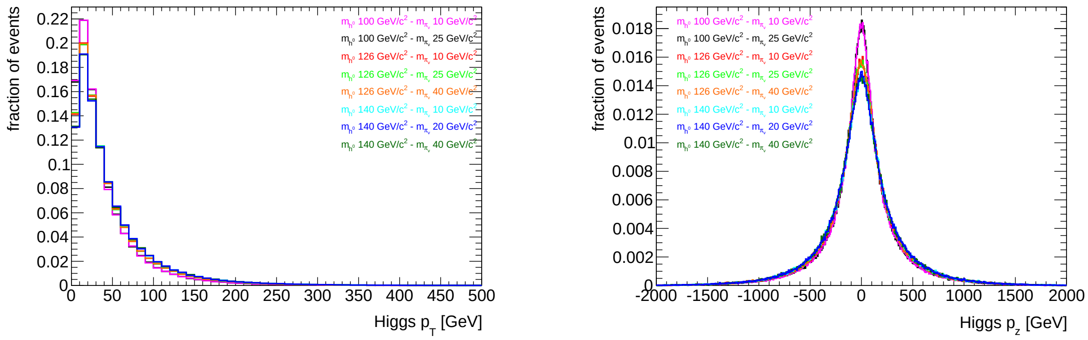

Figure 4.3: Transverse (left) and longitudinal (right) momentum of the Higgs for the eight signal samples.

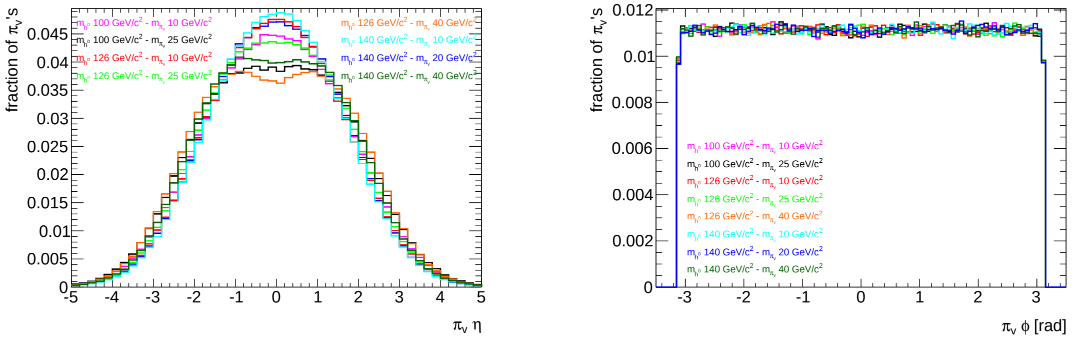

Figure 4.4: η and ϕ for the π_v's for the eight signal samples. The η shape seen in the samples with low Higgs-π_v mass difference are a reflection of the parent Higgs' η distribution shown in Figure 4.1

Large Higgs-π_v mass differences result in faster π_v's, while small Higgs-π_v mass differences result in slower π_v's. π_v's in the endcap typically have a higher boost in longitudinal direction and therefore slightly higher beta and gamma factors than π_v's found in the barrel. The single π_v p_T and the correlation between the p_T's of both π_v's in the same event are shown in Figure 4.8. The transverse momentum of each π_v is typically slightly larger than $\frac{1}{2}(m_h - 2\ m_{\pi_v}\ )$ due to the boost provided by the Higgs' p_T. The same boost results in the p_T of each π_v being somewhat anticorrelated with the p_T of the other. Depending on the angle at which the π_v's are produced relative to the Higgs' direction of motion, the Higgs' boost may add to the p_T of one π_v while simultaneously subtracting from the p_T of the oppositely-moving π_v.

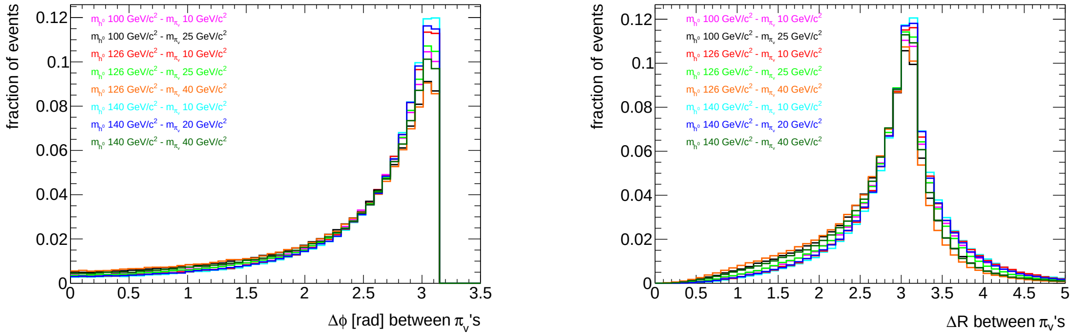

Figure 4.5: ϕ difference between the two π_v's (left) and ΔR between them (right). The π_v's are mostly produced back-to-back.

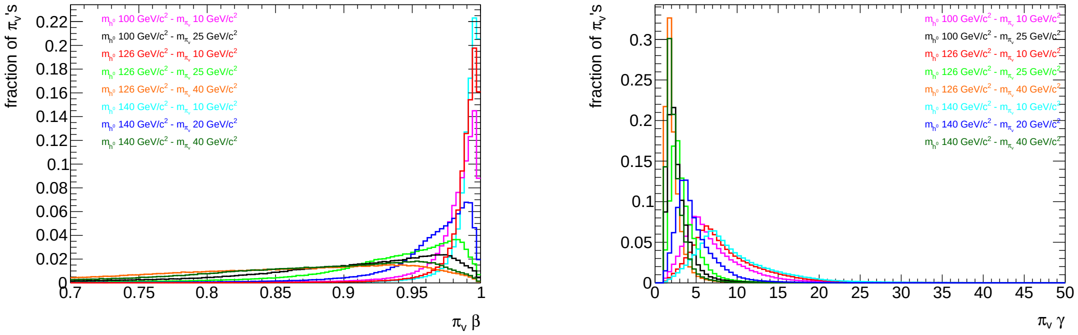

Figure 4.6: β (left) and γ (right) factor for π_v's in the barrel for the eight signal samples. Large Higgs-π_v mass differences result in faster π_v's, while small Higgs-π_v mass differences result in slower π_v's.

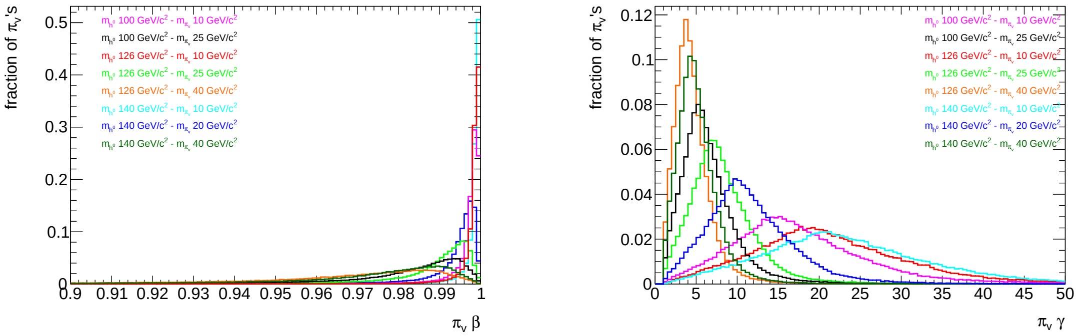

Figure 4.7: β (left) and γ (right) factors for π_v's in the endcap for the eight signal samples. Large Higgs-π_v mass differences result in faster π_v's, while small Higgs-π_v mass differences result in slower π_v's.

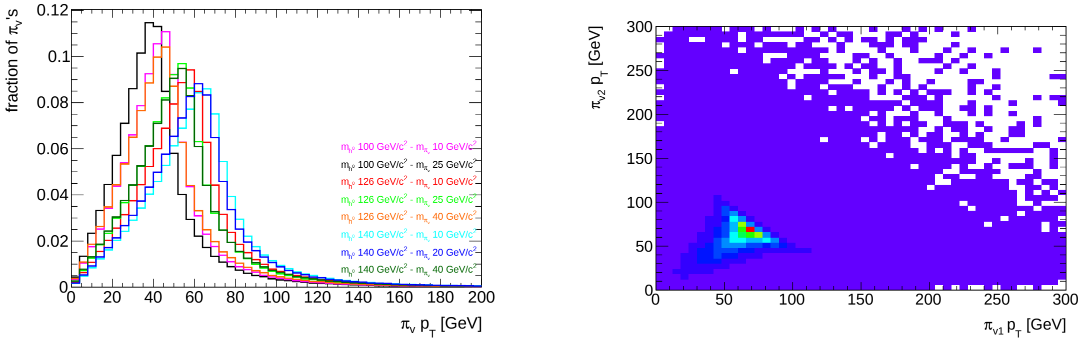

Figure 4.8: Transverse momentum for the π_v's (left), and transverse momentum of one π_v versus the other (right). The p_T of each π_v is largely determined by the Higgs-π_v mass difference and the angle at which the π_v's are produced in the Higgs' rest frame.

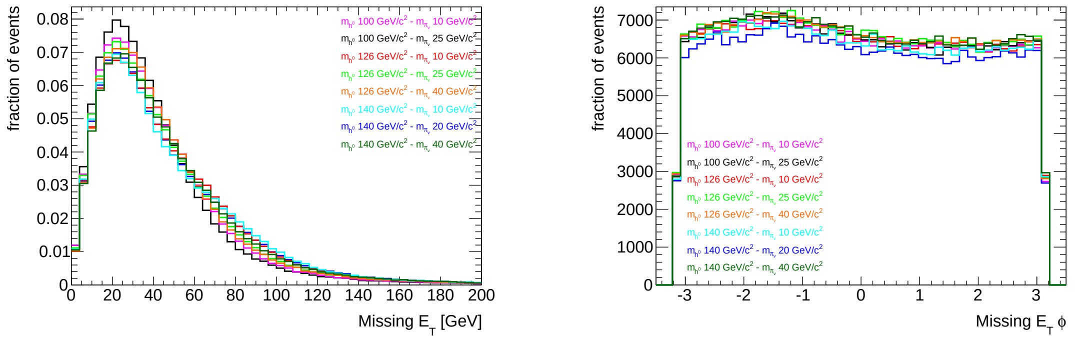

Figure 4.9: Missing transverse energy and its ϕ direction for the eight signal samples.

Missing transverse energy

Distributions of the missing transverse energy and the related ϕ are shown in Figure 4.9 for each of the eight datasets. The missing transverse energy is typically small in cases where both π_v's decay before exiting the calorimeters.

4.3 Monte Carlo QCD di-jet Samples

Simulated QCD dijet samples were used for data-MC comparison studies used to estimate various systematic errors relating to the agreement between MC and data. Simulated QCD samples were also used to study the the contribution to the QCD background from jets initiatiated by different parton types, and to study the general differences and possible discriminants between signal events and QCD background events.

The QCD Monte Carlo dijet samples are generated using PYTHIA 8.165 to simulate QCD hard-scatter processes with initial and final state partons. Eight samples with 1500000 events each were generated at E_{cm}= 8 TeV as part of the 2012 ATLAS Monte Carlo production run. The QCD dijet samples are filtered in order to produce flat statistics in bins of the p_T of the highest-p_T parton emerging from the hard scatter. The p_T ranges of the so-called "JZXW" samples are shown in Table 4.2.

JZXW	p_T range
JZ0W	0-20
JZ1W	20-80
JZ2W	80-200
JZ3W	200-500
JZ4W	500-1000
JZ5W	1000-1500
JZ6W	1500-2000
JZ7W	2000+

Table 4.2: Leading jet p_T range for each QCD Monte Carlo dijet sample.

The QCD Monte Carlo dijet samples corresponding to different hard-scatter p_T ranges can be weighted and combined in order to simulate the p_T spectrum of QCD jets produced in real data. This is done by weighting each JZXW sample by its cross-section and then scaling the total number of events to the integrated luminosity of the simulated data range. Additionally each JZXW sample is weighted by the efficiency of the filter used to reject events outside of the corresponding p_T range, and each event is weighted by the statistical weight provided by PYTHIA during the event generation process. A further weight is applied on an event-by-event basis to account for the difference between the simulated pile-up conditions and the amount of pile-up present during actual data-taking.

Chapter 5

ANALYSIS

5.1 Introduction

This analysis focuses on the search for long-lived neutral particles (LLNP) which decay in the ATLAS hadronic calorimeter (HCAL). The decay products of each LLNP deposit energy in the HCAL and are consequently reconstructed as a jet. Such jets feature several unique characteristics owing to the fact that each LLNP is invisible to the ATLAS detector until it decays. Because the LLNP are neutral, if they decay in the HCAL they neither produce charged tracks that point at the hadronic energy deposits, nor do they deposit energy in the electromagnetic calorimeter (ECAL). This is in contrast to ordinary jets which, consisting of charged and neutral particles produced near the IP, result in tracks in the Inner Detector (ID) and energy deposits in both the electromagnetic and hadronic calorimeters. The primary identifying characteristic of events containing LLNP that is exploited by this analysis is the reconstruction of trackless jets with little to no associated energy in the ECAL.

As described in Section 4.2 this analysis models LLNP as π_v's produced from the decay of a Higgs boson. Simulated signal events each contain two roughly back-to-back π_v's, each of which decays predominantly to $b\bar{b}$. Events are simulated for Higgs masses between 100 and 140 GeV and π_v masses between 10 and 40 GeV, and π_v lifetimes are chosen to give decays throughout the ATLAS detector volume. This analysis focuses its attention on decays in the HCAL.

Signal events are unlikely to be saved by ATLAS for further study unless they are selected by a trigger (see Section 2.8). A trigger that exploits the unique characteristics of LLNP decaying in the HCAL is used to select signal-candidate events for this analysis. This trigger is described in Section 5.2.

The primary identifying characteristics of events searched for-in this analysis are fairly unique, however they are not so unique as to exclude the possibility of their being the result of Standard Model physics, detector mis-measurement, or other sources unrelated to our signal. A background is any class of event that fakes our signal: anything that produces energy deposits in the HCAL while not leaving nearby energy deposits in the ECAL and not leaving nearby tracks in the ID. Possible backgrounds in this analysis include: detector malfunction (the ATLAS detector fails to reconstruct existing tracks and energy deposits or falsly registers hadronic energy deposition); beam halo (muons produced from collisions upstream of the ATLAS detector travel parallel to the beam and deposit energy in the HCAL); cosmic ray (cosmic ray muons deposit energy in the HCAL); and QCD dijet production (ordinary jets may sometimes consist of only neutral hadrons which in turn may sometimes travel several interaction lengths into the calorimeter before initiating a shower). A careful understanding of these backgrounds is necessary in order to assess the likelyhood that signal-candidate events observed in data are signal events or background events. An understanding of these backgrounds additionally motivates analysis cuts that may be used to reject them. Backgrounds are discussed in more detail in Secton 5.5.

Based on an examination of the characteristics of our signal and background events, a set of analysis cuts has been optimized to select signal events while discriminating against background events. The set of analysis cuts is described in Secton 5.4.

This chapter is organized as follows. Section 5.2 describes the signature-driven trigger we use to select the data, starting with a short section that describes the signal kinematics that the trigger and offline selection cuts take advantage of. Section 5.3 describes the dataset used in the analysis, Section 5.4 describes the cut-based analysis, Section 5.5 describes the determination of the backgrounds, Section 5.6 describes the determination of the systematic errors, and, finally, Section 5.7 contains the results.

5.2 Hidden Valley Trigger

The standard ATLAS trigger menu contains many low-threshold jet triggers that will accept our signal. However, as discussed in Section 2.8, they are highly prescaled and therefore lead to unacceptable losses in signal acceptance. As a result a signature-driven trigger has been developed which looks specifically for neutral long-lived particles that decay inside or just before the ATLAS hadronic calorimeter. Since events meeting the criteria of this trigger are rare, it does not need to be prescaled.

This section contains a quick description of the trigger we use in this analysis. This trigger and other LLNP triggers are described in greater detail in the supporting note [46].

5.2.1 Characteristics of decays in the Hadronic Calorimeter

Long-lived neutral particle decays occurring near the outer edge of the electromagnetic calorimeter (ECAL) or inside the hadronic calorimeter (HCAL) are characterized by jets with no nearby tracks pointing back to the IP and unconventional energy distributions in the calorimeter. The signature-driven trigger and the offline analysis cuts take advantage of these features.

Jets resulting from π_v's that decay beyond the ID should have few or no tracks pointing to them due to the fact that the π_v is electrically neutral. Pileup, however, can result in tracks that randomly point toward the π_v decays. Figure 5.1 shows the distribution of charged tracks with $p_T > 1.0$ GeV in a cone of $\Delta R < 0.2$ near jets resulting from Standard Model processes and near jets resulting from π_v decays.

The displaced formation of a jet alters the apparent jet width[1]. Figure 5.2 shows the jet width for a jet caused by the displaced decay of a π_v as and the jet width due to a Standard Model jet. The decay products of the π_v, usually $b\bar{b}$, do not have time to spatially separate before depositing energy in the calorimeters.

A π_v that decays near the outer radius of the ECAL or in the HCAL will deposit little energy in the ECAL: the fraction of energy deposited in the ECAL, f_{EM}, is anomalously small. This alters the $\log_{10}(E_{HAD}/E_{EM})$ distribution. Figure 5.3 shows the distribution of $\log_{10}(E_{HAD}/E_{EM})$ from jets

---

[1] Jet width is defined as the average distance of a jet constituent to the jet direction, weighted with the energy of the constituent.

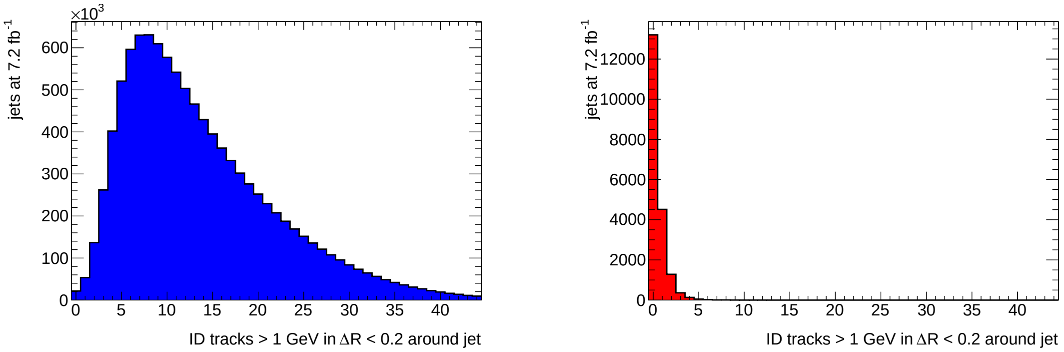

Figure 5.1: Number of charged tracks with $p_T > 1.0$ GeV in a cone of $\Delta R < 0.2$ around the jet axis, with jet $|\eta| < 2.5$ and $p_T < 40$ GeV. The left plot is for jets resulting from Standard Model processes (from the MC QCD dijet JZ0W-JZ7W samples) and the right plot is for jets resulting from π_v's decaying in the hadronic calorimeter or at the very edge of the EM calorimeter (from signal MC m$_H$=140 GeV and m$_\pi$=10 GeV).

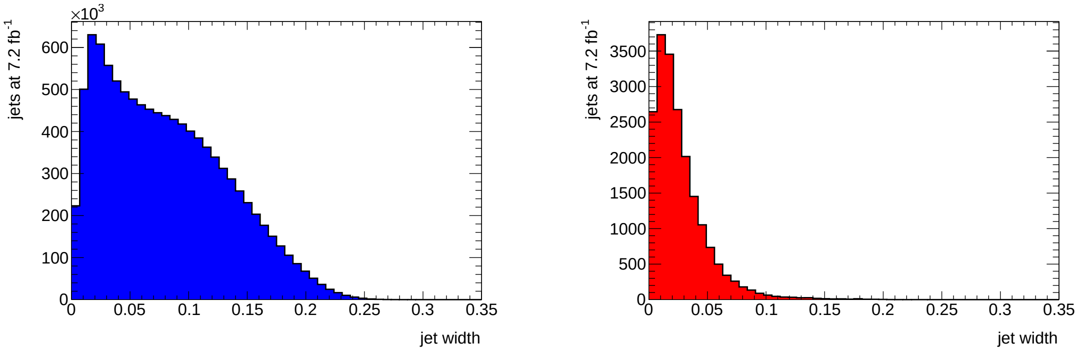

Figure 5.2: Distribution of jet width for jets with jet $|\eta| < 2.5$ and $p_T < 40$ GeV. On the left are Standard Model jets from MC QCD dijets JZ0W-JZ7W samples and on the right are jets generated by a π_v that decays near the outer radius of the ECAL or in the HCAL from signal MC m$_H$=140 GeV and m$_\pi$=10 GeV. The displaced jets do not have time to spatially separate resulting in the relatively narrow distribution.

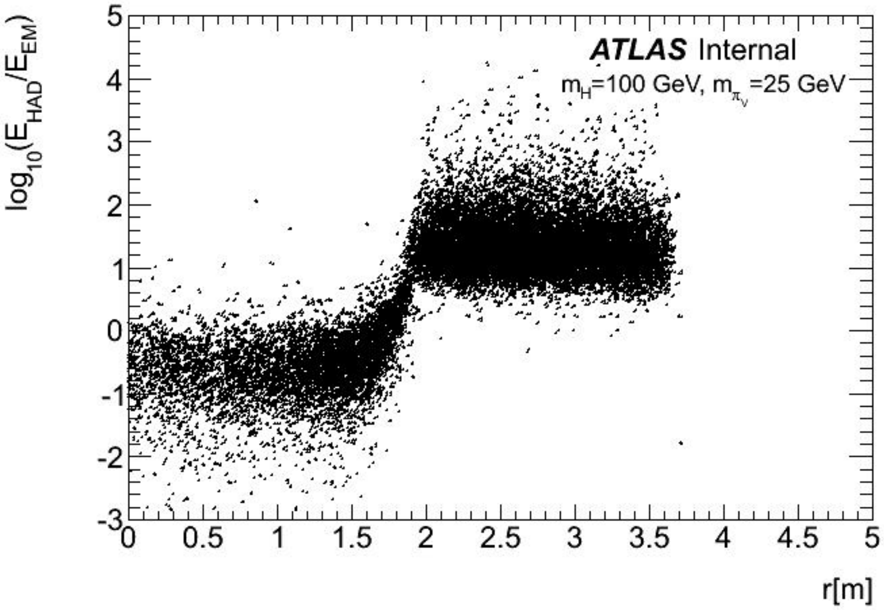

Figure 5.3: $\log_{10}(E_{HAD}/E_{EM})$ for all jets in the barrel calorimeter coming from π_v decays as a function of the π_v's radial decay position r. The sample contains jets from π_v's that decay throughout the detector and Standard Model jets. The Standard Model jets appear on the left hand side of the plot, and the π_v's that decay later in the calorimeter appear on the right hand side. This figure was taken from [46].

produced by π_v's as a function of π_v radial decay position in the barrel region. As the π_v decay gets close to the end of the ECAL (2.2 m), the ratio changes from a characteristic negative value for Standard Model jets to a positive value characteristic of LLNP decays.

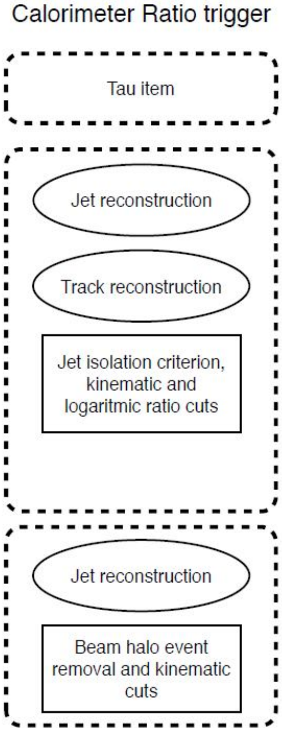

Figure 5.4: Schematic diagram of the algorithms used in the CalRatio Trigger. The ovals and boxes represent the Feature Extraction and Hypothesis algorithms, respectively.

5.2.2 The Calorimeter Ratio (CalRatio) Trigger

Figure 5.4 shows the sequence of algorithms used by the signature-driven trigger. The trigger is fed by the Level-1 trigger L1_TAU40. The Level-1 tau triggers select energy in a narrow region: 0.1×0.1 in $\Delta\eta \times \Delta\phi$. The narrow region allows the use of a lower E_T threshold while avoiding the prescale that would otherwise be required to reject the high rate of QCD background present at low jet E_T. The L1_TAU40 trigger was unprescaled during the full 2012 run.

At Level-2, the trigger uses $\log_{10}(E_{HAD}/E_{EM})$ and track isolation to further reduce the rate. Jet and track reconstruction are seeded by the Level-1 RoI provided by L1_TAU40. Figure 5.5 shows the distribution of $\log_{10}(E_{HAD}/E_{EM})$ for all jets that have passed our Level-1 requirements in several of our signal samples. The distributions contain two obvious peaks. The first, at ~ -0.75 is from Standard Model jets and from π_v decays in the inner detector. From the point of view of this analysis these jets cannot be distinguished form Standard Model jets. The second peak, centered near ~ 1.5,

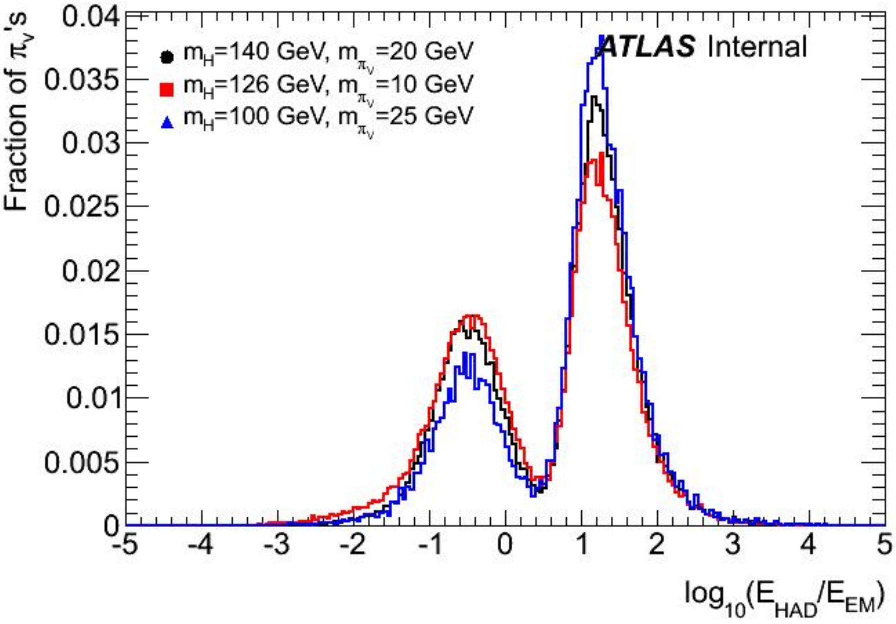

Figure 5.5: Distribution of $\log_{10}(E_{HAD}/E_{EM})$ for all π_v jets in events that pass the L1_TAU40 trigger in the barrel region ($|\eta| \leq 1.4$). The first peak at ~ -0.75 is from Standard Model jets in the sample, or from π_v's that decayed earlier than the EM calorimeter. The second peak at ~ 1.5 are from the π_v's with a displaced decay. This distribution is a projection of Figure 5.3. This figure was taken from [46].

is from π_v decays in the HCAL. In order to control the Level-2 rate the $\log_{10}(E_{HAD}/E_{EM})$ cut is chosen to be 1.2. Additionally the jet is required to have $E_T \geq 35$ GeV, and $|\eta| < 2.5$.

The π_v's with a displaced decay in the HCAL should, in addition to having high $\log_{10}(E_{HAD}/E_{EM})$, have no tracks pointing toward the associated energy deposits. The Level-2 hypothesis requires that no tracks with $p_T > 1.0$ GeV be found in the square region 0.2×0.2 in $\Delta\eta \times \Delta\phi$ around the jet axis. Tracks are found using the Level 2 SiTrack track-finding algorithm [49], a simple Kalman algorithm based filter.

The EventFilter trigger requires that a jet pass a refinement of the Level-2 criteria. The standard jet finding algorithm is run and at least one jet passing the Level-2 requirements must also have $E_T > 35$ GeV. In addition Beam Halo ("Line of Fire") cuts are applied, which are described in the next section.

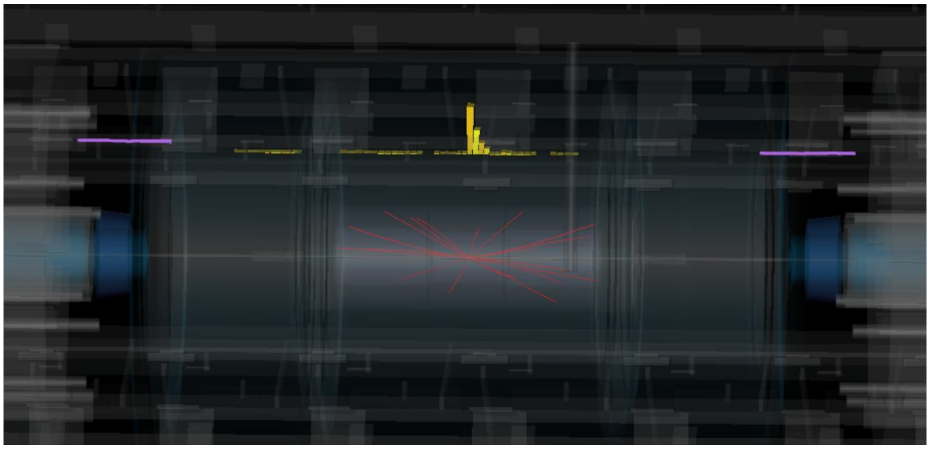

Figure 5.6: Event display showing a beam halo muon which has bremsstrahlunged inside of the hadronic calorimeter and caused the event to pass the CalRatio trigger. The two purple lines are reconstructed muon segments and the yellow boxes represent energy deposited in the hadronic calorimeter. Taken from [46].

Line Of Fire Removal

Beam halo muons travel parallel to the proton beam and result from interactions between the proton beam and stray air molecules or beam collimator materials. Beam halo muons that bremsstrahlung in the HCal can fake our signal by producing trackless jets with high $\log_{10}(E_{HAD}/E_{EM})$, and are therefore a potential source of background. These events are characterized by a muon segment parallel to the z-axis reconstructed on either side of the detector, and a line of calorimeter cells extending the length of the calorimeter in line with the jet. The reconstructed energy deposition looks like a “line of fire” in the calorimeter. Figure 5.6 shows an example of a beam halo event.

Two algorithms are used by the trigger to reject Beam Halo events. The first algorithm rejects events based on calorimeter cell timing. Beam halo muons typically arrive in-time with a proton bunch, entering ATLAS approximately 25 ns before a proton-proton collision takes place and leaving approximately in time with particles emerging from the collision. Therefore the timing of each energy deposit from a Beam Halo muon is generally inconsistent with the time required for a particle moving at the speed of light to travel from the IP to the calorimeter cell. The second algorithm rejects events for which two parallel muon segments are found reconstructed on either side of the calorimeter (see the purple lines in Figure 5.6) in coincidence with the jet’s position in phi. Refer-

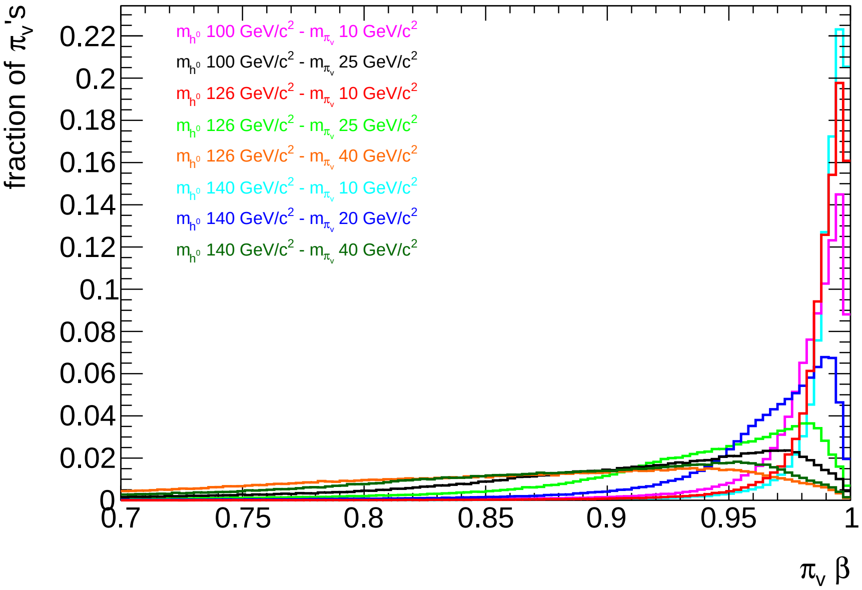

Figure 5.7: Distribution of β for π_v's in the signal samples. The speed is inversely proportional to the ratio of the π_v mass to the Higgs mass.

ence [53] contains additional details about these algorithms. Efficiencies were measured on 2011 data and it was found that the cell timing algorithm rejected $(91.0 \pm 0.2)\%$ of beam halo events and the muon-segment-based algorithm rejected $(80.1 \pm 0.2)\%$ of beam halo events. Details can be found in [46].

Trigger Timing

While the π_v decays to Standard Model particles whose corresponding energy deposits in the calorimeters can in principle be reconstructed normally, it must have a speed that is large enough such that its Standard Model decay products arrive in sync with the ATLAS trigger. Otherwise the data will be lost or wrongly associated with a later proton-proton collision. The speed of the π_v depends both on its mass and on the ratio of its mass to the Higgs mass. Figure 5.7 shows the speed, $\beta = v/c$, of π_v's in all of our signal samples. The size of the low-end tail is inversely proportional to the ratio of the mass of the π_v to the Higgs mass. Very few events have a speed lower than 0.7.

Figure 5.8 shows the fraction of π_v's in each sample that are less than 10 ns out-of-time for a

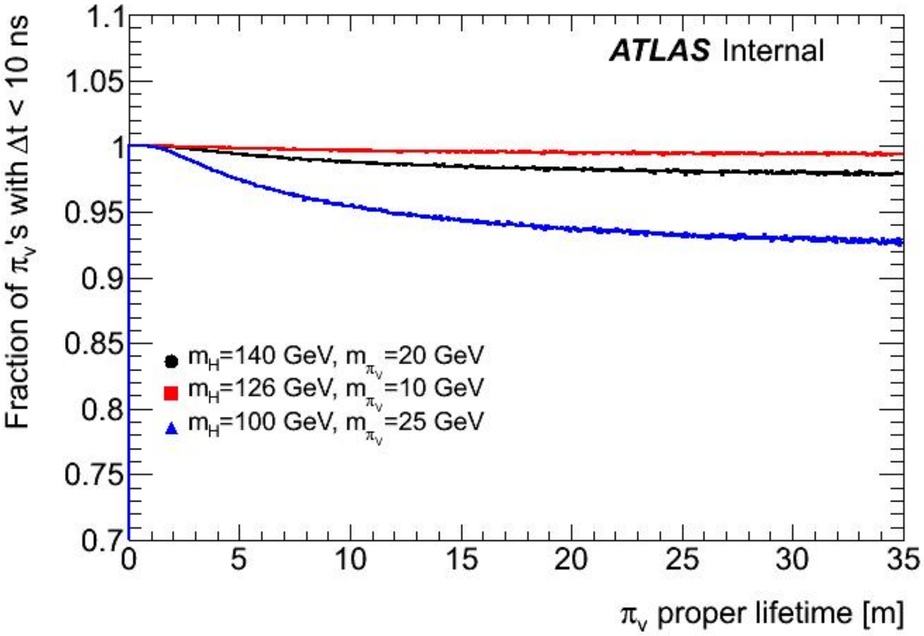

Figure 5.8: The fraction of π_v's that arrive less than 10 ns out of time. The samples with lower efficiencies are those with lower β, as seen in Figure 5.7. Taken from [46].

large range of proper lifetimes. The current ATLAS simulation of the calorimeter trigger correctly handles the time delay and reconstructs the correct energy. For collision data, the online Optimal Filtering Algorithm [50] is used to correctly determine the time shift of the amplitude, apply a correction and reconstruct the energy to within 1% for time shifts up to 12 ns [51]. The corrected energy is available at Level-2. Given how rarely our signal samples result in out-of-time energy deposits this analysis ignores any systematic due to this.

5.2.3 Trigger Efficiency

The trigger efficiency is defined as the fraction of signal events in which at least one π_v causes the CalRatio Trigger to fire. Table 5.1 summarizes the results for each of the signal samples. This efficiency strongly depends on the π_v decay position (and thus its lifetime), as shown in Figure 5.9; the trigger's selection algorithm is most efficient in the HCAL (from 2.2 m to 4 m). In Figure 5.9 results are reported for decays in the barrel and endcap regions separately: the lower efficiency in the endcap region is due to the underlying event resulting in increased energy deposition in the ECAL and an increased number of tracks spoiling the track isolation requirement. Figure 5.10 shows the trigger efficiency as a function of the π_v proper lifetime for each of the MC samples.

sample	cross section (pb)	trigger acceptance (%)	# of events in 20.8 fb^{-1}
m_H = 100 GeV, m_{π_v} = 10 GeV	30.12	3.16 ± 0.03	19797 ± 188
m_H = 100 GeV, m_{π_v} = 25 GeV	30.12	2.09 ± 0.03	13094 ± 188
m_H = 126 GeV, m_{π_v} = 10 GeV	19.22	5.93 ± 0.04	23707 ± 160
m_H = 126 GeV, m_{π_v} = 25 GeV	19.22	4.54 ± 0.04	18150 ± 160
m_H = 126 GeV, m_{π_v} = 40 GeV	19.22	3.33 ± 0.03	13313 ± 120
m_H = 140 GeV, m_{π_v} = 10 GeV	15.63	7.34 ± 0.05	23863 ± 163
m_H = 140 GeV, m_{π_v} = 20 GeV	15.63	6.35 ± 0.05	20644 ± 163
m_H = 140 GeV, m_{π_v} = 40 GeV	15.63	4.84 ± 0.04	15735 ± 130

Table 5.1: CalRatio trigger acceptance (%) for Monte Carlo signal samples, and the corresponding expected number of events passing the trigger in 20.8 fb^{-1} of data.

5.2.4 Trigger Systematic Uncertainty

The above studies of the CalRatio trigger's efficiency and corresponding signal acceptance are made possible by the MC simulation of our signal. The number of signal events expected to be selected by the CalRatio trigger in data is therefore dependent on the faithful modeling of the CalRatio trigger's performance in MC simulated data. In this section various comparisons between data and MC are made in order to evaluate the systematic corresponding to the assumption that the trigger's performance in MC is a faithful representation of its performance in data.

The CalRatio trigger includes three primary cuts: the $\log_{10}(E_{HAD}/E_{EM})$ cut; the E_T cut; and the track isolation cut. Each of these cuts were studied individually in order to evaluate, respectively, the difference between the trigger's reconstruction of $\log_{10}(E_{HAD}/E_{EM})$, E_T, and tracks, between data and MC.

The comparison is made using the MC dijet samples (see Section 4.3) and a clean sample of

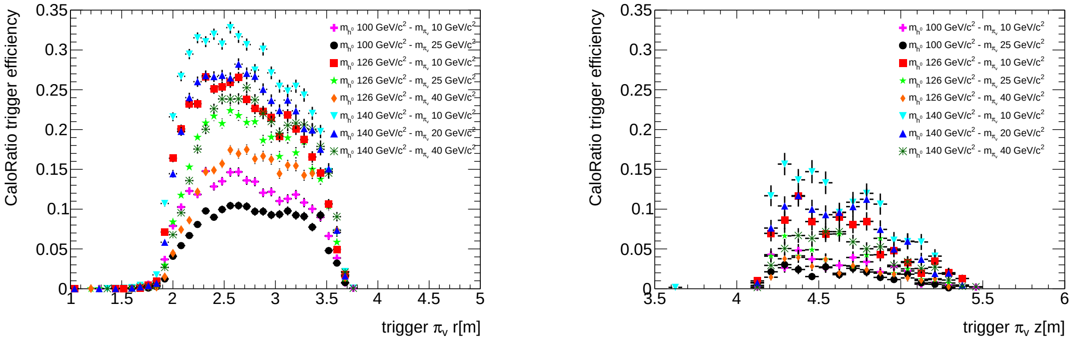

Figure 5.9: Trigger efficiency in the barrel ($|\eta| <= 1.7$) (left) and in endcap ($1.7 < |\eta| < 2.5$) (right) as a function of the trigger π_v radial decay position. Efficiency is defined as the number of π_v's firing the CaloRatio trigger and decaying at given length divided by the number of π_v's generated at that decay length. The differences in trigger efficiency are primarily a function of the kinematics that result from different Higgs-π_v mass differences. Larger mass differences result in larger π_v boosts, resulting in higher p_T jets more likely to pass the trigger's E_T threshold.

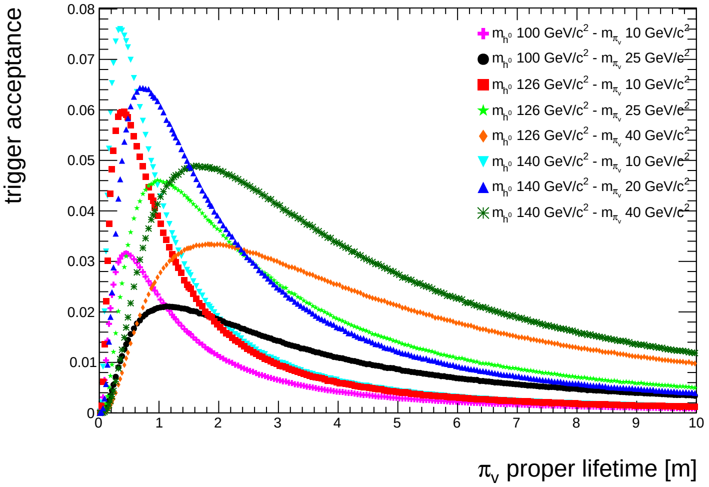

Figure 5.10: Trigger efficiency as a function of different π_v proper lifetimes for the eight MC samples. The differences in trigger efficiency are primarily a function of the kinematics that result from different Higgs-π_v mass differences. Larger mass differences result in larger π_v boosts, resulting in higher p_T jets more likely to pass the trigger's E_T threshold, and also resulting in π_v's of a given lifetime traveling further before decaying.

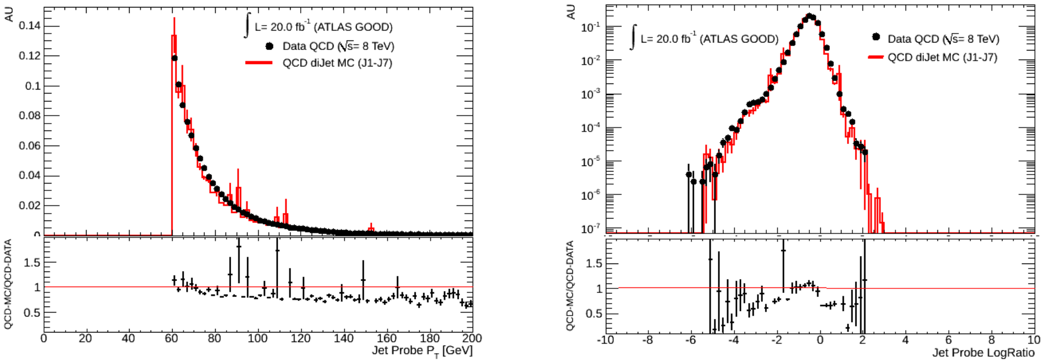

Figure 5.11: Comparison between data and MC: jet p_T (left) and jet $\log_{10}(E_{HAD}/E_{EM})$ (right).

QCD dijet events collected in 2012 data. The discrepancy between the performance of each cut in MC and in data is used to determine an uncertainty on each cut applied in the trigger. The trigger is then simulated on the MC signal sample and its cuts are each varied by the derived uncertainties in order to estimate the effect of the uncertainty in the trigger's performance on the signal acceptance.

Both MC and data events used in this study are required to pass two dedicated single jet triggers: EF_J35 and $EF\_b55\_NoCut\_J55$. The second of these triggers is designed for b-jet performance studies and is exploited for the study of the track isolation cut because it ensures that Level-2 tracking is run without biasing the event selection other than the requirement of a jet passing an E$_T$ cut. The good event criteria used in the analysis cut flow are applied (see Section 5.4), and, in order to enhance the QCD purity in data, standard tag-and-probe cuts are applied:

- Tag jet: Must meet ATLAS Good Medium criteria with $p_T > 40 GeV$, $|\eta| < 2.5$
- Probe jet: Must meet the HV Good Medium criteria with $p_T > 40 GeV$, $|\eta| < 2.5$, $\Delta\phi(tag, probe) \geq 2.5$

Only the probe jet is used in this study. The probe jet kinematic distributions in MC have been compared with those in data in order to verify that they show broad agreement, as shown in Figure 5.11 for the p_T and $\log_{10}(E_{HAD}/E_{EM})$ distributions.

To estimate the discrepancy between data and MC for the L2 E$_T$ cut, we determine the turn-on of the L2 cut in data and in MC as a function of the offline jet E$_T$. Figure 5.12 (left plot) shows

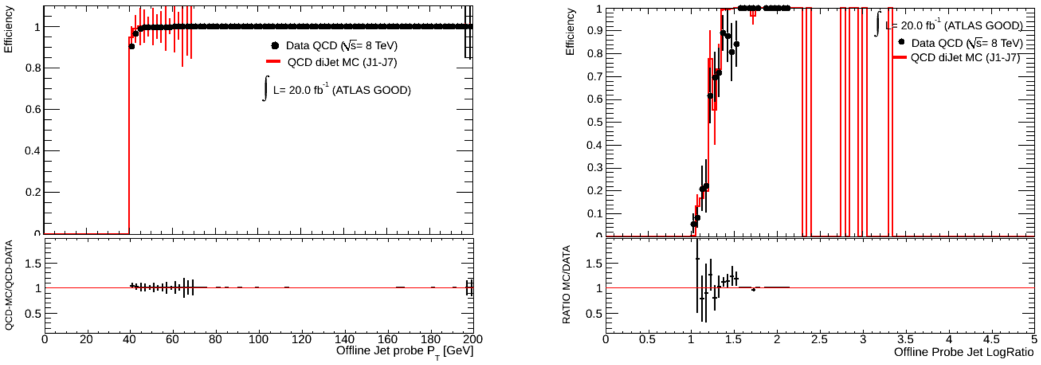

Figure 5.12: Efficiency curves for the E$_T$ cut (left) and $\log_{10}(E_{HAD}/E_{EM})$ cut (right) for the probe Jet. The quantities on the x-axis are offline quantities.

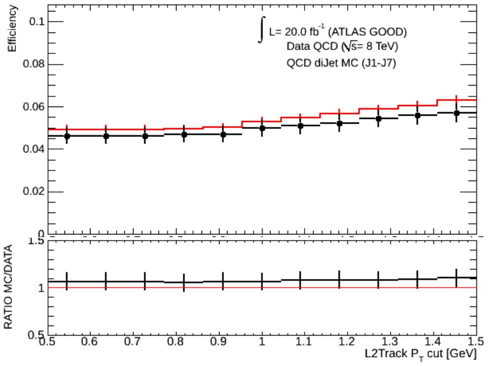

Figure 5.13: Efficiency curves for the track isolation cut. The p_T cut on the x-axis is online L2.

the turn-on curves in data and in MC as a function of the L2 jet E$_T$ cut. At 60 GeV the trigger turn-on has plateaued to 100% and so no systematic is taken for the jet E$_T$ cut. The same procedure is done for the $\log_{10}(E_{HAD}/E_{EM})$ cut. Figure 5.12 (right plot) shows a comparison of the two turn-on curves. The difference between data and MC for the working point $\log_{10}(E_{HAD}/E_{EM})$=1.2 is found to be about 11%. This value is used for varying the trigger cut on the signal sample to estimate the systematic uncertainty corresponding to this cut.

Concerning the track isolation requirement, the Figure 5.13 shows the ratio between data and MC as function of different p_T cuts applied to L2 tracks. The discrepancy obtained at the working point of 1 GeV is found to be about 1%.

We estimate the variation in acceptance of the trigger by varying the L2 trigger cuts individually in simulation and then adding the resulting variations in quadrature. In the Table 5.2 the variation used for each cut and the resulting variation in acceptance for the MC signal samples are reported.

Analysis Cut	Variation (%)
$E_T \geq 35$ GeV	negligible
$\log_{10}(E_{HAD}/E_{EM}) > 1.2$	11%
no tracks with $p_T > 1.0$ GeV (around jet cone 0.2)	1%

Table 5.2: Variation in trigger acceptance (%) in data and MC dijet events for each cut.

MC sample	acceptance variation (%) due to $\log_{10}(E_{HAD}/E_{EM})$	acceptance variation (%) due to ID track	Total (%)
m_H = 100 GeV, m_{π_v} = 10 GeV	+0.0; -8.0	+0.0; -0.0	+0.0; -8.0
m_H = 100 GeV, m_{π_v} = 25 GeV	+0.0; -6.0	+0.0; -0.0	+0.0; -6.0
m_H = 126 GeV, m_{π_v} = 10 GeV	+0.2; -8.0	+0.0; -1.0	+0.2; -8.1
m_H = 126 GeV, m_{π_v} = 25 GeV	+0.0; -9.3	+0.0; -0.3	+0.0; -9.3
m_H = 126 GeV, m_{π_v} = 40 GeV	+0.5; -7.0	+0,0; -0.4	+0.5; -7.0
m_H = 140 GeV, m_{π_v} = 10 GeV	+0.0; -6.6	+0.0; -0.0	+0.0; -6.6
m_H = 140 GeV, m_{π_v} = 20 GeV	+0.0; -6.0	+0.0; -0.0	+0.0; -6.0
m_H = 140 GeV, m_{π_v} = 40 GeV	+0.0; -8.5	+0.2; -0.0	+0.2; -8.5

Table 5.3: Calo Ratio trigger acceptance (%) for Monte Carlo signal samples.

5.3 Analysis Samples

The main samples used in this analysis are the 2012 Data and the signal Monte Carlo samples. The 2012 Data samples are described in this section. The signal Monte Carlo samples are described in Section 4.2. The samples used for data-driven background estimation are described in Section 5.4.

5.3.1 2012 Data Sample

This analysis uses 20.8 fb^{-1} of data recorded with the ATLAS detector during 2012. This represents 92% of the data delivered to ATLAS by the LHC in 2012, and represents 95% of the data recorded by ATLAS during 2012. Only data that fires the CalRatio trigger is used in this analysis , and all data is required to be included in the standard good runs list (GRL). The GRL is a catalog of the stretches of data that pass standard ATLAS data quality criteria (discussed in Section 3.7). In total 1628647 events are considered in this analysis.

The integrated luminosity of this dataset is calculated using standard ATLAS tools. The uncertainty on the integrated luminosity is +-2.8%. It is derived, following the same methodology as that detailed in Ref. [52], from a preliminary calibration of the luminosity scale derived from beam-separation scans performed in November 2012.

5.4 Analysis Strategy

In this section we describe the analysis selection cuts used for selecting two π_v decays in the ATLAS Hadronic Calorimeter. Basic data quality cuts are applied, along with cuts designed to select signal and remove background.

5.4.1 Characteristics of Hidden-Valley Events

This analysis requires the identification of two candidate π_v jets. This choice is motivated by the fact that single-jet backgrounds are at most weakly correlated: the existence of one jet that fakes our signal generally does not substantially increase the likelihood of finding a second such jet in the event. For example the two largest backgrounds to this analysis are cosmic ray muons and QCD dijets. Cosmic ray events are most often the result of a single muon passing from one side of the ATLAS detector to the other, depositing energy in one or more places along the way. In such cases the probability for the muon to deposit a large fraction of its energy in the calorimeter is small and does not depend strongly on whether it previously lost some of its energy in another part of the calorimeter. It does depend weakly on the muon energy: a muon's radiative energy loss in matter increases with muon energy. Therefore the probability for a muon to deposit a large amount of energy a *second time* in a single event is generally smaller than the probability for it to have deposited the energy a first time. In other words the probability for a single cosmic ray muon of energy E to fake two π_v jets in a single event is less than the square of the probability for the same cosmic ray muon to have faked a single π_v jet.

Similar logic applies to the mechanism by which a QCD dijet event can result in multiple fake π_v jets. This can occur only if the hadronization of each outgoing parton independently results in an atypical shower consisting only of neutral hadrons that leave no tracks in the ID, and which then independently travel multiple radiations lengths before showering atypically deep in the calorimeters. Since both the depth of shower development and the number of charged and neutral hadrons produced during hadronization are stochastic processes, the probability for a QCD dijet event to fake two π_v jets is expected to be roughly the square of the probability for it to fake a single π_v jet.

In the case of the signal process the reconstruction of a single π_v jet is highly correlated with the possible reconstruction of another. Nonetheless the requirement that two candidate π_v jets be

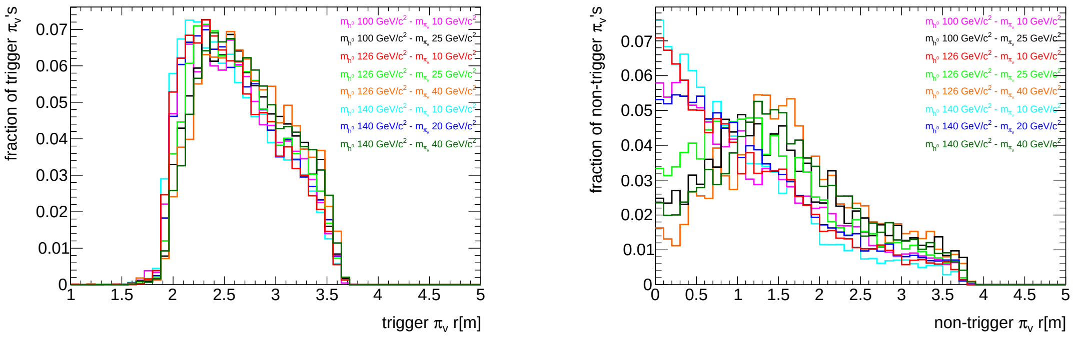

Figure 5.14: Decay length for the trigger-matched π_v (left) and for the non-trigger-matched π_v (right) in the barrel. The trigger-matched π_v mostly decays in the HCAL (from 2280 mm to 3880 mm) or near the end of the ECAL.

identified in a single event substantially reduces the acceptance of signal events; events in which one of the π_v's decays in the ID or MS will be thrown away. But because, as described above, the single-jet backgrounds are largely uncorrelated, the requirement that two candidate π_v jets be identified is a very strong discriminant against background.

In general only one of the π_v jets will cause the CalRatio trigger to fire (*trigger jet*) and the second jet may or may not have satisfied the CalRatio trigger requirements (*non-trigger jet*). Due to the rather tight selection applied by the trigger, these two jets have different kinematic properties. This section presents and describes the important properties upon which the rest of the analysis depends. Each π_v in each MC signal sample is matched to the nearest reconstructed jet in $\eta - \phi$ with ΔR(π_v,jet) < 0.2. Most figures contain kinematic distributions both for π_v's matched to the trigger jet and to the non-trigger jet separately.

Figure 5.14 shows the π_v decay position in the barrel HCal as a function of r: the trigger-matched π_v's decay at the outer radius of the ECAL and in the HCAL, while the non-trigger-matched π_v's mostly decay in the ID and the ECAL. This is a feature of the π_v lifetimes simulated in the MC signal samples; larger π_v lifetimes result in more non-trigger-matched π_v's decaying beyond the HCAL.

Figure 5.15 shows the transverse energy for the trigger jet. For each of the eight datasets, the turn-on after 60 GeV is visible. This is due to the 40-GeV jet energy requirement at the Level-1 tau-jet trigger, whose simple and coarse jet energy calculation is based on a jet cone narrower than is used offline. Additionally the jet energy calculated at Level-1 is not yet scaled from the EM to

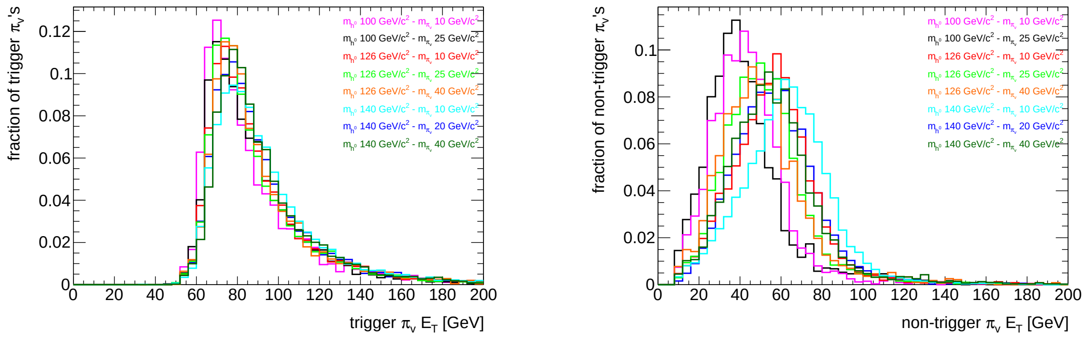

Figure 5.15: E_T for the trigger π_v (left) and non-trigger π_v (right) for the eight signal samples. The sharp turn-on in the E_T of the triggering jet is due to the L1_TAU40 trigger requirement in the CalRatio trigger. There is no trigger requirement on the second jet.

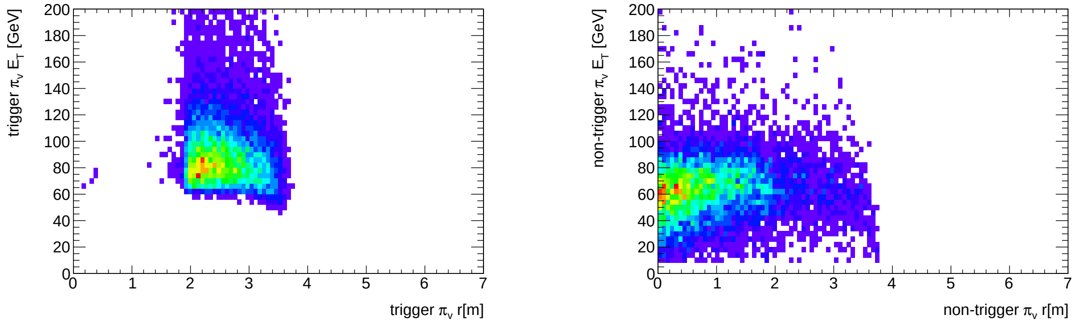

Figure 5.16: E_T for the trigger π_v (left) and non-trigger π_v (right) as a function of the π_v decay length for one of the signal samples.

the EM+JES scale (see Sections 3.3.2 and 2.8). In all plots, unless otherwise noted, the offline reconstructed jet energy is at the EM+JES scale. The transverse energy as a function of the π_v decay length is shown in Figure 5.16.

The offline $\log_{10}(E_{HAD}/E_{EM})$ distribution is shown in Figure 5.17. For the trigger-matched π_v's (left) the ratio is positive because trigger-matched π_v's decay near the outer edge of the ECAL or in the HCAL. For the non-trigger-matched π_v's (right) the ratio is negative because the majority of π_v's decay before the HCAL. Figure 5.18 shows the $\log_{10}(E_{HAD}/E_{EM})$ distribution as a function of the π_v decay length.

The isolation of each jet with respect to the ID tracks is, in addition to the $\log_{10}(E_{HAD}/E_{EM})$ cut,

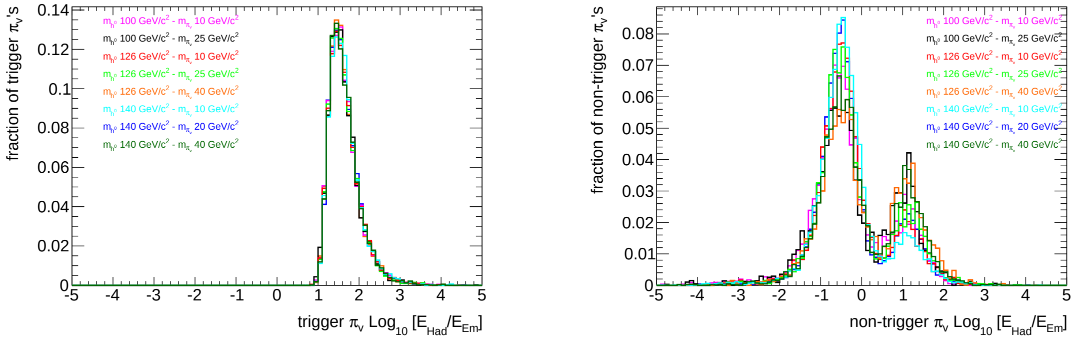

Figure 5.17: The log of the ratio of hadronic to electromagnetic energy deposition ($\log_{10}(E_{HAD}/E_{EM})$) for the trigger π_v (left) and non-trigger π_v (right) for the eight signal samples. The CalRatio trigger contains a cut on the ratio at 1.2.

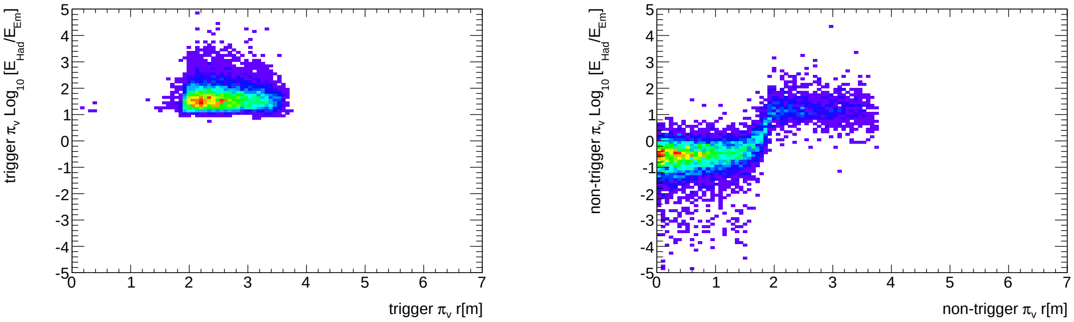

Figure 5.18: The log of the ratio of hadronic to electromagnetic energy deposition ($\log_{10}(E_{HAD}/E_{EM})$) for the trigger π_v (left) and non-trigger π_v (right) as a function of the π_v decay length for one of the data samples.

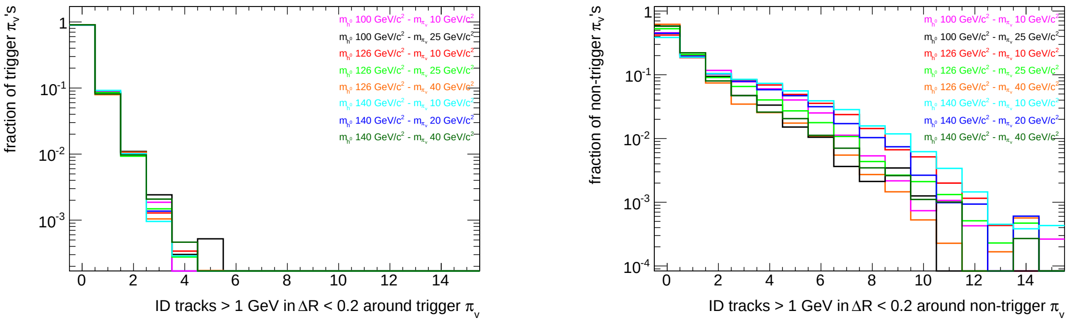

Figure 5.19: Number of ID tracks with transverse momentum greater than 1 GeV in a $\Delta R<0.2$ cone around the jet for trigger-matched π_v (left) and for non-trigger-matched π_v (right).

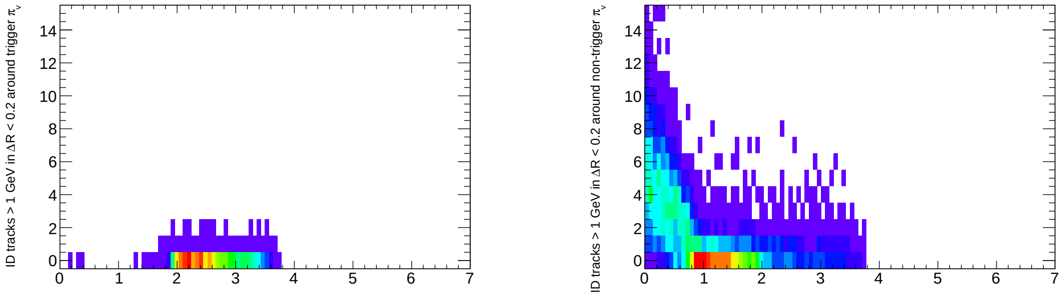

Figure 5.20: Number of ID tracks with transverse momentum greater than 1 GeV in a $\Delta R<0.2$ cone around the jet for the trigger-matched π_v (left) and for non-trigger-matched π_v (right) as a function of the π_v decay length. Red represents a large fraction of events; purple represents a small fraction of events.

another important discriminant between π_v decays in the HCAL and decays in other sub-detectors. Figure 5.19 shows the number of associated tracks for trigger-matched and non-trigger-matched jets in each of the signal samples. Due to the trigger selection, the trigger-matched jet rarely has a track associated with it. Figure 5.20 shows the multiplicity of the ID tracks with $p_T > 1$ GeV associated with the jet as a function of the associated π_v's decay length.

5.4.2 *Good Event Selection*

All data events have fired the CalRatio trigger and pass the ATLAS Good Run List (GRL) selection. Standard ATLAS selection cuts have been further applied to identify good collision events:

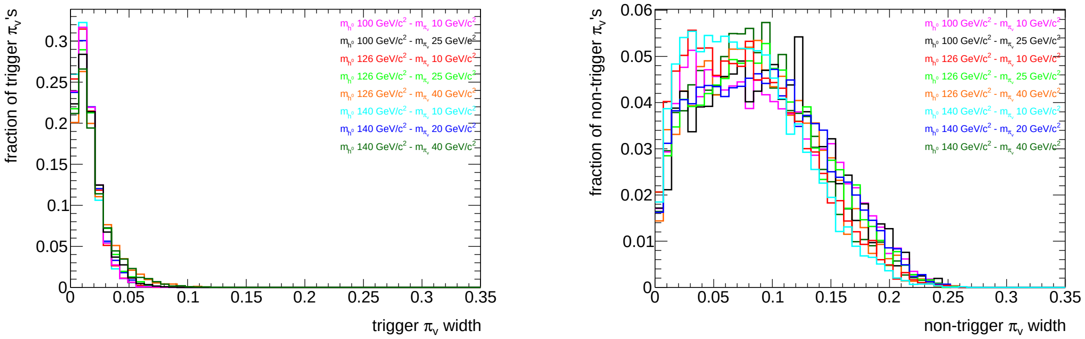

Figure 5.21: Jet width for the trigger-matched π_v (left) and for the non-trigger-matched π_v (right). The non-trigger jets include many jets resulting from π_v decays near the IP, and therefore look more similar to normal SM jets in the calorimeters.

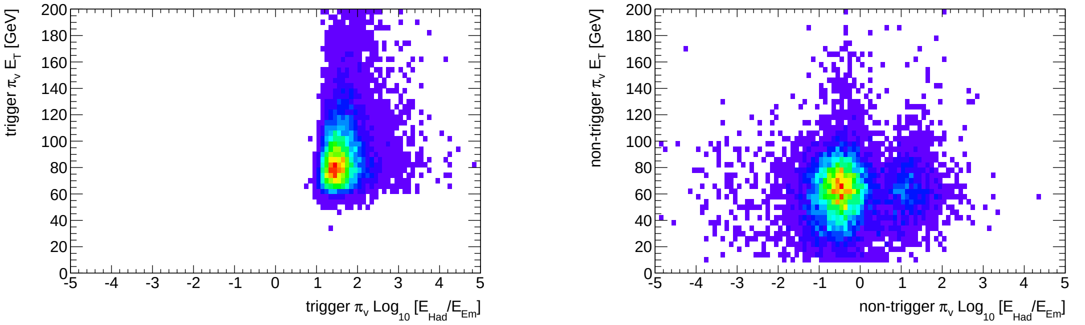

Figure 5.22: E$_T$ as a function of hadronic over electromagnetic energy ratio ($\log_{10}(E_{HAD}/E_{EM})$) for the trigger-matched π_v (left) and for the non-trigger-matched π_v (right). Red represents a large fraction of events; purple represents a small fraction of events.

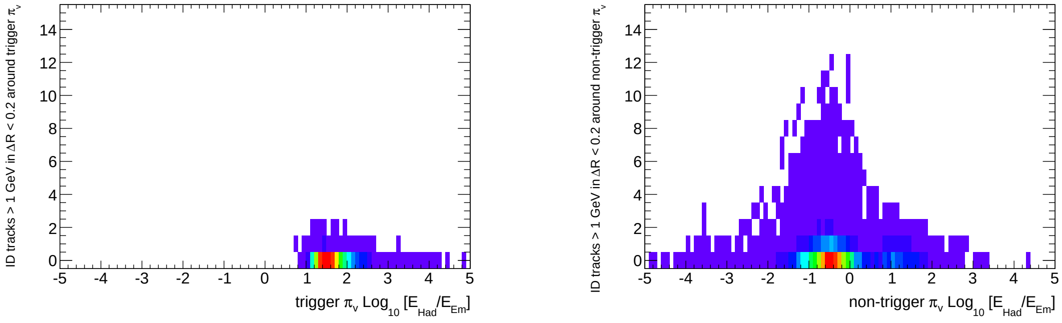

Figure 5.23: Number of ID tracks with transverse momentum higher than 1 GeV in a $\Delta R<0.2$ cone around the jet as a function of the log of the ratio of hadronic to electromagnetic energy deposition ($\log_{10}(E_{HAD}/E_{EM})$) for the trigger-matched π_v (left) and for the non-trigger-matched π_v (right). Red represents a large fraction of events; purple represents a small fraction of events.

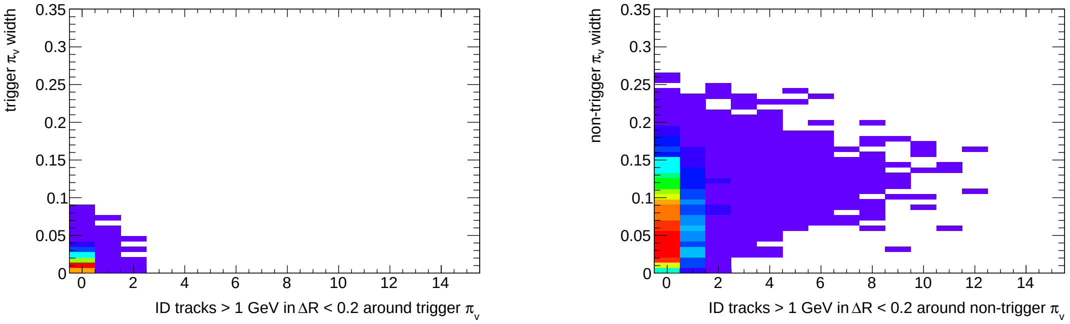

Figure 5.24: Jet width as a function of the number of ID tracks with transverse momentum higher than 1 GeV in a $\Delta R<0.2$ cone around the jet for the trigger-matched π_v (left) and for the non-trigger-matched π_v (right). Red represents a large fraction of events; purple represents a small fraction of events.

- At least 3 tracks in the Primary Vertex, each track has:
  - $p_T > 0.5$ GeV
  - Number of Pixel Hits ≥ 2
  - Number of Pixel + SCT Hits ≥ 9

The above Primary Vertex (PV) cut rejects events in which, for some reason, a hard scatter was not reconstructed. Both the GRL selection and the PV cut provide a discriminant against events in which the ATLAS detector's performance may be in question. The GRL selection addresses this concern specifically, however the GRL is not perfect and may contain rare events in which, for example, the ID is not reading out data correctly. In such cases QCD jets may be found to be trackless and therefore may fake our signal. The lack of a PV in such events is a strong indication that the event either suffers from a data quality problem or is a non-collision event mistakenly associated with the wrong bunch-crossing.

Because the PV cut does not make an η requirement on tracks associated with the PV, it is possible for an event to pass the PV cut in cases where the barrel (the central region) or the end caps (the forward region) of the ID separately suffer data quality issues at different times. In 2012 data a problem not caught by the GRL was discovered in which the barrel of the ID periodically operated at low efficiency. Therefore a cut was developed to reject such events:

- Event contains at least one track with:
  - $p_T > 0.5$ GeV
  - $|\eta| < 1$
  - Number of Pixel + SCT Hits ≥ 1

5.4.3 Clean event cuts

In addition to the good event selection described above, additional cuts must be applied in order to reject events that may contain noisy detector elements or for which there is some indication that the data may be corrupt or incomplete. Both the electromagnetic and hadronic calorimeters set flags on an event-by-event basis indicating the presence of a noise burst. Additionally event reconstruction sets a flag if the data is suspected of being corrupt or incomplete. Events for which any of these flags are thrown are rejected. Furthermore, the hadronic calorimeter was discovered to sporadically contain noisy cells that were neither caught by the standard flags or by the GRL, and so a database built after-the-fact is consulted and used to reject events containing noise bursts in the hadronic calorimeter.

5.4.4 Line of Fire cut

Events containing calorimeter activity associated with Beam Halo are removed. The event is rejected if any reconstructed jet in the event satisfies the Line Of Fire cuts described in Section 5.2.2.

5.4.5 Missing transverse energy

The p_T of all particles emerging from in a Standard Model collision event should sum to zero. In the case of Hidden Valley signal events in which both π_v's decay inside calorimeters, the p_T of all reconstructed objects should similarly sum to zero. In practice the measured E_T^{miss} is small but non-zero due to neutrinos[2] and energy mis-measurements. Nonetheless the small E_T^{miss} expected of collision events is a powerful discriminant against non-collision backgrounds such as Beam Halo, cosmic muons, and noisy or inefficient detector elements. In order to reject non-collision backgrounds we reject events that do not satisfy the cut $E_T^{miss} < 50$ GeV .

Figure 5.25 shows the E_T^{miss} at different stages of the analysis cut flow: for the full dataset; when the CaloRatio trigger is applied; and after the selection of the two offline jets (see below). The 50 GeV E_T^{miss} cut rejects approximately 10% of expected signal events (depending on the mass point) when applied after two-jet selection.

---

[2] Neutrinos can produce large E_T^{miss}, for example in W-boson decay, however such classes of events are so rare as to be irrelevant to this analysis.

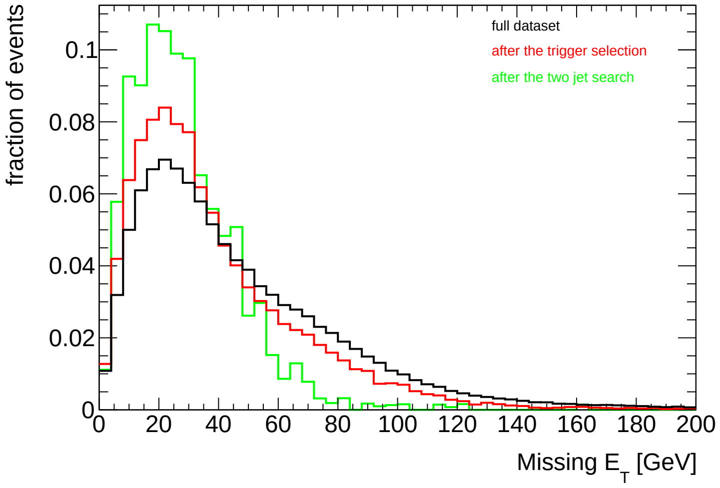

Figure 5.25: Missing transverse energy for one of the Monte Carlo samples given at different stages of the analysis cut flow.

5.4.6 Jet Selection

Quality cuts

Two π_v candidate jets are required in each event. Both jets are required to satisfy the *GoodHVMedium* criteria, which are based on the standard ATLAS jet quality criteria (described in Section 3.3.1), but with no constraint from below on the fraction of energy deposited in the ECAL (EM fraction). This slight modification is necessary in order to not reject signal jets which necessarilly have low EM fraction. A *GoodHVMedium* jet is a jet which is not *Bad* and not *Ugly*. A bad jet is likely the result of a non-collision background, while an ugly jet is located in a problematic calorimeter region and may not be well-measured. Criteria for *BadHVMedium* and *Ugly* jets are based on the following variables:

- EMf: The fraction of the jet's energy which is contained in the ECal.
- FMax: The largest fraction of energy contained in a single calorimeter layer.
- HECf: The fraction of the jet's energy which is contained in the HEC.

- LArQ: The fraction of LAr cells with a Q-factor[3] greater than 4000.
- HECQ: The fraction of HEC cells with a Q-factor greater than 4000.
- NegativeE: The total amount of negative energy[4] contained in the jet.
- Timing: The average timing[5] of all cells contained in the jet, weighted by the cell energy.
- η: The η of the jet.
- CHf: The jet charge fraction; the ratio of the sum of track p_T's associated with the jet to the calibrated jet p_T.
- TileGap3 fraction[6]: The fraction of jet energy contained in the TileGap3.
- Dead fraction: The fraction of the jet's energy that has been extrapolated into known dead cells (using the average of the surrounding cells' energies), or which is contained in cells flagged by data quality experts as problematic.

A jet is labelled *BadHVMedium* if it satisfies any of the collowing conditions:

- HECf > 0.50 and HECQ > 0.50 (HEC spikes)
- HECf $> 1-HECQ$ (HEC spikes)
- NegativeE > 60 GeV (HEC spikes)
- Timing > 10 ns (non-collision backgrounds)

---

[3] The cell Q-factor is a measure of the difference between the predicted and measured signal pulse shapes used to reconstruct the cell energy.

[4] A calorimeter cell can contribute a negative energy signal due to the application of a noise-suppression technique which shifts the zero-point energy to correspond to an average over calorimeter cells.

[5] The cell time is the time of the calorimeter signal relative to the bunch-crossing.

[6] TileGap3 is a component of the ATLAS calorimeter system which covers the transition between the barrel and endcap calorimeters. It can be seen as elements E1-E4 in Figure 2.13.

- EMf > 0.90 and LArQ > 0.80 and $|\eta| < 2.8$ (EM coherent noise)
- FMax > 0.99 and $|\eta| < 2.0$ (non-collision backgrounds)
- EMf > 0.95 and CHf < 0.05 and $|\eta| < 2.0$ (non-collision backgrounds)

A jet is flagged as "ugly" if it satisfies any of the following criteria:

- TileGap3 fraction $> 50\%$ of the total jet energy
- Dead fraction $> 50\%$ of the total jet energy.

Jets are rejected if they are either bad (BadHVMedium) or ugly.

An additional quality cut is applied to jets that is specifically designed to reject cosmic rays and other non-collision backgrounds. This cut is based on the jet timing, which is a cut already included in the above ATLAS jet quality criteria. The jet timing is the energy-weighted average calorimeter cell timing with respect to the arrival time expected for a particle emerging from the PV and travelling at the speed of light to the calorimeter cell's position. Therefore jet timings associated with collision events are expected to fluctuate about zero with a variance of a few nanoseconds (ns), while jet timings associated with non-collision backgrounds can be found anywhere within the 50 ns bunch-crossing window.

This analysis has developed a tighter cut based on an understanding of the jet timing distribution expected in our signal events, and the jet timing distribution expected in cosmic ray and QCD background events. The timing distribution of QCD background events is concentrated in the interval (-1,2) ns (see Figure 5.26), while the timing distribution of our signal events is concentrated in the interval (-1,5) ns (see Figure 5.27). As discussed in Section 5.2.2, depending on the Higgs and π_v mass difference, π_v's are sometimes slower than particles typically produced in proton-proton collisions, arriving in the calorimeter a few nanoseconds behind the expected time-of-arrival for a particle travelling at the speed of light. Because the time-of-arrival of cosmic rays is random, the timing distribution of jets in cosmic ray events is much broader than the (-1,5) ns interval required to select our signal events (this is discussed in more detail in Section 5.5.2), and therefore a cut of (-1,5) ns is applied to the jets used in this analysis.

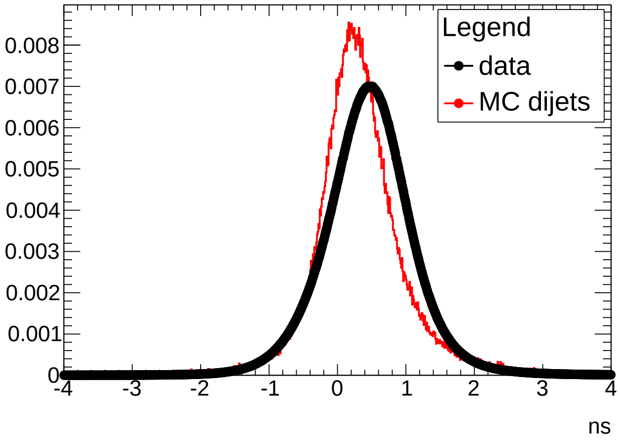

Figure 5.26: Jet timing for QCD dijet events, in units of nanoseconds. The timing distribution of QCD-enriched dijets selected in data is shown in black, and the timing distribution of the weighted QCD dijet samples is shown in red.

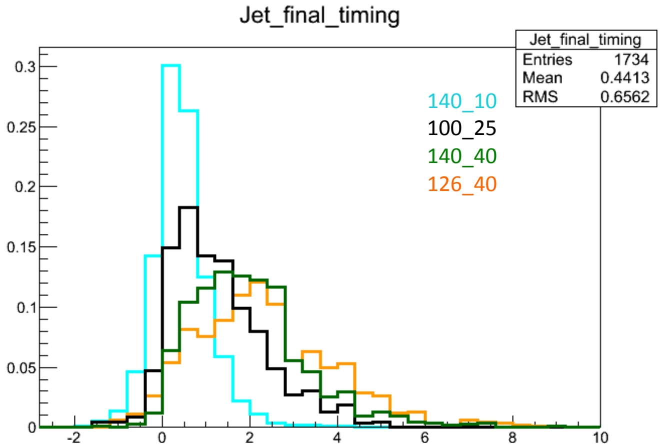

Figure 5.27: Jet timing for signal events, in units of nanoseconds. The jet timing distribution at the end of the analysis cut flow is shown for four of the signal sample mass points: (m_{h^0} , m_{π_v}) = (140,10) (blue); (100,25) (black); (140,40) green; (126,40) (orange). The samples with a larger difference between the Higgs and π_v mass feature higher π_v boosts and more typical jet timing distributions.

Analysis cuts

The following cuts on single jets have been optimized to identify π_v's decaying in the ATLAS Hadronic Calorimeter. We look for exactly two jets. The leading (highest E_T) jet in the event must be matched to the CaloRatio trigger jet. Both jets are required to pass the following cuts:

- **timing cut**: energy-weighted average cell timing in the (-1,5) ns range;
- **energy cut**: $E_T > 60$ GeV for the leading jet, $E_T > 40$ GeV for the sub-leading jet;
- **calo ratio cut**: $\log_{10}(E_{HAD}/E_{EM}) > 1.2$;
- **isolation cut**: no tracks in the ID in a $\Delta R < 0.2$ cone around the jet, with $p_T > 1.0$ GeV, Pixel hits ≥ 2, Pixel + SCT hits ≥ 9;
- **eta cut**:$|\eta| < 2.5$.

5.4.7 Pileup dependence

The MC sample generation included pile-up simulated based on reference data before the 2012 data taking period. The pileup conditions in the MC are therefore only a best-guess of the actual conditions. As a result the MC samples must be re-weighted using a standard ATLAS tool so that the average number of pileup interactions $< \mu >$ in MC is in agreement with data.

Figure 5.28 shows the unweighted and re-weighted $< \mu >$ (left) and number of good PV (right) distributions for one of the MC12 datasets (m_H = 140 GeV, m_{π_v} = 10 GeV) chosen as an example. Several variables have been found to depend on the $< \mu >$ value or, alternatively, on the number of good PV's. Figures 5.29, 5.30 and 5.31 show the trigger efficiency, reconstruction efficiency and global acceptance as a function of $< \mu >$ or of the number of PV's for the reference dataset. It is clear that the dependence of the global acceptance on pile-up conditions is mostly due to differences in the trigger efficiency. Figures 5.32 and 5.33 show the transverse energy, ID associated tracks, EM fraction, and $\log_{10}(E_{HAD}/E_{EM})$ for the candidate π_v offline trigger jet for π_v's that decay in the HCAL. While the transverse energy is found to be constant with respect to $< \mu >$, the $< \mu >$-dependence of the ID track distribution and EM fraction (and as a consequence

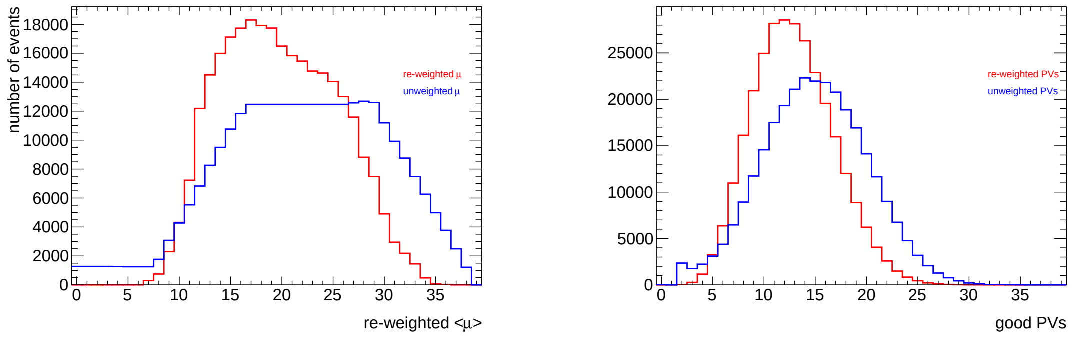

Figure 5.28: Unweighted and re-weighted distributions of the average number of pileup interactions ($< \mu >$) (left) and number of good primary vertices (right) for the m_H = 140 GeV, m_{π_v} = 40 GeV sample.

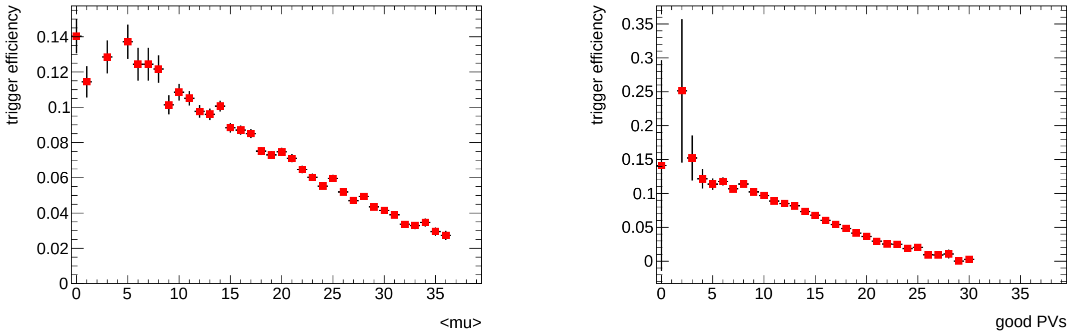

Figure 5.29: Trigger efficiency as a function of $< \mu >$ (left) and number of good primary vertices (right).

the $\log_{10}(E_{HAD}/E_{EM})$) is visible. This is also visible for the online trigger object $\log_{10}(E_{HAD}/E_{EM})$ in Figure 5.34.

5.4.8 *Cut Flow in signal Monte Carlo Samples*

Table 5.4 summarizes the cut flow applied to the 8 signal samples. Pile-up reweighting (see Section 4.3) has been applied using the standard ATLAS tool [48] and the number of events have been scaled to 20.8 fb^{-1} . More details for each dataset can be found in Appendix .1.

Starting from Table 5.4 we can estimate the trigger efficiency, the offline cut efficiency and the global acceptance of our selected final topology. Results are shown in Table 5.5. The global

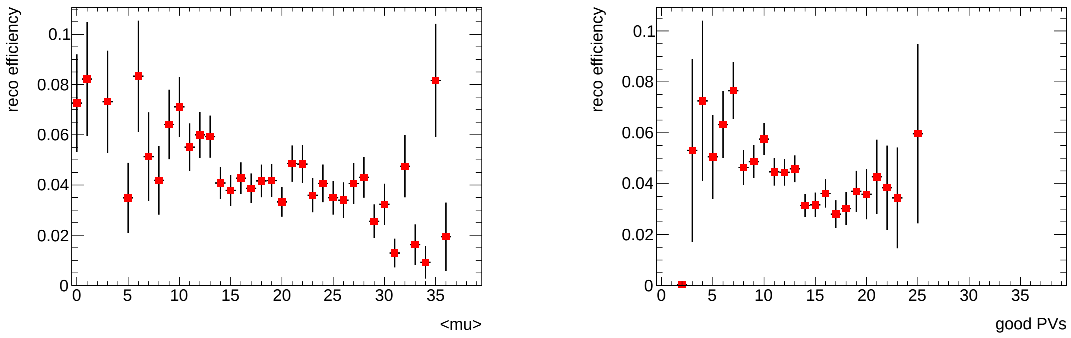

Figure 5.30: Reconstruction efficiency as a function of $< \mu >$ (left) and number of good primary vertices (right).

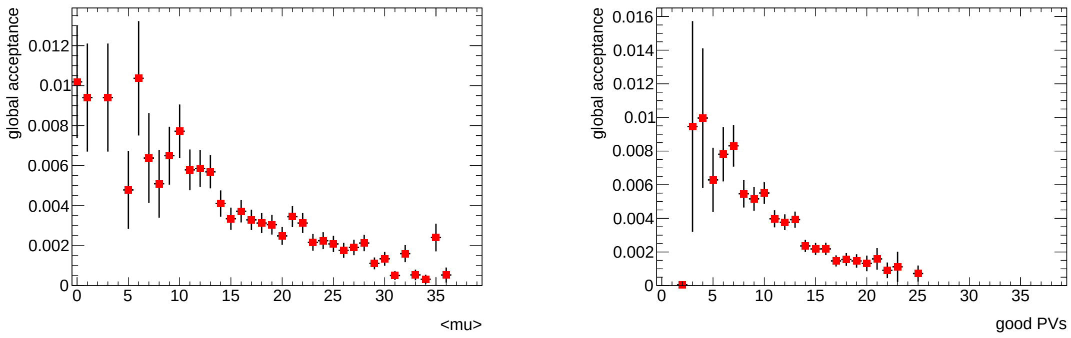

Figure 5.31: Global acceptance as a function of $< \mu >$ (left) and number of good primary vertices (right).

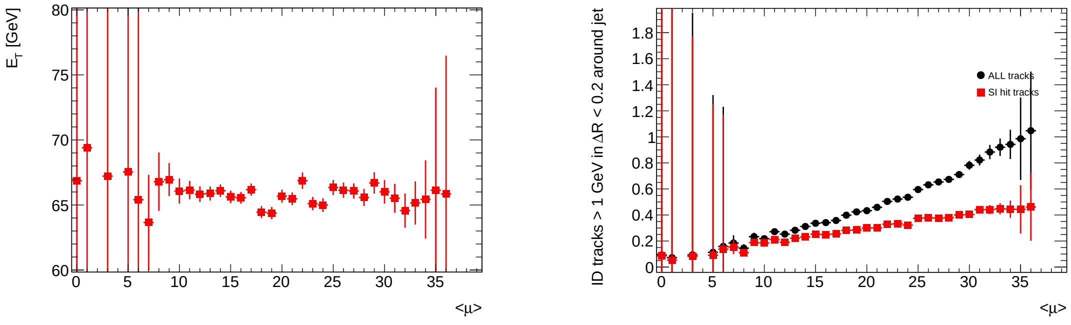

Figure 5.32: Transverse energy (left) and associated ID tracks (right) for the π_v's decaying in the HCAL as a function of $< \mu >$. Looser cuts on the quality of the ID tracks are shown in black, while the cuts used in this analysis are shown in red.

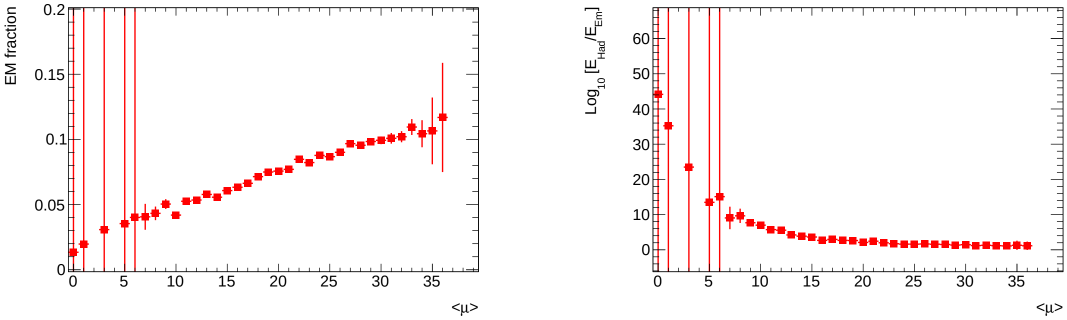

Figure 5.33: EM fraction (left) and $\log_{10}(E_{HAD}/E_{EM})$ (right) for the π_v's decaying in the HCAL as a function of $< \mu >$.

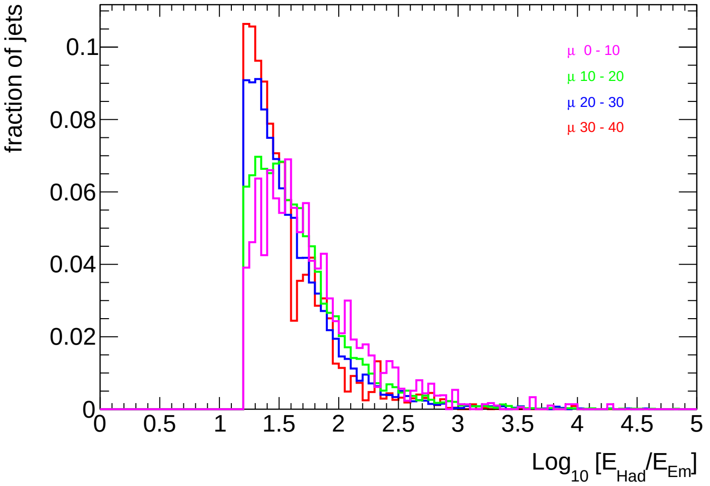

Figure 5.34: Trigger jet log ratio for the dataset m_H = 140 GeV, m_{π_v} = 10 GeV as a function of $< \mu >$.

Cut on events	Events	Events	Events	Events
	m$_H$ = 100 GeV m_{π_v} = 10 GeV	m$_H$ = 100 GeV m_{π_v} = 25 GeV	m$_H$ = 126 GeV m_{π_v} = 10 GeV	m$_H$ = 126 GeV m_{π_v} = 25 GeV
Processed Events	294697	295399	294899	299600
HV Trigger	8414	5586	15694	12339
PV	8413	5586	15692	12337
Line Of Fire	8108	5350	15050	11788
MET (< 50 GeV)	6275	4210	10895	8961
Two jet topology	296	168	671	562
→ **expected at 20.8 fb^{-1}**	697.2 ± 38.5	378.1 ± 28.3	1036.4 ± 37.4	836.3 ± 33.4
	m$_H$ = 126 GeV m_{π_v} = 40 GeV	m$_H$ = 140 GeV m_{π_v} = 10 GeV	m$_H$ = 140 GeV m_{π_v} = 20 GeV	m$_H$ = 140 GeV m_{π_v} = 40 GeV
Processed Events	299000	290599	281900	299699
HV Trigger	8999	19390	16193	13051
PV	8999	19389	16192	13049
Line Of Fire	8612	18604	15554	12490
MET (< 50 GeV)	6325	13553	11470	9162
Two jet topology	292	842	747	540
→ **expected at 20.8 fb^{-1}**	442.3 ± 24.3	1042.4 ± 34.1	986.1 ± 33.7	650.7 ± 26.6

Table 5.4: Cut flow for the eight MC samples. All numbers are scaled to the 2012 luminosity of 20.8 fb^{-1} , and pile-up re-weighting is applied.

sample	trigger eff.	reconstruction eff.	global acceptance
m_H = 100 GeV, m_{π_v} = 10 GeV	3.16 ± 0.03	3.52 ± 0.19	0.11 ± 0.01
m_H = 100 GeV, m_{π_v} = 25 GeV	2.09 ± 0.03	2.88 ± 0.21	0.06 ± 0.01
m_H = 126 GeV, m_{π_v} = 10 GeV	5.93 ± 0.04	4.37 ± 0.15	0.26 ± 0.01
m_H = 126 GeV, m_{π_v} = 25 GeV	4.54 ± 0.04	4.61 ± 0.18	0.21 ± 0.01
m_H = 126 GeV, m_{π_v} = 40 GeV	3.33 ± 0.03	3.32 ± 0.18	0.11 ± 0.01
m_H = 140 GeV, m_{π_v} = 10 GeV	7.35 ± 0.05	4.36 ± 0.14	0.32 ± 0.01
m_H = 140 GeV, m_{π_v} = 20 GeV	6.36 ± 0.05	4.77 ± 0.16	0.30 ± 0.01
m_H = 140 GeV, m_{π_v} = 40 GeV	4.85 ± 0.04	4.13 ± 0.17	0.20 ± 0.01

Table 5.5: Trigger, reconstruction and global efficiency (%) for the eight datasets.

efficiency has also been evaluated for a range of π_v proper lifetimes from 0 to 10 m, as shown in Figure 5.35.

- Trigger efficiency, defined as the number of events passing the CalRatio trigger divided by the total number of events;

- Offline cut efficiency, defined as the number of events with the two jet topology divided by the number of events passing our trigger;

- Global acceptance, defined as the number of events with the two jet topology divided by the total number of events (trigger efficiency multiplied by the offline cut efficiency).

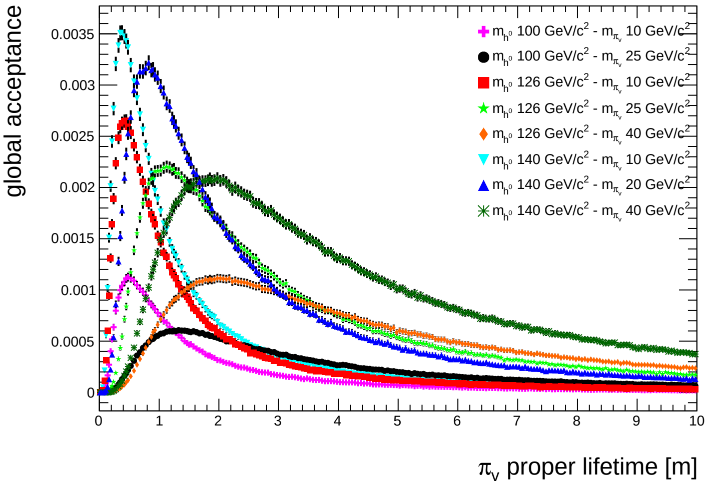

Figure 5.35: Global acceptance as a function of different π_v proper lifetimes for the eight MC samples.

5.5 Backgrounds

5.5.1 The QCD background Estimation

Jets produced from QCD physics contain some fraction of neutral and charged particles resulting from the hadronization of the outgoing quark or gluon. Rarely, the hadronization may result in a QCD jet consisting only of neutral hadrons. Such a Standard Model jet can be trackless and can deposit most of its energy in the hadronic calorimeter; it can fake the experimental signature of the jets in the signal sample. This signature can also be faked by Standard Model jets that pass through crack regions of the detector and/or for which there is a failure to properly reconstruct inner detector tracks and energy deposits in the electromagnetic calorimeter. The rare coincidence of two such neutral Standard Model jets represents a possible background to this analysis that is estimated in this section.

The strategy for estimating this background is to derive the probability of a single neutral QCD jet passing the analysis cuts, as a function of jet p_T and η. This is done using a tag-and-probe method on a large QCD data sample. For each N-jet event in the analysis data sample (see Section 5.3), we calculate the joint probability that the event contains two neutral QCD jets such that the event as a whole passes the analysis cuts. This probability is used to weight each event which is then summed for the whole sample to determine the background.

The Calculation of the Single-Jet Probabilities

The analysis cut flow (Section 5.4) requires that each of the two jets pass slightly different analysis cuts. The leading jet must satisfy the CalRatio trigger and a 60 GeV p_T cut; the subleading jet may or may not satisfy the CalRatio trigger, but must satisfy the less stringent 40 GeV p_T cut. Therefore two probabilities must be determined as a function of jet p_T and η: the probability for a QCD jet to pass the trigger and the offline analysis cuts, and the probability for a QCD jet to pass or not pass the trigger and satisfy the (looser) offline analysis cuts. The first probability is called ‘P’ and the second probability is called ‘Q’.

A tag-and-probe method is used to calculate P and Q on data periods A-L. In order to select an un-biased QCD sample in data, events were selected using the single-jet triggers EF_j15 through EF_j460. The analysis cut flow was applied to the events, except for the jet selection cuts. The

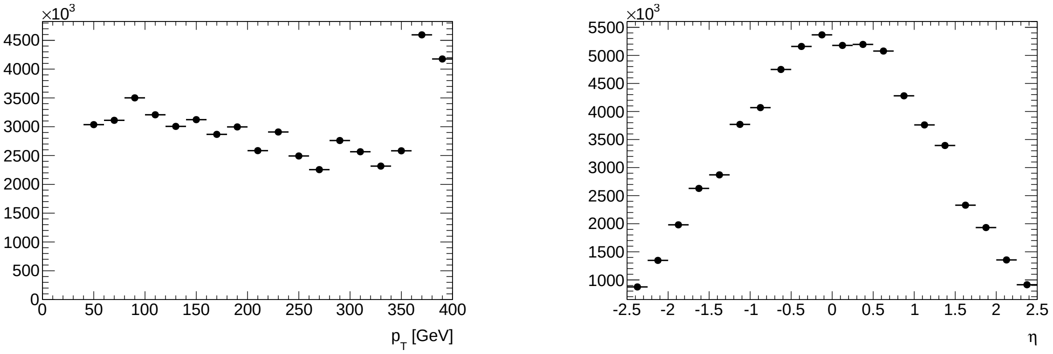

Figure 5.36: Probe jet p_T (left) and η (right) before multiplying by the prescale factor. The probe jet p_T distribution fluctuates up and down due to the trigger turn-ons.

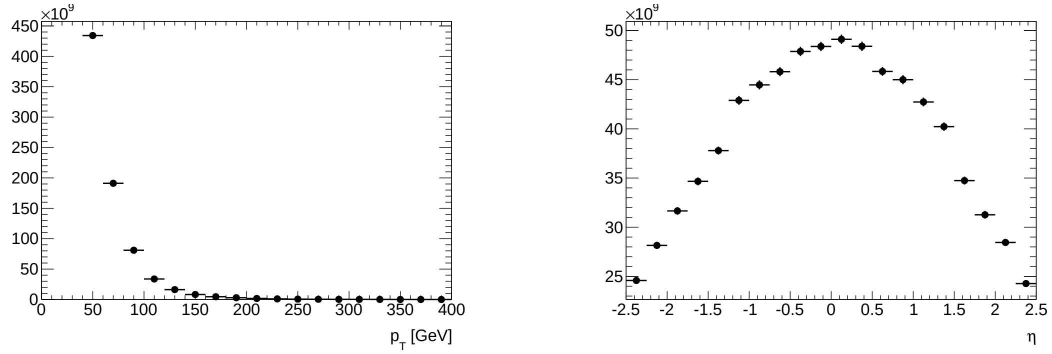

Figure 5.37: Probe jet p_T (left) and η (right) after multiplying by the prescale factor.

leading jet in each event was identified as the 'tag' jet, and the sub-leading jet identified as the 'probe' jet. Both tag and probe jets were required to satisfy $\Delta\phi(tag jet, probe jet) > 2.0$, $p_T > 40$ GeV, and the GoodHVMedium quality jet criteria. The p_T and η distribution of the probe jets before and after multiplying by the prescale factor can be seen in Figures 5.36 and 5.37, representing, respectively, the probe jet distributions in data selected using the prescaled single-jet triggers, and the probe jet distributions that would be expected if the triggers were unprescaled.

P can then be calculated (as a function of jet p_T and η) as the number of probe jets that satisfy the CalRatio trigger and pass the offline analysis cuts, divided by the the total number of probe jets considered, and Q can similarly be calculated as the number of probe jets passing the (looser) offline analysis cuts divided by the total number of probe jets considered.

One might assume that the choice of the probe jet as the subleading jet is arbitrary, and that therefore the leading jet can, in turn, also be taken as the probe jet in the above prescription, thus doubling the statistics used to calculate P and Q. It turns out that this is not true, a fact that will be discussed in Section 5.5.1.

There are not enough statistics to calculate P and Q as a function of both p_T and η directly; P and Q are each derived as a function of p_T (averaging over jet η), and also as a function of η (averaging over jet p_T). The assumption that p_T and η are uncorrelated (the associated systematic uncertainty is calculated in Section 5.5.1) leads to Equation 5.1 (derived in Appendix .2.4).

$$\begin{aligned} P(p_T,\eta) &= P(p_T)P(\eta)/<P> \\ Q(p_T,\eta) &= Q(p_T)Q(\eta)/<Q> \end{aligned} \tag{5.1}$$

The $<P>$ and $P(\eta)$ derived on the data selected using prescaled triggers is biased by the artificially flattened probe jet p_T distribition (Figure 5.36), whereas $P(p_T)$ is not biased because it is a function of jet p_T. This results in an overall scaling of $<P>$ and $P(\eta)$ that is the same in both the numerator and the denominator, thus cancelling out, as long as we take care to define $<P>\equiv<P(\eta)>$. When calculating $<P(\eta)>$, a weighted average is taken with respect to the η distribution of jets expected in data before prescale (Figure 5.37), in order to ensure that, apart from the above-mentioned scale factor, $<P>$ reflects the expected average of P in unprescaled data. What is said of P in the above paragraph is also true of Q.

Figures 5.38 and 5.39 show P and Q as a function of p_T and as a function of η. The distribution of P as a function of p_T "turns on" near $p_T = 60$ GeV due to the CalRatio trigger requirement and then "falls off" as the rise in p_T makes the isolation requirement less likely to be met. The distribution of Q as a function of p_T has no turn-on due to the lack of a trigger requirement on the jet, however it has the same fall-off as jet p_T rises. Both P and Q as a function of p_T are fitted to Landau distributions (Figure 5.40). In order to get a better Landau fit, the fit for P as a function of jet p_T was extended below the offline cut of 60 GeV.

In order to calculate the statistical error in the final result that is due to P and Q, the error on each of the fitted Landau distribution parameters is used to derive two conservative envelope functions for both P and Q (Figure 5.40), each of which is used in the calculation of a final result. The statistical

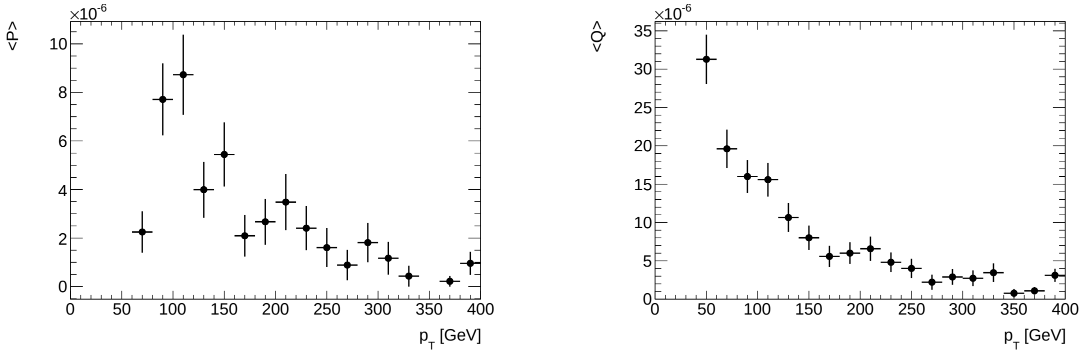

Figure 5.38: P (left) and Q (right) are plotted as a function of jet p_T.

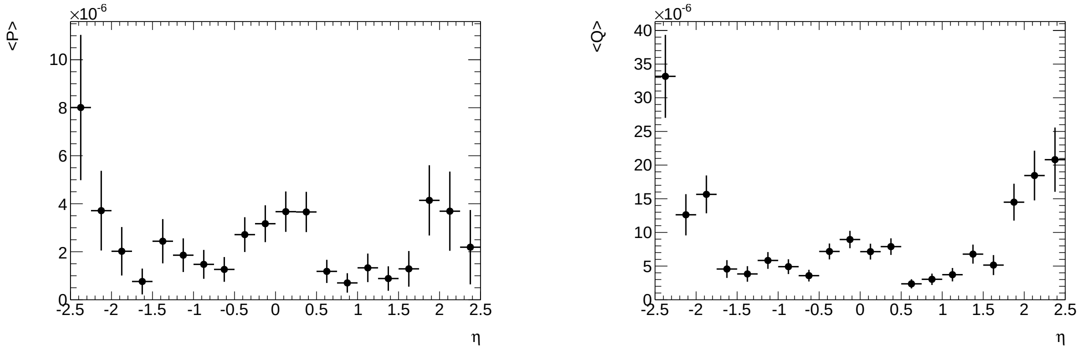

Figure 5.39: P (left) and Q (right) are plotted as a function of jet η.

error due to the fit is calculated as half the maximum change in the final result when different combinations of envelope functions are used. Because the distribution in η is largely a function of detector geometry no fit is made, and statistical errors are propagated based on the 1-σ statistical errors in the plots shown.

Leading vs Subleading jet probabilities

While the probability functions P and Q depend on both jet p_T and η, they have additionally been found to depend on whether the jet considered is the leading or the subleading jet in the event. By studying the truth information in Monte Carlo QCD dijet samples the origin of this discrepancy was discovered: the probabilities P and Q depend on the type of parton that initiates the jet. In the jet p_T range (40-80 GeV) containing the majority of jets contributing to the QCD background, the

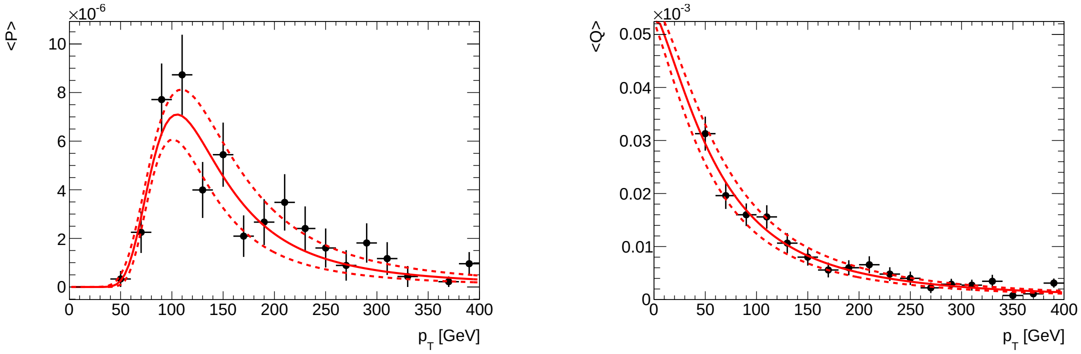

Figure 5.40: P (left) and Q (right) are plotted as a function of jet p_T and fit to a Landau distribution. P is allowed to extend below the offline cut of 60 GeV in order to include more data points in the fit. Errors on the fit parameters are used to derive two envelope Landau functions (dotted lines).

fraction of QCD dijets is roughly $\sim$ 10% $q\bar{q}$, $\sim$40% qg, and $\sim$ 50% gg. Quark jets are generally narrower than gluon jets and have fewer tracks, and are found to result in jets that are both more likely to be trackless as well as more likely to have a lower EM-fraction, as compared to gluon jets. Quark jets, in other words, have a higher average P and Q than gluon jets. Furthermore, due to their narrowness, quark jets are more likely than gluon jets to be reconstructed as the leading jet in a QCD dijet event, because more of their energy is likely to be contained inside the jet cone. Therefore the subpopulation of qg QCD dijets result in leading jets having a higher average P and Q compared to subleading jets. Therefore P and Q are measured separately for leading and subleading jets: in one case the leading jet is taken as the probe jet, and in the other case the subleading jet is taken as the probe jet. The P and Q probabilities therefore ultimately depend not only on jet p_T and η, but also on which jet in the event is considered. Figure 5.41 shows P and Q as a function of jet p_T for both leading and subleading jets separately.

N-jet combinatorics

Given a QCD event with N jets (N_j, defined as the number of jets passing the cuts that P and Q are defined with respect to), and probability functions P(j_x) and Q(j_x) each depending on the characteristics of a jet (such as p_T and η) indexed by 'j_x', we can calculate the probability (Equation 5.2, derived in Appendix .2.1) for the event to pass the analysis cuts which require exactly two jets:

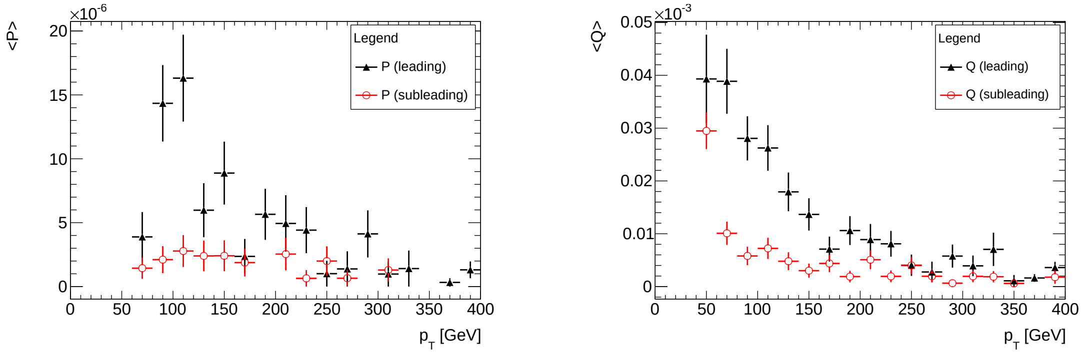

Figure 5.41: P (left) and Q (right) are plotted as a function of jet p_T for leading (black) and subleading (red) jets separately.

one jet to satisfy P's selection criteria and a second jet to satisfy Q's selection critera.

$$Prob(N_j) = \sum_{m=1}^{N_j} \sum_{n=m+1}^{N_j} [P(j_m)Q(j_n) + P(j_n)Q(j_m) - P(j_m)P(j_n)] \prod_{\substack{k=1\\ k\neq n\\ k\neq m}}^{N_j} (1 - Q(j_k)) \tag{5.2}$$

Equation 5.2 expresses the likelihood of a given QCD event, containing N_j jets with $p_T > 40$ GeV and $|\eta| < 2.5$, to pass the analysis cuts. Therefore the QCD background prediction is given by Equation 5.3.

$$N_{QCD} = \sum_{\text{Each event passing EF\_j15}} Prob(N_j) \times Prescale \tag{5.3}$$

Equation 5.3 represents the weighted sum of each event in the data sample, each event weighted by its probability of passing the analysis cuts, and by the prescale of the trigger used to select the event. This gives the number of events predicted to both pass the analysis cuts and be expected to be selected by an unprescaled trigger, because the prescale factor represents the number of events that would be selected by the trigger but have been rejected by the prescale. Since the CalRatio trigger is unprescaled, Equation 5.3 therefore represents the number of QCD events expected both to pass our analysis cuts and to be selected by the CalRatio trigger. An alternative equivalent form of Equation 5.3 is given in Appendix .2.3.

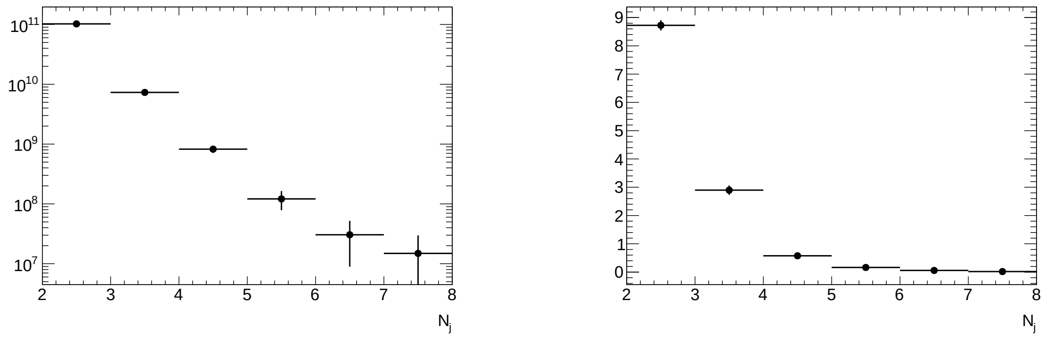

Figure 5.42: The number of predicted QCD events per N_j bin (left), and the predicted QCD background per N_j bin (right). The errors shown are those associated with $\sqrt{N}$ statistics. The EF_j15 trigger was used to select events.

Results

The application of Equation 5.3 to the full 2012 20.8 fb^{-1} data sample of data yields a predicted QCD background of 12.44 events. There are three associated statistical uncertainties. The dominant statistical uncertainty is due to the statistical error in the calculation of P and Q. The statistical error associated with P(p_T) and Q(p_T) is determined to be 6.28 events. This statistical error is based on the error on the fit of the data to Landau distributions. This error is used to derive the envelope functions shown in Figure 5.40. The statistical error due to the fit is calculated as half the maximum change in the final result when different combinations of envelope functions are used. The statistical error associated with P(η) and Q(η) is determined to be 0.43 events. The statistical error is based on the statistical errors shown in Figure 5.39. A Monte-Carlo procedure is used to calculate the predicted QCD background over many trials in which the value at each bin in Figure 5.39 is varied randomly according to normal distributions with width equal to each bin's corresponding error bands. Finally the statistical error associated with the number of predicted events in each N_j bin (selected using the EF_j15 trigger) is determined to be 0.16 events.

After the statistical errors and the systematic errors (see Section 5.5.1) are separately added in quadrature the final QCD background prediction is 12.44 ± 6.30 (stat) ± 0.90 (syst).

The number of predicted events in each N_j bin (selected using the EF_j15 trigger), and the predicted QCD background per N_j bin is given in Figure 5.42.

Cross-checks

The combinatoric procedure described in Section 5.5.1 may not be transparent. We can perform an order-of-magnitude cross-check by measuring the average values of P and Q. This must be a weighted-average to reflect the distribution of jet p_T's expected in data before the prescales are applied. This weighting is thus with respect to the probe jet p_T distribution measured in the QCD dijet sample with each event weighted by the prescale of the trigger used to select the event. We can then estimate the QCD background contribution from 2-jet events on 20.8 fb^{-1} of data by multiplying the probability for one jet to satisfy the P criteria by the probability for a second jet to satisfy the Q criteria, times the number of expected 2-jet events in the data sample:

$$\begin{aligned} N_{QCD}^{2\,jets} &= \quad <P> \times <Q> \times N_{EVT}^{2\,jets} \\ &= (1.92 \times 10^{-6}) \times (2.51 \times 10^{-5}) \times (1.02 \times 10^{11}) = 4.92 \end{aligned} \tag{5.4}$$

The fact that this result is lower than the final QCD background prediction is expected; the full combinatoric formula for the 2-jet probability given in Appendix .2.1 is nearly twice $<P> \times <Q>$, since there are two possible combinations of jets that satisfy the analysis cuts. Furthermore in the above example we have neglected the smaller contribution from events with more than 2 jets above 40 GeV. If we use the full combinatoric formula for the 2-jet probability, the result becomes:

$$N_{QCD}^{2\,jets} = (2\times <P> \times <Q> - <P> \times <P>) \times N_{EVT}^{2\,jets} = 9.47 \tag{5.5}$$

The 3-jet and 4-jet terms add 2.03 and 0.46 events, respectively. Summing the terms up to $N_j = 7$, this cross-check predicts a total QCD background of 12.15 events, a result within 2% of the final result.

Another cross-check on the estimate of the number of events per N_j bin was done by using the independent datasets selected using the EF_j25, EF_j35 and EF_j55 triggers. The number of predicted events in each N_j bin for each of these triggers is given in Figures 5.43, 5.44, and 5.45. The p_T thresholds of the triggers EF_j15, EF_j25, EF_j35, are all sufficiently below the 40 GeV cut in the N_j definition that they are expected to yield consistent estimates of the number of events per N_j bin. A comparison of each of the three results is shown in Figure 5.46.

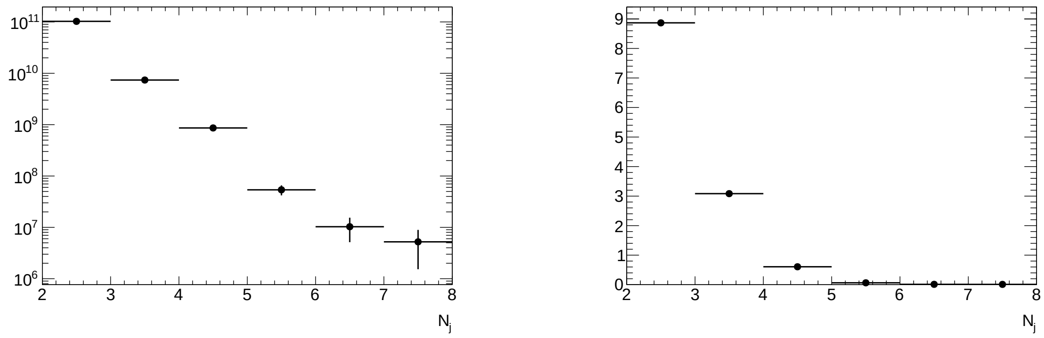

Figure 5.43: The number of predicted QCD events per N_j bin (left), and the predicted QCD background per N_j bin (right). The errors shown are those associated with $\sqrt{N}$ statistics. The EF_j25 trigger was used to select events.

The p_T thresholds of the triggers EF_j15, EF_j25, EF_j35 and EF_j55, are all sufficiently below the 60 GeV cut on the leading jet that is used in this analysis. Consequently the final result is expected to be consistent across each of these independent datasets. The predicted QCD background per N_j bin for each of the triggers is given in Figures 5.43, 5.44, and 5.45. A comparison of each of the four results is shown in Figure 5.46. Final results from each independent dataset are found to disagree with one another by less than 0.1 events. This provides not only a cross-check on the number of events per N_j bin and on the extraction of the trigger prescales, but also a cross-check on the jet p_T and η distributions that are sampled by the P and Q functions in Equation 5.2. A comparison of the results for each trigger are shown in Figure 5.46.

The QCD background prediction using Equation 5.1 is expected to be well approximated by averaging over jet η due to the relative flatness of $P(\eta)$ and $Q(\eta)$, Figure 5.39, in the region near $\eta = 0$ that is most strongly sampled by jets in data, Figure 5.37. The final result calculated using Equation 5.1 was found to differ from the result calculated using only the η-averaged $P(p_T)$ and $Q(p_T)$ by less than 2%.

Another cross-check relies on the expectation that events selected by our CalRatio trigger (but to which the full set of analysis cuts are not applied) are dominated by QCD background. An estimate of this background was calculated using the probability P derived in this section. The same procedure was used as in the QCD background calculation, but only a single jet probability was

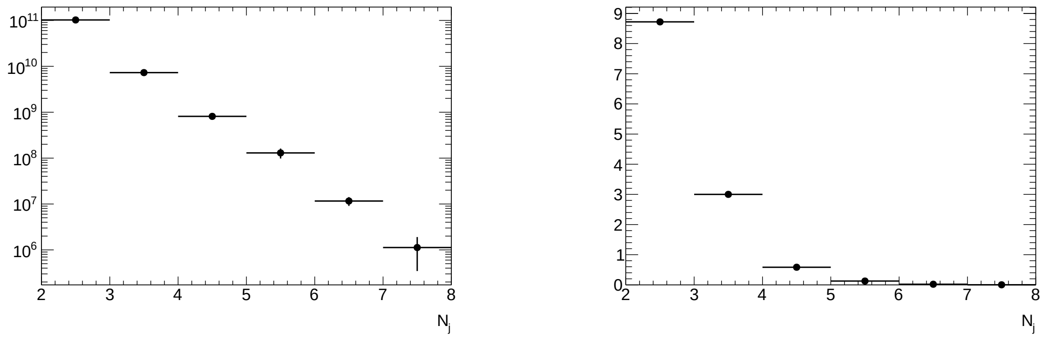

Figure 5.44: The number of predicted QCD events per N_j bin (left), and the predicted QCD background per N_j bin (right). The errors shown are those associated with $\sqrt{N}$ statistics. The EF_j35 trigger was used to select events.

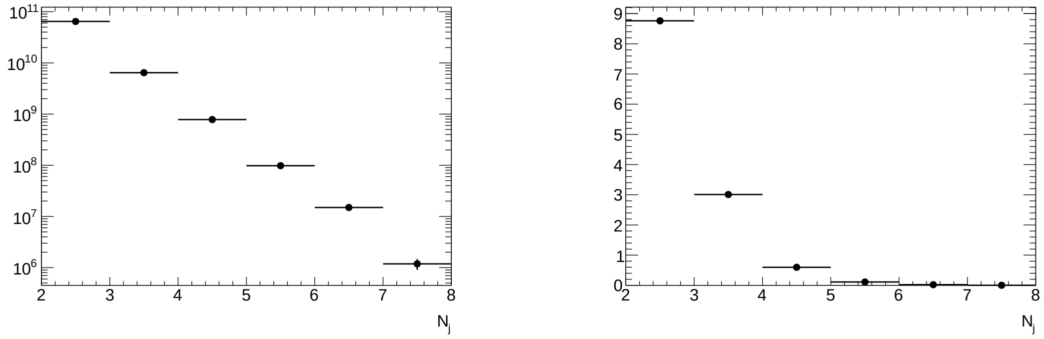

Figure 5.45: The number of predicted QCD events per N_j bin (left), and the predicted QCD background per N_j bin (right). The errors shown are those associated with $\sqrt{N}$ statistics. The EF_j55 trigger was used to select events.

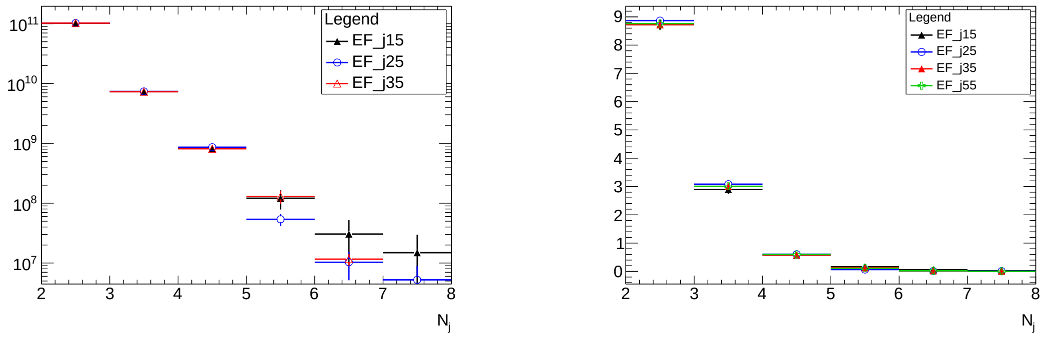

Figure 5.46: The number of predicted QCD events per N_j bin (left), and the predicted QCD background per N_j bin (right). The errors shown are those associated with $\sqrt{N}$ statistics. Results for events selected using different triggers are compared.

applied to each event. 828344 events in data were found to contain a single jet passing the trigger and offline analysis cuts, while 779300 ± 216100 events were predicted.

As a further cross-check of the QCD background calculation, the weighted average probability $< Q >$ was multiplied by the number of events in data found to contain a single jet passing the CalRatio trigger and offline cuts and for which a second jet with $p_T > 40$ GeV was found in the event. The result is $557610 \times 2.51 \times 10^{-5} = 14.00$ events. This is a rough cross-check that only uses the average Q and does not account for the p_T or η of the second jet in the event, whether it is the leading or subleading jet, or whether there are more the two jets in the event.

Systematic Uncertainties

Jet p_T and η are assumed to be uncorrelated in order to express P(p_T,η) as a function of P(p_T) and P(η) (Equation 5.1), and similarly for Q. Jet p_T and η are in fact slightly correlated. The systematic uncertainty associated with this assumption was determined by measuring, on the tag-and-probe QCD dijet sample, the maximum variation in average jet p_T as η was varied and the maximum variation in the average jet η as p_T was varied. The maximum variation in average jet p_T and η were each 2%. The systematic uncertainty was calculated by shifting the jet p_T or η upwards and downwards by 2% in the P and Q functions, and taking half the difference between the maximum change in the final result. The systematic error is calculated to be 6%, or 0.75 events (Table 5.6).

The selection of the QCD dijet sample that is used to calculate P and Q includes a $\Delta\phi > 2.0$ cut between the leading and the subleading jet. Since this cut is not included in the analysis cuts, the assumption that it does not bias the results leads to a systematic uncertainty. Although the $\Delta\phi$ cut is not expected to bias the results (there is no reason why P and Q would depend on this variable except for jets very close together), the systematic uncertainty was conservatively calculated by re-deriving the P and Q functions without the cut applied, and taking the difference between the final results based on P and Q functions with and without the cut applied. The systematic error is calculated to be 4%, or 0.50 events (Table 5.6).

The cosmic ray background (Section 5.5.2) is a possible source of contamination of the P and Q functions. A rough upper bound can be put on the cosmic contamination by comparing the number of expected cosmic ray background events in which one jet would satisfy the P criteria (in the presence of a second jet with $p_T > 40$ GeV, as required by the dijet tag-and-probe procedure) while passing one of the prescaled single-jet triggers used to select the QCD diject events, to the number of events satisfying the P criteria that is measured on data. The number of expected cosmic ray events satisfying the Q criteria cannot be determined using the cosmic background procedure, because each selected event contains a jet satisfying the CalRatio trigger, thus biasing any attempt to derive Q, for which no such requirement is made. The p_T distribution of jets in the cosmic ray events (see Section 5.5.2), however, provides an indication that the relative cosmic contamination of Q is likely to be less than the relative contamination of P. The cosmic background procedure (Section 5.5.2) predicts that fewer than ten events in data contain both a single jet passing the P criteria and a second jet with $p_T > 40$ GeV. Due to the very high prescale ($\sim$1000) of the single jet triggers in the cosmic jet p_T range the cosmic contamination of the samples used to calculate P (and therefore Q) is determined to be negligable.

The presence of some unaccounted-for background in the QCD tag-and-probe sample (such as cosmics, or a malfunction in the electromagnetic calorimeter) could take the form of a subsample of events in which there is a correlation between one jet passing the P or Q criteria, and a second jet passing the P or Q criteria. The QCD tag-and-probe sample contains zero events in which multiple jets simultaneously pass either the Q or P criteria. Therefore there is currently no evidence of any correlation between jets in the QCD tag-and-probe sample. If no correlation is present we expect 0.003 events in which both jets pass the Q criteria, and 0.001 events in which one jet passes the Q criteria and another jet passes the P criteria.

The presence of the signal in data would contaminate the P and Q functions. A rough upper bound can be put on the signal contamination by comparing the maximum number of signal events predicted in which one jet would satisfy the P or Q criteria and pass one of the prescaled single-jet triggers used to select the QCD diject events, to the number of events satisfying the P or Q criteria that is measured on data. Table 5.4 shows that at most $\sim$1000 signal events are predicted in 20.8 fb^{-1} of data, and Figure 73 shows the p_T distribution of the jets in those events that pass the cut flow. The prescale on the single jet triggers covering the full distribution of jet p_T's is always over 1000, and therefore the expected signal contamination is less than a single event, and so will be assumed negligible. It should be noted that if signal contamination were present, it would serve to inflate our background estimate and therefore decrease our sensitivity rather than increase it.

The strategy for calculating the QCD Background is based on the assumption that the neutrality of one Standard Model jet in an event does not influence the likelihood for another Standard Model jet in the same event to be neutral. The justification of this assumption is that the fragmentation and hadronization of each jet into a distribution of hadron varieties is assumed to be an independent random process. As discussed in the above sub-section “Leading vs Subleading jet probabilities,” quark- and gluon-intiated jets have different probabilities of being neutral. The presence of qq, qg, and gg sub-populations of QCD dijets represents a potential correlation, and therefore a systematic uncertainty, that is still being investigated.

Origin	Systematic Error
Correlation of p_T and η	0.75
$\Delta\phi$ cut	0.50
Cosmic contamination	0.0
Signal contamination	0.0

Table 5.6: Systematic errors (absolute) in the QCD background estimate for the 20.8 fb^{-1} data range.

5.5.2 Cosmic Ray Background Estimation

Cosmic ray muons in ATLAS come mostly from the skyward direction, and arrive mainly from the two large access shafts (see Figure 5.47), though high-enough energy muons (above a few hundred GeV) can easily traverse hundreds of meters of earth and so can arrive at ATLAS from almost any skyward direction.

Cosmic ray muons interact with the detector as minimum-ionizing particles, most losing only a few GeV of energy even when traversing the entirety of the ATLAS detector. However muons can lose energy in other ways, for example through bremsstrahlung, the production of electron positron pairs, and photoproduction, especially at high energy. The muon energy loss in matter follows a Landau distribution, and therefore rarely high-energy muons will deposit a significant amount of energy. Energy deposition in the calorimeter from a muon will typically lead to an imbalance in

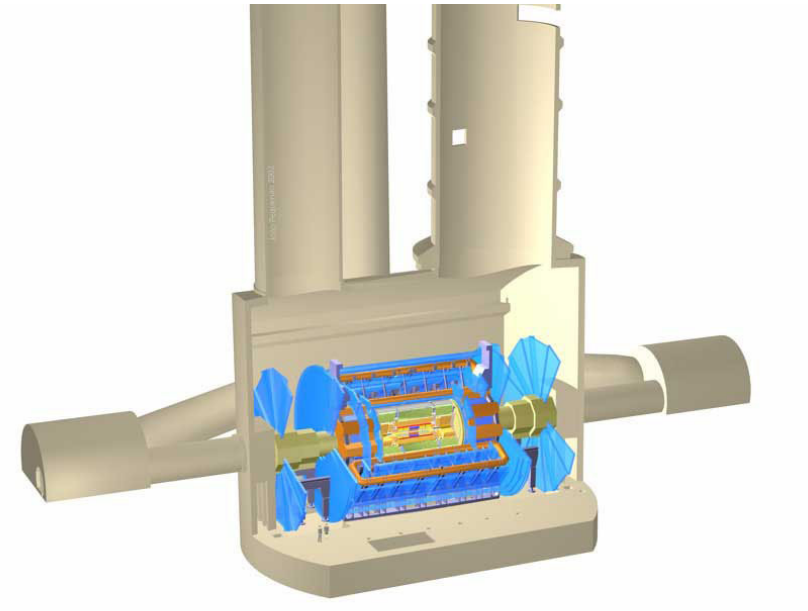

Figure 5.47: ATLAS geometry. Cosmic ray muons are expected to arrive through the two large access shafts.

the tranverse energy in the event, which is one reason why the analysis cut flow includes a cut on E_T^{miss}. Such events must be rejected because they can fake our signal events; the energy deposits left by cosmic ray muons can be reconstructed as jets. If a muon passes through the detector far enough from the IP that it fails to produce an ID track and at the same time results in multiple energy depositis in different sections of the hadronic calorimeter, then multiple trackless jets are produced with high $\log_{10}(E_{HAD}/E_{EM})$. This scenario represents a class of background events whose contribution to the number of events collected in data must be estimated.

A detailed analysis of the properties of the events generated by cosmic ray muons is reported in this section, along with a discussion of cuts used to suppress this background in the analysis.

Bunch structure at the LHC and empty bunch crossings in ATLAS

The LHC bunch structure (see Section 2.1.3) is important to this analysis because it includes intervals in which no collisions take place in the ATLAS detector. Such collision-less intervals provide an ideal environment for the study of non-collision backgrounds such as cosmic ray events.

The LHC beam is subdivided into 35640 RF-buckets of which nominally every tenth can contain a bunch (see Section 2.1.3). The nominal LHC configuration for proton-proton collisions contains 3564 bunch-crossings per revolution, each of which is given a unique bunch-crossing identifier (BCID) corresponding to the 25 ns interval in which a proton-bunch might be contained. Not all BCIDs are filled with proton bunches: nominally 2808 of the 3564 bunch-crossings are filled. In 2012 data taking the LHC operated with larger 50 ns bunch spacings, resulting in 1380 possible filled bunches per beam.

Three categories of bunch crossings are relevant for this analysis:

- Paired: a bunch in each beam is filled with protons
- Unpaired Isolated: a proton bunch is in only one LHC beam with no corresponding bunch in the other beam within 3 BCIDs
- Empty: a BCID containing no proton bunches (also called “Cosmic”)

“Paired” (also referred to as “colliding”) bunch crossings result in collisions occuring in the corresponding BCIDs. “Unpaired” bunches do not result in collisions at ATLAS, but may collide elsewhere along the LHC ring. Unpaired bunches that undergo no collision at any IP are referred to as “isolated.” “Empty” bunch crossings are 50 ns intervals in which no proton bunches have passed through the ATLAS detector for at least 250 ns. The existence of such empty bunch crossings can be exploited in order to study the presence and rate of non-collision-related backgrounds.

Rates of background events in empty bunch crossings that pass our dedicated CalRatio trigger can be studied by collecting data using a version of our trigger which is active only in empty bunch crossings (see the sub-section titled “Cosmics trigger and offline cuts”). However in order to derive the per-bunch-crossing rate of observed events, the bunch group configuration has to be taken into account. The pattern of bunch crossing types and the trigger prescales corresponding to a given bunch group can be retrieved from the ATLAS runquery database, and so the number of relevant bunch crossings and corresponding trigger prescales for each lumiblock can be determined. The application of this procedure in order to account for the difference between the observed cosmic rate and the expected rate in collision data is discussed in the sub-section titled “Scale factor determination.”

Cosmic trigger and offline cuts

The cosmics background has been studied using data collected using a version of the CalRatio trigger that is only active during empty bunch crossings. At Level-2 and the Event Filter this trigger is identical to that which is used on filled bunch crossings (see Section 5.2). The Level-2 trigger, however, is seeded by $L1\_TAU8\_EMPTY$ rather than $L1\_TAU40$. $L1\_TAU8\_EMPTY$ is an identical but lower-threshold trigger than $L1\_TAU40$; $L1\_TAU40$ is emulated by requiring that the triggering jet in the event pass a 40 GeV $L1\_TAU$ jet E_T threshold.

The cut flow used in the cosmics analysis is idential to that which is applied to collision data (discussed in Section 5.4), except for the removal of the jet timing cut and the primary vertex cut. The removal of the timing cut allows for a more precise calculation of the prediction background with a reduced uncertainy. This is achieved by scaling the number of events surviving the cut flow without the timing cut by the fraction of two-jet events expected to be found within the (-1,5) ns analysis window. Such a scaling is justified by the observation that the jet timing distribution is flat for cosmic events (this is expected since cosmic events are randomly distributed relative to the LHC bunch crossings). This is discussed in more detail below.

The primary vertex cut is used to reject non-collision events, and therefore the cut must be removed in order to specifically study events which by definition should not contain a primary vertex. The removal of this cut is not expected to result in a systematic error, because the existence of a cosmic ray muon in a collision event is not expected to have any effect on the reconstruction of primary vertices. The effect the greater abundance of tracks in collision events (as compared to the collision-less events used here to study cosmic rays) has on the track isolation requirement is discussed below.

Properties of empty bunch-crossing events

All histograms in this section were made after applying the Line-of-Fire beam halo rejection cut and clean event criteria to events passing the CalRatio trigger on empty bunch crossings.

Figure 5.48 shows the η vs ϕ distribution of the jets after the application of the E_T^{miss} cut (left) and the E_T^{miss} distribution of cosmic events which fire the cosmic trigger (right). The high mean E_T^{miss} present in cosmic events with respect to signal events motivated the presence of an MET cut

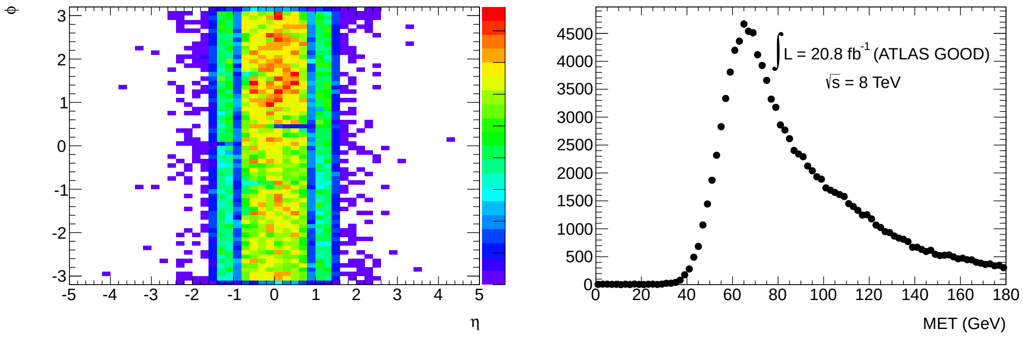

Figure 5.48: The distribution of jet η and ϕ for jets in triggered cosmic events (left) and the MET distribution of the events (right).

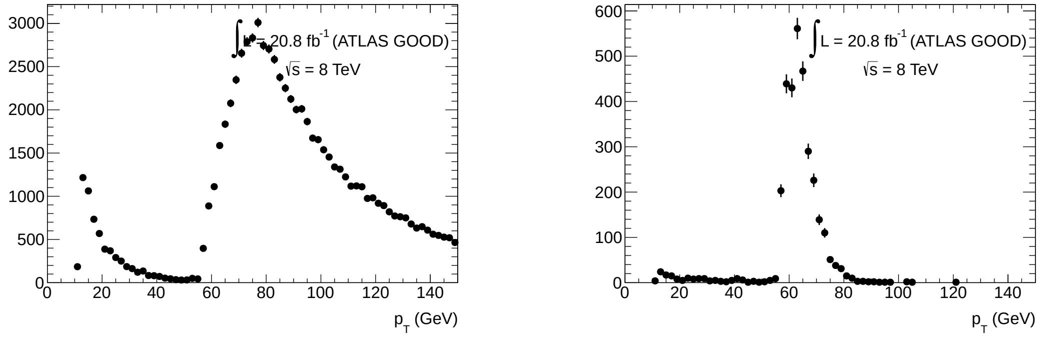

Figure 5.49: The distribution of jet p_T for jets in triggered cosmic events displayed without (left) and with (right) the $MET < 50$ GeV cut. The jets in the lower p_T peak are among the non-triggering jets present in the event.

in the offline analysis.

Figure 5.49 shows the p_T distribution of jets in triggered events without the E_T^{miss} cut (left) and with the E_T^{miss} cut (right). Figure 5.50 similarly shows the $\log_{10}(E_{HAD}/E_{EM})$ distribution of jets in triggered events without the E_T^{miss} cut (left) and with the E_T^{miss} cut (right). A large number of events (approximately 60%) have a $\log_{10}(E_{HAD}/E_{EM})$ of ∞ due to their having $E_{EM} \approx 0$.

The jets present in triggered events tend to be trackless. Furthermore, most events contain only a single jet. Only 12% of events have more than one jet, however, over 99% of all jets are trackless. Consequently the requirement of a second jet eliminates a large number of events while the trackless requirement on jets does not significantly affect the cosmic cut flow.

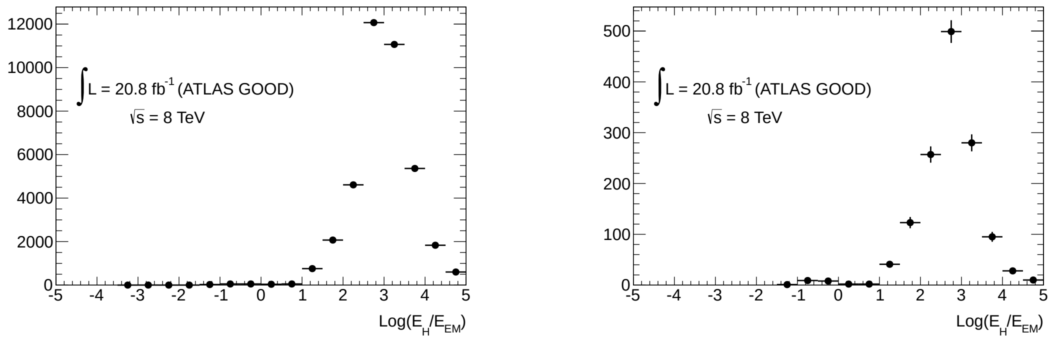

Figure 5.50: The distribution of jet $\log_{10}(E_{HAD}/E_{EM})$ for jets in triggered cosmic events displayed without (left) and with (right) the $MET < 50$ GeV cut. The barely visible negative-mean peak is much more prominent in typical collision events.

Cosmic events cut flow

The cut flow for events triggered in the empty bunch crossings is shown in Table 5.7 and the remaining jet-selection cut flow is shown in Table 5.8.

Cut	Number of Events
CalRatio Triggered Events	138678
No Line Of Fire Jets	130578
No DQ Flags	130394
MET (< 50 GeV)	4425

Table 5.7: Event selection cut events that fired the empty bunch crossings CalRatio trigger.

The E_T^{miss} cut is responsible for the largest relative reduction in the number of events surviving the cut flow. Only a small fraction of the remaining events contain a second jet of sufficient energy to pass the second jet requirement of the analysis. A total of 4 events still remain after the full cut flow and are used to calculate the predicted number of cosmic background events in the full 2012 dataset. The relevant properties of these events are summarized in Table 5.9 and Table 5.10.

There are differences between the conditions during which cosmics data was collected (empty bunch crossings) and during which collisions data was collected (paired bunch crossings). In par-

Cut	Number of Events
Look for a Trigger Jet (first π_v)	
Trigger object matches offline jet	3077
Jet $E_T > 60$ GeV	2386
$\log_{10}(E_{HAD}/E_{EM}) > 1.2$	2386
No tracks with $p_T > 1.0$	2386
Jet $\eta < 2.5$	2386
Second Jet (second π_v)	
Jet $E_T > 40$ GeV	6
$\log_{10}(E_{HAD}/E_{EM}) > 1.2$	4
No tracks with $p_T > 1.0$ GeV	4
$\eta < 2.5$	4
Only 2 HV jets	4

Table 5.8: Jet selection cut flow for events firing the CalRatio empty bunch crossing trigger.

Event	Leading-Triggering Jet			Second Jet		
Event	E_T (GeV)	$\log_{10}(E_{HAD}/E_{EM})$	Timing	E_T (GeV)	$\log_{10}(E_{HAD}/E_{EM})$	Timing
1	68.81	2.47	4.06	40.92	∞	-5.95
2	80.37	∞	-2.15	74.88	∞	7.70
3	83.95	∞	-6.75	42.08	2.02	2.78
4	96.65	∞	8.84	72.03	∞	3.48

Table 5.9: Jet properties of the four events surviving the cut flow. A value of ∞ for $\log_{10}(E_{HAD}/E_{EM})$ corresponds to an $E_{EM} = 0$.

ticular the expected absense of ID tracks in an empty bunch compared to the abundance of tracks in a collision (due to the underlying event and pileup) has to be accounted for. Furthermore, the lack of a timing cut in the analysis cut flow for empty buch crossing events requires the prediction to be scaled to the time window used in the analysis. Additionally a scale factor must be applied to

Event	Leading-Triggering Jet		Second Jet	
Event	η	ϕ	η	ϕ
1	0.02	-1.22	-0.09	2.71
2	1.55	2.16	1.23	-1.41
3	0.25	-0.64	0.76	-2.98
4	-1.22	-2.50	-0.05	-0.26

Table 5.10: Jet properties of the four events surviving the cut flow.

account for the relative difference in live time between the empty and filled BCID's. In other words the number of events measured on empty bunch crossings must be scaled to the number of collision bunch crossings in which the trigger was active.

Track isolation and coincidence

Cosmic events in ATLAS produce only zero or a small number of ID tracks, while collision events typically feature a large number of tracks. The cosmic ray background is measured on empty bunch crossings, while cosmic background events in collision data occur during colliding bunch crossings. A cosmic event may by itself result in energy deposits reconstructed as jets with no matching ID tracks (thus faking our signal), however a collision event may produce tracks that are in coincidence with the η-ϕ location of one or more of the jets, thus spoiling their isolation criteria. Therefore some percentage of events predicted by the cosmic background rate on empty bunch crossings will be rejected by the analysis cut flow in collision data.

In order to determine this percentage, a random trigger[7] was used to determine the probability of a track randomly intersecting a given $\Delta R = 0.2$ region of space as a function of $|\eta|$. A histogram of this probability is displayed in Figure 5.51. With this information, each cosmic event was weighted by the probability that neither of its jets would be coincident with a random track had that event occured during a collision. These weights all lie between 0.37 and 0.46 and are listed in Table 5.11.

---

[7] A random trigger is completely unbiased: the trigger fires randomly with a very high prescale.

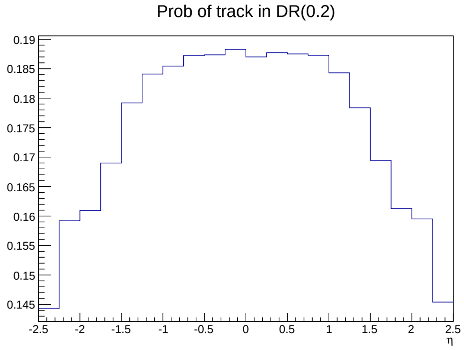

Figure 5.51: The probability as a function of η of a random track resulting in a jet failing the track isolation criteria.

Event	Weight
1	0.417
2	0.374
3	0.427
4	0.455

Table 5.11: Event weights due to the η-dependent probability of track coincidence with the jet.

Time scaling

The timing cut was not applied during the analysis of empty bunch crossing events. Because the scale factor that accounts for the ratio of empty bunch crossings to filled bunch crossings is roughly a factor of 3, the result is a predicted cosmic background that cannot be constrained to be less than $\sim$3 events. In order to reduce the uncertainty and determine a more precise prediction the timing cut was removed from the analysis, leaving an effective timing cut from -10 ns to 10 ns due to the timing cut present in the CalRatio good jet criteria. A scale factor due to the timing was calculated by determining the probability that two jets both had timing between -1 ns and 5 ns using all two jet events where both jets pass the CalRatio good jet criteria and where the event passes the data quality cuts. Out of 2937 such events, 365, or 12.4%, have both jets within the time window. The left hand side of Figure 5.52 shows the distribution of the timing of the subleading jet versus the timing of the

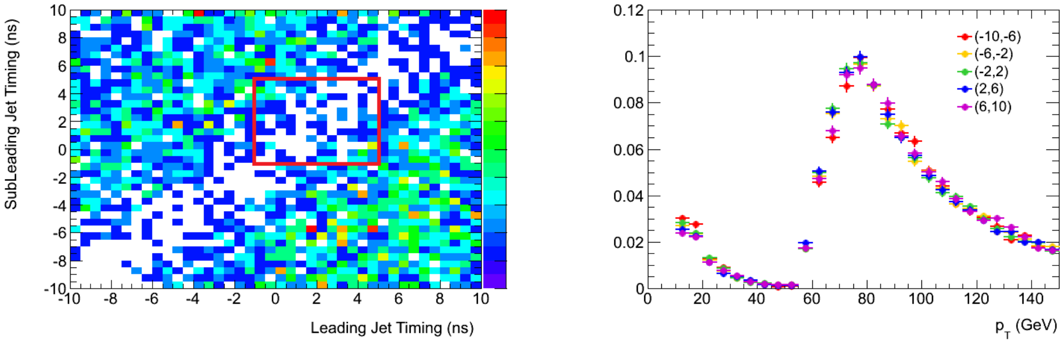

Figure 5.52: Leading vs Subleading jet timing distribution (left), and a comparison of jet E_T in different jet timing windows (right). The (-1,5) ns analysis cut window is marked by a red square.

leading jet. The (-1,5) ns analysis cut window is marked by a red square.

For this method to be valid the properties of a jet of cosmic origin cannot be dependent on its time of arrival. In order to test if this was the case all good jets from events passing the data quality cuts were broken into five samples depending on their timing, these being (-10,-6), (-6,-2), (-2,2), (2,6), and (6,10) ns. Various properties of these five jets were then compared. No two samples showed a significant difference for any variable relevant to this analysis. As an example the jet E_T for the five samples is shown on the right hand side of Figure 5.52.

Out of 2937 candidate dijet events 147 had both jets with timing in the (-1,5) ns window. The ratio of these two numbers, 0.050, is the scale factor to account for the jet timing cut applied in the full analysis cut flow on data.

BC Scale factor determination

In order to scale the number of events passing the cut flow on empty bunch crossings to the number of cosmic events expected in filled bunch crossings, the ratio of empty bunches to filled bunches was calculated. In each case the total number of bunch crossings included only those from lumiblocks in the GoodRunsList and those for which the relevant trigger was active. While the CalRatio trigger is unprescaled on collision data, the version of the trigger active in empty bunch crossings can be prescaled. This is taken into account by weighting each event passing the cosmic cut flow by its corresponding trigger prescale: the ratio of the number of bunch crossings in a given lumiblock to

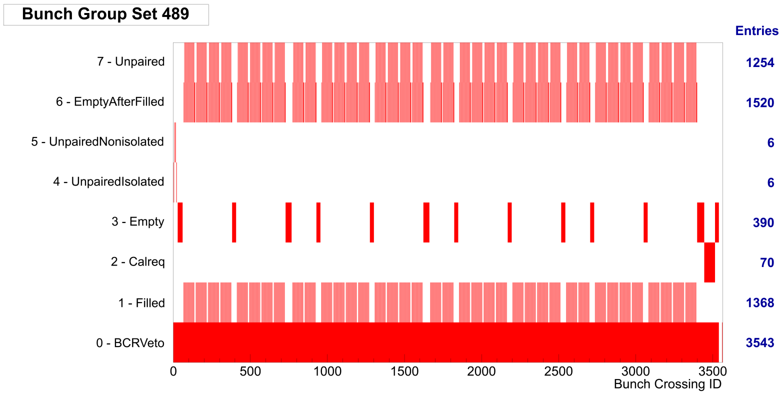

Figure 5.53: The typical bunch structure for LBs in which the surviving events are found. There are 390 empty BCs for every 1368 filled ones.

the value of the prescale for that lumiblock (LB) gives the number of bunch crossings for which the trigger was active. For each LB the prescale and number of bunch crossings per LB was extracted from an ATLAS database. The number of bunch crossings for which the trigger was active was then summed on a lumiblock-by-lumiblock basis. The two totals were then used to calculate the scale factor.

During the periods A through L it was found that about 5% of LBs passing the GRL and with the cosmics trigger active had the trigger prescaled, which also corresponds to about 12% of empty bunch crossings being present in prescaled lumiblocks. The fraction of bunch crossings which were empty were three times higher on average for period A than for other periods. The typical bunch group set (BGS) used in periods other than A was BGS 489, which uses 390 empty bunch crossings and 1368 filled bunch crossings per LB (Figure 5.53). Less than 0.02% of LBs from filled bunch crossings were prescaled, all from period B.

The total number of bunch crossings for which the cosmics trigger was actually active is 45.4×10^6, while the number of filled bunch crossings for which the relevant trigger was active is 129.7×10^6. These ratio of these two, Equation 5.6, yields the scale factor SF.

$$SF = \frac{Number\ of\ Filled\ Bunch\ Crossings}{Number\ of\ Empty\ Bunch\ Crossings} \tag{5.6}$$

The scale factor is calculated to be 2.851. The ratio is equivalent to the ratios of the live times of the triggers, and represents the fact that on average there are ∼3 filled bunch crossings for every unfilled bunch crossing.

The reader may be interested to know the total “live time” during which cosmic data was collected for this analysis. Assuming in this analysis the dead time fraction of the trigger used is negligible and that the length of a LB is equal to 60 seconds for all of the periods, we can define the “live time” of the trigger:

$$Live\ Trigger\ Time\ = 60\,s \times \Sigma_{i=1}^{nLB} \frac{Number\ of\ BCID\ (per\ LB)}{3564} * LB_i \tag{5.7}$$

Using this formula, we find the live time of the cosmics trigger to be $7.65 * 10^5$ s, or about 212 hours and 28 minutes. This shows that the data collected for the cosmic background analysis roughly corresponds to turning off the LHC and letting the ATLAS detector sit and collect cosmic ray events over a period of ∼9 days.

Combining the weights provided by the track coincidence study with the scale factors calculated from the BC ratio and time scaling yields a predicted number of cosmics events in the full 2012 data set of 0.33 +- 0.58(stat) events.

5.5.3 Beam Halo Background

Beam Halo muons are produced when protons collide with stray air molecules or beam collimation structures, and behave similarly to cosmic ray muons except they travel parallel to the beam direction and occur during filled or unpaired bunch crossings. Like a cosmic ray muon, a beam halo muon can deposit energy as it passes through the HCAL and therefore may fake our signal. An analysis similar to the 2012 cosmic background analysis (see Section 5.5.2) but using data collected in unpaired (rather than empty) bunch crossings was carried out on 2011 data, and showed the Beam Halo background to be negligable. The background from Beam Halo in 2012 is expected to be lower than in 2011 due to cleaner beam operating conditions. This understanding is confirmed by noting that the Line of Fire Beam Halo rejection cut, which rejects upwards of 80% of Beam Halo events (see Section 5.2.2), removes zero events if applied late in the analysis cut flow. There is currently no evidence of any Beam Halo background in any of the data surviving the 2012 cut flow on collision data.

Higgs mass (GeV)	cross section (pb)	uncertainty
m_H = 100 GeV	30.12	+15.7%, -14.9%
m_H = 126 GeV	19.22	+14.7%, -14.7%
m_H = 140 GeV	15.63	+14.3%, -14.5%

Table 5.12: Total uncertainty on Higgs production cross section.

5.6 Systematic uncertainties on the acceptance

The background model in this analysis is data driven. There are systematics associated with the methods, and those systematics are detailed in the QCD section (Section 5.5.1) and in the cosmics section (Section 5.5.2). Other data-based systematics include the luminosity (Section 5.3.1).

The signal model is Monte Carlo generated and therefore there are systematics associated with how faithfully the simulated signal events model real collision data. This section details those systematics.

5.6.1 Higgs production cross section

The uncertainties on the Higgs production cross sections are taken from the Higgs cross section working group [44]. Table 5.12 summarizes the cross sections and their total uncertainties for the different Higgs masses.

5.6.2 Jet Energy Scale Uncertainty

The JetTauEtMiss working group provides the tool “JESUncertaintyProvider” which provides the Jet Energy Scale (JES) uncertainty for each jet as a function of p_T, η and the number of primary vertices (see Section 3.3.2 for a discussion of the JES). The uncertainty in the energy of each jet can then be propagated through the analysis. The JES uncertainty provided by the JESUncertaintyProvider is derived on Standard Model jets, which typically contain a large fraction of energy deposited in the Electromagnetic Calorimeter (ECal), or a large “EM-fraction”. The jets resulting from the π_v’s in our signal sample that decay in or near the Hadronic Calorimeter (HCal), however, deposit most of their energy in the HCal; they have low EM-fraction. Given the different material and geometry of the ECal and HCal, it is expected that the JES for jets whose energy is entirely deposited in the ECal or HCal would be somewhat different from the standard JES that is the result of an average over the EM-fraction distribution of Standard Model jets. Since in this analysis no attempt is made to correct for this possible systematic difference between the JES on Standard Model jets and the JES on jets with low EM-fraction, an additional JES uncertainty must be measured on top of the standard JES uncertainty provided by the JESUncertaintyProvider. The strategy for measuring this additional uncertainty is to follow one of the JetTauEtMissGroup's standard tag-and-probe intercalibration procedures in order to measure the JES uncertainty as a function of jet EM-fraction.

The same tag-and-probe procedure is applied to both QCD dijet MC and collision data. The idea is to find a sub-sample of dijets whose p_T should balance to zero. This requires applying standard QCD selection cuts as well as standard data quality and background rejection cuts (the same applied in the QCD background analysis, Section 5.5.1), as well as rejecting events with ISR/FSR (which might spoil the p_T balance of the two leading jets) by requiring that any third jet in the event have less that 25% of the energy of the average p_T of the two leading jets. Once two leading back-to-back jets are identified in events passing the QCD selection cuts, the p_T balance of the two jets is studied as a function of jet EM-fraction. The p_T balance is parametrized by the asymmetry:

$$A = \frac{p_T^{probe} - p_T^{tag}}{p_T^{avg}} \tag{5.8}$$

$$\text{where} \quad p_T^{avg} = \frac{p_T^{probe} + p_T^{tag}}{2} \tag{5.9}$$

The JES uncertainty is measured as the difference between the mean asymmetry measured in data and on MC, and the JER uncertainty is measured as the difference between the RMS width of the asymmetry distribution measured in data and on MC. Because very few jets have EM-fractions in our signal region ($f_{EM} < 0.05$) this method is statistics limited. The JES and JER uncertainties were measured in four EM-fraction bins of roughly equal statistics, and then extrapolated into the signal region. The jet response as a funcion of EM-fraction is expected to be linear because a jet's energy is reconstructed to first order as a linear combination of the energy deposition in the ECAL and HCAL. Therefore the asymmetry as a function of EM-fraction is fitted to a line and extrapolated

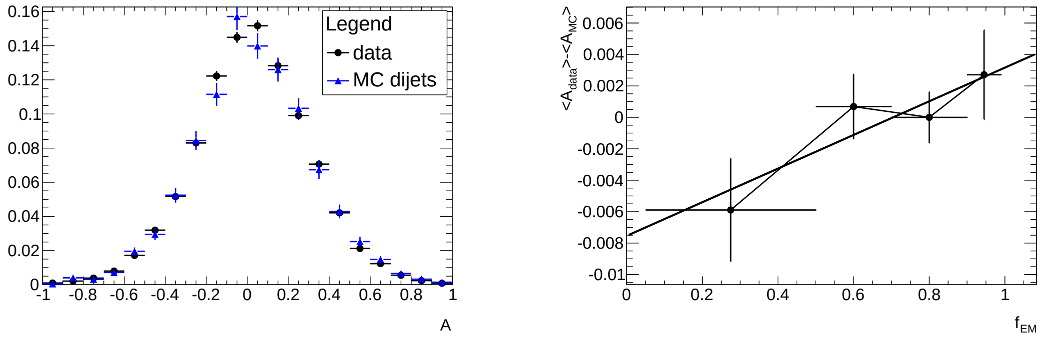

Figure 5.54: Left: the asymmetry distribution for data (black) and MC (blue) for events selected by the EF_j55 trigger in the lowest EM-fraction bin. Right: the difference between the mean asymmetry in data and MC as a function of EM-fraction cut. A linear fit extrapolates into the signal region (f_{EM} < 0.05).

into the signal region. This procedure is applied separately for samples of events passing four single jet triggers (EF _J25 through EF _J80) providing samples of jet energies in ranges near our expected signal jet energies (40-80 GeV). The additional JES uncertainty for jets in our signal region is taken to be the largest extrapolated value between the four data samples considered, and is found to be 3%. The additional JER uncertainty was found to be consistent with zero. Figure 5.54 shows example asymmetry distributions for data and MC in one EM-fraction bin, and the extrapolation of the difference in mean asymmetries into the signal region for events selected by the EF_j55 trigger.

5.6.3 PileUp

The standard ATLAS pileup re-weighting procedure has been used to weight each signal event in order to better approximate the pileup conditions in data (see Section 5.4.7). The associated systematic uncertainty has been evaluated through a direct data vs MC comparison. The $<\mu>$ distributions for 2012 collision data and the reference MC dataset (m_H = 140 GeV, m_{π_v} = 10 GeV) is depicted in Figure 5.55. The data-MC ratio (Figure 5.56 (left)) has been used to correct the original weights assigned by the standard ATLAS re-weighting tool, and the new set of weights (Figure 5.56 (right)) is applied to the MC datasets. The global acceptance variation (0.2%), computed by comparing results using the standard weights and the corrected weights, is taken as systematic uncertainty due to modeling of pileup.

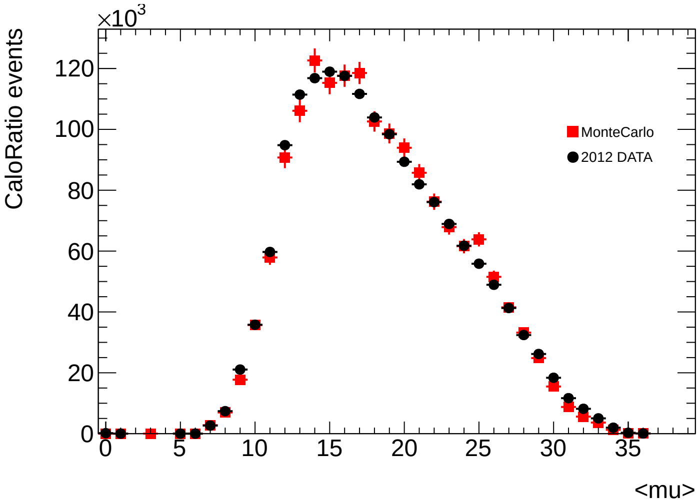

Figure 5.55: $< \mu >$ distribution in collision data and in the reference MC dataset (m_H = 140 GeV, m_{π_v} = 10 GeV).

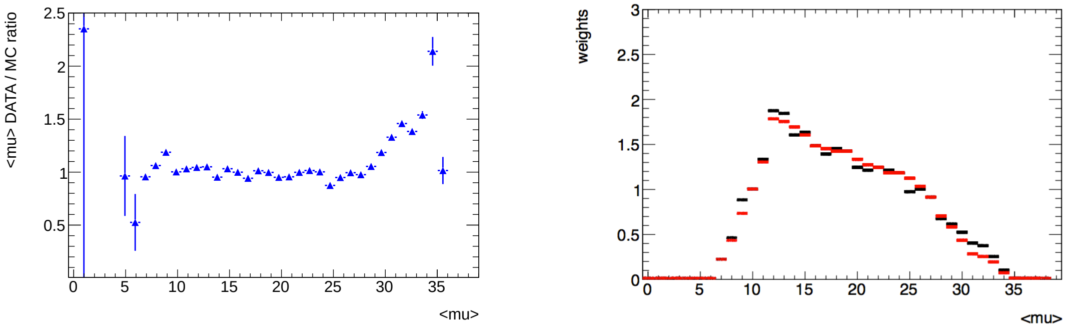

Figure 5.56: Ratio of $< \mu >$ distribution in collision data and MC (left); standard and corrected weights as a function of $< \mu >$ (right).

5.6.4 PDF

The PDF uncertainty is calculated following the Top group's recommended procedure. Each event in the signal MC dataset is reweighted according to three different PDF's (MSTW2008nlo68cl, CT10, and NNPDF2.3) and their error sets (PDF's with parameters varied). For each new PDF the weight of each event is given in Equation 5.10, where PDF_0 represents the old PDF.

$$w = \frac{PDF(x_1, f_1, Q) \times PDF(x_2, f_2, Q)}{PDF_0(x_1, f_1, Q) \times PDF_0(x_2, f_2, Q)} \tag{5.10}$$

The analysis cut flow is re-run and the final number of predicted events are found for each of the three new PDF's and their error sets. The uncertainty within a given PDF set (the Intra-PDF uncertainty) is calculated by determining the RMS width of the distribution of events passing the analysis cut flow after weighting each event with respect to the PDF's error set. The Inter-PDF uncertainty is the variation in the central value of the number of events passing the analysis cut flow between each of the three PDF sets. The Full-PDF uncertainty is taken to be a combination of both uncertainties: one half the difference between the highest mean value plus its 1-σ error and the lowest mean value minus its 1-σ error. The Full-PDF uncertainty was calculated for two of the MC datasets which have different Higgs and π_v masses. The dataset with a Higgs mass of 140 GeV and a π_v mass of 10 GeV was found to have a PDF systematic of 2.1%, and the dataset with a Higgs mass of 126 GeV and a π_v mass of 40 GeV was found to have a PDF systematic of 2.0%. The PDF systematics for all MC datasets in the analysis is taken to be the larger of the two values: 2.1%.

5.6.5 Trigger

The trigger systematics on the signal sample are described in Section 5.2.4.

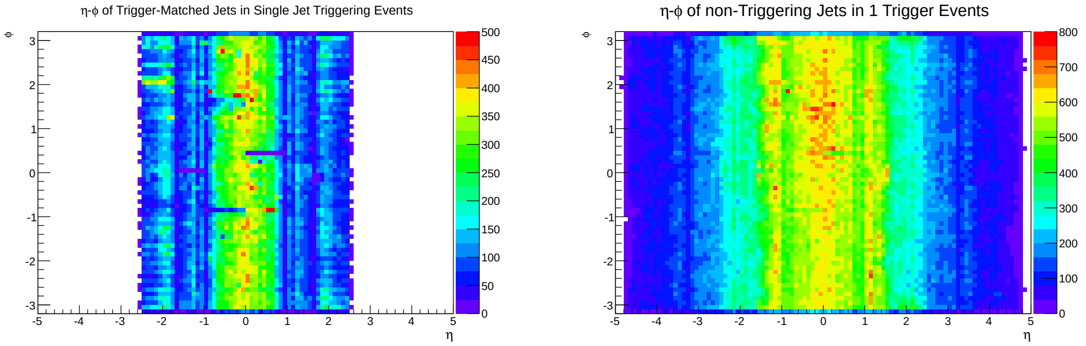

Figure 5.57: Left: the η-ϕ distribution of triggering jets in events passing all event-level cuts and in which the triggering jet is measured offline. Right: the η-ϕ distribution of non-triggering jets in the same events. The Z-axis is capped at 500 events per bin for the triggering jets due to the presence of a noisy calorimeter cell near $\eta = -1$, $\phi = 2$.

5.7 Results and Limits

5.7.1 Properties of triggered events

The analysis cut flow described in Section 5.4 was applied to the 20.8 fb^{-1} of 2012 collision data. The η-ϕ distribution of triggering jets in events passing all event-level cuts and in which the triggering jet is matched to an offline jet is shown on the left in Figure 5.57. The η-ϕ distribution of non-triggering jets in the same events is shown on the left in Figure 5.57. The majority of events ($\sim$99.5%) contain only a single triggering jet. Triggering jets are restricted to a smaller range of η than non-triggering jets due to the η cut applied in the trigger.

For the following histograms only the event-level cuts have been applied. No other cuts from the E_T^{miss} cut onward are applied unless otherwise stated. Events passing the event-level cuts will for brevity be referred to as “clean events.”

Figure 5.58 shows the p_T distribution of all jets in all triggered events on the left and the $\log_{10}(E_{HAD}/E_{EM})$ distribution is shown on the right. The $\log_{10}(E_{HAD}/E_{EM})$ distribution represents a superposition of triggering jets at the higher p_T peak and other jets present in the event at the lower peak. Non-triggering jets in the event are typically low p_T and do not have high $\log_{10}(E_{HAD}/E_{EM})$. Both jets, however, will eventually be subjected to a $\log_{10}(E_{HAD}/E_{EM}) > 1.2$ cut offline. The primary effect of this cut is to remove events containing low p_T and low $\log_{10}(E_{HAD}/E_{EM})$ non-triggering

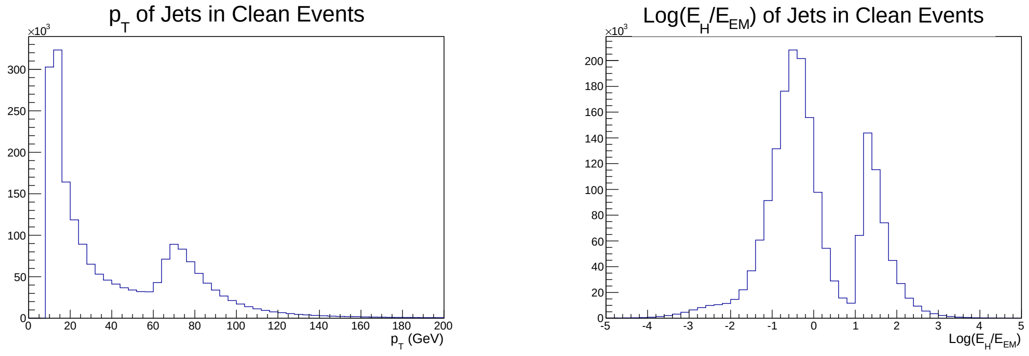

Figure 5.58: Jet p_T distribution (left) and, $\log_{10}(E_{HAD}/E_{EM})$ distribution (right) for all jets in clean CalRatio triggered collision events.

jets. This is described in Section 5.7.2.

Figure 5.59 shows the number of tracks within $\Delta R < 0.2$ of offline jets matched to the triggering jets in events with one triggering jet (left), and also the number of tracks associated with non-triggering jets in the same events (right). When the trackless criteria is applied to the jets identified online the majority of triggered jets ($\sim$83%) are still found to be trackless. Approximately $\sim$31% of the non-triggering jets are found to be trackless.

Figure 5.60 shows the number of jets per event (left) and the E_T^{miss} distribution of events for triggered events (right). Though the number of jets per event is generally more than two, the two-jet requirement in the cut flow pertains only to jets which pass the full cut flow including the 40 GeV cut, trackless, and $\log_{10}(E_{HAD}/E_{EM})$ requirement. In no event considered was a third jet found to pass the cut flow. The 50 GeV E_T^{miss} cut removes $\sim$23% of events. In comparison the E_T^{miss} cut removes $\sim$99% of cosmic events.

5.7.2 Events passing the full set of cuts

Table 5.13 shows the number of events surviving at each stage of the analysis cut flow. There were 1628647 triggered events passing the GRL in the analysis period and a total of 24 events survived the full set of cuts. The η-ϕ distribution of the two jets in each of the 24 events is displayed on the left in Figure 5.61. Green data points indicate jets to which the 60 GeV and corresponding cuts were applied, while red points indicate jets to which the 40 GeV cut was applied. The right hand

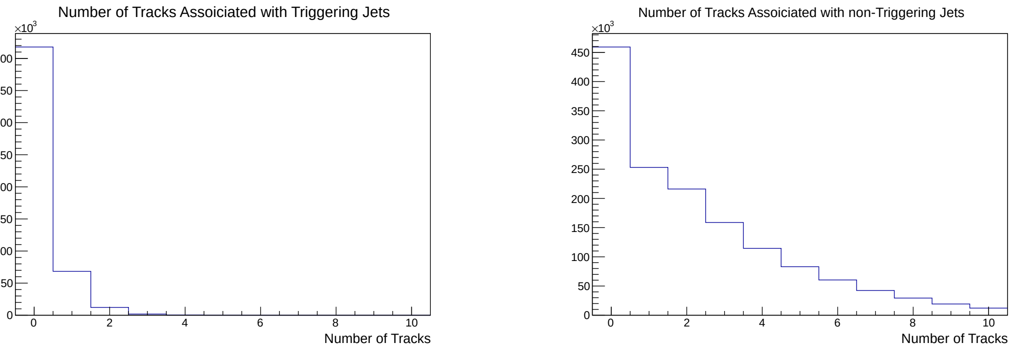

Figure 5.59: The number of tracks with $p_T > 1$ GeV within $\Delta R < 0.2$ of jets. The left-hand histogram corresponds to offline jets which have been matched to CalRatio trigger jets. The right-hand histogram corresponds to all other jets in the events of the left-hand histogram.

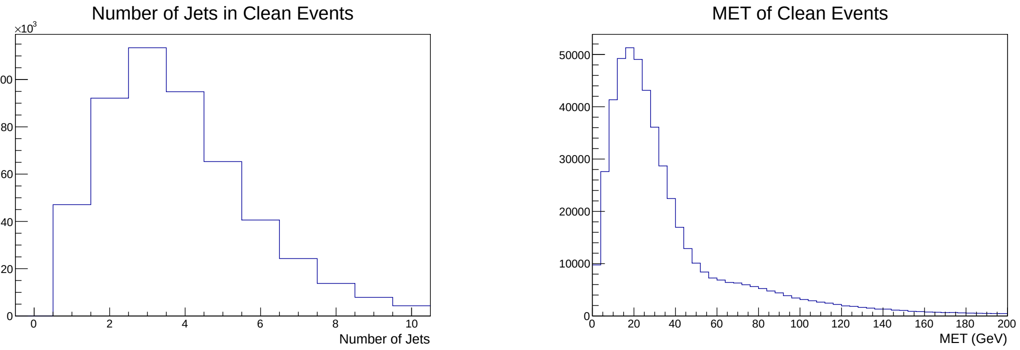

Figure 5.60: Distribution of the number of jets per CalRatio triggered event in collision (left), and the E_T^{miss} distribution for these events (right).

side of Figure 5.61 displays the $\Delta\phi$ distribution of the jets surviving the full set of cuts. Figure 5.63 shows the p_T distribution (left) and $\log_{10}(E_{HAD}/E_{EM})$ distribution (right) for jets surviving the full set of cuts, and Figure 5.64 shows the jet timing distribution for jets surviving the full set of cuts.

Cut on events	Events
HV Trigger	1628647
Primary vertex	1627943
Line Of Fire	1493744
MET ($<$ 50 GeV)	1142175
Cut on first jet	
Jet with timing in (-1,5) ns	1059331
E$_T$ $>$ 60 GeV	1045699
Log Ratio$>$1.2	890519
No track pt $>$ 1.0 GeV	828423
$\|\eta\| < 2.5$	828344
Cut on second jet	
Jet with timing in (-1,5) ns	811662
E$_T$ $>$ 40 GeV	557610
Log Ratio$>$1.2	318
No track pt $>$ 1.0 GeV	97
$\|\eta\| < 2.5$	24

Table 5.13: Selection cut flow for data events.

The cut responsible for the greatest fractional reduction in the number of surviving events with respect to the previous cut is the $\log_{10}(E_{HAD}/E_{EM})$ cut on the second jet. These jets represent non-triggering jets from events with only one triggering jet and so they were consequently not previously subjected to a cut on their $\log_{10}(E_{HAD}/E_{EM})$. The distribution of the $\log_{10}(E_{HAD}/E_{EM})$ of all non-triggering jets for which the triggering jet passes the 60 GeV and corresponding cuts is on the left of Figure 5.65 while the p_T distribution for these jets is shown on the right. Only 0.40% of these jets

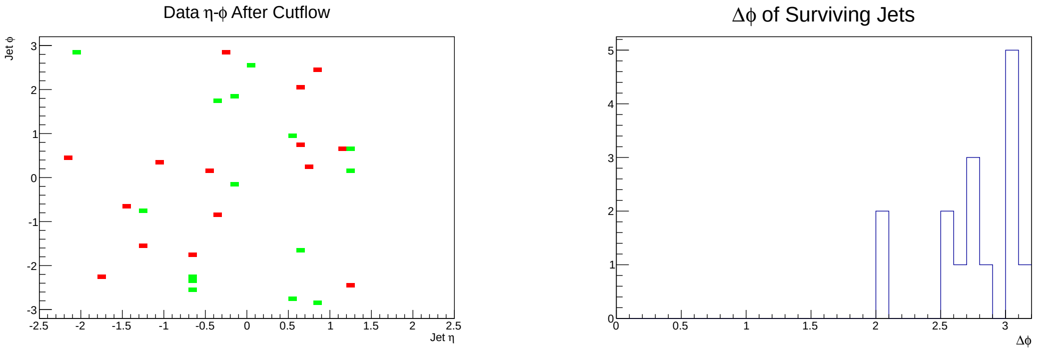

Figure 5.61: The left hand histogram shows the η-ϕ distribution of pairs of jets surving the full analysis cut flow. Green data points correspond to jets subjected to the 60 GeV and corresponding cuts while red data points correspond to jets subjected to the 40 GeV cut. The $\Delta\phi$ distribution of the 24 jet pairs is displayed on the left.

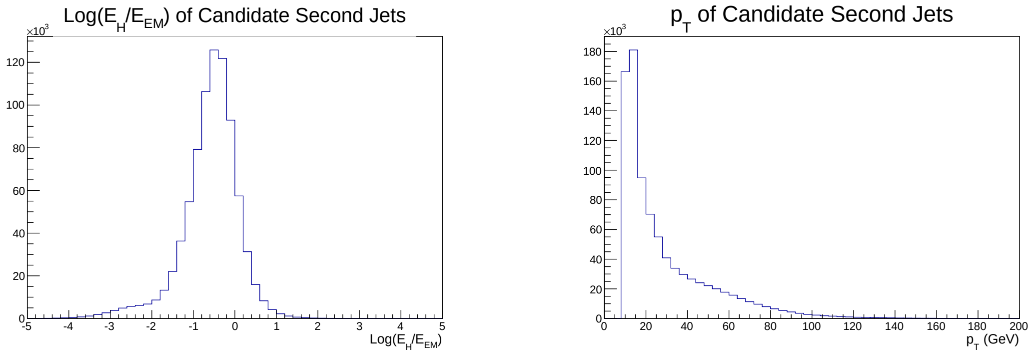

Figure 5.62: (Left) The $\log_{10}(E_{HAD}/E_{EM})$ distribution for candidate second jets in events with one triggering jet passing the 60 GeV cut. The majority of jets posses values of $\log_{10}(E_{HAD}/E_{EM})$ well below the threshold of 1.2. (Right) The p_T distribution of the same jets.

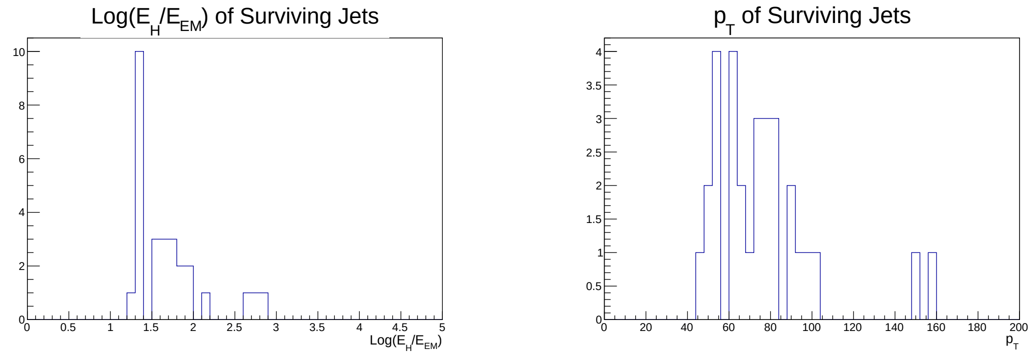

Figure 5.63: Left: the $\log_{10}(E_{HAD}/E_{EM})$ distribution for jets in events passing the full analysis cut flow. Right: the p_T distribution of the same jets.

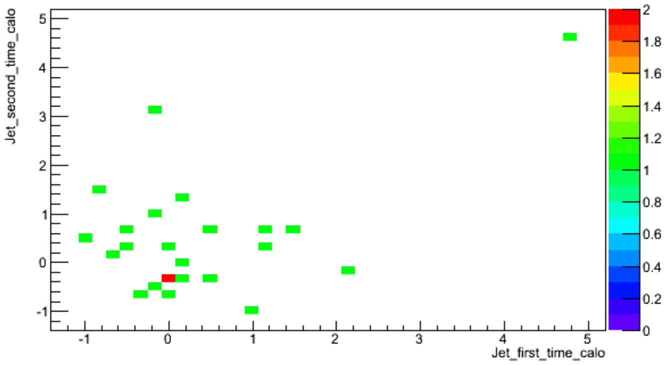

Figure 5.64: The jet timing distribution for the triggering jet (x-axis) and second jet (y-axis) of the final 24 events passing the full analysis cut flow.

pass the $\log_{10}(E_{HAD}/E_{EM})$ cut, which corresponds to an even lower 0.07% of events surviving relative to the previous p_T cut. The 40 GeV p_T cut has a less significant effect but still removes a large fraction of events. Assuming the majority of these jets are QCD jets then the low $\log_{10}(E_{HAD}/E_{EM})$, corresponding to a high EM fraction, is typical. After these cuts the majority of events remaining are expected to be QCD background events.

The jet p_T, η, timing, and other distributions that have been checked, are all consistent with the hypothesis that the majority of the jets surviving the full analysis cut flow are due to Standard Model QCD. Additionally, each of the 24 events passing the cut flow have been studied using an ATLAS event visualizer. One event has been clearly identified as due to a cosmic shower, due to the clear presence of atypical muon segments, calorimeter energy deposits, and calorimeter cell timings. This is consistent with the cosmic background prediction of 0.33 +- 0.58(stat) events. The remaining 23 events show no indications of beam halo or detector-related background.

5.7.3 Comparison of data with expected background

24 events are found to pass the full analysis cut flow on 20.8 fb^{-1} of 2012 collision data, while 12.8 $\pm$ 6.4 events are expected if the background hypothesis is correct. The number of events seen in data is larger than the expected background by about 1-σ, and therefore the excess of events seen relative to the expected background likely represents a relatively common upward statistical fluctuation of

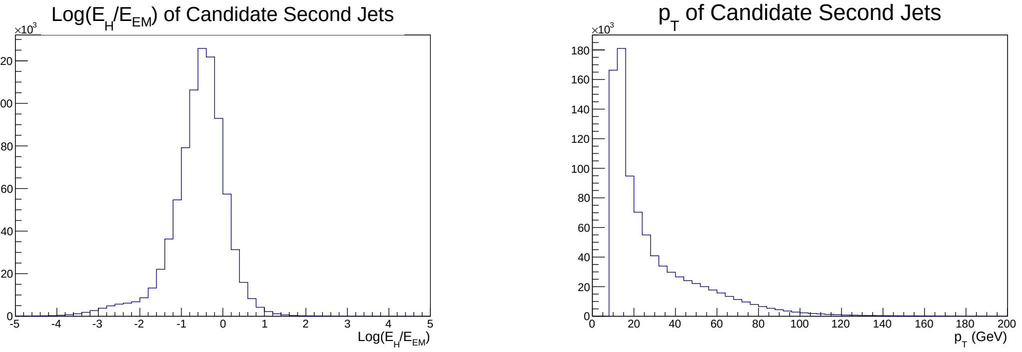

Figure 5.65: (Left) The $\log_{10}(E_{HAD}/E_{EM})$ distribution for candidate second jets in events with one triggering jet passing the 60 GeV cut. The majority of jets posses values of $\log_{10}(E_{HAD}/E_{EM})$ well below the threshold of 1.2. (Right) The p_T distribution of the same jets.

the data. The 24 events passing the analysis cut flow show neither any visual indication, nor any indication in the distributions of jet variables that have been studied, of being consistent with the signal hypothesis. Therefore this analysis does not interpret the observed 1-σ excess in data as anything other than either a statistical fluctuation or a possible indication that the systematic errors in this analysis have been underestimated. As a result this analysis places limits on the signal hypothesis.

5.7.4 Limit evaluation

Given the number of expected signal and background events and the number of observed events passing our cut flow, we place a 95% CLs [54] upper limit on the the cross-section for the production of signal events over a range of possible π_v lifetimes for each of the simulated Higgs and π_v mass points, and assuming a 100% branching fraction for $h^0 \to \pi_v \pi_v$.

The CLs method (also called the modified frequentist confidence level) gives the probability, CL$_s$, of collecting the observed data given the signal hypothesis. It is the ratio of two frequentist probabilities, CL$_{s+b}$ and CL$_b$. CL$_{s+b}$ is the probability for collecting the observed data given the signal plus background hypothesis, and CL$_b$ is the probability of collecting the observed data given the background-only hypothesis. The CL$_s$ probability is used to exclude the signal hypothesis at the 95% confidence level as a function of a signal strength parameter. The signal strength parameter,

σ/σ_{SM}, is a multiplicative factor for the expected number of signal events, which parametrizes the production cross-section as an unknown variable. σ/σ_{SM} =1 corresponds to the case that the production cross-section for the signal is equal to the SM Higgs production cross-section. Given the expected number of signal and background events, the CLs method is used to determine the *expected* 95% exclusion limits on the signal hypothesis. The number of events observed in data is used to determine the *observed* 95% exclusion limits on the signal hypothesis. Statistical fluctuations often result in the expected and observed exclusion limits differing by up to 1 or 2 σ.

The efficiency of our selection cut-flow on each signal dataset is shown in Table 5.5. This efficiency is a function of the average π_v decay length that corresponds to each of the simulated π_v lifetimes reported in Table 4.1. A re-weighting procedure is used to predict the fraction of signal events that would be accepted by our analysis as a function of π_v proper lifetime. A large sample of π_v decays was generated (500000 events for each proper lifetime value) for a range of lifetimes from 0 to 25 m, and the resulting efficiencies for each proper lifetime (shown in Figure 5.35) are then converted into the number of expected signal events at 20.8 fb^{-1} , assuming a 100% branching fraction for $h^0 \to \pi_v\pi_v$.

The number of events observed in data, the predicted number of observed signal events, the expected background estimation, and all the systematic uncertainties are used as input in deriving the upper limit on the cross section. We run the CLs procedure to calculate a 95% confidence interval at each point in the π_v proper lifetime for each of the eight signal samples. Results are given in Figures 5.66 and Figures 5.67. For the m$_H$ = 126 GeV, m_{π_v} = 10 GeV benchmark sample, assuming the SM Higgs production cross-section and 100% branching fraction for $h^0 \to \pi_v\pi_v$, this analysis places an upper limit on the π_v's proper lifetime of ~0.08 m, which is an improvement over a previous analysis [45] which placed an upper limit on the π_v's lifetime, for various Higgs and π_v mass combinations, as low as ~0.45 m. The lower limits on the π_v's proper lifetime placed by this analysis have not been fully evaluated because the simulation of the π_v's proper lifetime described above is currently limited to 25 m. For the m$_H$ = 126 GeV, m_{π_v} = 10 GeV benchmark sample, the 95% confidence interval excludes π_v lifetimes between ~0.08 and ~6 m, and for the m$_H$ = 126 GeV, m_{π_v} = 40 GeV benchmark sample, the 95% confidence interval excludes π_v lifetimes between ~0.4 and ~20 m.

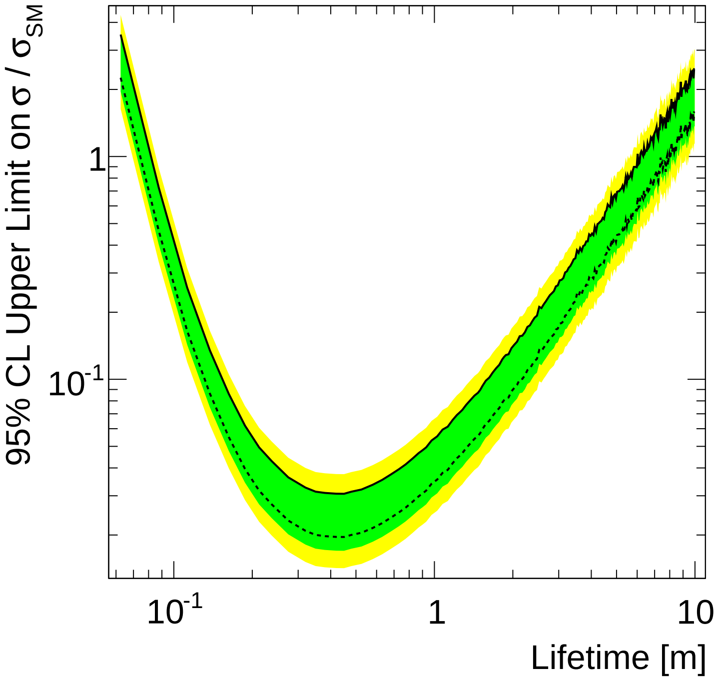

Figure 5.66: Expected (dashed) and observed (solid) 95% confidence limits on σ/σ_{SM} as a function of the π_v proper decay length for the m_H = 126 GeV, m_{π_v} = 10 GeV benchmark sample. The green and yellow bands represent 1- and 2-σ uncertainties, respectively, on the expected limits. The 1-σ excess of observed events over the expected background is reflected in the observed limit's position, above the expected limit, between the yellow and green bands.

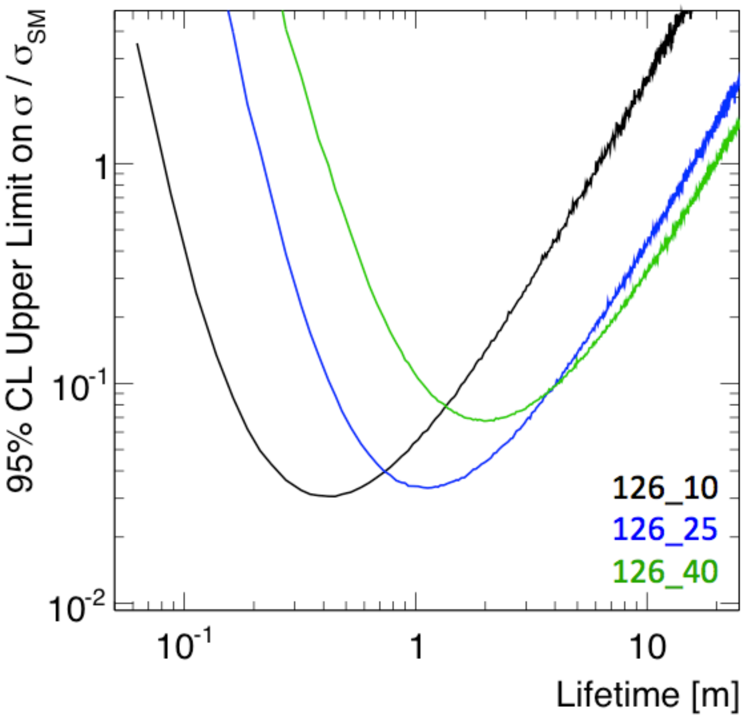

Figure 5.67: Observed confidence limits on σ/σ_{SM} as a function of the π_v proper decay length for: the m$_H$ = 126 GeV, m_{π_v} = 10 GeV benchmark sample (black); the m$_H$ = 126 GeV, m_{π_v} = 25 GeV benchmark sample (blue); and the m$_H$ = 126 GeV, m_{π_v} = 40 GeV benchmark sample (green).

APPENDICES

.1 Analysis cut flow

.1.1 Signal MonteCarlo

Here we report full details of the analysis cut flow for the eight MC signal samples. The full cut flow and the expected number of signal events in data for each signal dataset is shown in Tables 14 and 15.

Some kinematic variables for π_v's in events surviving the cut flow are shown in the following figures. Figure 68 shows π_v's transverse momentum and decay length. Figure 69 shows π_v's hadronic (left) and electromagnetic energy deposition (right). Figure 70 shows π_v's η and ϕ. Figure 71 shows the (η, ϕ) map for the π_v's-jets (left) and for each cell of the π_v-jets (right). Figure 72 shows the number of cells per jet at different stages of the analysis cut flow (left) and the jet-cell distance for the final π_v's. Figure 73 shows the jet multiplicity and p_T of all jets after they have passed selection cuts. Figure 74 shows the jet η and ϕ for all jets that survive the cut flow. Figure 75 shows the jet mass and width for jets that survive the cut flow.

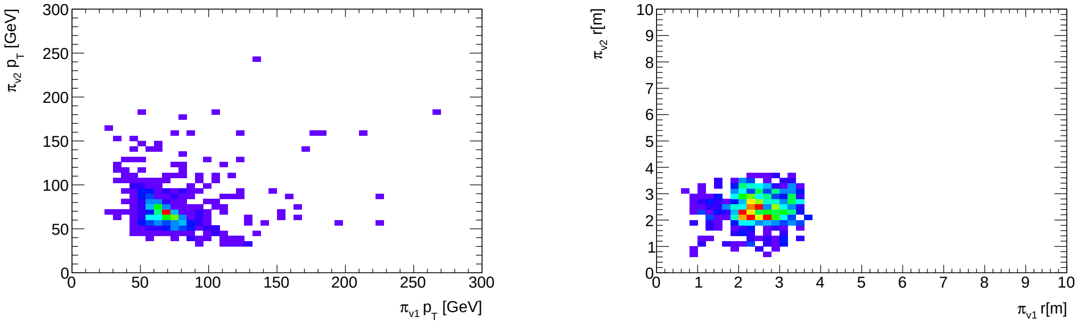

Figure 68: p_T (left) and decay length (right) for both π_v's at the end of the cut flow.

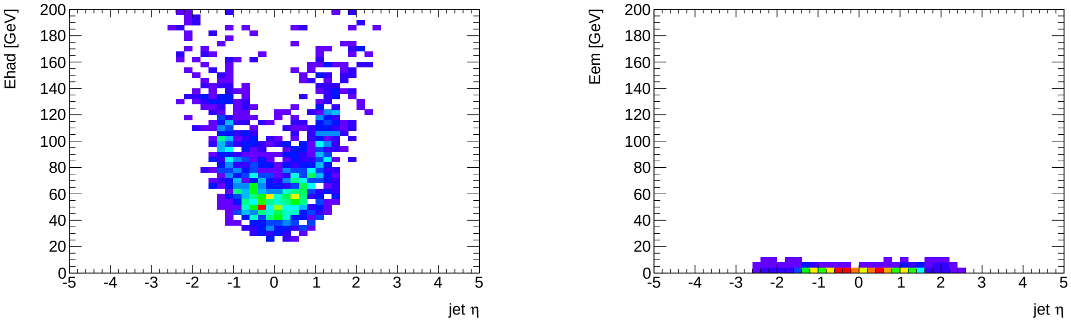

Figure 69: Hadronic (left) and electromagnetic (energy right) for both π_v's at the end of the cut flow.

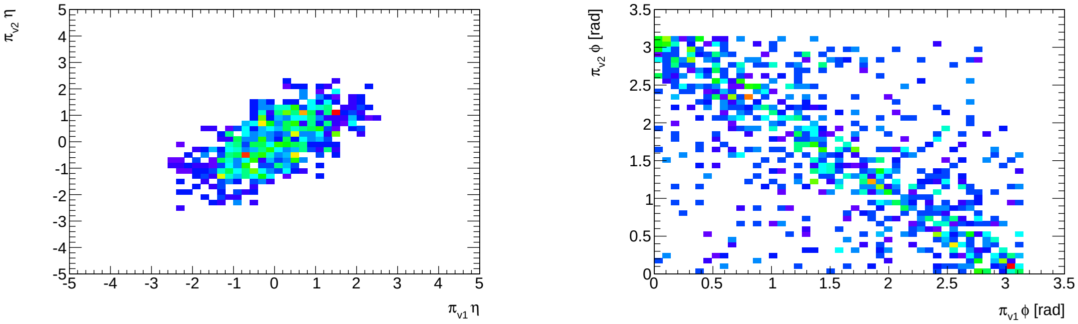

Figure 70: η (left) and ϕ (right) for both π_v's at the end of the cut flow.

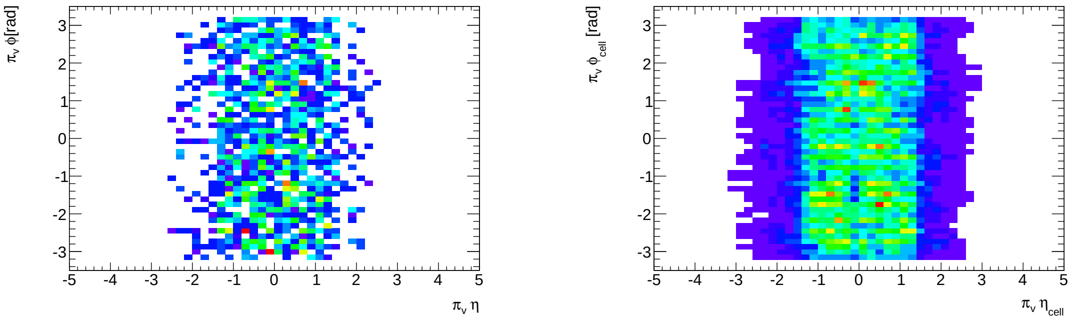

Figure 71: (η, ϕ) map for the final π_v-jets (left) and for all the cells of the π_v-jets.

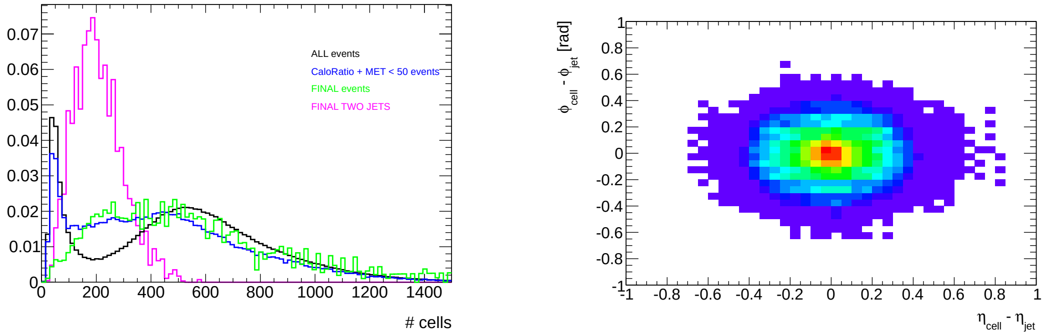

Figure 72: Number of cells per jet at different stages of the analysis cut flow (left) and jet-cell distance for the final π_v's.

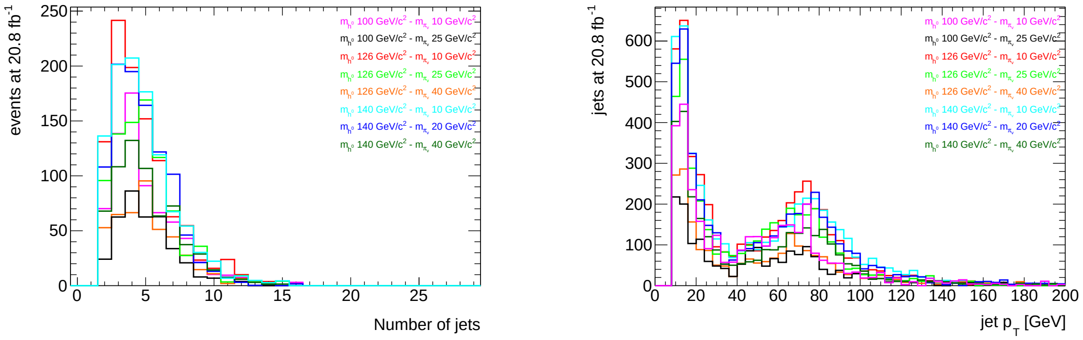

Figure 73: Jet multiplicity (left) and p_T (right) of all the jets at the end of the cut flow.

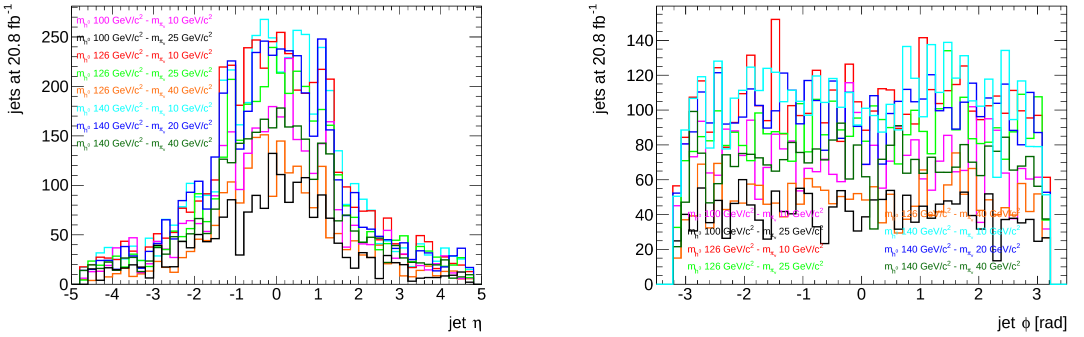

Figure 74: Eta (left) and phi (right) for all the jets at the end of the cut flow.

Cut on events	Events	Events	Events	Events
	m$_H$ = 100 GeV m_{π_v} = 10 GeV	m$_H$ = 100 GeV m_{π_v} = 25 GeV	m$_H$ = 126 GeV m_{π_v} = 10 GeV	m$_H$ = 126 GeV m_{π_v} = 25 GeV
Processed Events	294697	295399	294899	299600
HV Trigger	8414	5586	15694	12339
Primary vertex	8413	5586	15692	12337
Line Of Fire	8108	5350	15050	11788
MET ($<$ 50 GeV)	6275	4210	10895	8961
Cut on first jet				
Jet with timing in (-1,5) ns	6099	4131	10688	8803
E$_T$ $>$ 60 GeV	5938	4022	10517	8655
Log Ratio$>$1.2	5504	3728	9786	8080
No track p$_T$ $>$ 1.0 GeV	5328	3601	9469	7784
$\|\eta\| < 2.5$	5328	3601	9469	7784
Cut on second jet				
Jet with timing in (-1,5) ns	5244	3568	9307	7687
E$_T$ $>$ 40 GeV	3792	2426	7787	5832
Log Ratio$>$1.2	350	193	801	661
No track p$_T$ $>$ 1.0 GeV	298	168	679	565
$\|\eta\| < 2.5$	296	168	671	562
→ **expected at 20.8 fb^{-1}**	697.2 ± 38.5	378.1 ± 28.3	1036.4 ± 37.4	836.3 ± 33.4

Table 14: Selection cut flow for four of the eight MC samples. The final number of events expected at the 2012 luminosity of 20.8 fb^{-1} with pile-up re-weighting applied, is also provided.

Cut on events	Events	Events	Events	Events
	m$_H$ = 126 GeV m_{π_v} = 40 GeV	m$_H$ = 140 GeV m_{π_v} = 10 GeV	m$_H$ = 140 GeV m_{π_v} = 20 GeV	m$_H$ = 140 GeV m_{π_v} = 40 GeV
Processed Events	299000	290599	281900	299699
HV Trigger	8999	19390	16193	13051
Primary vertex	8999	19389	16192	13049
Line Of Fire	8612	18604	15554	12490
MET ($<$ 50 GeV)	6325	13553	11470	9162
Cut on first jet				
Jet with timing in (-1,5) ns	6159	13202	11246	8973
E$_T$ $>$ 60 GeV	6071	13048	11086	8865
Log Ratio$>$1.2	5644	12221	10406	8317
No track p$_T$ $>$ 1.0 GeV	5439	11782	10024	8025
$\|\eta\| < 2.5$	5439	11780	10023	8024
Cut on second jet				
Jet with timing in (-1,5) ns	5370	11620	9898	7944
E$_T$ $>$ 40 GeV	3789	10291	8209	5994
Log Ratio$>$1.2	350	1055	909	677
No track p$_T$ $>$ 1.0 GeV	292	862	757	548
$\|\eta\| < 2.5$	292	842	747	540
$\rightarrow$ **expected at 20.8 fb^{-1}**	442.3 ± 24.3	1042.4 ± 34.1	986.1 ± 33.7	650.7 ± 26.6

Table 15: Selection cut flow for four of the eight MC samples. The final number of events expected at the 2012 luminosity of 20.8 fb^{-1} with pile-up re-weighting applied, is also provided.

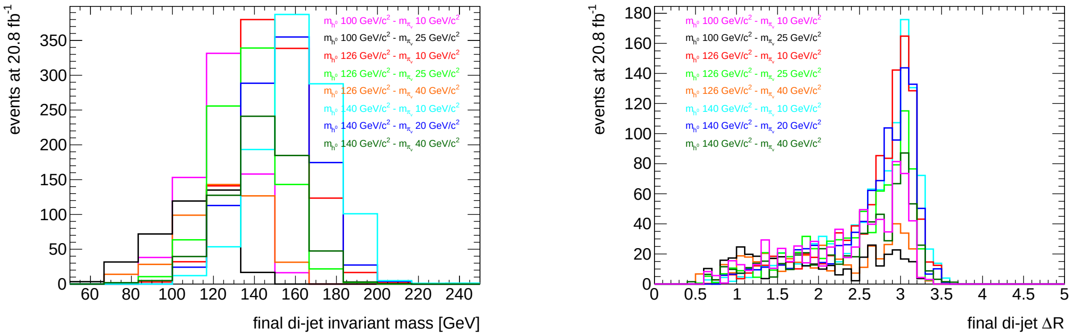

Figure 75: Invariant mass (left) and ΔR (right) for the two jets passing offline cuts.

.2 Derivation of Formulae

.2.1 Derivation of the QCD Background Probability Formula

Equation 5.2 represents the probability for an event containing N_j jets above 40 GeV to pass the analysis cuts, given p_T- and η-dependent probability functions P and Q for a single jet to pass the analysis cuts. The derivation of Equation 5.2 requires breaking up Q into two parts: $Q(j_i) \equiv Q_1(j_i) + Q_2(j_i)$. Q_1 is defined to be the probability for a 40 GeV probe jet to pass the CalRatio trigger and satisfy the offline EM-fraction and trackless cuts, and Q_2 is defined to be the probability for a 40 GeV probe jet to NOT pass the CalRatio trigger but satisfy the offline EM-fraction and trackless cuts. Therefore Q is simply the probability for a 40 GeV probe jet to satisfy the offline EM-fraction and trackless cuts. P is defined to be the probability for a 40 GeV probe jet to pass the CalRatio trigger and offline EM-fraction and trackless cuts and a 60 GeV E_T cut.

The formula to be derived is for the probability for an event to pass the HV analysis cuts, given probabilities for each individual jet to pass analysis cuts. An event passes the HV analysis cuts if it includes one jet passing the P criteria, and exactly one other jet satisfying the Q_1 or Q_2 criteria. Note that the pairs $\{P, Q_1\}$, and $\{P, Q_2\}$ represent mutually exclusive criteria.

Derivation of equation 5.2 for $N_j = 2$:

There are four possible cases:
A: jet 1 satisfies P criteria, jet 2 satisfies Q_1 criteria
B: jet 1 satisfies Q_1 criteria, jet 2 satisfies P criteria
C: jet 1 satisfies P criteria, jet 2 satisfies Q_2 criteria
D: jet 1 satisfies Q_2 criteria, jet 2 satisfies P criteria

In general:
P(A or B or C or D) = $P(A) + P(B) + P(C) + P(D)$
$- P(AB) - P(BC) - P(AC) - P(AD) - P(BD) - P(CD)$
$+ P(ABD) + P(ACD) + P(BCD) + P(ABC)$
$- P(ABCD)$

Since the pairs $\{P,\ Q_2\}$, and $\{Q_1,\ Q_2\}$ are mutually exclusive, cases BC, AC, AD, BD, CD cannot be satisfied simultaneously:

$$= P(A) + P(B) + P(C) + P(D)$$
$$- P(AB) - \cancelto{0}{P(BC)} - \cancelto{0}{P(AC)} - \cancelto{0}{P(AD)} - \cancelto{0}{P(BD)} - \cancelto{0}{P(CD)}$$
$$+ \cancelto{0}{P(ABD)} + \cancelto{0}{P(ACD)} + \cancelto{0}{P(BCD)} + \cancelto{0}{P(ABC)}$$
$$- \cancelto{0}{P(ABCD)}$$
$$= P(A) + P(B) + P(C) + P(D) - P(AB)$$

Finally P(AB) = $P(j_1)P(j_2)$, since a jet satisfying P will always satisfy Q_1:

$$= P(j_1)Q_1(j_2) + P(j_2)Q_1(j_1) + P(j_1)Q_2(j_2) + P(j_2)Q_2(j_1) - P(j_1)P(j_2)$$
$$= P(j_1)(Q_1(j_2) + Q_2(j_2)) + P(j_2)(Q_1(j_1) + Q_2(j_1)) - P(j_1)P(j_2)$$
$$= P(j_1)Q(j_2) + P(j_2)Q(j_1) - P(j_1)P(j_2)$$

Derivation of equation 5.2 for $N_j = 3$*:*

There are three possible cases to consider that might give rise to a non-zero probability:

A: jet 1 does not satisfy the P or Q criteria

B: jet 2 does not satisfy the P or Q criteria

C: jet 3 does not satisfy the P or Q criteria

We can ask what is the probability of either A or B or C satisfying the analysis cuts.

In general:

P(A or B or C) = $P(A) + P(B) + P(C) - \cancelto{0}{P(AB)} - \cancelto{0}{P(BC)} - \cancelto{0}{P(AC)} + \cancelto{0}{P(ABC)}$

(remembering that any two pairings of cases A, B, or C cannot be satisfied simultaneously)

= $P(A) + P(B) + P(C)$

And for each of the above terms we can just apply the $N_j = 2$ formula:

$$= [P(j_2)Q(j_3) + P(j_3)Q(j_2) - P(j_2)P(j_3)](1 - Q(j_1))$$

$+[P(j_1)Q(j_3)+P(j_3)Q(j_1)-P(j_1)P(j_3)](1-Q(j_2))$
$+[P(j_1)Q(j_2)+P(j_2)Q(j_1)-P(j_1)P(j_2)](1-Q(j_3))$

The result is easily extended to all $N_j > 2$ using N choose 2 combinatorics, since the result can be factored into results for $N_j = 2$ corresponding to each possible jet pairing, as in the above example. This is made possible by the requirement that no more than two jets satisfy the P or Q criteria. The result, Equation 5.2, follows directly.

Examples of equation 5.2 for $N_j = 2,3,4$

$N_j = 2$
$[P(j_1)Q(j_2)+P(j_2)Q(j_1)-P(j_1)P(j_2)]$

$N_j = 3$
$[P(j_1)Q(j_2)+P(j_2)Q(j_1)-P(j_1)P(j_2)](1-Q(j_3))$
$+[P(j_1)Q(j_3)+P(j_3)Q(j_1)-P(j_1)P(j_3)](1-Q(j_2))$
$+[P(j_2)Q(j_3)+P(j_3)Q(j_2)-P(j_2)P(j_3)](1-Q(j_1))$

$N_j = 4$
$[P(j_1)Q(j_2)+P(j_2)Q(j_1)-P(j_1)P(j_2)](1-Q(j_3))(1-Q(j_4))$
$+[P(j_1)Q(j_3)+P(j_3)Q(j_1)-P(j_1)P(j_3)](1-Q(j_2))(1-Q(j_4))$
$+[P(j_1)Q(j_4)+P(j_4)Q(j_1)-P(j_1)P(j_4)](1-Q(j_2))(1-Q(j_3))$
$+[P(j_2)Q(j_3)+P(j_3)Q(j_2)-P(j_2)P(j_3)](1-Q(j_1))(1-Q(j_4))$
$+[P(j_2)Q(j_4)+P(j_4)Q(j_2)-P(j_2)P(j_4)](1-Q(j_1))(1-Q(j_3))$
$+[P(j_3)Q(j_4)+P(j_4)Q(j_3)-P(j_3)P(j_4)](1-Q(j_1))(1-Q(j_2))$

.2.2 *Derivation of P and Q as a function of jet* p_T *and* η

Equation 5.1 is derived, based on the assumption that p_T and η are uncorrelated.

We will to derive an expression for $P(X|AB)$, where ‘X’ is a jet passing the analysis cuts, ‘A’ is the jet’s p_T, and ‘B’ is the jet’s η.

$$P(X|AB) = \frac{P(XAB)}{P(AB)}$$

and

$$P(XAB) = P(X)P(A|X)P(B|AX)$$

The assumption that A and B are uncorrelated implies that:

$$P(AB) = P(A)P(B)$$

and

$$P(B|AX) = P(B|X)$$

so that

$$P(X|AB) = \frac{P(X)P(A|X)P(B|X)}{P(A)P(B)}$$

finally the application of Bayes’ Theorem gives:

$$P(X|AB) = \frac{P(X|A)P(X|B)}{P(X)} = \frac{P(p_T)P(\eta)}{<P>}$$

and similarly for Q.

.2.3 Equivalent forms of Equation 5.3

Equation 5.3 expresses the procedure used to calculate the QCD background. An equivalent form of this equation, given by Equation 11 may be helpful in understanding some of the cross-checks performed in Section 5.5.1.

$$N_{QCD} = \sum_{N_j=2}^{\infty} < Prob(N_j) > \times N_{EVT}(N_j) \tag{11}$$

The factor $N_{EVT}(N_j)$ can be taken directly from data, by multiplying the number of events with N_j jets passing the EF_j15 trigger multiplied by its prescale factor. This gives the number of events that would be expected to be selected by an unprescaled trigger, because the prescale factor represents the number of events that would pass an unprescaled trigger but are rejected by the prescale. Since the CalRatio trigger is unprescaled, this represents the number of events expected to pass the CalRatio trigger.

The factor $< Prob(N_j) >$ represents the average of $Prob(N_j)$ over the expected distribution of jet P_T's and η's in data. In order to reflect the jet distribution expected in data before prescaling, the average must be weighted by the prescale of the trigger selecting each event (Equation 12).

$$\begin{aligned} < Prob(N_j) > &= \frac{\sum_{\text{Each event passing EF\_j15}} Prob(N_j) \times Prescale}{\sum_{\text{Each event passing EF\_j15}} Prescale} \\ &= \frac{\sum_{\text{Each event passing EF\_j15}} Prob(N_j) \times Prescale}{N_{EVT}(N_j)} \end{aligned} \tag{12}$$

Plugging Equation 12 into Equation 11 yields Equation 5.3, the equation used to calculate the QCD background. Though Equations 11 and 5.3 are equivalent, Equation 5.3 is simpler: $< Prob(N_j) >$ and $N_{EVT}(N_j)$ are not calculated separately for each N_j bin; each event in the dataset is weighted by its p_T- and η-dependent probability factor and the trigger prescale, and finally summed.

.2.4 Derivation of P and Q as a function of jet p_T and η

Equation 5.1 is derived, based on the assumption that p_T and η are uncorrelated.

We will to derive an expression for $P(X|AB)$, where 'X' is a jet passing the analysis cuts, 'A' is the jet's p_T, and 'B' is the jet's η.

$$P(X|AB) = \frac{P(XAB)}{P(AB)}$$

and

$$P(XAB) = P(X)P(A|X)P(B|AX)$$

The assumption that A and B are uncorrelated implies that:

$$P(AB) = P(A)P(B)$$

and

$$P(B|AX) = P(B|X)$$

so that

$$P(X|AB) = \frac{P(X)P(A|X)P(B|X)}{P(A)P(B)}$$

finally the application of Bayes' Theorem gives:

$$P(X|AB) = \frac{P(X|A)P(X|B)}{P(X)} = \frac{P(p_T)P(\eta)}{<P>}$$

and similarly for Q.

BIBLIOGRAPHY

[1] Adapted from the Wikimedia Commons file ”Image:Standard_Model_of_Elementary_Particles.svg,” http://en.wikipedia.org

[2] J. Pati and A. Salam, Phys. Rev. D10 (1974), 275. Lepton number as the fourth ”color”

[3] Howard Georgi and Sheldon Glashow, Unity of All Elementary-Particle Forces, Physical Review Letters, 32 (1974) 438.

[4] N. Arkani-Hamed, S. Dimopoulos, S. Kachru and , “Predictive landscapes and new physics at a TeV,” hep-th/0501082.

[5] P. Candelas, G. T. Horowitz, A. Strominger and E. Witten, Symmetry breaking patterns in superstring models, Nucl. Phys. B 258, 46 (1985).

[6] B. S. Acharya, E. Witten and ,“Chiral fermions from manifolds of G(2) holonomy,” hep-th/0109152.

[7] M. Cvetic, P. Langacker and G. Shiu, Phys. Rev. D 66, 066004 (2002) [arXiv:hep-ph/0205252]

[8] R. Blumenhagen, M. Cvetic, P. Langacker, G. Shiu and ,“Toward realistic intersecting D-brane models,” Ann. Rev. Nucl. Part. Sci. **55**, 71 (2005) [hep-th/0502005]

[9] G. Cleaver, M. Cvetic, J. R. Espinosa, L. L. Everett, P. Langacker and J. Wang, Phys. Rev. D 59, 055005 (1999); Phys. Rev. D 59, 115003 (1999).

[10] A. D. Martin, et al., Eur. Phys. J. C **63**, 189 (2009).

[11] S. Dimopoulos et al., Phys.Rev.Lett. **76**, 3494 (1996).

[12] R. Barbier et al., Phys. Rept. **420**, 1 (2005).

[13] D. Tucker-Smith and N. Weiner, Phys. Rev. D **64**, 043502 (2001).

[14] LHC Higgs Cross Section Working Group, S. Dittmaier, C. Mariotti, G. Passarino, and R. Tanaka (Eds.), *Handbook of LHC Higgs Cross Sections: 1. Inclusive Observables*, CERN-2011-002 (CERN, Geneva, 2011), `arXiv:1101.0593 [hep-ph]`.

[15] L. Evans, Annu. Rev. Nucl. Part. Sci. **61** 435 (2011).

[16] T. Cornelissen et. al., ATL-SOFT-PUB-2007-007, (2007).

[17] The ATLAS Collaboration, arXiv:0901.0512 (2008).

[18] The ATLAS Collaboration, ATLAS-CONF-2010-069, (2010).

[19] The ATLAS Collaboration, ATLAS-CONF-2010-005, (2010).

[20] The ATLAS Collaboration, ATLAS-CONF-2010-077, (2010).

[21] The ATLAS Collaboration, ATLAS-CONF-2010-073, (2010).

[22] The ATLAS Collaboration, ATLAS-CONF-2010-015, (2010).

[23] The ATLAS Collaboration, ATLAS-CONF-2010-001, (2010).

[24] The ATLAS Collaboration, ATLAS-CONF-2010-016, (2010).

[25] M. Cacciari, et al., JHEP **04**, 063 (2008).

[26] The ATLAS Collaboration, ATLAS-CONF-2010-038, (2010).

[27] The ATLAS Collaboration, arXiv:1108.5602

[28] The ATLAS Collaboration, ATLAS-CONF-2011-116, (2011).

[29] The ATLAS Collaboration, Eur. Phys. J. C**71**, 1630 (2011).

[30] S. van der Meer, CERN-ISR-PO-68-31, (1968).

[31] S. Agostinelli et al., Nuclear Instruments and Methods, 506 250 (2003).

[32] The ATLAS Collaboration, ATLAS-CONF-2011-031, (2010)

[33] The ATLAS Collaboration, ATLAS-COM-CONF-2012-015, (2012)

[34] L. J. Hall and M. Suzuki, Nucl. Phys. B 231 (1984), 419

[35] S. Dimopoulos, M. Dine, S. Raby and S. D. Thomas, Phys. Rev. Lett. 76 (1996), 3494
C. H. Chen and J. F. Gunion, Phys. Rev. D (1998), 075005

[36] U. Ellwanger and C. Hugonie, Eur. Phys. J. C 13 (2000), 681
S. Hesselbach, F. Franke and H. Fraas, Phys. Lett. B 492 (2000) 140

[37] K. T. Matchev and S. D. Thomas, Phys. Rev. D 62 (2000) 077702

[38] N. Arkani-Hamed and S. Dimopoulos, JHEP 0506 (2005), 073
A. Arvanitaki, S. Dimopoulos, A. Pierce, S. Rajendran and J. Wacker, arXiv:hep-ph/0506242

[39] M. J. Strassler and K. M. Zurek, Phys. Lett. B 651 (2007) 374-379.

[40] M. J. Strassler and K. M. Zurek, Phys. Lett. B 661 (2008) 263-267,

[41] N. Arkani-Hamed and N. Weiner, JHEP 12 (2008) 104

[42] T. Han, Z. Si, K. M. Zurek and M. J. Strassler, JHEP 07 (2008) 008

[43] S. Gopalakrishna, S. Jung and J. D. Wells, Phys. Rev. D78 (2008), 055002

[44] `https://twiki.cern.ch/twiki/bin/view/LHCPhysics/CERNYellowReportPageAt8TeV`

[45] The ATLAS Collaboratoin, *Search for a light Higgs boson decaying to long-lived weakly-interacting particles in proton-proton collisions at* $\sqrt{s} = 7$ *TeV with the ATLAS detector* Phys.Rev.Lett. 108 (2012) 251801

[46] D. Blackburn, G. Ciapetti, A. Coccaro, H. Lubatti, A. Policicchio, D. Ventura, *Triggers for Displaced Decays of Long-Lived Neutral Particles in the ATLAS Detector*, arXiv:1305.2284, and supporting note can be found at https://cds.cern.ch/record/1489578

[47] T. Sjostrand, S. Mrenna and P. Z. Skands, PHYTHIA 6.4 *Physics and Manual*, JHEP 05 (2006) 026 arXiv:hep-ph/0603175,

[48] `https://twiki.cern.ch/twiki/bin/viewauth/AtlasProtected/ExtendedPileupReweighting`

[49] M. Sutton, “Tracking at level 2 for the ATLAS high level trigger,” Nucl. Instrum. Meth. A **582**, 761 (2007).

[50] E. Fullana et al., *Digital Signal Reconstruction in the ATLAS Hadronic Tile Calorimeter*, IEEE447 Transactions on Nuclear Science, 53, 4, 2189 (2006)

[51] Alberto Valero, *Implementation and Performance of the Signal Reconstruction in the ATLAS449 Hadronic Tile Calorimeter*, ATL-TILECAL-PROC-2011-008.

[52] The ATLAS Collaboration, *Improved luminosity determination in pp collisions at sqrt(s) = 7 TeV using the ATLAS detector at the LHC*, Submitted to EPJC, arXiv:1302.4393

[53] S. Alkire, *Line of Fire in Hidden Valley Events*, ATL-COM-PHYS-2011-844

[54] A. L. Read, *Presentation of search results: the CL(s) technique*, Journal of Physics G: Nuclear and Particle Physics **29** (2002) no. 10, 2693

[55] M. Aharrouche, J. Colas, L. Di Ciaccio, M. El Kacimi, O. Gaumer, M. Gouanere, D. Goujdami and R. Lafaye *et al.*, Nucl. Instrum. Meth. A **597**, 178 (2008).

[56] R. Leitner, V. Shmakova, and P Tas *et al.*, ATL-TILECAL-PUB-2007-002.

VITA

Orin Harris was born in Santa Rosa, California, in 1982. He received his Bachelor of Science in physics and mathematics from UC Santa Barbara in 2005. After receiving a Masters of Science from the University of Washington, Seattle, in 2007 he moved to Geneva, Switzerland and joined the ATLAS experiment at CERN. Based on his research, in 2013, Orin earned his Doctor of Philosophy at the University of Washington in Physics.